Synthesis of Carbon Nanotubes on Carbon Supports and the Purification of Carbon Nanotubes

vorgelegt von
M.Sc. Chemistry

Ali Rinaldi
Jakarta

Von der Fakultät II - Mathematik und Naturwissenschaften
der Technischen Universität Berlin
zur Erlangung des akademischen Grades
Doktor der Naturwissenschaften
Dr.rer.nat.

genehmigte Dissertation

Promotionsausschuss:

Vorsitzender:	Prof. Dr. T. Ressler
Berichter/Gutachter:	Prof. Dr. R. Schlögl
Berichter/Gutachter:	Prof. Dr. R. Schomäcker
Berichter/Gutachter:	Prof. Dr. De Chen

Tag der wissenschaftlichen Aussprache: 17. Dezember 2010

Berlin 2010
D 83

Acknowledgements

First and foremost, I would like to offer my greatest gratitude to my supervisor, Prof. Robert Schlögl for giving me the opportunity to work in the Inorganic chemistry department of the Fritz-Haber Institute. Prof. Schlögl has given me the guidance, advice and penetrating criticism throughout my study, which has helped in building my practical and intellectual skills. I would like also to offer my greatest gratitude to Prof. Dangsheng Su, our group leader in the Carbon group where I did my work for 4 years. His continuing support and guidance have allowed me to gain confidence, knowledge and finally finish my study. Their persistence and guidance for producing scientific publications have prepared me well during the writing of this thesis.

I would like also to thank the thesis committee Prof. Reinhard Schomäcker, Prof. De Chen and Prof. Thorsten Ressler for their inputs and patience.

Special gratitude to Dr. Jean-Philippe Tessonnier who has immensely contributed to the development of my scientific journey in the Fritz-Haber Institute. We spent long-hours discussions, critical debates, and with his constructive suggestions and continuous supports he practically nurtured me in these exciting 4 years.

My sincere gratitude is also extended to all the researchers, lab technicians in and fellow students in Inorganic Chemistry of The Fritz-Haber Institute. In particular, I thank the Carbon Group for their generous support and smile during the long hours in the lab and Microscopes. I thank Wiebke Frandsen, Gisela Weinberg, Norbert Pfänder and Achim Klein-Hoffmann for their moral and technical supports especially with the microscopes. I thank Dr. Manfred E. Schuster for acquiring the Titan TEM images and for his continuous support and friendship. Also, I would like to thank Dr. Frank Girgsdies and Dr. Raoul Blume for their technical supports in XRD and XPS and for their critical discussions.

I would like to thank Dr. Benjamin Frank for his always straightforward and efficient suggestions. Also with his technical and scientific support in ODH reaction and TPD experiments. I am excited that our wonderful collaboration has resulted in several publications.

I am indebted to Dr. Olaf Timpe who has over the years helped me in various ways. Interesting discussions to exotic ideas, his encyclopedia-like suggestions, and his diverse laboratory experiences that are always useful for all who laid their hands on the lab. I enjoyed those fantastic times doing exploratory science with the sun. Special thanks for Gisela Lorenz for without her attention and care, students such as my self will find it difficult to reach great discipline in the lab and classroom. I thank Ute Röper, Bärbel Lehmann, Elisabeth Stankewitz, Edith Kitzelmann, Daniel Brennecke, Nuruz Ansari, and Dr. Raoul Naumann for their kind assistance when I was in need of help. Also, I would

like to thank Waruno Mahdi for his knowledge-dense discussions and kind help to proofread my dissertation.

I am indebted to the Max-Planck Gesselschaft and EnerChem the financial support.

Special thanks to Dr. Fachri Atamny for his kind friendship and moral supports. I will always value those moments where he educated me to organize my life.

I appreciate the assistance, moral supports of kind, intelligent and interesting people whom I have had the privilege to know and befriend in the Fritz-Haber Institute. They are Dr. Samer Aburous, Dr. Thomas Hansen, Dr. Bernd Kubias, Jan Mizera, Dr. Aihua Zhang, Dr. Xiaowei Chen, Dr. Juan Delgado, Hermann Sauer, Dr. Mark Willinger, Dr. Di Wang, Dr. Liu Xi, Dr. Jian Zhang, and Dr. Yuri Kolenko.

Also, I would like to give my gratitude to the nice people in AC department who have directly and/or indirectly helped me in anyway possible in the Institute. They are Weiqing Zheng, Sylvia Reiche, Dr. Lidong Shao, Dr. Julian Tornow, Dr. Rosa Arrigo, Till Wolfram, Tom Cotter, Kazuhiko Amakawa, Stefan Kißner, Lenard-Istvan Csepei, Dr. Malte Behrens, Stefanie Kühl, Antje Ota, Dr. Lide Yao, Dr. Wei Zhang, and Dr. Bing Sen Zhang.

It would be difficult to list all of my special and close friends one by one here, but I would like to show my appreciation to all of them for the love, emotional support, laughter, and caring they provided, either from near or far. I feel truly blessed and grateful to have them in my life. There are no words that can thank them enough for lending me their shoulders through the difficult times and making my life so ever colorful for the past 4 years. Special thanks to the people in Masjid Alfalah Berlin (IWKZ.ev) and those lovely friends I shared table with in El Reda.

I wish to thank my beloved little family for providing the constant moral support and love, particularly my wife, Mila, with her support and sacrifice that I manage to survive these tough two years.

Lastly and most importantly, I owe my deepest gratitude to my precious and beloved parents and sister. They have raised me, supported me, loved me and always believed in me. To them, I dedicate this thesis.

Synthesis of Carbon Nanotubes on Carbon Supports and the Purification of Carbon Nanotubes

Ali Rinaldi

Abstract

Carbon materials are of great relevance in catalysis. In heterogeneous catalytic reactions they can act as reactant, poison, catalyst support and as product. The interaction between carbon and supported catalyst remains an unresolved issue of considerable importance in material science, catalysis and nanotechnology. The stability of the catalyst and the carbon support especially under catalyst pretreatment and reaction conditions is also important for their application in catalysis. The first part of this thesis focuses on the catalytic synthesis of carbon nanotubes/nanofibers (CNT/CNF) by ethylene feed on carbon supported-Ni catalyst as the probe reaction to investigate metal-carbon support interaction. Surface and bulk sensitive characterization techniques such as high-resolution transmission electron microscopy (HR-TEM), X-ray diffraction (XRD) and X-ray photoemission spectroscopy (XPS) were used in this investigation. The study shows that carbon atoms from defective supports are not spectator species but are readily incorporated in the Ni, thus forming metastable non-stoichiometric carbide with different catalytic activity than the pure metal. *In-situ* XRD and XPS methods show that atomic carbon dissolved in Ni nanoparticles controls the growth as either CNF or CNT when the catalyst is exposed to ethylene. This work explains many of the differences observed in catalytic activity when metals are supported on carbon, and opens a new approach in heterogeneous catalysis, in that the catalytic activity of metals is adjusted through formation of metastable carbides, either by nano- engineering of the carbon support or by exposing the active phase to an amorphous carbon precursor.

The second part of this thesis deals with the removal of disordered pyrolytic carbon from commercial CNT samples and its effect on the stability of the CNT under oxidative condition. TEM, thermal gravimetric analysis and Raman spectroscopy were used to monitor the efficiency of removing the disordered carbon materials. This study also investigates the effect of disordered pyrolytic carbon on the catalytic performance of the CNT samples for oxidative dehydrogenation (ODH) of ethylbenzene and propane. The methods investigated in this study were mild nitric acid washing, air-oxidation, and ultrasonic irradiation. Ultrasonic irradiation is shown to be the effective method to remove the pyrolytic carbon and oxidation debris from as-received and oxidized CNTs respectively without creating excessive damage to the CNTs. The study also points out the positive trend for the selectivity of styrene and propene in the ODH reactions with increasing graphitic character of the CNT samples.

Die Synthese von Kohlenstoffnanoröhren auf Kohlenstoofträgern und die Aufreinigung von Kohlenstoffnanoröhren

Ali Rinaldi

Zusammenfassung

Kohlenstoffsubstanzen sind von großer Bedeutung in der Katalyse. Sie können als Reagent, Reaktionsgift, Katalysatorenträger, sowie als Produkt einer heterogenen katalytischen Reaktion auftreten. Die Wechselwirkung zwischen Kohlenstoffträger und Katalysator bleibt eine weiterhin ungeklärte Frage von erheblicher Bedeutung für die Materialforschung, Katalyse und Nanotechnologie. Auch die Beständigkeit des Katalysators und des Kohlenstoffträgers, insbesondere unter den bei der Vorbearbeitung des Katalysators herrschenden und den Reaktionsbedingungen, sind bei deren Einsatz in der Katalyse von Bedeutung. Der erste Teil der Dissertation konzentriert sich auf die katalytische Synthese von Kohlenstoffnanoröhren (*carbon nanotube* — CNT) und -nanofasern (*c. nanofiber* — CNF) durch die Zufuhr von Ethylen auf einen Ni-Katalysator auf Kohlenstoffträger als Versuchsreaktion um die Metall-Kohlenstoffwechselwirkung zu erforschen. Es wurden oberflächen- und tiefenempfindliche Darstellungstechniken verwendet, wie hochauflösende Transmissionselektronenmikroskopie (*high-resolution transmission electron microscopy* — HR-TEM), Röntgenbeugung (*X-ray diffraction* — XRD) und Röntgenphotoemissionsspektroskopie (*X-ray photoemission spectroscopy* — XPS). Die Untersuchung ergab, dass die Kohlenstoffatome eines mangelhaft strukturierten Trägers eine keineswegs unbeteiligte Rolle spielen, sondern werden leicht in das Ni einverleibt und bilden somit metastabile nicht-stöchiometrische Karbide, die andere katalytische Eigenschaften aufweisen als das reine Metall. *In-situ* XRD- und XPS-Untersuchungen zeigten, dass in Ni-Nanopartikeln gelöster atomarer Kohlenstoff das Wachstum entweder von CNF oder von CNT bedingt wenn Ethylen auf den Katalysator zugeführt wird. Die Arbeit enträtzelt manche Unterschiede in der zu beobachtenden katalytischen Wirkung von Metallen auf Kohlenstoffträgern und eröffnet einen neuen Ansatz in der heterogenen Katalyse, indem die katalytische Wirkung durch Bildung von metastabilen Karbiden nach Bedarf angepasst wird, entweder durch Nano-Bearbeitung des Kohlenstoffträgers, oder indem die aktive Phase mit der amorphen Kohlenstoffrohsubstanz in Berührung gebracht wird.

Der zweite Teil der Dissertation befasst sich mit der Entfernung von ungeordnetem pyrolytischem Kohlenstoff von kommerziellen CNT-Proben und den Folgen davon auf die Stabilität des CNT-s unter oxidierenden Bedingungen. Zur Erkundung der Wirksamkeit, mit welcher der ungeordnete Kohlenstoff entfernt wurde, sind TEM, thermogravimetrische Analyse und Ramanspektroskopie verwendet worden. Es wurde zugleich auch die Wirkung von ungeordnetem pyrolytischem Kohlenstoff auf die katalytische Wirksamkeit der CNT-Proben bei der oxidativen Dehydrogenisierung (ODH) von Ethylbenzol und Propan untersucht. In dieser Arbeit wurden die Bearbeitung mit schwacher Salpetersäure, die Luftoxidation und die Ultrschallreinigung als verwendete Verfahren untersucht. Die Ultraschallreinigung erwies sich als wirksame Methode zur Entfernung des pyrolytischen Kohlenstoffs und der Oxidationsabfallprodukte sowohl aus unbearbeiteten, wie auch aus oxidierten CNT-Proben, ohne dass diese übermäßig beschädigt wurden. Die Untersuchung ergab auch einen positiven Einfluss auf die Styrol- bzw. Propylenbildungsselektivität in ODH-Reaktionen bei wachsenden graphitischen Merkmalen der CNT-Proben.

Table of Content

Chapter 1: Introduction

1.1 Motivation of this Thesis

Carbon is a versatile material which, depending on its hybridization and assembly in one-, two- or three-dimensional networks, exhibits important electronic and chemical properties with countless practical applications. For example, it is found in printer inks, pencils, water purification systems, thermal isolation and antistatic materials. More elaborate carbon materials such as carbon nanotubes are also employed in nanotechnology, with applications in sensing or field emission. Black carbon is cheap, easy to synthesize and to modify. Thus, it is also particularly suited as a support for heterogeneous catalysis as both the structure (macroscopic shape, porosity) and the surface chemistry can be tailored depending on the target application. In catalysis, the support is known to act on heat and mass transfer but also on the active phase through strong metal-support interactions (SMSI effect). In the case of black carbon, the structural order (graphitic character) adds one level of complexity but also one degree of freedom for logical catalyst design. It is of crucial importance to study how the graphitic character influences the anchoring of the nanoparticles and eventually modifies the catalytic activity of the metal. Varying the graphitic order might offer new and fascinating possibilities for catalyst design.

Carbon materials with tunable microstructure and surface chemical properties are of significant interest for the use as catalyst support. For composites, electronic and porous macroshaping carbon inter-connects; growing secondary carbon nanofilaments onto a carbon fiber support in particular is of special interest.

However there are still issues that have not been made clear about the inertness and structure-activity effect exerted by various carbon supports especially with different graphitic character. Steps and edges are known to be the classical geometric barrier to attach metal nanoparticles however the nature of this interaction remains unclear. There are suggestions especially from amorphous carbon supported metal catalyst that there is already carbon contamination to the catalyst. Nevertheless direct evidence for this interaction is yet to be presented.

This is of great importance especially in the application of CNTs, and CNFs as carbon support as in most cases their surface will be partially coated with disordered pyrolytic carbons. It is also of considerable suspicion that HNO_3 treatment to functionalize and purify CNTs and CNFs sample create oxidation debris as it has been demonstrated previously by experiment with carbon black.

And thus a systematic investigation of reaction involving carbon as support and as catalyst is required. CNT synthesis on carbon supported metal catalyst and oxidative dehydrogenation (ODH) reaction are selected in this work. In addition a novel mild method to remove structural impurities from commercial CNT samples is also proposed.

At the end of the day this thesis should satisfy several points mentioned in the following:

- To prove or probe the metal-carbon interaction of carbon support with different surface character.
- To propose a novel way to control microstructure of CNT especially on carbon support.
- To come with a novel and modest way to remove pyrolytic carbon
- To show the importance of removing pyrolytic carbon for a catalytic reaction

Chapter 2 present the overview of carbon materials commonly used in catalysis. The general synthesis mechanism of soot/pyrolytic carbon and catalytic synthesis of CNTs/CNFs are

discussed. The CNTs/CNFs application as carbon-carbon composite and application as catalyst and catalyst support are addressed. The presence of carbon as impurities in and/or on metal catalyst and the effect in their catalytic activity is discussed. The overview is aimed at highlighting the issues of carbons in their solid graphitic and amorphous forms, atomic and molecular forms, in the adsorbed and dissolved state of atomic carbon on the surface and in the bulk of metals within the discussion of heterogeneous catalysis.

Chapter 3 describes the experimental works and characterization methods used throughout this thesis, such CNT synthesis, Ultrasonication, high-resolution transmission electron microscopy (HR-TEM), Raman spectroscopy, Temperature programmed oxidation (TPO), and Temperature programmed desorption (TPD), in situ X-ray Diffraction (XRD) and in situ X-ray photoelectron Spectroscopy (XPS).

Chapter 4 present the experimental results on the role of carbon supports on the growth of CNTs/CNTs; comparing AC, graphite and herringbone CNFs.

Chapter 5 presents the investigation of metal-carbon support interaction with using CNT synthesis as the probe reaction and VGCNF supports annealed at different temperature as the model support for Ni catalyst

Chapter 6 presents several methods to purify CNT commercial samples from pyrolytic carbon and metal catalyst.

Chapter 7 presents the effect of oxidative purification and heat treatment in the reactivity of the CNT samples for ODH reaction of hydrocarbons.

Chapter 8 presents the conclusion and outlook of the metal catalyst-carbon support interaction, CNT synthesis mechanism, and purification of CNTs from pyrolytic carbons.

Chapter 2: Carbon in Catalysis

2.1. Carbon materials

The element carbon plays a dominant role in the sustainability of life form on earth. The flexibility of bonding with other elements forms the basis of organic chemistry and thus life. From similar argument the flexibility of the carbon-carbon bonding in three different geometries give molecular and solid carbon materials broad range properties to be exploited in various applications. These carbon materials range from nonporous to highly porous, from amorphous to crystalline, from zero-dimension to three-dimensional, from insulator to conductors and from hydrophobic to hydrophilic surfaces. In addition to the uniform bonding geometries, the combination of the three geometries to form carbon-carbon bonds network allows almost unlimited possibilities of carbon materials with each unique properties. Not surprisingly carbon materials have significant economical, industrial and technological importance in today's lifestyle.

Carbon is the sixth element in the periodic table with the ground electronic state having $1s^2\ 2s^2\ 2p^2$configuration. The carbon atom hybridized orbital account for the sp^3, sp^2 and sp configurations of tetrahedral, trigonal and linear symmetries respectively. The sp^3 hybridization is the basis for diamond and aliphatic compounds and the sp^2 hybridization is for graphite and aromatic compounds. The uniform and combination Carbon-Carbon bonding of sp^3 and sp^2 character in carbon materials will be the underlying focus of this chapter and therein in this thesis.

The type of hybridization present in carbon materials will have a profound effect in their properties. Diamond having sp^3 hybridization and tetrahedral

geometry is an isotropic material, transparent, super hard and with a negligible electronic conductivity. Graphite on the other hand with the sp^2 hybridization is anisotropic, soft and a semi metal only within the basal plane. Figure 2-1 shows the unit cell of diamond and graphite.

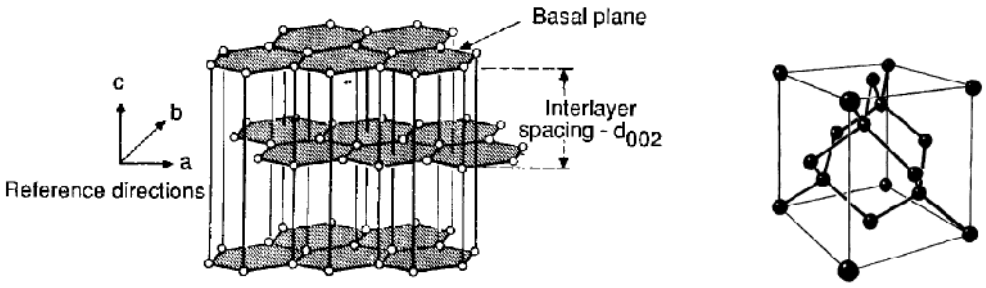

Figure 2-1. The structure of hexagonal graphite with trigonal geometry from sp^2 hybridization (a), the cubic unit cell of diamond having tetragonal bonding geometry from sp^3 hybridization (b).[1]

Thus the inter-nuclear bond length of different hybridizations will be different which will have chemical and physical consequences. The basal plane of graphite is inert and as strong as diamond, where as the interplanar bonds are very weak which gives graphite the soft and lubricant properties. Chemical reactivity is also profoundly different for the basal and the prismatic edge planes in graphite. Combustion in perfect graphite for example will preferably start from the prismatic edges. These anisotropies in graphite of physical and chemical characters are the result of the trigonal geometry. Thus geometrical change of homonuclear carbon materials eg; vacancies, defects, bending, the presence of pentagon- or heptagon-ring within the hexagonal network in graphite will altered these properties. In addition the broad possibilities of hetero elements present in carbon materials due to the moderate electronegativity of carbon are able to modify the electronic properties.

Figure 2-2 shows the example of the wide range of materials with different physical characteristic known in literature due to the different hybridization and

different amount of hetero-element (in the example is hydrogen). Such flexibility is the main reason of the many interest in carbon materials.

The weak interplanar forces in graphite allow for the swelling and the intercalation of atoms and molecules. Depending on the electronic character of the intercalates (donor or acceptor), the electronic properties of the intercalated graphite will be modified. Graphite intercalated SbF_5 and Li are two examples of this type of material as high conductive material and battery applications that have been investigated extensively.[2,3]

Fullerene is another allotrope of carbon. It is a family of molecular carbon cage with all of the carbon in the sp^2 hybridization. Figure 2-3 depicts the chemical structure of C_{60} fullerene. Due to the strain caused by the curvature (facilitated by pentagons to create positive curvature in the hexagon network), fullerenes have profoundly different chemistry from the planar graphite. The planarity of sp^2-hybridized (trigonal) of carbon atoms in graphite implies that the pyramidalization angle of $\theta_p = 0^o$ whereas an sp^3-hybridized (tetragonal) carbon atom requires $\theta_p = 19.5^o$. The deviation from planarity in these molecules reduces the orbital overlap of the π electrons resulting in the localization of the double bonds. The deviation of the orbital hybridization from that of graphite due to the curvature changes the hybridization of the σ bonds. This makes the hybridization of σ bonds in fullerenes to come between sp^3 diamond and sp^2 graphite, depending on the bending angle (Fig 2-3b). As a consequence to this strain, fullerenes are more reactive than graphite. C_{60} for example is highly light and air-sensitive at room temperature.[4]

Other carbon materials known and that have been investigated involves carbon black, onion carbon, activated carbon (AC), soot, amorphous carbon, carbon nanotubes (CNTs), carbon nanofibers (CNFs), carbon fibers (CF), vapor grown carbon fibers [VGCFs] and diamond-like carbons. These materials are combinations of the basics allotropes namely graphite and diamond.

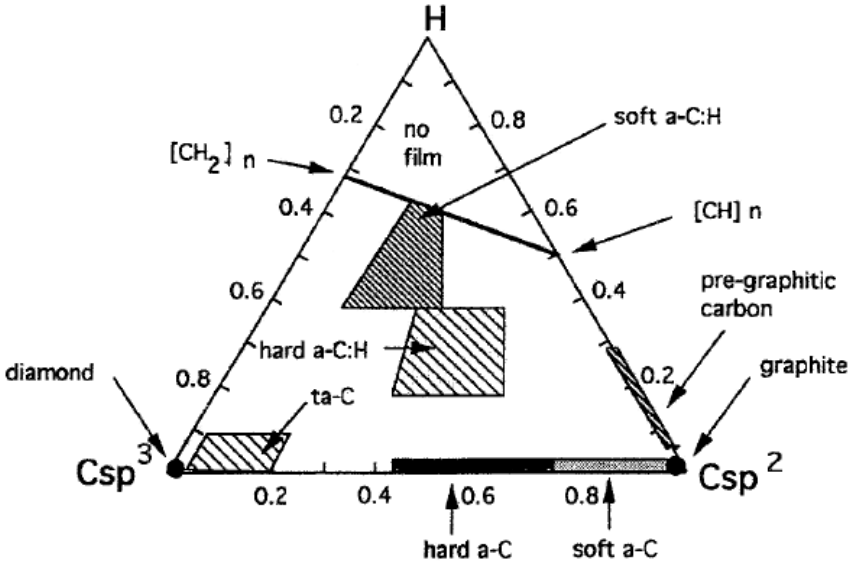

Figure 2-2. Classification diagram of carbon materials.[2]

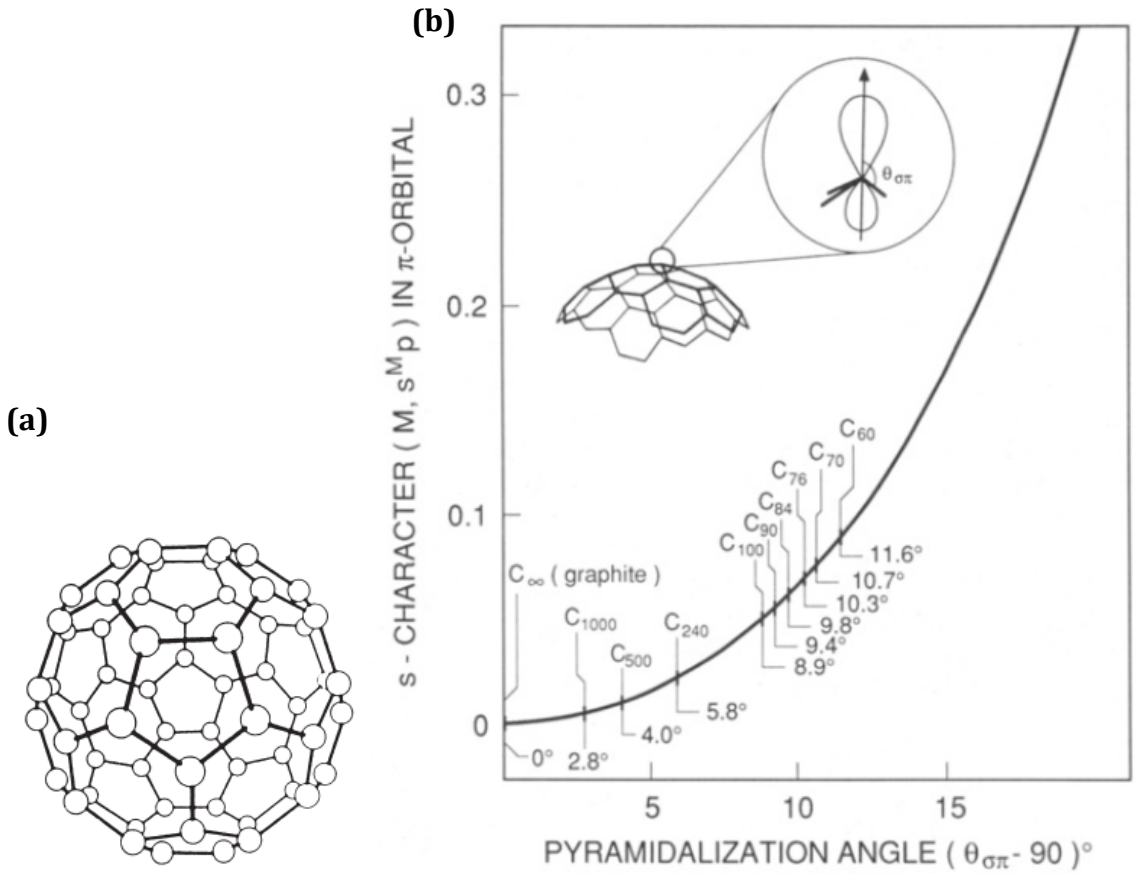

Figure 2-3. The structure of Fullerenes (a) and rehybridization as a function of pyramidalization angle in fullerenes compound.[5]

Similar to fullerene, curvature-induced pyramidalization and misalignment of the π orbitals of the carbon atoms in CNTs and soot induces local strain. And thus CNTs and soot materials are expected to be more reactive than a flat graphene sheet. In the case of CNTs, especially the single-walled CNT (SWNT), the end caps resemble a hemispherical fullerene and this ensures that the end caps will always be reactive compared to the perfect SWNT side-wall.

Carbon black, fullerene black and engine soot are produced from pyrolysis of hydrocarbons or incomplete combustion of fuels (Fig 2-4).[6-10] The growth mechanism and microstructure of these nanocarbon materials have been proposed to resemble that of the fullerene.[7,11] Thus the rich chemistry of these fullerene-like materials originates from the strain of the curved short graphene sheet.[9,12]

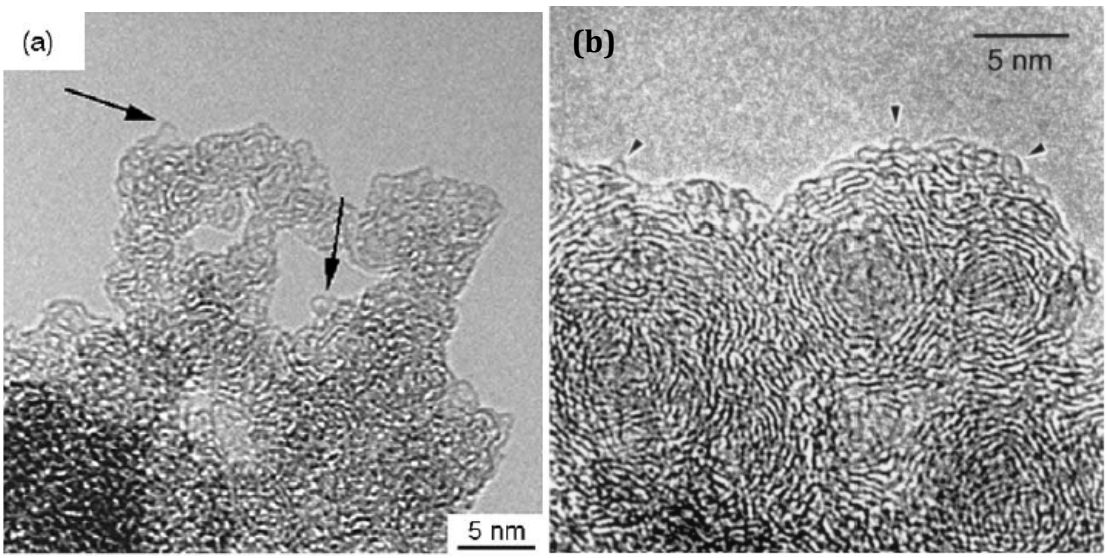

Figure 2-4. HRTEM images of soot samples collected from fuel combustion product showing fullerene-like structure.[6,9]

2.2. Carbon nanofilaments

Filamentous carbons have been extensively investigated as early as 1960s as side products in the petroleum and nuclear industries. Filamentous carbon caused severe technical problems. Various forms and microstructures of filamentous carbon were reported to deposit on metal surface after exposure with carbon-containing gases within a broad range of temperature from 323 to 1000^{o}C. Thus the early works

related to carbon filaments was to control their formation aiming to prevent the carbon deposition. The characterization of the carbon filament and the quantification of both the solid and gaseous product under reaction condition were carried out by the pioneering work of Alstrup and Baker in the 70s for the study of steam reforming catalysis and in situ TEM works respectively.[13]

The investigation of carbon filaments further attracts researchers with the advent of HRTEM followed by the discovery of CNTs by Iijima in 1991.[14] Thus numerous papers arise with respect to the synthesis and applications of filamentous carbon materials.

The filamentous carbon material can have various microstructures; the graphene layer can stack perpendicular, parallel or in a certain inclination angle relative to the filament axis with and without hollow channel. Platelets, herringbone CNFs and CNTs are terms used in the literature to describe filamentous carbon of different microstructure shown in the schematic representation in Fig 2-5.[15]

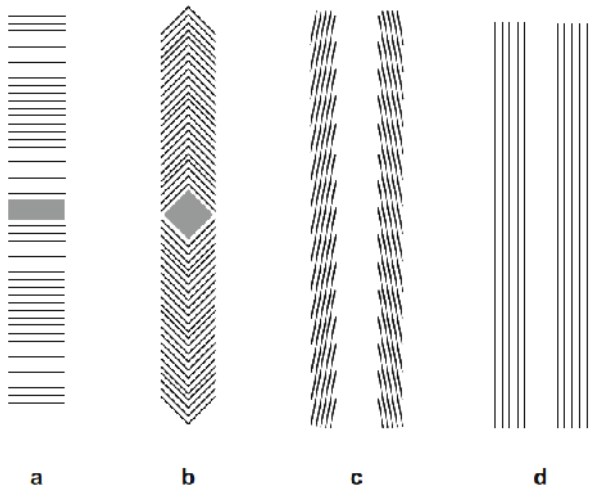

Figure 2-5. Schematic representation of platelet (a) fishbone (b) hollow CNF (c) and Multiwalled CNT (d).

There are several chemical and physical ways to synthesize CNTs such as arc-discharge, laser ablation and chemical vapor deposition (CVD). In the arc discharge

technique CNTs is grown on graphite electrodes during the direct current arc-discharge evaporation of carbon in the presence of inert atmosphere such as He or Ar. The crystallinity of CNTs produced from this method is high, however control of the diameter and length are extremely difficult. The synthesis via arc-discharge requires high-purity graphite electrodes, and He, Ar gasses, thus it makes the process expensive.

Laser ablation is another well-known method to synthesize CNTs. In this method CNTs are grown by laser vaporization of a target composed of graphite and transition metals mixture in He or Ar atmosphere inside a furnace at high temperatures. This technique is not economically advantageous, as it requires high purity graphite targets and high laser power.

The most feasible method to date is Catalytic chemical vapor deposition (CCVD). This method involves the catalytic decomposition of hydrocarbons or CO onto metal nanoparticle surface at temperatures ranging from 450- 1000^{o}C. Under a supported metal catalyst system, the CNTs or CNFs can have base growth or tip growth mechanism depending on for example the metal-support interaction under the reaction condition. Silicon, silica, alumina and graphite are substrates used in the literature to support the metal catalyst. For a given catalyst system, the quality and quantity of the grown carbon nanofilament depends on the reaction condition such as temperature, pressure, carbon source, and growth time. It has been shown extensively that the type of metal, catalyst composition and the support play a significant role in the microstructure of the carbon nanofilament produced[16]. Calcination-reduction and annealing treatments of the catalyst have been shown to play an important role in the filament synthesis.

The CNT synthesis via CVD can also be used without a support. This is normally carried out by flowing a solution of hydrocarbon and metal-organic complex such as Ferrocene or Nickelocene to a furnace. Typical CNTs aggregates produced in normal CCVD (supported catalyst) and floating-CCVD (non supported catalyst) techniques are shown in Figure 2-6. For synthesis from supported catalyst, the support may be destroyed as a result of growth from the inner part of the

support. Similar condition occurred from historical interest of carbon filament growth from steam reforming catalyst where the filament mechanically destroys the catalyst physically and later to some extent chemically.

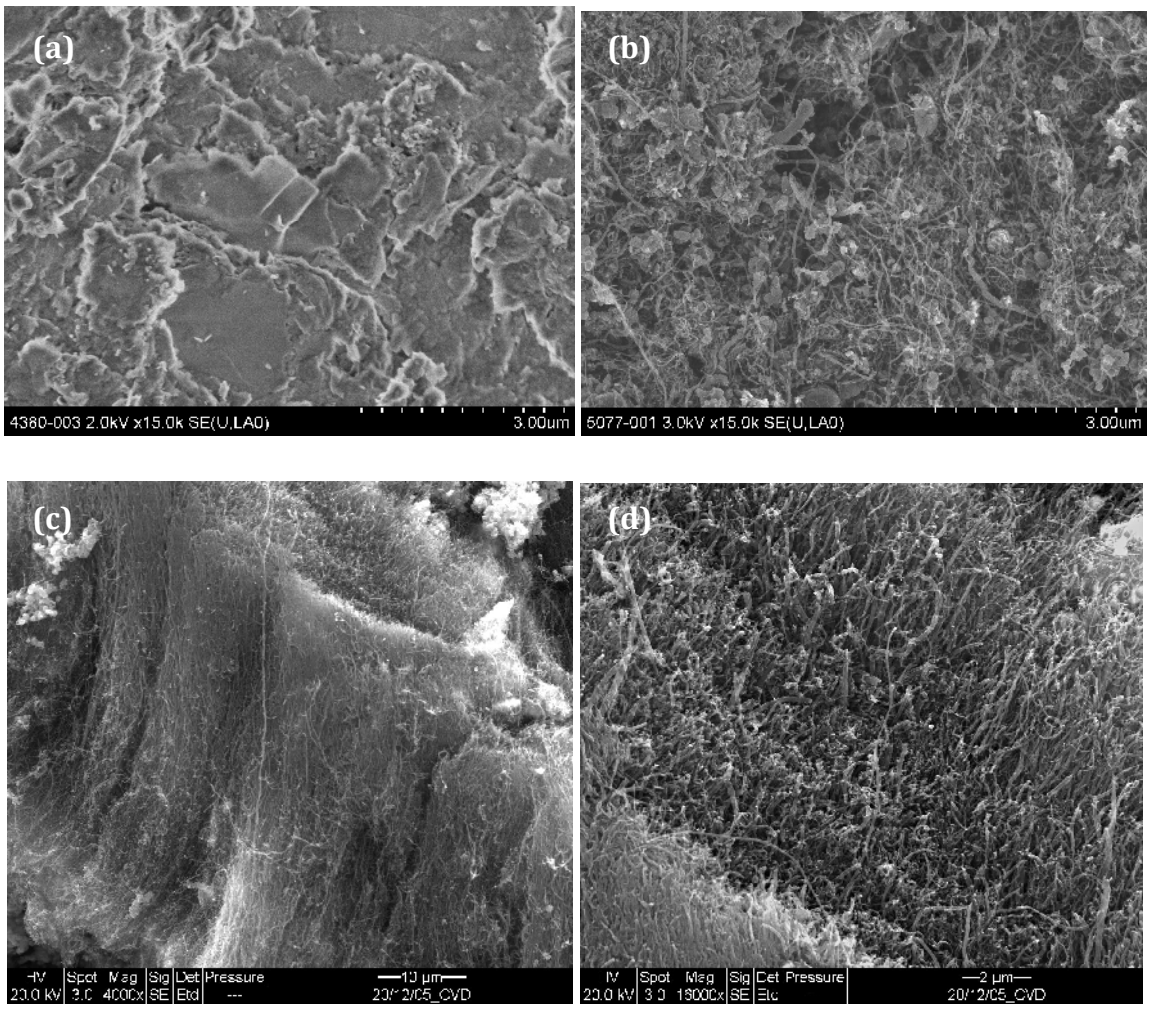

Figure 2-6. Typical entangled CNTs synthesized from CCVD process of supported catalyst showing before (a) and after growth[17] (b) and aligned CNTs from Floating CCVD process using ferrocene as catalyst (c & d).

2.2.1 Carbon nanofilament growth mechanism

Carbon nanofilament synthesis via CCVD method are considered to follow a mechanism where carbon containing gas (or gasses) is first decomposed on the metal nanoparticle surface followed by diffusion of carbon atoms and finally precipitate into graphitic filaments at the other side of the nanoparticle. Since the

early 70s, efforts to obtained detail insight into the CNT mechanism have been carried out with controlled atmosphere electron microscopy (CAEM) by Baker and colleagues.[18] The work demonstrated for the first time that carbon deposition takes place behind an advancing catalyst particle while having the front face of particle remaining clean (Fig 2-7). Kinetic data acquired from the CAEM study revealed that the activation energy for filament growth was about the same as the activation energy of bulk diffusion of carbon in bulk Ni metal.[13,19] The observation led Baker to postulate bulk diffusion of carbon to be the rate limiting step in filament synthesis.

Later in 1984 Tibbetts proposed the idea that the catalytic particles might be liquid during the growth.[20] However the fundamental problem with the idea is that conditions used in CCVD to grow multiwalled CNTs was too low to allow liquefaction of the metal nanoparticles or eutectic mixtures of the metals. In addition Baker had previously pointed out that the activation energy of CNT growth correlates nicely with carbon diffusion in *solid* metals.

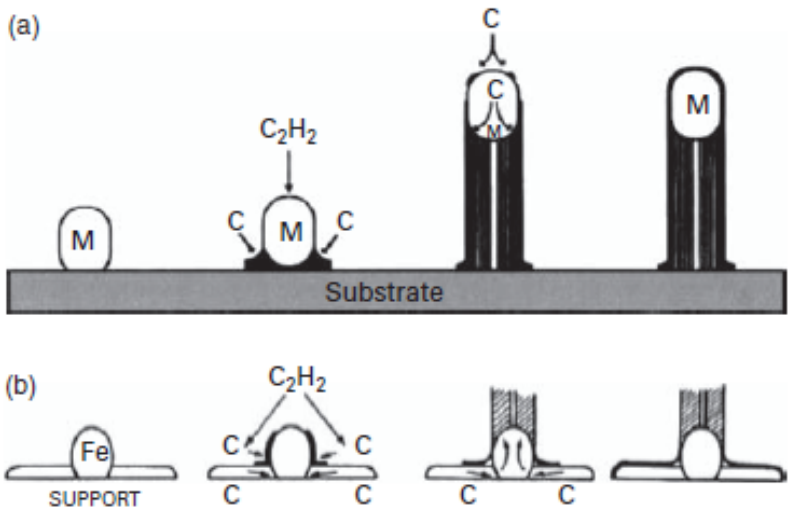

Figure 2-7. An illustration of tip-growth (a) and base-growth (b) mechanism of carbon nanofilament via the bulk and surface diffusion of carbon. The gaseous carbon source is first decomposed on the metal catalyst surface, giving carbon atoms that diffuse through surface and/or the bulk of the catalyst before precipitating as graphitic carbon filament on the other side of the catalyst particle.

An alternative for bulk diffusion of carbon came also in the mid 70s by Baird et al. that suggested the diffusion of carbon on the metal surface.[21] The support for this model came only in 2004 where the advanced improvements in environmental electron microscopy allow the observation of CNT growth at atomic resolution. In the experiment Helveg et al. demonstrated that Ni nanoparticles remain crystalline and metallic throughout the growth process.[22] During the nucleation and growth of graphene layers, the nanoparticles undergo repeated abrupt shape changes driven by reaction between catalyst and carbon vapor. The nanoparticles apparently facilitate the formation of CNTs acting as template as carbon atoms diffuse across the metal surface. HRTEM images in their study revealed monoatomic steps present in the particle and that graphene sheets terminate at these steps. The work also revealed that smaller Ni nanoparticles tend to grow multiwalled CNTs with the graphene sheets aligned parallel to the filament axis whereas larger ones resulted in graphitic herringbone CNFs structure.

Controlled atmosphere HRTEM studies have shown the dynamic of nanoparticles during the nucleation and growth of CNTs and CNFs with different microstructures. During the steady growth occasional interruptions such as the formation of graphene layers perpendicular to the growth axis (bamboo-like structure) and bending were observed. Such interruptions are preceded by nanoparticle shape changes. One can draw an argument that the equilibrium carbon diffusion was interrupted during such process leading to a defective and discontinuity of the graphitic network. Thus the history of the catalyst dynamics can be backtracked by graphitic tracks it left behind.

Another area of controversy on the CNT and CNF growth mechanism is the involvement of metal carbide phase in the growth process. It was proposed that metastable carbide phase is first formed after the exposure of the carbon source and later decomposed into metal and solid carbons. However, Baker and colleagues have shown that carbide is not active to grow carbon nanofilament and that it is not a prerequisite to grow CNT, as Ru (that is not known to form bulk carbide) is quite an active metal to grow carbon filament.[23,19] On the other hand it has been demonstrated by in situ TEM study of multiwalled CNT synthesis that Iron catalyst

forms a stable carbide phases during the course of the growth.[24] The discrepancies for the role of carbide may have originated from the variation of conditions used in the literatures. Other ex situ investigations with Ni and Fe catalysts have suggested the role of carbide as intermediate step and active site for CNT growth.[25,26,27]

The issue of carbon diffusion, its pathways and energy as the origin or consequence of the catalyst structure are thus of crucial importance to the growth process.

The idea that solid carbon can act as carbon source for a given catalyst system to grow carbon nanofilaments has already been proposed. Kanzow et al reported the formation of graphitic filaments by heating fullerene blacks covered with thin Ni films at 1000^{o}C.[28] Studies of single wall CNTs production using laser ablation method suggested the solid-state mechanism model where the growth occurs in the latter stage when the carbons are in the condensed phase. Gorbunov et al and Kataura et al demonstrated the production of SWNT after heating soot obtained from laser ablation of Ni-Co graphite target in inert atmosphere at temperatures <1000^{o}C.[29,30,31] Their reports clearly demonstrate the conversion of disordered carbons into CNTs promoted by metal particles. Due to the high temperature applied for the experiments above it is believed that the metal nanoparticles are in the molten state. An interesting work by Ichihashi et al of amorphous carbon nanofilament conversion into graphitic CNT by Fe catalyst suggests the solid-quasi liquid-solid mechanism of CNT synthesis.[32] They demonstrated the conversion process by annealing experiment inside a TEM instrument. The resolution however was not high enough to notice the Fe atoms arrangements during the nanoparticle movement in the amorphous filament. Similar to the observation by Helveg et al. for CNT growth, the Fe nanoparticles undergo shape changes during the course of the conversion reaction. The shape changes are also shown to be in accordance with the presence of bamboo-like structure in the CNTs. Another similarity to the characteristic of CNT growth is the fragmentation of the nanoparticles during the reaction leaving fragments of smaller nanoparticles in the CNT channels. The experiment demonstrated the best example of how CNT growth and carbon graphitization are very likely to follow the same general

mechanism of carbon-carbon bond breaking, carbon atom dissolution and diffusion and finally graphitic carbon precipitation.

2.2.2. Impurities in and on carbon nanofilaments samples

The CCVD technique is economically more feasible compared to the other techniques with easiness to control the properties of the filaments. However as with the other techniques most CNTs or CNFs produced contain impurities such as pyrolytic carbon and metal catalyst. With very active catalyst the final concentration of the metal catalyst in a batch of CNTs can be very low and thus can be neglected.

Filamentous carbon contains pyrolytic carbon; disorganized form of carbon that mostly coated the outer walls. The extent of coating can vary from one filament to the other within the agglomerate. Some filaments show random coatings and some more homogeneous coatings. The pyrolytic carbon can be easily noticed in TEM images from numerous publications. Figure 2-8 shows the typical example from the commercial as-received CNTs containing pyrolytic carbon.

So far there is only limited knowledge about the microstructure of pyrolytic carbon present as impurities on the CNTs samples.[33] However from the extensive studies concerning soot, carbon black, and non-crystalline carbons, it can be deduced that the microstructure strongly depends on the conditions applied during the CCVD process. For instance, different hydrocarbons as the carbon source may pyrolyze into fragments with different morphology and dimensions attached to the CNTs surface. Thus a broad range of hydrogen content and sp^2/sp^3 hybridization ratios can be expected for the pyrolytic carbon impurities. This variance in nature with the graphite can be expected to bring out particular chemical and physical properties. In comparison with the graphitic structure, pyrolytic carbon exposes more defects per unit volume and allows for additional reactivity at these defects. The pyrolytic impurities tend to enhance functionalization and thereby can induce the combustion of the graphitic CNTs by creating hotspots during their exothermic oxidations.[34]

However such defective carbon coating can also be exploited to produce carbon materials with tunable properties as for example vapor grown CNT (VGCNFs).[35] It is the case, whereby the disorganized carbons are deliberately allowed to coat homogeneously and develop long-range order to a certain extent onto the parent CNTs or CNFs (Figure 2-8d).

Pyrolytic carbon can then be classified based on its hybridization compositions. Broad ranges of sp2-sp3 carbon mixtures are known to exist within the carbon materials with little range order.[36] The hydrogen content can vary broadly within the C-C network. Earlier studies dealing with the mechanism of soot formation have pointed out the polyacetylene and polyaromatics routes for the conversion of hydrocarbon into solid carbons.[37] The involvements of polyacetylene have been ruled in due to the detection in the flames during fuels combustion.[10,37] The concentration of polyacetylene decreases at the region where the size of carbon particles increases. In the case of polyaromatic route, all sooting flames contain aromatic hydrocarbons. In addition this also supports the polyacetylene route, as the polyacetylene will eventually condensate to form polyaromatic structures.[38,39] Despite the ongoing debate to what is the dominant route in the soot formation, there seems to be a general agreement for carbon molecules condensation to involve radicals and ions.[8,40]

From the literature on soot formations mentioned above provoke one to think wether the interaction between pyrolytic carbon and the CNT surface is merely physical and/or also chemical. The interaction is considered physical based from the argument that the CNTs merely provide a surface for the carbon clusters to nucleate. The irregular texture of the pyrolytic carbon provides some kind of a wrapping mechanism on the CNT body. In addition the π- π interaction[41,42] between the polyene and/or polyaromatics with the graphitic surface may lead to the decrease of the nucleation energy of the pyrolytic carbon onto the CNT surface. The fact that the pyrolytic carbon is randomly dispersed onto the CNT surface (not limited to defects sites) provides the argument for the physical interaction.

The support for the argument for the chemical interaction comes from the radical scavenging activity of the CNTs and possible radical generation under the pyrolytic conditions.[43-46] High electrophilicity of CNTs attributed to high strain sites are very likely to be reactive towards the additions with free radicals. Envisaging the CNTs' radical scavenging reactivity, radical-containing soot nuclei and/or developed network of solid carbons can terminate at the high-energy sites on the CNTs. In addition, the graphitic prismatic edges and structural defects in CNTs under CCVD condition (non oxidative atmosphere at high temperatures) can be the initiation sites to potentially catalyze carbon polymerization via free radical mechanism.[47] Finally there would be a covalent C-C bond between the graphitic surface and the pyrolytic carbon. Although there has yet to be literature (at the time when this dissertation was written) that discusses the interaction between graphitic surface on the CNTs and the pyrolytic carbon, the proposed ideas still seem plausible in accordance with the graphite chemistry.

The complexity of pyrolytic carbon is reflected by the broad variation of textures observed from TEM images in the literatures. The various textures include flat, curvy, fullerene-like and soot-like. Such structural variation may also represent a variation of different chemical properties, thus making it rather difficult to generalize a purification method of a specific optimized treatment for a particular sample. Especially with the well-known selective oxidation approach, the reactivity difference between pyrolytic carbon and the parent CNTs can vary broadly. Hence the optimization of a particular method for different samples can vary broadly.

Numerous studies have devoted to the purification of CNT samples with the aim to remove single or multi layers of pyrolytic carbons. The abundant curvature present in pyrolytic carbons allow for their removal with selective oxidation[48] approach by variety of oxidants such as CO_2[49-51] air[52-56] HNO_3[57-61] and H_2O_2.[62,63] The chosen purification method influences the chemical and physical properties of the purified CNTs, i.e. they may open CNT caps, induce CNT fragmentation, and functionalization of inner and/or outer walls. Of all the purification methods, treatment with HNO_3 has drawn most attention due to simplicity and also the advantage to simultaneously remove residual catalyst particles impurities.[57,64,65]

Moderate synthetic condition and more active catalysts lead eventually to a minimum amount of pyrolytic carbon and catalyst impurities. However mono or multi layers coating of pyrolytic carbon and oxidation debris are still frequently observed on as-received and oxidized- CNTs respectively. Such condition is enough to cause problems especially in application under oxidative environment, and application that exploit the contact between a substrate and graphitic surface of the CNTs. Such situation is of crucial importance in catalysis, electrochemistry, and composite sciences. Issues attributed to the effect of carbon microstructure have been addressed in the literatures for the referred applications.

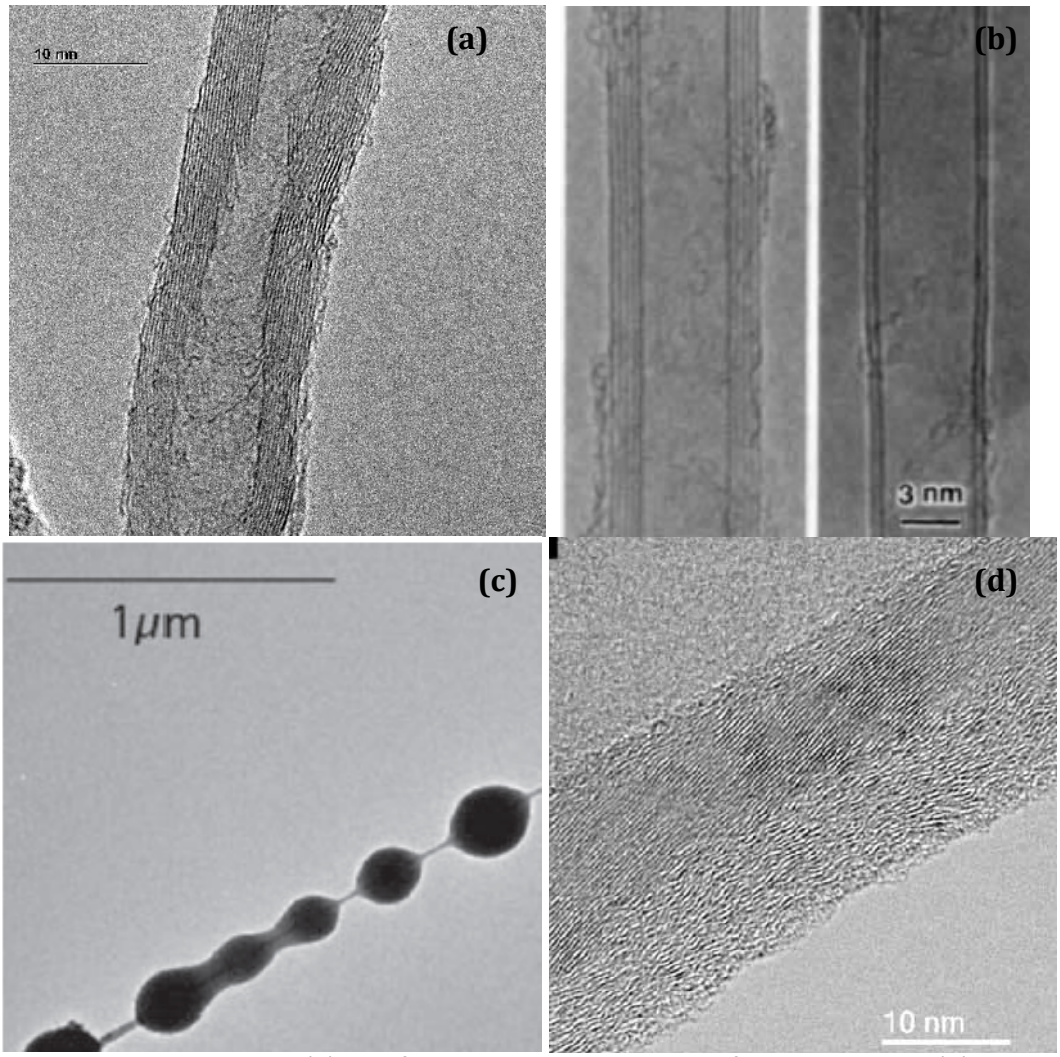

Figure 2-8. Commercial CNTs (a) the first high-resolution TEM of CNTs by Iijima (b), both images show the presence of pyrolytic carbon on the surface if the CNTs.[14] Deliberate deposition of pyrolytic carbon on CNTs is a well-known method to prepare Vapor grown CNTs (c & d).[66,15]

2.3. Application of Carbon nanofilaments

2.3.1. Carbon nanofilaments in composites

Carbon fibers, carbon black, CNTs and CNFs are widely used as reinforcement of certain matrix materials to form composites. Carbon fibers for example were extensively studied for their optimum graphitic structure and surface functionalities to obtain the best mechanical, electrical, magnetic and thermal properties. Methods such as graphitizations, oxidations of the carbon surface and whiskerization have been applied to improve the carbon fiber-matrix interaction.[67,68] The increasing interest of CNFs and CNTs in composites arises from the theorized and proven observations that physical properties of carbon fibers such as surface area, conductivity and strength improves exponentially as the size gets towards the nanoscale regime. Similar to the parent carbon fibers, these CNTs and CNTs materials varied their chemical and physical properties with the microstructure. The ratio of prismatic and basal planes and the presence of structural and topological defects in the graphene layers offer possibility to tune the chemistry and physics of these nanocarbon materials.[69,68]

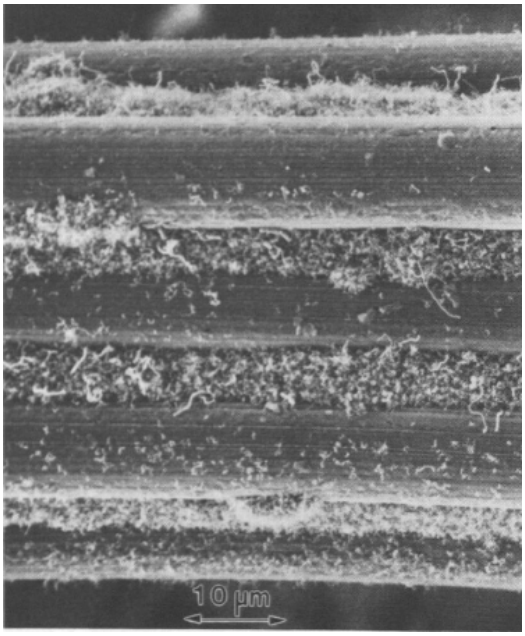

Figure 2-9. Carbon nanofilaments grown on the surface of carbon fibers.[70]

One way to modify both the macro and microstructure of the final carbon material is by directly growing secondary CNFs or CNTs onto a carbon fibers or CNT supports with mono or bimetallic catalyst.[71-77,70,78] Such method is somewhat similar approach to what has been done in material composites with whizkerization of carbon fibers to enhance the carbon-polymer interaction (Fig 2-9).[70] The secondary CNTs or CNFs provide more surface area and depending on the texture of the filament may facilitate further entanglement of the final carbon material resulting in a macroscopic body. Thus eventually the chemistry can be tuned based on the microstructure of the secondary CNTs or CNFs.

The secondary CNFs or CNTs grown on carbon fibers or CNTs support have found other applications in the field of electronics as the conductivity and electrical capacity of the carbon materials was improved.[79,80]

During the past several years, metal-free catalysts have attracted considerable interest, especially in industrial application. However, only graphitic nanocarbons exhibit excellent long-term stability and high catalytic activity.[81,82] On the other hand, the powdery form of nanocarbons makes them unsuitable for use in fixed-bed reactors on an industrial scale. The compactions of loose nanocarbons used in previous work, before being transferred into the reactor, were evidence of severe technical difficulties. Therefore, immobilizing the graphitic nanocarbons onto a carbon-based support allows for better reactants diffusion, and prevents hot spots, pressure drops and avoids chemical discontinuities in such a carbon-carbon composite.[83] Considering the issues described above, mass production of immobilized nanocarbons on a carbon support is desirable for industrial applications in chemical reactors. In the current literature for CNTs and CNFs synthesis, catalytic chemical vapor deposition (CCVD) method is most likely to be the promising method to produce bulk quantity of CNTs and CNFs for composite and other bulk applications.

Albeit the appreciable interest none however have ever discussed or study the effect of metal catalyst on carbon supports with the microstructure of the grown CNFs and/or CNTs.

2.3.2. Carbon nanofilaments in catalysis

Application of carbon materials as catalyst supports have been widely reported with a broad scope of reaction applications.[84,85,86,87,88,89,90,91,92,93] As a support, activated carbon (AC) has attracted much interest because it offers advantages such as high thermal stability, high surface area, and cheap and easy recovery of the metal catalyst by simple combustion. Carbon-carbon composites may represent combinations of carbons having different dimensions (nano with micro) and/or different orderings (graphitic or disordered). Su et al. has successfully synthesized CNFs on AC support with Fe catalyst using C_2H_4 as the carbon source.[94,95] Such composites have found applications both as adsorbents[96,94] and in catalysis.

Carbon materials cannot be used as catalyst supports under high temperature and pressure in oxidative and reducing atmosphere. In details the limits however depend on the graphitic nature of the carbon materials and the type of metal catalyst present on the supports. Nevertheless there are still appreciable interests due to superiority of carbon materials over traditional catalyst support, e.g.;

1. Available in macroscopic shapes[97,83,97-99]
2. Tunable surface chemical properties [100,101,102]

   The possibility to alter the ratio of basal/prismatic plane and controlling the amount of defects present in a carbon material either by selection of type of carbon materials and/or by selection of synthesis conditions with and/or without post treatment allow the attachment of hetero-atoms (O, N, H) on the carbon surface. Such flexibility in carbon allows unlimited possibility to tailor the carbon surface with functional groups.

   Different thermal stability of the surface functional groups allows the control of surface functional groups on carbon material by gradual heat treatments. As a support the type and amount of functional groups on the surface will have a profound role in the dispersion and stability of a catalyst on carbon surface. In addition the surface functional groups have to provide the polarity/affinity for the solvent/solutions for a maximum wetting.

In the preparation of the catalyst the choice of a proper precursor is determined for example by the surface charge of the carbon to achieve maximum interaction between the precursor and the surface anchoring sites.[69] During the calcination, reduction and catalytic reaction, the functional groups have to attain certain stability to allow the anchoring of catalyst particles on its surface and to avoid the sintering of catalyst particles.[103]

3. Tunable electronic properties

Carbon fiber with varying crystallinity and registry of graphene planes orientation has been synthesized and has shown broad range of electronic properties. And it has been shown by Baker et al and De Jong et al that carbon nanofiber with different microstructure exposing different prismatic edges show different reactivity of Pt catalyst.[91,23,104]

2.3.3. Carbon nanofilaments as catalysts for ODH reactions

Activated carbons have shown catalytic reactivity towards Oxidative Dehydrogenation of ethyl benzene into styrene.[105] The microporous carbon material suffers from deactivation due to the polymerized/amorphous carbon deposition blocking the porosity.[106] Selectivity is an issue for AC due to the broad range of surface functionalities present.[105] Nanocarbons, especially CNTs and CNFs have shown promising catalytic activity for ODH reactions.[83,107-109]

The advantage of using carbon material as ODH catalyst is the milder working condition with lower temperature and without the excess supply of steam as in the current industrial process for metal oxide catalyst.[110]

Recently, it was shown that CNTs with surface modification have a high potential for activation of lower hydrocarbons.[107,108,109,111,112] The most sustainable synthesis method for large scale application is the CCVD process. However the produced CNTs show a variety of topological and structural defects and in addition, ill-defined carbonaceous structures originating from pyrolytic carbons are attached to the

surface of the graphitic structure. The deviation from the ideal CNT structure drastically reduces the outstanding mechanic strength, affects the electronic properties, heat conductivity, and chemical stability and thus limits their application. In most cases further post treatments are required to achieve the desired properties.

From the point of view of environment, CNTs as catalyst enable a clean disposal by combustion after a certain lifetime making them attractive alternatives to conventional (toxic) metal oxide catalysts for a more sustainable process of alkene production. Oxidative stability and the catalytic activity make CNTs superior to other classical carbon and nanocarbons for catalysis applications.[81,82] The microstructure and surface functionalities of CNTs have been shown to affect their catalytic performance during the ODH reactions.[113]

2.4. Carbon impurities in metal catalyst: Carbon on surface, subsurface and bulk of metal catalyst

It was generally understood that the presence of carbon on catalyst surface poisons the catalyst. There is a clear correlation between the carbon build up with the loss of activity over time a case of catalyst deactivation.[114,115] However the effect is not always negative. The presences of submonolayer carbon atoms or islands adsorbed onto a metal surface or subsurface or into the bulk of a metal during reaction involving hydrocarbons have been shown to play a crucial role in the activity of the metal catalyst.[116-118]

From considering carbon (on metal surface) as poison, the concept has extended to surface reactivity modifier. The effect of surface carbons was acknowledged from the observations whereby a metal surface, already containing large amount of carbons can still perform reactions involving hydrocarbons at a high rate.

The function of carbon deposits on metal surface have been described to act as dynamic cover for highly reactive (thus non selective) sites[119,120], as a weak

adsorption sites[121], promoter for surface and subsurface reconstruction[122], and as a ligand to modify the electronic structure of the metal.[116]

Extensive investigations from surface science techniques have proposed the presence of broad range of carbon species adsorbed on a metal surface. The carbon species can be categorized into two types; one is the hydrogen-poor deposits and the other is hydrogen-rich carbon deposits, with the latter being more reactive in combustion. The hydrogen-poor deposits can be in a form of monolayer or multilayers of molecular carbons and/or graphitic islands adsorbed on the surface. If the carbon deposits still allow the participation of the metal in a reaction then these deposits may be a part of the active sites.

An example for modifying the surface reactivity is acetic acid decomposition on Pd(110). On Pd surface acetic acid decomposes into CO_2, H_2 gases and adsorbed carbon atoms. On a clean Pd(110) surface the acetic acid decomposes and eventually the adsorbed carbons (atomic and/or molecular) block the sites and deactivate the surface. If the surface was pre-dosed with sub monolayer amount of carbon prior to acetic acid exposure, the decomposition is stabilized and the temperature is shifted to ~60^{o}C higher.[123] The shift indicates that the pre-adsorbed carbons act as poison to the decomposition of acetic acid. However for the pre-dosed surface, at slightly higher temperature, acetic acid decomposes at much longer time even with continuous carbon depositions (diffusing to the bulk) without apparent deactivation.

In the case for acrolein decomposition on a clean surface of Pd(110) at ambient temperature, acrolein dehydrogenates into H_2, adsorbed CO and CH_x. The selectivity of the decomposition however changes to decarbonylation producing C_2H_4 and CO if the metal surface is pre-adsorbed with carbon and the reaction temperature is slightly higher. The decarbonylation selectivity only occurs under such carbon-passivated Pd surface and in a narrow temperature window. At higher temperature the dehydrogenation is again dominant with the carbon deposits diffusing into the subsurface layers. The acrolein decomposition on Pd(110) give the example of how adsorbed carbons can alter the selectivity of metal surface.[123]

Similar to CO hydrogenation, early Temperature programmed reduction (TPR) studies show the presence of several carbon species with different hydrogenation reactivity on the metal surface.[124,125] The carbon species is shown to determine the hydrocarbon production activity of the metal surface. The investigation of iron catalyst for Fischer-Tropsch synthesis with combination of microstructural, bulk and surface sensitive characterizations shows the presence of oxide and carbide after the reaction. The work clearly point out the importance of the carbidic phase for the Fischer-Tropsch reactivity.[126] However the argument that carbidic phase might play a dominant role in Fischer-Tropsch however is still debated due to the fact other catalyst such cobalt and ruthenium do not form carbide under the Fischer-Tropsch conditions.[127] Several studies have revealed a correlation between chain lengthening probability in Fischer-Tropsch catalysts and the extent of carbidization.[118] Due to the lack of microstructural data of the catalyst in study, the possibility for the existence of subsurface or dissolved carbon and their role cannot be excluded. Nevertheless carbon diffusion from surface to subsurface and to the bulk is prerequisite to the presence of carbide or dissolves carbon in the metal catalyst lattice.[128]

The evidence for carbon as a part of the active site in the metal-catalyzed reaction of hydrocarbon is more obvious in the literature. The process is complex and involves numerous carbon species and position; surface, subsurface and dissolved carbons in the metal. Teschner et al have nicely elaborated the model of Pd foil catalyst active in pentyne hydrogenation. They point out the selectivity issue in alkyne hydrogenation with the Pd-C surface phase.[129] The example of the carbonaceous deposits effect in a working catalyst has also been reported for the case of Pt black for n-hexane conversion reactions. An initial induction period of the reaction was observed prior to the rise of selectivity to higher hydrocarbons. The catalyst characterization of that particular period showed the presence of carbonaceous species in and on the Pt catalyst.

The issue with carbon diffusion in metal nanoparticles has long brought the attention in catalysis especially in metal catalyst with appreciable solubility of carbon such as Fe, Co and Ni. The carbon diffusion is proposed to determine the growth of

filamentous carbon, considered as unwanted by-product in e.g. steam reforming catalysis. The lifetime of the catalyst is highly dependent on the carbon diffusion and formation of stable graphitic islands on the metal surface, finally leading to metal encapsulation and/or carbon filament growth. Thus the inaccessible active sites and particle attrition cause the catalyst deactivation. Baker et al first proposed the mechanism of carbon filament growth as hydrocarbon molecule adsorbed on metal surface, (i) decompose, and (ii) the carbon diffuse into the bulk and (iii) precipitate as graphitic carbon deposits.[18] They proposed that the thermal gradient between the exothermic hydrocarbon decomposition and the endothermic graphite precipitation as the driving force for the carbon diffusion. Figure 2-7 shows the schematic representation of the mechanism proposed by Baker et al. Since carbon solubility in a metal decreases with temperature, carbon precipitation will occur on the cooler part of the catalyst particle. Hence according to this model carbon concentration gradient is also the driving force for growth. This thermal gradient argument is however debated as carbon filament can also grown from endothermic decomposition of e g CH_4 , C_4H_{10}, etc.

The bulk diffusion mechanism for carbon filament growth considers the metal to reach carbon saturation prior to nucleation into graphene for CNTs or CNFs. Often due to their elongated /droplet-like shape, the catalyst particles are considered to reach a liquid/molten state. According to the mechanism proposed after the molten metal-carbon solution reaches saturation the carbon filament begin to extrude from the catalyst particle and continuous dissolution of carbon will supply the filament growth process. This so called VLS mechanism (vapor-liquid-solid) was first coined to explain the growth of silicon and germanium filaments and later adopted for carbon filament process.[130] The liquid metal concept was irrelevant for carbon filaments as most CNFs were grown at temperatures way below the expected melting point of a given nanoparticle metal-carbon solution.

The presence of carbon as adsorbate has been shown to exert electronic effect and induce reconstruction of the metal surface. McCarthy and Madix observed a reduction in H and CO binding energy on Ni(110) surface after the surface was populated with submonolayer amount of surface carbons, in

comparison with a clean Ni(110).[131] The reduction was explained as a result of the strong Ni-C bonds that make fewer Ni valence electrons available for bonding with H and CO. Somorjai in the early study has shown reversible reconstruction of Ni(100) face induced by the surface adsorption of carbon.[132,122] The study showed that half a monolayer of carbon adsorbed on Ni(100) face induced the reconstruction of Ni atoms on the surface to be displaced outward and thus allowing the carbon atoms to go deeper to bond with next Ni layer. In addition, as has been shown in theoretical calculation studies and surface science studies with single crystalline metal with certain orientation, carbon atoms and graphene islands have different stability on different surface orientations. The results are in agreement with the faceting observed in catalyst particles during and after carbon filament growth.

The dynamics of carbons as adsorbate and as solute in metal catalyst notably Ni, Co, and Fe are expected to occur in the case of catalytic gasification and catalytic graphitization processes.[133-135] The difficulties for characterization is expected to be greater as the support in these cases is also the substrate. In the extensive work of graphite gasification in oxidative and reducing atmosphere Baker elegantly showed with in situ TEM (Controlled atmosphere electron microscope) a relation between the onsets of catalytic gasification with particle mobility of the particle. He also points out the correlation between the onsets of mobility with the Tamman temperature of a given metal for a series of metals active for carbon gasifications.[136]

In general the initial contact of metal surface with hydrocarbons may give a combination of surface, subsurface carbon species, metastable alkylidine species and also stable graphene islands. The reaction conditions being the most important temperature and partial pressure of gasses involved will decide the distribution of these species. And thus the effect of the carbon deposits on the metal catalyst is temperature and pressure dependent.

References

(1) Marsh, H.; Rodríguez-Reinoso, F. *Activated carbon*; Elsevier, 2006.
(2) Burchell, T. *Carbon Materials for Advanced Technologies*; 1st ed.; Elsevier Science, 1999.
(3) Inagaki, M. *New carbons*; Elsevier, 2000.
(4) Hirsch, A. In *Fullerenes and Related Structures*; 1999; pp. 1-65.
(5) Haddon, R. C. Electronic structure, conductivity and superconductivity of alkali metal doped (C60). *Accounts of Chemical Research* **1992**, *25*, 127-133.
(6) Donnet, J. B.; Johnson, M. P.; Norman, D. T.; Wang, T. K. Fullerenic carbon in carbon black furnaces. *Carbon* **2000**, *38*, 1885-1886.
(7) Homann, K. Fullerenes and Soot Formation— New Pathways to Large Particles in Flames. *Angewandte Chemie International Edition* **1998**, *37*, 2434-2451.
(8) Donnet, J.; Bansal, R. C.; Wang, M. *Carbon black*; CRC Press, 1993.
(9) Müller, J.; Su, D.; Jentoft, R.; Kröhnert, J.; Jentoft, F.; Schlögl, R. Morphology-controlled reactivity of carbonaceous materials towards oxidation. *Catalysis Today* **2005**, *102-103*, 259-265.
(10) Homann, K. H.; Wagner, H. G. Chemistry of Carbon Formation in Flames. *Proceedings of the Royal Society of London. Series A, Mathematical and Physical Sciences* **1968**, *307*, 141-152.
(11) Kroto, H. W. Space, stars, C60 and soot. *Science* **1988**, *242*, 1139.
(12) Cataldo, F. The impact of a fullerene-like concept in carbon black science. *Carbon* **2002**, *40*, 157-162.
(13) Baker, R. T. K.; Harris, P. S. In *Chemistry and Physics of Carbon*; Thrower, P., Ed.; Marcel Dekker Inc.: New York, 1978; Vol. 14, pp. 83-165.
(14) Iijima, S. Helical microtubules of graphitic carbon. *Nature* **1991**, *354*, 56-58.
(15) Tessonnier, J.; Rosenthal, D.; Hansen, T. W.; Hess, C.; Schuster, M. E.; Blume, R.; Girgsdies, F.; Pfänder, N.; Timpe, O.; Su, D. S.; Schlögl, R. Analysis of the structure and chemical properties of some commercial carbon nanostructures. *Carbon* **2009**, *47*, 1779-1798.
(16) O'Connell, M. J. *Carbon nanotubes*; CRC Press, 2006.
(17) Rinaldi, A.; Zhang, J.; Mizera, J.; Girgsdies, F.; Wang, N.; Hamid, S. B. A.; Schlogl, R.; Su, D. S. Facile synthesis of carbon nanotube/natural bentonite composites as a stable catalyst for styrene synthesis. *Chem. Commun.* **2008**, 6528-6530.
(18) Baker, R. T. K.; Barber, M. A.; Harris, P. S.; Feates, F. S.; Waite, R. J. Nucleation and growth of carbon deposits from the nickel catalyzed decomposition of acetylene. *Journal of Catalysis* **1972**, *26*, 51-62.
(19) Baker, R. T. K.; Yates, D. J. C.; Dumesic, J. A. In *Coke Formation on Metal Surfaces*; American Chemical society, 1982; Vol. 202, pp. 1-21.
(20) Tibbetts, G. G. Why are carbon filaments tubular? *Journal of Crystal Growth* **1984**, *66*, 632-638.
(21) Baird, T.; Fryer, J.; Grant, B. Carbon formation on iron and nickel foils by hydrocarbon pyrolysis--reactions at 700°C. *Carbon* **1974**, *12*, 591-602.
(22) Helveg, S.; Lopez-Cartes, C.; Sehested, J.; Hansen, P. L.; Clausen, B. S.; Rostrup-Nielsen, J. R.; Abild-Pedersen, F.; Norskov, J. K. Atomic-scale imaging of carbon nanofibre growth. *Nature* **2004**, *427*, 426-429.
(23) Baker, R. T. K.; Chludzinski, J. J. In-situ electron microscopy studies of the behavior of supported ruthenium particles. 2. Carbon deposition from catalyzed decomposition of acetylene. *The Journal of Physical Chemistry* **1986**, *90*, 4734-4738.
(24) Yoshida, H.; Takeda, S.; Uchiyama, T.; Kohno, H.; Homma, Y. Atomic-Scale In-situ Observation of Carbon Nanotube Growth from Solid State Iron Carbide Nanoparticles. *Nano Letters* **2008**, *8*, 2082-2086.
(25) de Bokx, P. K.; Kock, A. J. H. M.; Boellaard, E.; Klop, W.; Geus, J. W. The formation of filamentous carbon on iron and nickel catalysts : I. Thermodynamics. *Journal of Catalysis* **1985**, *96*, 454-467.
(26) Schaper, A. K.; Hou, H.; Greiner, A.; Phillipp, F. The role of iron carbide in multiwalled

carbon nanotube growth. *Journal of Catalysis* **2004**, *222*, 250-254.
(27) Ni, L.; Kuroda, K.; Zhou, L.; Ohta, K.; Matsuishi, K.; Nakamura, J. Decomposition of metal carbides as an elementary step of carbon nanotube synthesis. *Carbon* **2009**, *47*, 3054-3062.
(28) Kanzow, H.; Ding, A.; Nissen, J.; Sauer, H.; Belz, T.; Schlögl, R. Formation of chains of graphitic nanoparticles by heating fullerene blacks covered with thin metal films **2000**.
(29) Gorbunov, A.; Jost, O.; Pompe, W.; Graff, A. Solid-liquid-solid growth mechanism of single-wall carbon nanotubes. *Carbon* **2002**, *40*, 113-118.
(30) Sen, R.; Suzuki, S.; Kataura, H.; Achiba, Y. Growth of single-walled carbon nanotubes from the condensed phase. *Chemical Physics Letters* **2001**, *349*, 383-388.
(31) Harris, P. J. Solid state growth mechanisms for carbon nanotubes. *Carbon* **2007**, *45*, 229-239.
(32) Ichihashi, T.; Fujita, J.; Ishida, M.; Ochiai, Y. In situ observation of carbon-nanopillar tubulization caused by liquidlike iron particles. *Phys. Rev. Lett* **2004**, *92*, 215702.
(33) Verdejo, R.; Lamoriniere, S.; Cottam, B.; Bismarck, A.; Shaffer, M. Removal of oxidation debris from multi-walled carbon nanotubes. *Chem. Commun.* **2007**, 513-515.
(34) Shimada, T.; Yanase, H.; Morishita, K.; Hayashi, J.; Chiba, T. Points of onset of gasification in a multi-walled carbon nanotube having an imperfect structure. *Carbon* **2004**, *42*, 1635-1639.
(35) Allouche, H.; Monthioux, M. Chemical vapor deposition of pyrolytic carbon on carbon nanotubes. Part 2. Texture and structure. *Carbon* **2005**, *43*, 1265-1278.
(36) Robertson, J. Amorphous carbon. *Current Opinion in Solid State and Materials Science* **1996**, *1*, 557-561.
(37) Lahaye, J.; Prado, G. In *Petroleum Derived Carbons*; ACS symposium Series; American Chemical society, 1976; Vol. 21, pp. 335-347.
(38) Glasier, G. F.; Filfil, R.; Pacey, P. D. Formation of polycyclic aromatic hydrocarbons coincident with pyrolytic carbon deposition. *Carbon* **2001**, *39*, 497-506.
(39) Palmer, H.; Voet, A.; Lahaye, J. Mass spectra of hydrocarbon byproducts in the formation of carbon blacks. *Carbon* **1968**, *6*, 65-70.
(40) Fenoglio, I.; Tomatis, M.; Lison, D.; Muller, J.; Fonseca, A.; Nagy, J. B.; Fubini, B. Reactivity of carbon nanotubes: Free radical generation or scavenging activity? *Free Radical Biology and Medicine* **2006**, *40*, 1227-1233.
(41) Wang, C.; Guo, Z.; Fu, S.; Wu, W.; Zhu, D. Polymers containing fullerene or carbon nanotube structures. *Progress in Polymer Science* **2004**, *29*, 1079-1141.
(42) Curran, S. A.; Ajayan, P. M.; Blau, W. J.; Carroll, D. L.; Coleman, J. N.; Dalton, A. B.; Davey, A. P.; Drury, A.; McCarthy, B.; Maier, S.; Strevens, A. A Composite from Poly(m-phenylenevinylene-co-2,5-dioctoxy-p-phenylenevinylene) and Carbon Nanotubes: A Novel Material for Molecular Optoelectronics. *Adv. Mater.* **1998**, *10*, 1091-1093.
(43) Krusic, P. J.; Wasserman, E.; Keizer, P.; Morton, J.; Preston, K. Radical Reactions of C60. *Science* **1991**, *254*, 1183-1185.
(44) Watts, P. C. P.; Fearon, P. K.; Hsu, W. K.; Billingham, N. C.; Kroto, H. W.; Walton, D. R. M. Carbon nanotubes as polymer antioxidants. *J. Mater. Chem.* **2003**, *13*, 491-495.
(45) Xu, X.; Pacey, P. D. Interactions between acetylene and carbon nanotubes at 893 and 1019 K. *Carbon* **2001**, *39*, 1835-1847.
(46) Fenoglio, I.; Greco, G.; Tomatis, M.; Muller, J.; Raymundo-Piñero, E.; Béguin, F.; Fonseca, A.; Nagy, J. B.; Lison, D.; Fubini, B. Structural Defects Play a Major Role in the Acute Lung Toxicity of Multiwall Carbon Nanotubes: Physicochemical Aspects. *Chemical Research in Toxicology* **2008**, *21*, 1690-1697.
(47) Bandosz, T. In *Carbon Material for Catalysis*; Serp, P.; Figueiredo, J. L., Eds.; John Wiley and Sons, 2008; pp. 68-69.
(48) Brukh, R.; Mitra, S. Kinetics of carbon nanotube oxidation. *J. Mater. Chem.* **2007**, *17*, 619-623.
(49) Smith, M. R.; Hedges, S. W.; LaCount, R.; Kern, D.; Shah, N.; Huffman, G. P.; Bockrath, B. Selective oxidation of single-walled carbon nanotubes using carbon dioxide. *Carbon* **2003**, *41*, 1221-1230.
(50) Delpeux, S.; Szostak, K.; Frackowiak, E.; Béguin, F. An efficient two-step process for producing opened multi-walled carbon nanotubes of high purity. *Chemical Physics Letters*

2005, *404*, 374-378.
(51) Tsang, S. C.; Harris, P. J. F.; Green, M. L. H. Thinning and opening of carbon nanotubes by oxidation using carbon dioxide. *Nature* **1993**, *362*, 520-522.
(52) Li, C.; Wang, D.; Liang, T.; Wang, X.; Wu, J.; Hu, X.; Liang, J. Oxidation of multiwalled carbon nanotubes by air: benefits for electric double layer capacitors. *Powder Technology* **2004**, *142*, 175-179.
(53) Park, Y. S.; Choi, Y. C.; Kim, K. S.; Chung, D.; Bae, D. J.; An, K. H.; Lim, S. C.; Zhu, X. Y.; Lee, Y. H. High yield purification of multiwalled carbon nanotubes by selective oxidation during thermal annealing. *Carbon* **2001**, *39*, 655-661.
(54) Shaffer, M. S. P.; Fan, X.; Windle, A. H. Dispersion and packing of carbon nanotubes. *Carbon* **1998**, *36*, 1603-1612.
(55) Ando, Y.; Zhao, X.; Shimoyama, H. Structure analysis of purified multiwalled carbon nanotubes. *Carbon* **2001**, *39*, 569-574.
(56) Osswald, S.; Flahaut, E.; Ye, H.; Gogotsi, Y. Elimination of D-band in Raman spectra of double-wall carbon nanotubes by oxidation. *Chemical Physics Letters* **2005**, *402*, 422-427.
(57) Hu, H.; Zhao, B.; Itkis, M. E.; Haddon, R. C. Nitric Acid Purification of Single-Walled Carbon Nanotubes. *The Journal of Physical Chemistry B* **2003**, *107*, 13838-13842.
(58) Rinzler, A.; Liu, J.; Dai, H.; Nikolaev, P.; Huffman, C.; Rodríguez-Macías, F.; Boul, P.; Lu, A.; Heymann, D.; Colbert, D.; Lee, R.; Fischer, J.; Rao, A.; Eklund, P.; Smalley, R. Large-scale purification of single-wall carbon nanotubes: process, product, and characterization. *Applied Physics A: Materials Science & Processing* **1998**, *67*, 29-37.
(59) Jia, Z.; Wang, Z.; Liang, J.; Wei, B.; Wu, D. Production of short multi-walled carbon nanotubes. *Carbon* **1999**, *37*, 903-906.
(60) Shao, L.; Tobias, G.; Salzmann, C. G.; Ballesteros, B.; Hong, S. Y.; Crossley, A.; Davis, B. G.; Green, M. L. H. Removal of amorphous carbon for the efficient sidewall functionalisation of single-walled carbon nanotubes. *Chem. Commun.* **2007**, 5090-5092.
(61) Fogden, S.; Verdejo, R.; Cottam, B.; Shaffer, M. Purification of single walled carbon nanotubes: The problem with oxidation debris. *Chemical Physics Letters* **2008**, *460*, 162-167.
(62) Hernadi, K.; Siska, A.; Thiên-Nga, L.; Forró, L.; Kiricsi, I. Reactivity of different kinds of carbon during oxidative purification of catalytically prepared carbon nanotubes. *Solid State Ionics* **2001**, *141-142*, 203-209.
(63) Suzuki, T.; Suhama, K.; Zhao, X.; Inoue, S.; Nishikawa, N.; Ando, Y. Purification of single-wall carbon nanotubes produced by arc plasma jet method. *Diamond and Related Materials 16*, 1116-1120.
(64) Pellicer, E.; González-Guerrero, A. B.; Nogués, J.; Lechuga, L. M.; Mendoza, E. Assessment of catalyst particle removal in multi-wall carbon nanotubes by highly sensitive magnetic measurements. *Carbon* **2009**, *47*, 758-763.
(65) Ismail, A. F.; Goh, P. S.; Tee, J. C.; Sanip, S. M.; Aziz, M. A REVIEW OF PURIFICATION TECHNIQUES FOR CARBON NANOTUBES. *NANO* **2008**, *03*, 127.
(66) de Heer, W. A.; Poncharal, P.; Berger, C.; Gezo, J.; Song, Z.; Bettini, J.; Ugarte, D. Liquid Carbon, Carbon-Glass Beads, and the Crystallization of Carbon Nanotubes. *Science* **2005**, *307*, 907-910.
(67) Donnet, J. *Carbon fibers*; CRC Press, 1998.
(68) Morgan, P. *Carbon Fibers and Their Composites*; 1st ed.; CRC Press, 2005.
(69) Schlögl, R. In *Handbook of Heterogeneous Catalysis*; Ertl, G.; Knözinger, H.; Schüth, F.; Weitkamp, J., Eds.; Wiley-VCH, 2008; pp. 357-427.
(70) Downs, W.; Baker, R. Novel carbon fiber-carbon filament structures. *Carbon* **1991**, *29*, 1173-1179.
(71) Xia, W.; Chen, X.; Kundu, S.; Wang, X.; Grundmeier, G.; Wang, Y.; Bron, M.; Schuhmann, W.; Muhler, M. Chemical vapor synthesis of secondary carbon nanotubes catalyzed by iron nanoparticles electrodeposited on primary carbon nanotubes. *Surface and Coatings Technology* **2007**, *201*, 9232-9237.
(72) Bron, M.; Xia, W.; Chen, X.; Jin, C.; Kundu, S.; Nagaiah, T.; Chetty, R.; Schilling, T.; Li, N.; Schuhmann, W.; Muhler, M. Elektrokatalyse in Brennstoffzellen und Elektrolyseuren: Kohlenstoff-Nanoröhren-basierte Katalysatoren und neuartige Untersuchungsmethoden.

Chemie Ingenieur Technik **2009**, *81*, 581-589.
(73) Duan, H.; Liang, J.; Xia, Z. Synthetic hierarchical nanostructures: growth of carbon nanofibers on microfibers by chemical vapor deposition. *Materials Science and Engineering: B* **2010**, *166*, 190-195.
(74) Handuja, S.; Srivastava, P.; Vankar, V. Utilization of catalyst deactivation for the growth of aligned and random carbon nanotubes by a single-step process. *Physica E: Low-dimensional Systems and Nanostructures* **2009**, *41*, 1210-1216.
(75) Thostenson, E. T.; Li, W. Z.; Wang, D. Z.; Ren, Z. F.; Chou, T. W. Carbon nanotube/carbon fiber hybrid multiscale composites. *J. Appl. Phys.* **2002**, *91*, 6034.
(76) Lim, S.; Yoon, S.; Shimizu, Y.; Jung, H.; Mochida, I. Surface Control of Activated Carbon Fiber by Growth of Carbon Nanofiber. *Langmuir* **2004**, *20*, 5559-5563.
(77) Down, W.; Baker, R. Modification of the surface properties of carbon fibers via the catalytic growth of carbon nanofibers. *J. Mater. Res.* **1995**, *10*, 625-633.
(78) Kurachi, H.; Uemura, S.; Yotani, J.; Nagasako, T.; Yamada, H.; Ezaki, T.; Maesoba, T.; Nakao, T.; Ito, M.; Sakurai, A.; Shimoda, H.; Saito, Y.; Shinohara, H. Formation of Secondary Thin Carbon Nanotubes on Thick Ones and Improvement in Field-Emission Uniformity. *Jpn. J. Appl. Phys.* **2006**, *45*, 5307-5310.
(79) Li, N.; Chen, X.; Stoica, L.; Xia, W.; Qian, J.; Aßmann, J.; Schuhmann, W.; Muhler, M. The Catalytic Synthesis of Three-Dimensional Hierarchical Carbon Nanotube Composites with High Electrical Conductivity Based on Electrochemical Iron Deposition. *Advanced Materials* **2007**, *19*, 2957-2960.
(80) Zhang, J.; Hu, Y.; Tessonnier, J.; Weinberg, G.; Maier, J.; Schlögl, R.; Su, D. S. CNFs@CNTs: Superior Carbon for Electrochemical Energy Storage. *Advanced Materials* **2008**, *20*, 1450-1455.
(81) Mestl, G.; Maksimova, N. I.; Keller, N.; Roddatis, V. V.; Schlögl, R. Carbon Nanofilaments in Heterogeneous Catalysis: An Industrial Application for New Carbon Materials?13. *Angewandte Chemie International Edition* **2001**, *40*, 2066-2068.
(82) Su, D.; Maksimova, N.; Delgado, J.; Keller, N.; Mestl, G.; Ledoux, M.; Schlögl, R. Nanocarbons in selective oxidative dehydrogenation reaction. *Catalysis Today* **2005**, *102-103*, 110-114.
(83) Delgado, J.; Su, D.; Rebmann, G.; Keller, N.; Gajovic, A.; Schlögl, R. Immobilized carbon nanofibers as industrial catalyst for ODH reactions. *Journal of Catalysis* **2006**, *244*, 126-129.
(84) *Handbook of Heterogeneous Catalysis*; Ertl, G.; Kn��zinger, H.; Sch��th, F.; Weitkamp, J., Eds.; Wiley-VCH Verlag GmbH & Co. KGaA: Weinheim, Germany, 2008.
(85) Furimsky, E. *Carbons and carbon-supported catalysts in hydroprocessing*; Royal Society of Chemistry, 2008.
(86) Rodríguez-reinoso, F. The role of carbon materials in heterogeneous catalysis. *Carbon* **1998**, *36*, 159-175.
(87) Rodriguez, N. M.; Kim, M.; Baker, R. T. K. Carbon Nanofibers: A Unique Catalyst Support Medium. *The Journal of Physical Chemistry* **1994**, *98*, 13108-13111.
(88) Kowalczyk, Z.; Jodzis, S.; Raróg, W.; Zielinski, J.; Pielaszek, J.; Presz, A. Carbon-supported ruthenium catalyst for the synthesis of ammonia. The effect of the carbon support and barium promoter on the performance. *Applied Catalysis A: General* **1999**, *184*, 95-102.
(89) Albers, P.; Burmeister, R.; Seibold, K.; Prescher, G.; Parker, S. F.; Ross, D. K. Investigations of Palladium Catalysts on Different Carbon Supports. *Journal of Catalysis* **1999**, *181*, 145-154.
(90) Chambers, A.; Nemes, T.; Rodriguez, N. M.; Baker, R. T. K. Catalytic Behavior of Graphite Nanofiber Supported Nickel Particles. 1. Comparison with Other Support Media. *The Journal of Physical Chemistry B* **1998**, *102*, 2251-2258.
(91) Baker, R. T. K.; Laubernds, K.; Wootsch, A.; Paál, Z. Pt/Graphite Nanofiber Catalyst in n-Hexane Test Reaction. *Journal of Catalysis* **2000**, *193*, 165-167.
(92) Wu, G.; Chen, Y.; Xu, B. Remarkable support effect of SWNTs in Pt catalyst for methanol electrooxidation. *Electrochemistry Communications* **2005**, *7*, 1237-1243.
(93) Bahome, M. C.; Jewell, L. L.; Hildebrandt, D.; Glasser, D.; Coville, N. J. Fischer-Tropsch

synthesis over iron catalysts supported on carbon nanotubes. *Applied Catalysis A: General* **2005**, *287*, 60-67.
(94) Su, D. S.; Chen, X.; Weinberg, G.; Klein-Hofmann, A.; Timpe, O.; Hamid, S. B. A.; Schlögl, R. Hierarchically Structured Carbon: Synthesis of Carbon Nanofibers Nested inside or Immobilized onto Modified Activated Carbon. *Angewandte Chemie International Edition* **2005**, *44*, 5488-5492.
(95) Chen, X.; Su, D. S.; Hamid, S. B.; Schlögl, R. The morphology, porosity and productivity control of carbon nanofibers or nanotubes on modified activated carbon. *Carbon* **2007**, *45*, 895-898.
(96) Bae, S.; Sagehashi, M.; Sakoda, A. Activated carbon membrane with filamentous carbon for water treatment. *Carbon* **2003**, *41*, 2973-2979.
(97) Ledoux, M.; Pham-Huu, C. Carbon nanostructures with macroscopic shaping for catalytic applications. *Catalysis Today* **2005**, *102-103*, 2-14.
(98) Louis, B.; Vieira, R.; Carvalho, A.; Amadou, J.; Ledoux, M.; Pham-Huu, C. Carbon nanofibers grown over graphite supported Ni catalyst: relationship between octopus-like growth mechanism and macro-shaping. *Topics in Catalysis* **2007**, *45*, 75-80.
(99) Pham-Huu, C.; Ledoux, M. Carbon nanomaterials with controlled macroscopic shapes as new catalytic materials. *Topics in Catalysis* **2006**, *40*, 49-63.
(100) Serp, P.; Figueiredo, J. L. *Carbon Materials for Catalysis*; John Wiley and Sons, 2008.
(101) Derbyshire, F.; de Beer, V.; Abotsi, G.; Scaroni, A.; Solar, J.; Skrovanek, D. The influence of surface functionality on the activity of carbon-supported catalysts. *Applied Catalysis* **1986**, *27*, 117-131.
(102) Tessonnier, J.; Rosenthal, D.; Girgsdies, F.; Amadou, J.; Begin, D.; Pham-Huu, C.; Su, D. S.; Schlogl, R. Influence of the graphitisation of hollow carbon nanofibers on their functionalisation and subsequent filling with metal nanoparticles. *Chem. Commun.* **2009**, 7158-7160.
(103) Toebes, M. L.; Prinsloo, F. F.; Bitter, J. H.; van Dillen, A. J.; de Jong, K. P. Influence of oxygen-containing surface groups on the activity and selectivity of carbon nanofiber-supported ruthenium catalysts in the hydrogenation of cinnamaldehyde. *Journal of Catalysis* **2003**, *214*, 78-87.
(104) Zhang, Y.; Toebes, M. L.; van der Eerden, A.; O'Grady, W. E.; de Jong, K. P.; Koningsberger, D. C. Metal Particle Size and Structure of the Metal−Support Interface of Carbon-Supported Platinum Catalysts as Determined with EXAFS Spectroscopy. *The Journal of Physical Chemistry B* **2004**, *108*, 18509-18519.
(105) Pereira, M. F. R.; Órfão, J. J. M.; Figueiredo, J. L. Oxidative dehydrogenation of ethylbenzene on activated carbon catalysts. I. Influence of surface chemical groups. *Applied Catalysis A: General* **1999**, *184*, 153-160.
(106) Pereira, M. F. R.; Órfão, J. J. M.; Figueiredo, J. L. Oxidative dehydrogenation of ethylbenzene on activated carbon catalysts: 3. Catalyst deactivation. *Applied Catalysis A: General* **2001**, *218*, 307-318.
(107) Liu, X.; Su, D. S.; Schlögl, R. Oxidative dehydrogenation of 1-butene to butadiene over carbon nanotube catalysts. *Carbon* **2008**, *46*, 547-549.
(108) Zhang, J.; Liu, X.; Blume, R.; Zhang, A.; Schlogl, R.; Su, D. S. Surface-Modified Carbon Nanotubes Catalyze Oxidative Dehydrogenation of n-Butane. *Science* **2008**, *322*, 73-77.
(109) Frank, B.; Morassutto, M.; Schomäcker, R.; Schlögl, R.; Su, D. Oxidative Dehydrogenation of Ethane over Multiwalled Carbon Nanotubes. *ChemCatChem* **2010**, *2*, 644-648.
(110) Cavani, F.; Trifirò, F. Alternative processes for the production of styrene. *Applied Catalysis A: General* **1995**, *133*, 219-239.
(111) Zhang, J.; Su, D.; Zhang, A.; Wang, D.; Schlögl, R.; Hébert, C. Nanocarbon as Robust Catalyst: Mechanistic Insight into Carbon-Mediated Catalysis13. *Angewandte Chemie* **2007**, *119*, 7460-7464.
(112) Frank, B.; Zhang, J.; Blume, R.; Schlögl, R.; Su, D. Heteroatoms Increase the Selectivity in Oxidative Dehydrogenation Reactions on Nanocarbons13. *Angewandte Chemie International Edition* **2009**, *48*, 6913-6917.
(113) Delgado, J.; Chen, X.; Tessonnier, J.; Schuster, M.; Del Rio, E.; Schlögl, R.; Su, D. Influence

of the microstructure of carbon nanotubes on the oxidative dehydrogenation of ethylbenzene to styrene. *Catalysis Today* **2010**, *150*, 49-54.
(114) Moulijn, J. A.; van Diepen, A. E.; Kapteijn, F. Catalyst deactivation: is it predictable?: What to do? *Applied Catalysis A: General* **2001**, *212*, 3-16.
(115) Duprez, D.; Fadili, K.; Barbier, J. Regeneration of Nickel Catalysts Deactivated by Filamentous Carbon. *Industrial & Engineering Chemistry Research* **1997**, *36*, 3180-3187.
(116) Teschner, D.; Borsodi, J.; Wootsch, A.; Revay, Z.; Havecker, M.; Knop-Gericke, A.; Jackson, S. D.; Schlogl, R. The Roles of Subsurface Carbon and Hydrogen in Palladium-Catalyzed Alkyne Hydrogenation. *Science* **2008**, *320*, 86-89.
(117) Unmuth, E. E.; Schwartz, L. H.; Butt, J. B. Iron alloy Fischer-Tropsch catalysts : I: Carburization studies of the Fe---Ni system. *Journal of Catalysis* **1980**, *63*, 404-414.
(118) Barbier, A.; Brum Pereira, E.; Martin, G. The role of bulk H and C species in the chain lengthening of Fischer-Tropsch synthesis over nickel. *Catalysis Letters* **1997**, *45*, 221-226.
(119) West, L. A. Effects of Surface Disorder, Various Surface Structures of Chemisorbed Gases and Carbon on Helium Atomic Beam Scattering from the (100) Surface of Platinum. *J. Chem. Phys.* **1971**, *54*, 2864.
(120) Bowker, M.; Gilbert, L.; Counsell, J.; Morgan, C. Dehydrogenation versus Decarbonylation of Oxygenates on Pd(110): Pure, Clean Pd Is a Poor Catalyst†. *The Journal of Physical Chemistry C 0*.
(121) Kennedy, D. R.; Webb, G.; Jackson, S. D.; Lennon, D. Propyne hydrogenation over alumina-supported palladium and platinum catalysts. *Applied Catalysis A: General* **2004**, *259*, 109-120.
(122) Somorjai, G. A. In *Bonding Energetics in organometallic compunds*; ACS symposium series; ACS, 1990; Vol. 428, p. 218.
(123) Bowker, M.; Aslam, T.; Morgan, C.; Perkins, N. In *Catalysis in Application*; The Royal Society of Chemistry: Cambridge, 2003; pp. 1-8.
(124) Bartholomew, C. H. Carbon Deposition in Steam Reforming and Methanation. *Catalysis Reviews: Science and Engineering* **1982**, *24*, 67.
(125) McCarty, J. G.; Wise, H. Hydrogenation of surface carbon on alumina-supported nickel. *Journal of Catalysis* **1979**, *57*, 406-416.
(126) Steynberg, A.; Dry, M. *Fischer-Tropsch Technology*; 1st ed.; Elsevier Science, 2004.
(127) Joyner, R.; Darling, G.; Pendry, J. Stability of bulk and surface carbide layers and their relation to the Fischer-Tropsch hydrocarbon synthesis. *Surface Science* **1988**, *205*, 513-522.
(128) Wiltner, A.; Linsmeier, C.; Jacob, T. Carbon reaction and diffusion on Ni(111), Ni(100), and Fe(110): Kinetic parameters from x-ray photoelectron spectroscopy and density functional theory analysis. *J. Chem. Phys.* **2008**, *129*, 084704.
(129) Teschner, D.; Vass, E.; Hävecker, M.; Zafeiratos, S.; Schnörch, P.; Sauer, H.; Knop-Gericke, A.; Schlögl, R.; Chamam, M.; Wootsch, A.; Canning, A. S.; Gamman, J. J.; Jackson, S. D.; McGregor, J.; Gladden, L. F. Alkyne hydrogenation over Pd catalysts: A new paradigm. *J. Catal.* **2006**, *242*, 26-37.
(130) WAGNER, R. VAPOR-LIQUID-SOLID MECHANISM OF SINGLE CRYSTAL GROWTH (NEW METHOD GROWTH CATALYSIS FROM IMPURITY WHISKER EPITAXIAL + LARGE CRYSTALS SI E). *TRANSACTIONS OF THE METALLURGICAL SOCIETY OF AIME* **1965**, *233*, 1053.
(131) McCarty, J. G.; Madix, R. J. The adsorption of CO, H2, H2, CO2 and H2O on carburized and graphitized Ni(110). *Surface Science* **1976**, *54*, 121-138.
(132) Somorjai, G. A. The flexible surface. Correlation between reactivity and restructuring ability. *Langmuir* **1991**, *7*, 3176-3182.
(133) Anton, R. On the reaction kinetics of Ni with amorphous carbon. *Carbon* **2008**, *46*, 656-662.
(134) Holstein, W.; Moorhead, R.; Poppa, H.; Boudart, M. In *Chemistry and Physics of Carbon*; Marcel Dekker Inc.: New York.
(135) Baker, R. T. K. In *Carbon and coal gasification: science and technology*; Figueiredo, J.; Moulijn, J., Eds.; NATO ASI; Springer: Dordrecht, 1986; pp. 231-268.
(136) Baker, R. T. K. In Situ Electron Microscopy Studies of Catalyst Particle Behavior. *Catalysis Revs.* **1979**, *19*, 161-209.

Chapter 3:

Experimental and Characterization methods

3.1. The synthesis of CNT from carbon supported Ni catalyst

3.1.1. Impregnation of Ni catalyst on AC

The AC was derived from palm kernel shell obtained from NanoC sdn bhd. Malaysia. The AC was previously treated with concentrated HNO_3 (70%, Sigma Aldrich) to eliminate inorganic impurities, such as Fe and Si, which would lead to heterogeneity of the produced CNFs. Later in the following text, AC is referred as the HNO_3-treated support. The AC samples were ground and sieved to a ≤50 μm particle size before impregnated via the wet-impregnation method with $Ni(NO_3)_2$ in an acetone solution to achieve Ni weight loading of 1%. The samples were further dried overnight at 40^{o}C in static air. Microscopy image of the AC support is shown in Figure 3-2a.

3.1.2. Impregnation of Ni catalyst on graphite

As-received graphite sample (TIMCAL SFG150) was impregnated with 0.1M $Ni(NO_3)_2$ acetone solution to achieve ~1 wt% Ni content. The impregnated graphite was then dried at room temperature overnight. Acetone was chosen as the solvent considering the hydrophobicity of graphite surface. Calcination, reduction and growth conditions were of similar temperatures, gas compositions, reactor and swinging speed with that of CNT synthesis

on Ni/activated carbon. The ethylene/Hydrogen exposures were performed for 2, 5, 60 and 120 min.

The as-received graphite sample was obtained from TIMCAL with average grain size of 150 microns and surface area of 1.6 m^2/g. Microscopy image of the graphite support is shown in Figure 3-2b.

3.1.3. Impregnation of Ni catalyst on VGCNF

Commercial vapor-grown carbon nanofibers (Pyrograf Products Inc., U.S.A.) annealed at either 900^o C (product PR24-PS, referred to as defective carbon support) or 3000^{o}C (product PR24-HHT, referred to as graphitized carbon support) were impregnated with $Ni(NO_3)_2$ in acetone using the incipient wetness technique. The description of the carbon supports is presented in Chapter 4. The Ni concentration was set to achieve a 5 wt% Ni loading. The impregnated samples were dried at 25^{o}C overnight. Microscopy images of the VGCNF supports are shown in Figure 3-2c &d.

3.1.4. Carbon nanofilament synthesis

Calcination, reduction and growth were carried out stepwise in a tubular quartz reactor (UTPI, Figure 3-1 and appendix 3-1). Calcination was performed at 250^{o}C under 5% O_2 in He for 1 h ramping from ambient temperature at 5 K/min. The calcined sample was subsequently reduced at 300^{o}C under 15% H_2 in He for 1 h before ramping 5 K/min to growth temperature at 700^{o}C in He. The sample was exposed to a C_2H_4/H_2 gas mixture for 5 min before cooling (natural cooling) to ambient temperature under He.

For CT synthesis on Ni/AC the growth time set at 60minutes and the growth temperature were varied from 500-850^{o}C.

For CNT synthesis on Ni/graphite the growth time were varied from 2 – 120 min.

For CNT synthesis on Ni/VGCNF (labeled defective and graphitic carbon) the growth time was set for 5 min.

In the case of the pre-dosing experiment for Ni/graphitic carbon, the reduced catalyst was exposed to 1 or 3 mL of C_2H_4 at 300, 400,450 and 500°C before continuing to ramp (5 K/min) to growth temperature 700°C in Argon gas. The purity of the gasses used are as follows: C_2H_4 (99.95%), He (99.999%), H_2 (99.999%), Ar (99.999%) and O_2 (99.999%).

Scheme 3-1 show the general growth procedure used in this thesis. Table 3-1 present the CNT growth experiments reported in this thesis.

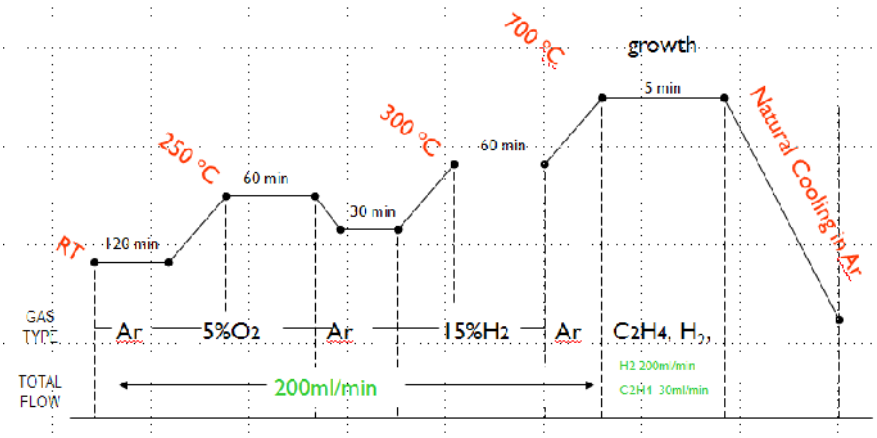

Scheme 3-1. Calcination, reduction and CNT growth procedure used in this thesis.

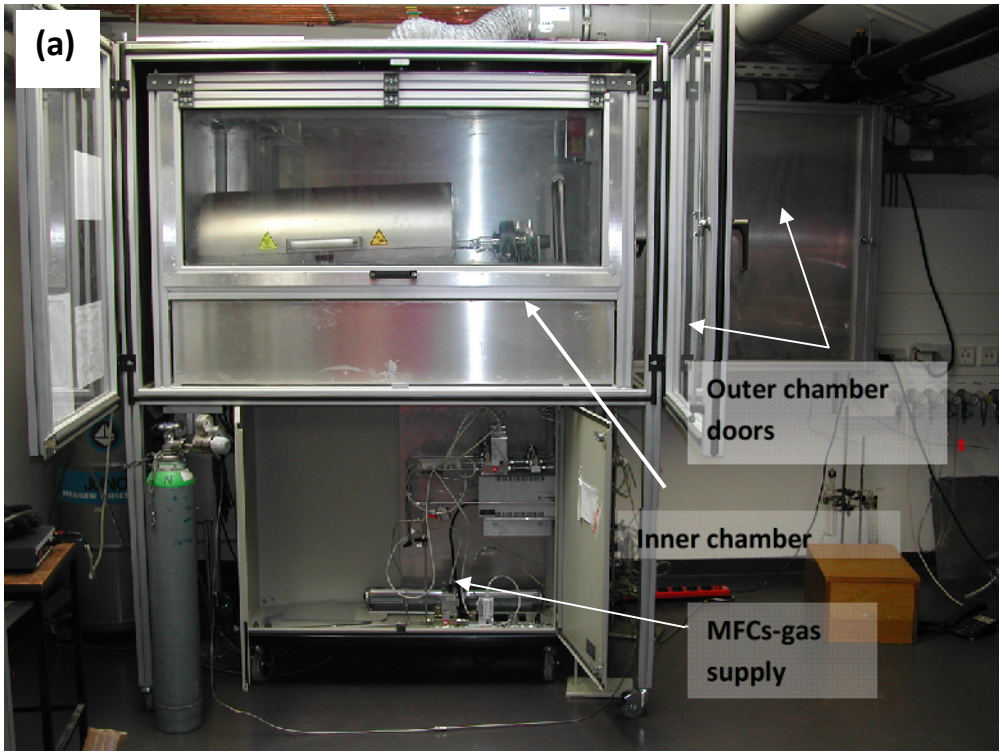
(a)
Outer chamber doors
Inner chamber
MFCs-gas supply

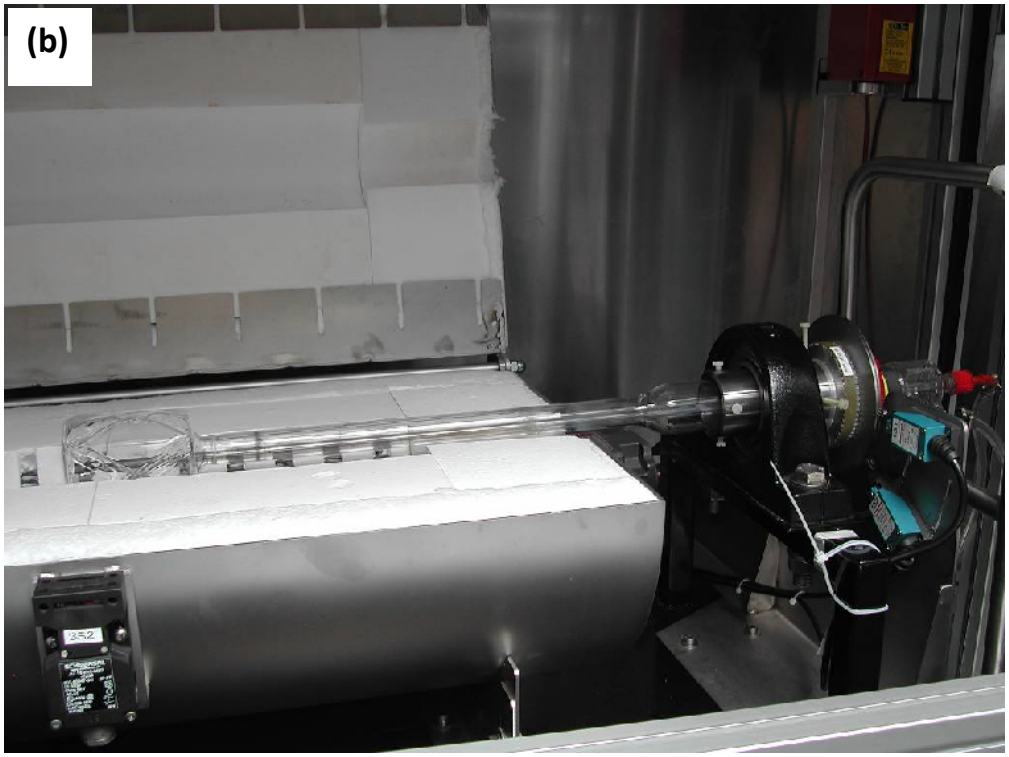
(b)

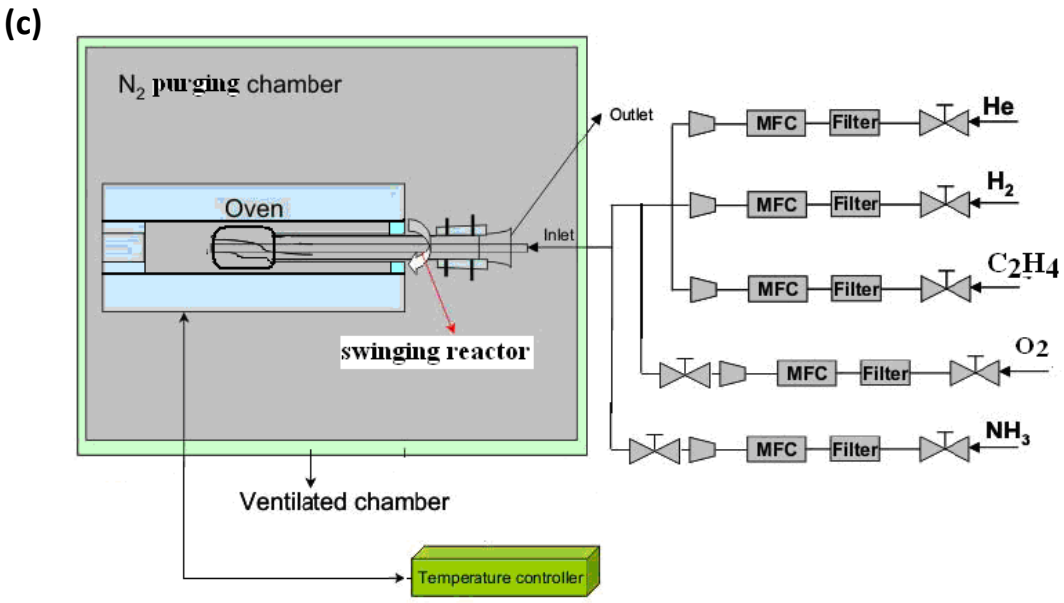

Figure 3-1. Overview photograph of the UTP furnace (a) inside the furnace (b) and the schematic diagram of the gas lines (c). The N_2 purging chamber is a security measure to avoid O_2 from the atmosphere to diffuse into the hot zone and the reactor.

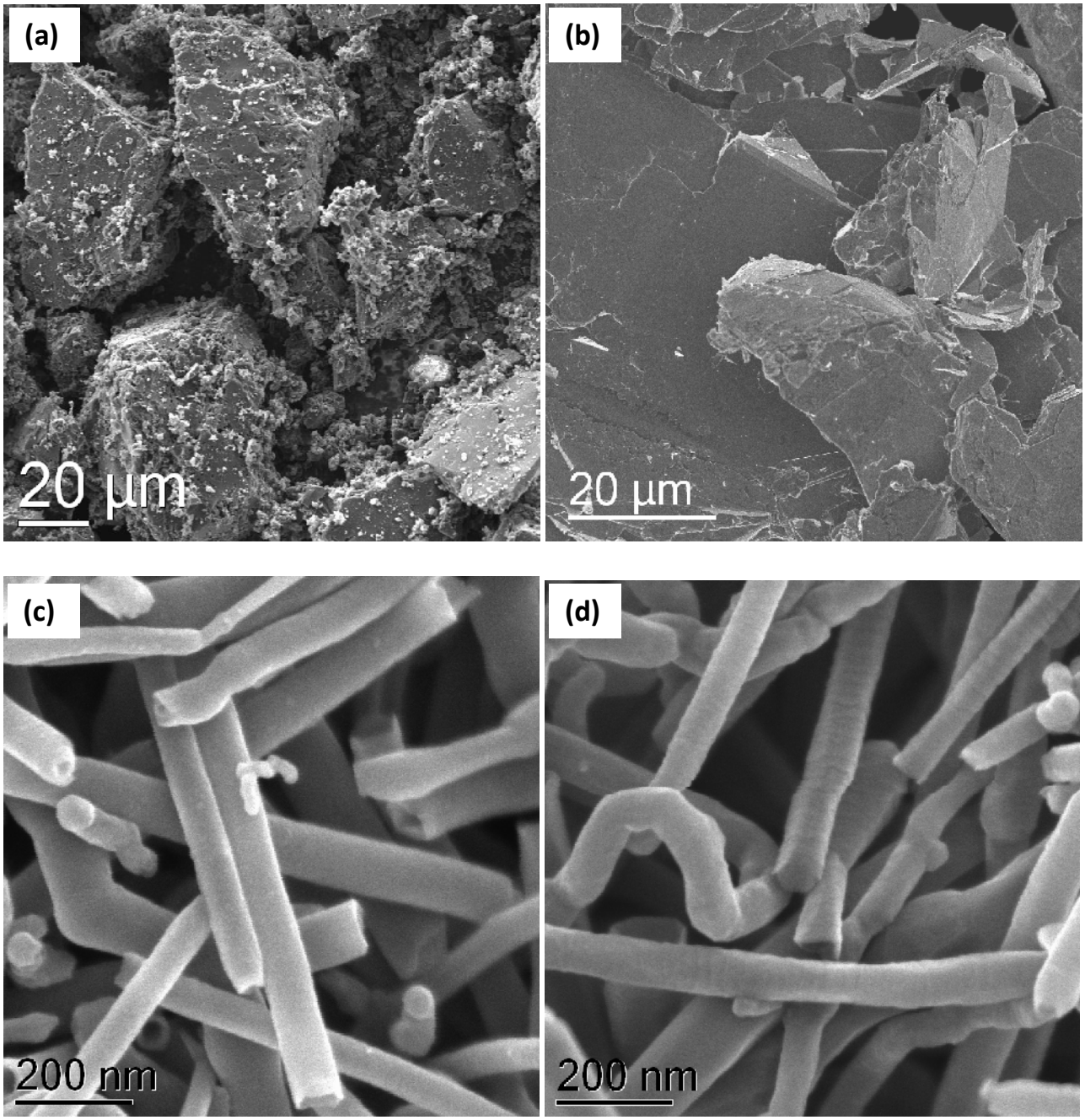

Figure 3-2. SEM images of Carbon materials used as support for Ni catalyst to grow CNTs and CNFs. AC (a), graphite (b) defective VGCF (c) and graphitic VGCNF (d). The carbon supports present different shapes, texture and graphitic ordering. The disordered microporous AC support show granules shape of 50um in average size (a), nonporous graphite support showing flakes of 150um in average size and the macroporous VGCFs with filamentous shape with the average outer diameter of 150nm (c & d). Notice that the high temperature annealing treatment transformed the surface of VGCF from smooth (c) into jagged surface(d).

Table 3.1. CNT growth experiments by 1wt% Ni supported on carbon reported in this thesis. Catalyst activation is as follows: Calcination (cal) was performed at 250^{o}C for 1 h in 5%O_2/Ar, Reduction (red) 300^{o}C 5% H_2/Ar 1 h, Heat treatment (HT) 5% H_2/Ar 1 h at growth temperature.

Carbon Support	**Catalyst Treatment**	**Growth Temperature (^{o}C)**	**Growth time (min)**
AC	Cal-red	500	120
AC	Cal-red	550	120
AC	Cal-red	600	120
AC	Cal-red	600	180
AC	Cal-red	600	240
AC	Cal-red	600	300
AC	Cal-red	700	120
AC	Cal-red	850	120
AC	Cal-red-HT	500	120
AC	Cal-red-HT	550	120
AC	Cal-red-HT	600	120
Graphite	Cal-red	550	120
Graphite	Cal-red	700	2
Graphite	Cal-red	700	5
Graphite	Cal-red	700	10
Graphite	Cal-red	700	60
Graphite	Cal-red	700	120
PR24-PS (defective)	Cal-red	700	5
PR24-HHT (graphitic)	Cal-red	700	5

3.2. Removal of amorphous carbon from CNT surface

The pristine CNT samples used in this study were purchased from NC3100 (Nanocyl, Belgium) and Baytubes (Bayer). The CNTs are of multiwalled tubular structure with an average external diameter of approximately 9 nm. The microstructural and textural details of these two commercial samples are given in the beginning of Chapter 6.

3.2.1 Mild HNO_3 treatment

The CNTs were dispersed in water by ultrasonication for 10 min prior to the treatment with 3 M HNO_3 at room temperature for 24 h under stirring followed by filtration and washing with water. The obtained black solid was treated with 1 M NaOH under stirring for 24 h, subsequently filtered and subjected to a 24 h Soxhlet extraction with water and another 24 h with acetone, followed by drying in an oven at 100^{o}C for 24 h under air.

For ODH experiments in Chapter 7 the washed CNTs were subjected to heat treatment in a graphite oven under flowing Ar flow at 900, 1300, and 1700^{o}C for 2 h. The samples were cooled in Ar to room temperature prior to the exposure to air.

3.2.2 Ultrasonic Irradiation of CNTs

One of the common usages of ultrasonic treatment has been for cleaning purposes. In fact most chemical laboratories will have access to an ultrasonic cleaning bath. When ultrasonic wave of high power is applied to a liquid system, cavitations process may take place. Cavitation is the formation, growth and the collapse of the bubbles in the liquid. The ultrasonic wave produces alternating compression and rarefaction of the liquid irradiated. During the rarefaction part of the ultrasonic wave irradiation the micro bubbles containing liquid vapour or dissolved gas are formed. The stability of the micro bubbles depends on the energy of the ultrasonic wave and physicochemical properties of the liquid, and the dissolved solute and/or gas.

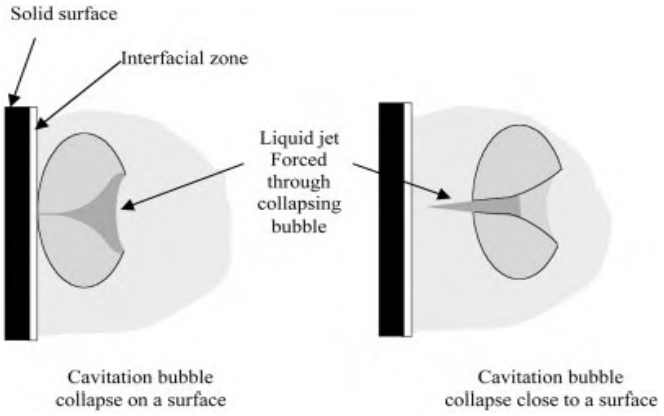

Figure 3-3. Graphical representation of the effect of ultrasonication in a liquid near a solid surface.[1]

The micro bubbles can either be stable at a certain size for many cycles or continue to grow until finally violently collapse or implode. The implosion is the attractive part in the exploitation of ultrasonic in many applications e.g. medical, biology, and environmental. Figure 3-3 shows the graphical representation of the implosion process. It is claimed that the implosion energy reached as high as 1000 atm in pressure and temperatures up to 4700^{o}C creating a micro-sized hotpots.[2] Especially in the application of sonocation for chemical reaction (sonochemistry) the increase in reactivity is rationalized from the hot spots and mass transport perspective.

Mechanical mixing as a result of acoustic streaming (movement of liquid by the sonic wave) in sonocation have been attributed to be one of the cause for activity increase in for example reaction involving emulsions and in phase-transfer catalyst system. That however is not the cavitation effect in sonochemistry.

In catalysis, recent developments in the delaminated zeolite materials have also demonstrated the usefulness of the ultrasonic irradiation to increase the pore size for better accessibility of reactants in the microporous channels.[3] Sonocation have shown advantages in catalyst preparations where the impregnation efficiency of metal precursor onto a support is

increased. In the case of palladium catalyst supported on alumina and activated carbon, sonocation have been reported to significantly improve the dispersion. [4,5]

Aside from the acoustic mixing, especially in metal surfaces the cavitation implosion can create local deformations effect, provide cleaning effect from impurities and surface oxides and cause surface pitting. All of which can have consequences in the synthesis/population of active sites on a catalyst surface.

An interesting example in catalysis with respect to nanoparticles is the synthesis of amorphous metal by sonocation.[6] The amorphous metal was demonstrated to exhibit an order of magnitude increase in activity at lower temperature for Fischer-Tropsch reaction and dehydrogenation of saturated hydrocarbons in the case of amorphous iron.[7,8] The nanoparticles prepared by sonocation can be synthesized as supported or unsupported system.[1] Other nanostructured materials generated by high-intensity ultrasonic irradiation have been reported to be active for hydrocarbon reforming and CO hydrogenation.[9]

There are several examples in the literature where the microstructure of the nanoparticles can be altered in the ultrasonic-assisted synthesis by changing the solvent.[10] The support microstructure for the ultrasonic-assisted synthesis of nanoparticles was shown to play a role in the distribution of metal nanoparticles.[11] In the case of Pd nanoclusters, there is a prospect and certainly a challenge to prepare the Pd via ultrasonic-assisted method with varying percentage of interstitial carbon from the sonolysis decomposition of organic-containing precursor.[12]

To summarize, there are broad range of possibilities of what ultrasonic irradiation can achieve in nanoparticles synthesis in general and especially for catalysis[13].

The effect of ultrasonic treatment was investigated for pristine Baytubes as well as for the oxidized Baytubes. For oxidation treatment the pristine CNT sample was washed with 3 M HNO_3 at ambient temperature for 24 h followed by filtration and rinsing with deionized water. For the ultrasonic irradiation experiments 1gram of CNT sample were suspended in a 10% by volume of ethanol/water solution. A probe-type Ultrasonic Homogenizer GM2200

manufactured by Bandelin with the sound frequency of 20 kHz and 200 W of maximum power output was used. The ultrasonic treatment was performed at 10% power in pulse mode with an active interval of 0.5 s. The temperature of the suspension was kept constant at 0-4^{o}C in an icebath. The obtained solid was subsequently washed with warm 1 M NaOH followed by Soxhlett extraction with water and acetone, respectively, each for 24 h.

3.3. Characterization Techniques

3.3.1 Electron Microscope

The electron microscopes used throughout the work of this thesis are as follows:

1. A Hitachi S-5200 Scanning Electron Microscope (SEM) coupled with EDX detector for elemental analysis was used to investigate the surface morphologies of the nanoparticles and of the VGCNFs. The samples under investigation have been deposited on conduction carbon tape. All images were acquired using an acceleration voltage of 3 kV for better resolution of surface features, and 15 kV to investigate the inner cavity of the VGCNFs.
2. A TEM equipped with a LaB_6 emitter (Philips CM200) operated at 200 kV was used to perform overview investigations of particle size and carbon nanofilament (CNF or MWCNT) microstructure.
3. For high resolution images (Chapter 4) The samples were characterized ex-situ for high resolution investigations by a Cs-corrected transmission electron microscope operated at 80-300 kV (FEI Titan).

3.3.2 X-ray Diffraction

The *in-situ* XRD data was collected on a STOE Theta/theta X-ray diffractometer equipped with Paar XRK 900 in-situ reactor chamber. The wall of the reactor was kept at 25^{o}C by a cooling

water thermostat. Calcined samples were packed on the catalyst bed in the *in-situ* cell to obtain plain and smooth sample surface. The calcined sample was then reduced (in H_2/He atmosphere at 300^{o}C for 1 h), exposed to C_2H_4 (only in the case for the pre-dosing experiment at 400^{o}C) and exposed to C_2H_4 for CNT growth (at 700^{o}C). The system was allowed to cool down to 25^{o}C under He environment for XRD measurements after each subsequent step. The XRD patterns were acquired with Cu Kα radiation using a secondary graphite monochromator and a scintillation counter. The scanning angle range was 20-90^o 2θ with a step width of 0.02^o and counting time of 10 s/step.

A fundamental parameters approach of X-ray line-profile fitting of the samples follows the Double-Voigt Approach.[14] In the Double-Voigt Approach, the sample contribution to the peak profile is a convolution of two Voigt functions, one of which has a 1/cos(θ) dependence attributed to crystallite size related peak broadening, while the other one has a tan(θ) dependence attributed to strain related broadening. This approach may be considered as an indirect application of a Williamson-Hall analysis.[15,16] In a Williamson-Hall analysis, the peak widths are determined individually and plotted, multiplied with cos(θ), on the y axis as a function of 4sin(θ) (x axis). Then the data points are fitted with a straight line, with the intercept representing the crystallite or domain size and the slope the strain. The Double-Voigt fitting procedure implemented in Topas implicitly assumes that this correlation is valid, describing all calculated peak profiles in a way that they fall on such a straight line. The "size" and "strain" fit parameters represent the intercept and slope of this line. The advantage of this approach is that it is possible to extract physically reasonable parameters even if the peak profiles overlap significantly, a case where a direct Williamson-Hall analysis must fail because the individual peak profiles cannot be extracted. The Double-Voigt Approach will fail if the peak profiles do not exhibit the implied dependence, resulting in a fit with systematic deviations of the calculated from the measured peak shapes.

3.3.3. X-ray photoelectron spectroscopy

The *in-situ* XPS experiments were performed at the ISISS beamline located at the BESSY II synchrotron. The calcined samples were pelletized and transferred into the reaction cell. The cell temperature was raised to 300^{o}C under 0.5 mbar of H_2 for reduction and ramped to 700^{o}C in inert before finally exposing to C_2H_4 at 0.5 mbar. For the pre-dosing experiment the reduced sample was exposed to 0.5 mbar of C_2H_4 at 400^{o}C. The spectra were collected immediately after each treatment in vacuum without further cooling. The probe size was ~ 100 µm x 1 mm. The $Ni2p_{3/2}$ spectra were acquired at a photon energy of 1050 eV with a spectral resolution of 0.3 eV and electron mean free path of 7 Å. Background correction was performed by using a Shirley background. The spectra were fitted using the Levenberg-Marquardt algorithm to minimize the χ^2. Peak shapes were modeled by using asymmetric Doniach-Sunjic functions convoluted with Gaussian profiles. The accuracy of the fitted peak positions is ≈ 0.05 eV.

3.3.4. Texture and porosity

The textural properties of the AC support and CNF/AC composite were measured on the basis of the N_2 isotherm performed with a Quantachrome instrument. Surface area and micropore volume were calculated using the Dubinin-Radushkevich (DR) equation. The mesopore volume was determined as the difference between the total pore and micropore volume.

For the investigation of commercial CNTs purification: Specific surface areas (BET method) were determined from the N_2 adsorption isotherm (Quantachrome, Autosorb-1) carried on out-gassed samples (vacuum, 200^{o}C, 2 h). Whereas the pore size distribution were calculated following the BJH equation.

3.3.5. Raman spectroscopy

Raman spectroscopy is a sensitive method to changes that distort the translational symmetry of graphite.[17] the dominant features are the Raman-allowed line at 1580 cm^{-1} and the disorder-induced line at 1360 cm^{-1}. In addition a feature near 1620 cm^{-1} is seen in some samples. In particular in the commercial CNT samples used in this thesis, the contribution of the 1360 cm^{-1} and 1620 cm^{-1} are quite appreciable suggesting that the samples very likely contain other carbonaceous materials such as amorphous carbon and polyene like material originating from the pyrolysis of hydrocarbons. Indeed the commercial CNT samples used in the current study contain the structural characteristic to that of carbon black and soot (Figure 3-4).

Raman spectroscopy was done on HORIBA Jobin Yvon spectrometer at an excitation line 633 nm 10x objectives. The spectra were collected at acquisition time of 120 sec. From the fitting procedure[18] the ratio of the D and G intensity ($\mathbf{I_D/I_G}$) was extracted for a semi-quantitative analysis of the presence of defective and graphitic carbon in the sample.

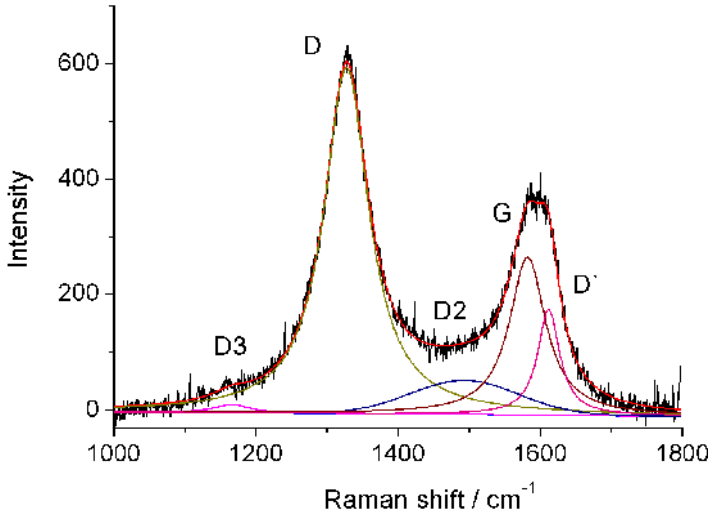

Figure 3-4. Fitting procedure of Raman spectrum from commercial CNT sample. The Lorentzian peak at 1600 cm^{-1} (G) results from the graphitic structure of the sample, the lorentzian peak at 1320 cm^{-1} (D) is attributed to the presence defects and edges. The lorentzian peak at 1620 cm^{-1} (D`) and 1180 cm^{-1} (D3) are assign to small graphite domains and polyene-like carbons respectively. The Gaussian peak at 1500 is assigned to amorphous carbon.[18]

3.3.6. Thermal analysis

The thermal analysis for the carbon sample was carried out as follows:

1. Temperature programmed Desorption (TPD)

   Desorption experiments were performed on a quartz tubular reactor (7mm inner diameter) with approximately 0.5 g of sample. The sample is flown with 25 ml/min of Helium. The sample is first flushed at 100^{o}C for 1 hour to remove the desorbed water and followed by 10 K/min to 850^{o}C. The gases evolved were analyzed with MS (analyzed mass: 4, 18, 28, and 44) and analyzed with GC instrument every 3minutes at 30^{o}C per step.

2. Temperature programmed oxidation (TPO)

   The oxidative purification treatment of the CNTs was monitored by thermal analysis system comprising TGA (STA-449 Netsch) equipped with a mass spectrometer (Pfeiffer Omnistar, Avi applied vacuum GmbH) as a detector. Each analysis was performed with 5mg of sample powder at 5 K/min with 5% O_2 in Argon (total of 100ml/min).

   T_{50} is used as an indicative variable to put the combustion reactivity into a value. T_{50} is the temperature where the relative weight decreases 50%.

   In principle the TPO/TG profile changes with increasing heterogeneity in the sample. With respect to the treatment applied in this thesis, the effect can involves the change in the amount of amorphous carbon and/or pyrolytic carbon, and the change in the defects density. The change in the graphitic character of the sample will lead to the decrease of the defect density and increase of the activation energy of the combustion reaction. Removal of catalyst particles from the carbon sample will also lead to the increase of energy activation of combustion, Interpretation of the data involves the expected response from changes that involves catalyst impurities, amorphous carbon and/or pyrolytic carbon and finally the sample's defect density. (Appendix 3-2)

3. Temperature programmed Reduction (TPR)

   The temperature-programmed reduction of the Ni/AC fresh sample was carried out under 5% H_2 in N_2 with a temperature ramping of 5 K/min using a Netzcsh TG/SDTA coupled with an MS quadruple Omnistar detector.

3.3.7. Oxidative Dehydrogenation (ODH) reactions

The ODH reactions of ethylbenzene (EB) to styrene (ST) as well as of propane to propene were performed in conventional quartz tubular reactors of 6 mm inner diameter. 50 mg of selected CNT samples were placed between two quartz-wool plugs. For ODH of ethylbenzene the reactant gas mixture comprises EB (2.1%), O_2 (O_2/EB=1) and He with the total flow rate of 15 mL min^{-1}. The flow rate was set to be free from film diffusion within the kinetic regime.[19] For ODH of propane, the reactant concentrations and flow rate were somewhat higher (C_3H_8/O_2/He = 2.5/2.5/45 mL min^{-1}). The temperature was increased up to 400^{o}C with a ramp of 20 K/min in pure He flow and then the reaction was started. The chemical compositions of reactant and product mixture, which allowed for the calculation of ethylbenzene and propane conversions as well as styrene and propene selectivities, were quantified by a gas chromatograph (Varian CP-3800) equipped with TCD and FID detectors. Prior to taking the used CNTs samples for further characterization, the reactor was cooled down to ambient under He. For both substrates at the given reaction conditions, the experiment without catalyst revealed no hydrocarbon conversion (detection limit of the GC is in the low ppm range for hydrocarbons). Thus, the observed reactions can be solely referred to the reactants interaction with the catalyst surface.

References

(1) Mason, T. J.; Lorimer, J. P. *Applied sonochemistry*; Wiley-VCH, 2002.
(2) Didenko, Y. T.; McNamara, W. B.; Suslick, K. S. Hot Spot Conditions during Cavitation in Water. *Journal of the American Chemical Society* **1999**, *121*, 5817-5818.
(3) Corma, A.; Fornes, V.; Pergher, S. B.; Maesen, T. L. M.; Buglass, J. G. Delaminated zeolite precursors as selective acidic catalysts. *Nature* **1998**, *396*, 353-356.
(4) Giannantonio, R.; Ragaini, V.; Magni, P. Dispersion measurement by the single introduction method coupled with the back-sorption procedure: A chemisorption and TPD study of the different chemisorbed hydrogen species : I. Pt, Ru, and Rh on Alumina. *Journal of Catalysis* **1994**, *146*, 103-115.
(5) Ragaini, V.; Giannantonio, R.; Magni, P.; Lucarelli, L.; Leofanti, G. Dispersion measurement by the single introduction method coupled with the back-sorption procedure: A chemisorption and TPD study of the different chemisorbed hydrogen species : II. Pd on Alumina. *Journal of Catalysis* **1994**, *146*, 116-125.
(6) Koltypin, Y.; Fernandez, A.; Rojas, T. C.; Campora, J.; Palma, P.; Prozorov, R.; Gedanken, A. Encapsulation of Nickel Nanoparticles in Carbon Obtained by the Sonochemical Decomposition of Ni(C8H12)2. *Chemistry of Materials* **1999**, *11*, 1331-1335.
(7) Suslick K.S.[1]; Hyeon T.; Fang M.; Cichowlas A.A. Sonochemical synthesis of nanostructured catalysts. *Materials Science and Engineering: A* **1995**, *204*, 186-192.
(8) Suslick, K. S.; Hyeon, T.; Fang, M.; Cichowlas, A. A. In *Advanced Catalysts and Nanostructured Materials*; Academic Press: San Diego, 1996; pp. 197-212.
(9) Suslick, K. S.; Hyeon, T.; Fang, M. Nanostructured Materials Generated by High-Intensity Ultrasound: Sonochemical Synthesis and Catalytic Studies. *Chemistry of Materials* **1996**, *8*, 2172-2179.
(10) Dhas, N. A.; Gedanken, A. Sonochemical preparation and properties of nanostructured palladium metallic clusters. *J. Mater. Chem.* **1998**, *8*, 445-450.
(11) Zhong, Z.; Mastai, Y.; Koltypin, Y.; Zhao, Y.; Gedanken, A. Sonochemical Coating of Nanosized Nickel on Alumina Submicrospheres and the Interaction between the Nickel and Nickel Oxide with the Substrate. *Chemistry of Materials* **1999**, *11*, 2350-2359.
(12) Okitsu, K.; Mizukoshi, Y.; Bandow, H.; Yamamoto, T. A.; Nagata, Y.; Maeda, Y. Synthesis of Palladium Nanoparticles with Interstitial Carbon by Sonochemical Reduction of Tetrachloropalladate(II) in Aqueous Solution. *The Journal of Physical Chemistry B* **1997**, *101*, 5470-5472.
(13) Cataldo, F. Ultrasound-induced cracking and pyrolysis of some aromatic and naphthenic hydrocarbons. *Ultrasonics Sonochemistry* **2000**, *7*, 35-43.
(14) Snyder, R. L.; Fiala, J.; Bunge, H. J. *Defect and microstructure analysis by diffraction*; Oxford University Press, 1999.
(15) Schafler, E.; Zehetbauer, M.; Ungàr, T. Measurement of screw and edge dislocation density by means of X-ray Bragg profile analysis. *Materials Science and Engineering A* **2001**, *319-321*, 220-223.
(16) Williamson, G.; Hall, W. X-ray line broadening from filed aluminium and wolfram. *Acta Metallurgica* **1953**, *1*, 22-31.
(17) Tuinstra, F. Raman Spectrum of Graphite. *J. Chem. Phys.* **1970**, *53*, 1126.
(18) Sadezky, A.; Muckenhuber, H.; Grothe, H.; Niessner, R.; Pöschl, U. Raman microspectroscopy of soot and related carbonaceous materials: Spectral analysis and structural information. *Carbon* **2005**, *43*, 1731-1742.
(19) Zhang, J.; Su, D.; Zhang, A.; Wang, D.; Schlögl, R.; Hébert, C. Nanocarbon as Robust Catalyst: Mechanistic Insight into Carbon-Mediated Catalysis13. *Angewandte Chemie* **2007**, *119*, 7460-7464.

Chapter 4:

CNT synthesis via CCVD on carbon supported Ni catalyst

Carbon materials possess unique characteristics, as they can exist in different forms that exhibit various functionalities. These materials range from sp^2-hybridized graphitic materials, such as graphite, CNFs and CNTs, to turbostratic carbons consisting of sp^2 and sp^3 mixtures such as carbon black, soot and activated carbons, to the sp^3-hybridized diamond. The different allotropes offer a broad range of physical and chemical properties. The effect of the interaction between transition metal catalyst and carbon support is discussed in this chapter. The investigation uses the Ni-catalyzed synthesis of CNTs as a probe reaction. The study starts with activated carbon (AC), graphite and Herringbone CNFs as the supports. The carbon materials are very common materials used as support in catalysis. They represent carbon with different degree of graphitic character and exposure of prismatic and basal plane. This study; in particular with Ni/AC catalyst, show the substantial effect of annealing in hydrogen prior to the exposure with ethylene/hydrogen to enhance the growth rate.

4.1. Carbon nanofilament synthesis on Ni/AC

The filaments grown from Ni/AC catalyst show CNF microstructure with mostly defective platelet-like character. At high synthesis temperature (850^{o}C), the filaments have multiwalled CNT microstructure. The detail will be described in the following.

4.1.1. Texture and microstructure of the CNF/AC composites

The textural properties of the reduced Ni/AC samples and the CNF/AC composites produced at different temperatures are summarized in Table 4-1. In general, there is a gradual increase in the mesopore volume of the sample after reduction and after CNF growth. The N_2 isotherms in Figure 4-1a show the appearance of hysteresis after CNF growth over the whole temperature range. Such N_2 condensation at high relative pressure is assigned to the condensation in between the CNFs. Indeed, this observation is in agreement with our SEM images in Figure 4-2, which show that the as grown CNFs are highly entangled, providing spaces for N_2 molecules to condensate at high relative pressure. The samples are labeled according to captions in Table 4-1. The NC500 sample showed no observable formation of CNF by SEM.

Table 4-1. Samples assignment and textural properties of CNF/AC composites.

Sample*	Growth temp°C	Δ Weight % after CNF growth	DR SA m^2/g	Micropore volume cm^3/g	Total pore volume cm^3/g	Mesopore Volume cm^3/g
AC	-	-	1233	0.438	0.455	0.017
Red 300	-	-21	1454	0.517	0.565	0.048
T550[a]	-	-24.7	1485	0.527	0.585	0.058
NC500	500	-27	nd[b]	nd	nd	nd
NC550	550	-10.3	1588	0.56	0.659	0.099
NC600	600	-2.6	1135	0.494	0.645	0.151
NC700	700	16.2	1491	0.53	0.66	0.130
NC850	850	25	598	0.212	0.325	0.113
NCT500	500	-29	1347	0.479	0.55	0.071
NCT550	550	-20.2	1525	0.542	0.725	0.183

[a]T refers to subsequent reduction at 550°C for 1 h 5% H_2/Ar after reduction at 300°C

[b]Not determined

*Red, NC, and NCT refer to the reduced sample, growth, and growth with subsequent reduction respectively.

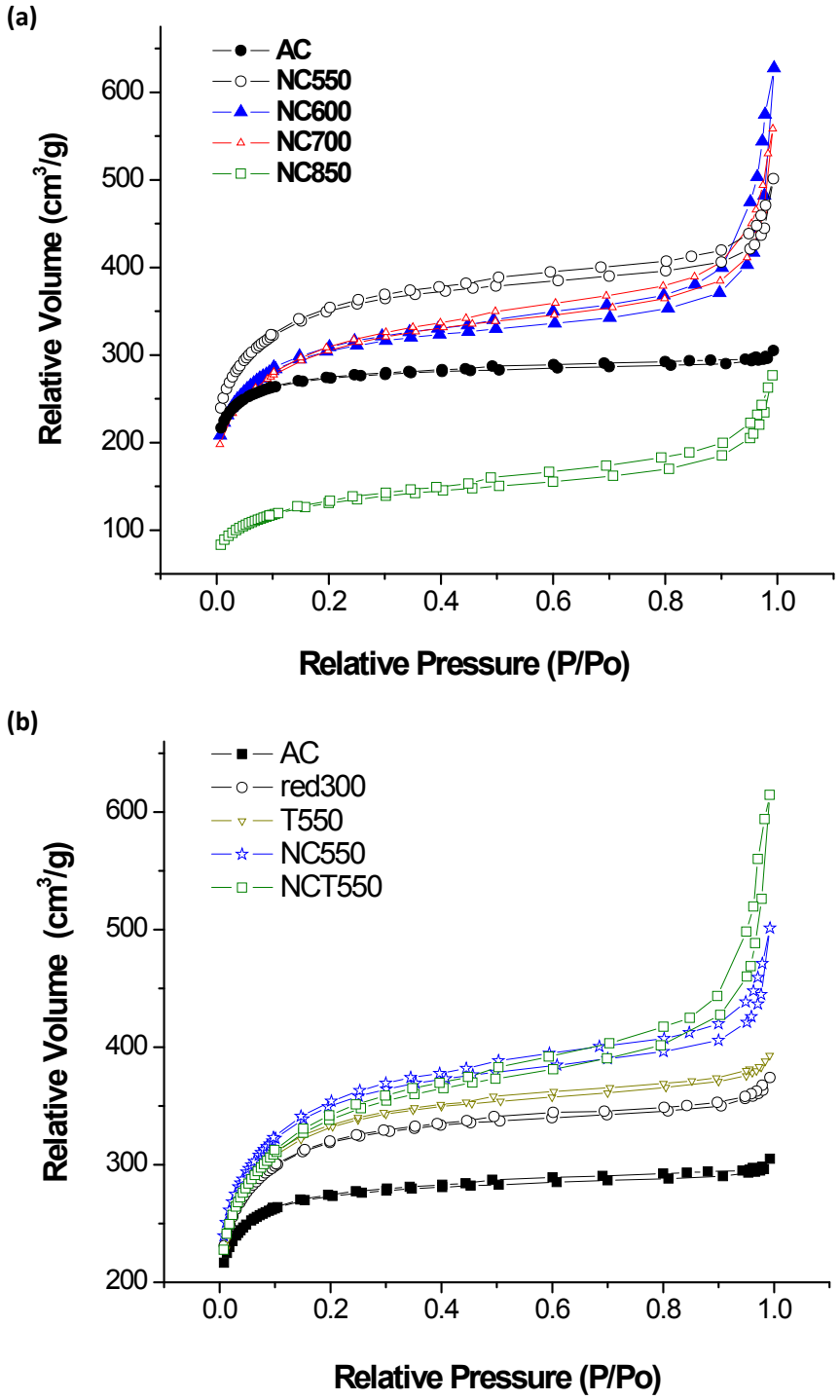

Figure 4-1. N_2 isotherm of the CNF/AC composites synthesized at different temperatures (a) and the effect of reduction and subsequent treatment to the N_2 isotherm of Ni/AC catalyst and CNF/AC composites (b). The micropore and mesopore adsorption changes with increasing growth density of CNFs. For experiments with minimum and/or the absence of CNF growth the micropore adsorption is enhanced (NC550, red300, T550). When CNFs growth gradually increases the hysteresis in the isotherm develops.

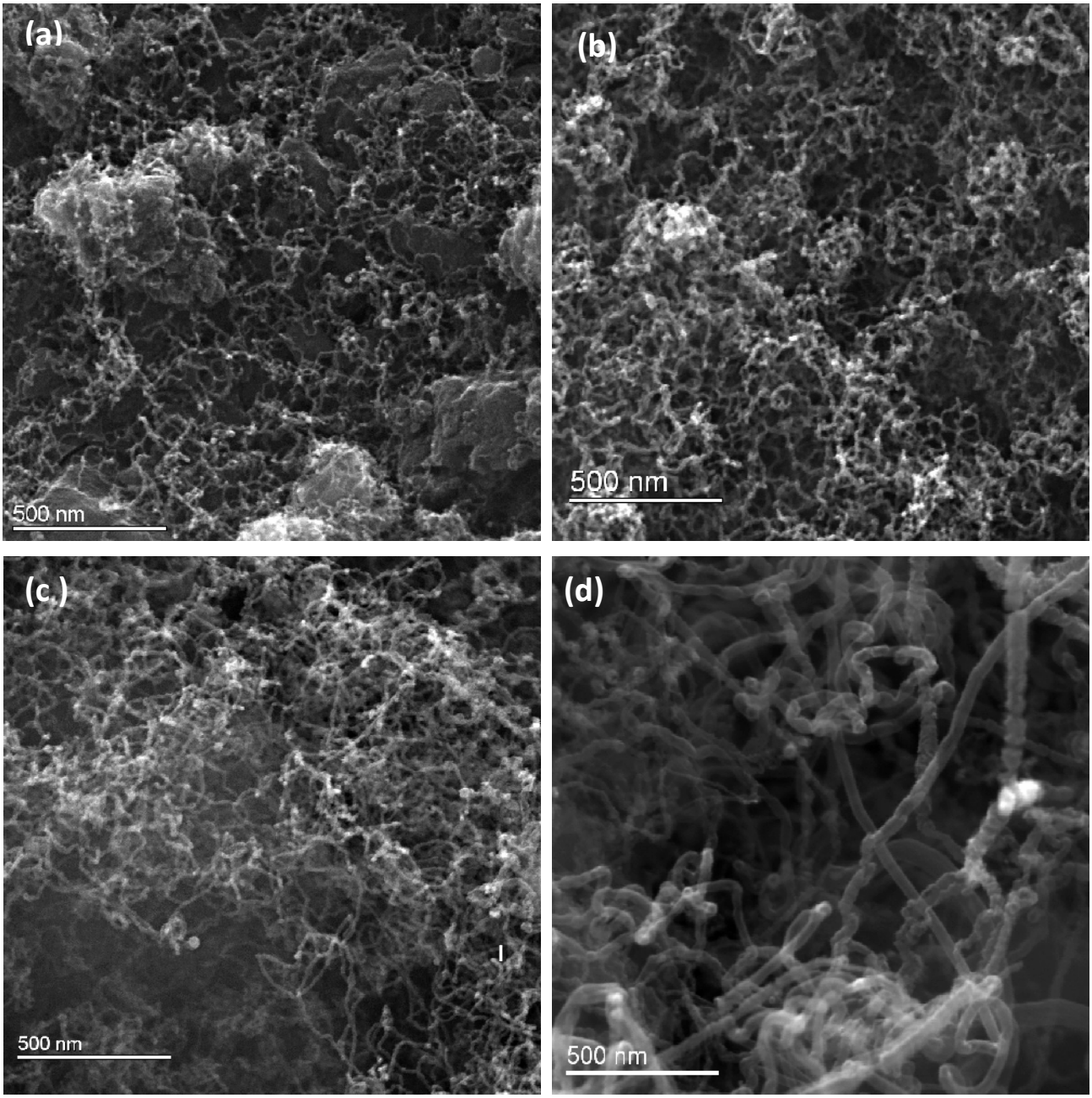

Figure 4-2. SEM images of the CNF/AC composites: NC550 (a), NC600 (b), NC700 (c) and NC850 (d). The CNF growth density increases with increasing temperature. At 850°C however the texture of CNFs changes towards smoother and straighter filaments.

For composites synthesized at 550°C (NC550) and 600°C (NC600), there is a positive relationship between the mesopore content and weight change after CNF growth (Table 4-1). At

higher temperatures, however, the mesoporosity of the composites depended less on the CNF growth. This is mostly due to different level of CNF entanglement that occurs at different growth temperatures. CNFs grown at higher temperatures tend to give straighter filaments (Fig. 4-2d), most likely due to better graphene stacking of the CNF (Fig. 4-3). From TEM investigation presented in Fig 4-3, for CNF grown at 550^{o}C the microstructure shows a poorly defined or highly defective carbon of platelet-like graphene arrangements. Similar defective carbon filaments grown at low temperature have been reported previously.[1,2] The CNF microstructures give defective platelets and more graphitic platelets when grown at 600^{o}C and 700^{o}C respectively. CNFs with graphene wall parallel to the filament axis with hollow channel were observed for growth at 850^{o}C. NC850 give straight CNF morphology (Fig. 4-2d) showing less entanglement as featured in the N_2 isotherm at a higher relative pressure (Fig. 4-1).

Over longer period of growth the composite continues to entangle forming macroscopic agglomerates (Fig. 4-4). The octopus mode of growth and the defective character of the CNFs facilitate the macro shaping formation. N_2 isotherms in Fig 4-5 demonstrate the continuous growth by the gradual decrease of relative porosity as a result of the CNF growth. The gradual drop of the hysteresis is likely due to densification of the material as a result of the growth.

The variation of the graphitic character of the samples under study was investigated by X-ray powder diffraction (Fig. 4-6). The X-ray diffraction patterns did not show sharp graphite (002) and (100) signals for composites synthesized at low temperatures. Only the composite synthesized at 850^{o}C showed appreciable intensity for the graphite (002) diffraction signal, which might reflect the additive effect of both the improved graphitic character and the higher fraction of carbon nanofilament (Fig. 4-3d and Table 4-1). None of the composites' diffraction patterns showed the presence of Ni metal or Ni carbide, possibly due to the low percentage of Ni in the composites and/or due to fine dispersion of the Ni crystallites.

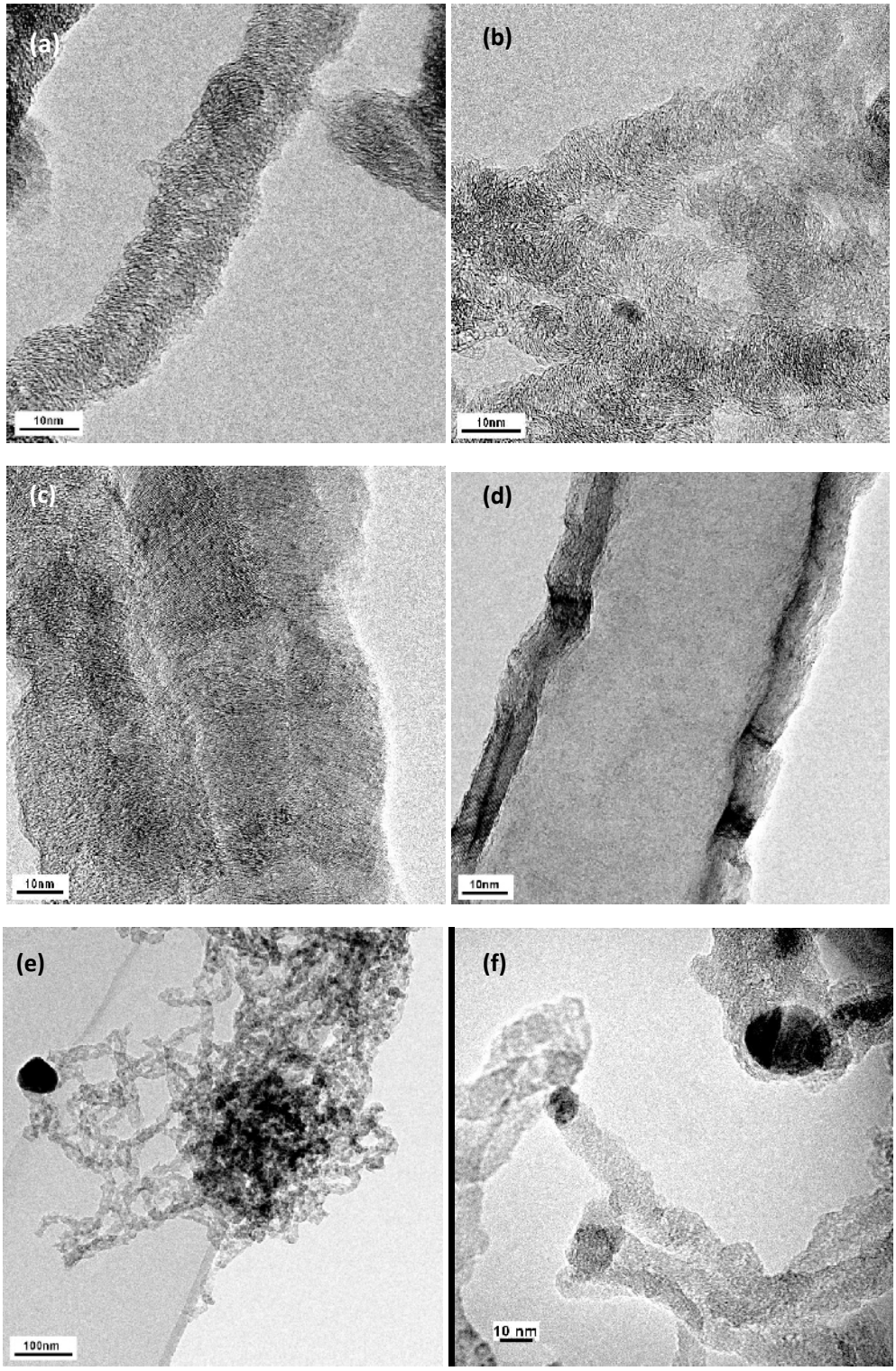

Figure 4-3. Microstructure of CNF in NC550 (a), NC600 (b), NC700 (c), NC850 (d), and octopus (e) and single directional CNF (f) typically present in CNF/AC composites. The growth at high temperature demonstrate CNF with higher ordering.

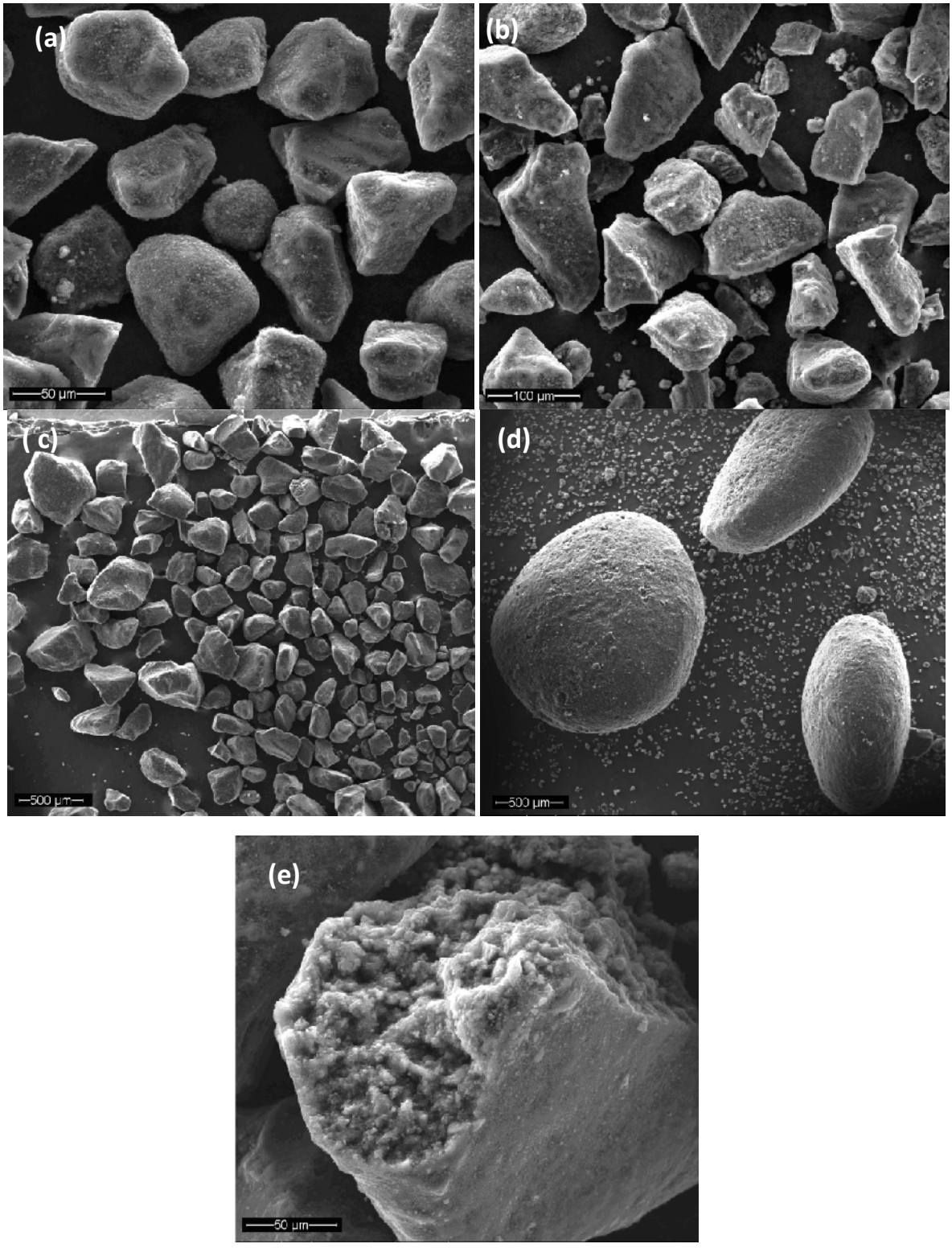

Figure 4-4. Low magnification SEM images of CNF/AC composites synthesized at 600^{o}C for 2 (a), 3 (b), 4 (c) and 5 h (d), and showing the agglomeration of smaller AC particles by the CNF entanglement (e).

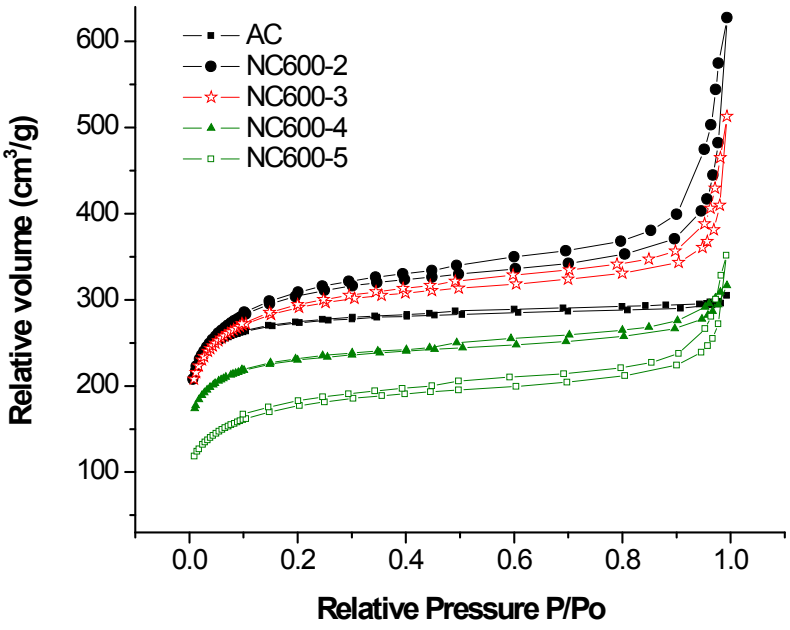

Figure 4-5. N_2 isotherm of CNF/AC composites synthesized at 600°C (NC600) for 2, 3, 4, and 5 h. The composite becomes gradually mesoporus with increasing CNFs content.

The average CNF diameter in the composites was shown to increase with the synthesis temperature (Fig. 4-7). The increase may be primarily due to sintering of the Ni particles facilitated by the surface modifications (surface functional groups decomposition) of the AC supports, assuming direct relationship between Ni particle size and CNF diameter. The average CNF diameter increased dramatically for composites synthesized at 850°C. This behavior may also be due to the change in the growth mode from a mixture of octopus and single directional nanofilaments grown at 550-700°C to preferentially single direction nanofilaments for composite grown at 850°C (Fig. 4-3e and f). The octopus CNFs are mostly observed from bigger Ni particles, which is in agreement with previous studies.[3,4,5,6,7,8,9,10] Several effects, such as particle size, surface reconstructions, exposed facets and rate of ethylene decomposition, were proposed to explain the CNF growth preferences.[11,12,13,14]

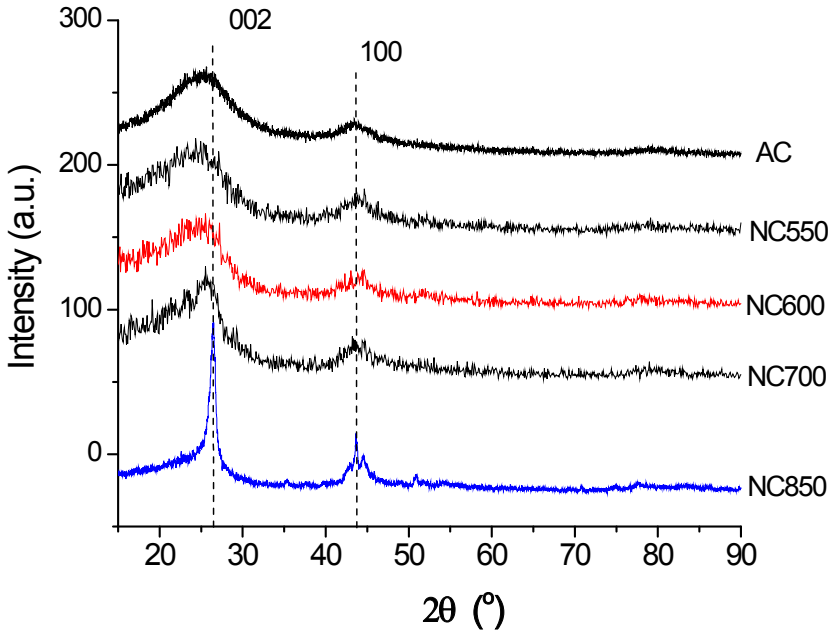

Figure 4-6. XRD patterns of the AC and CNF/AC composites. In agreement with TEM investigation, the CNFs grown at 850oC exhibit the highest graphitic ordering in the series.

The octopus CNFs are beneficial for establishing a bulk macroscopic structure due to entanglement from multiple directions for each catalyst particle.[6,9]

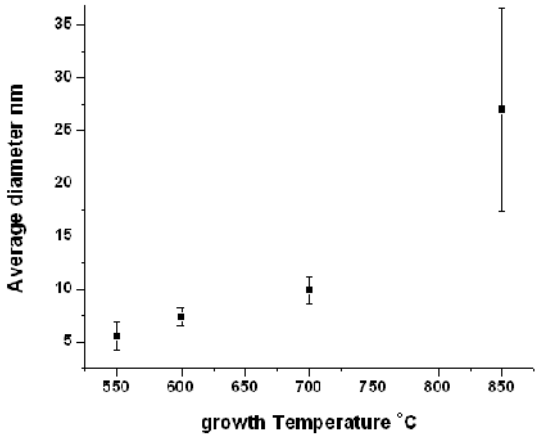

Figure 4-7: Average diameters of CNF grown at different temperatures. The CNFs outer diameter was measured from electron microscopy data. The increasing average diameter strongly suggests that the catalyst sinters with higher growth temperature.

4.1.2. The catalytic gasification of the AC support by Ni catalyst

Ni catalyzes the gasification of the carbon supports under hydrogen.[15,16,17,18,19,20,21,22,23,24] As shown in Table 4-1, the weight changes after growth indicate the extent of gasification during both reduction and CNF growth. The gasification, producing CH_4, is so dominant that the supported catalyst loses significant amount of its mass after reduction. Figures 4-8a and b show the evolution of gaseous products from the Ni/AC catalyst during heating under inert gas (Ar) and 5% H_2/Ar respectively. In both cases the surface functional groups present on the AC support decompose during heating.[15,25] Methane was only detected when the Ni/AC catalysts was heated under reducing atmosphere. *It is still unclear whether the catalytic gasification proceeds via spillover of hydrogen and/or gasification of carbon on the Ni surface as a result of carbon atoms diffusing from the metal-carbon support interface*.[15,17,26,27]

Figure 4-8b shows that CH_4 starts to evolve at around 250^{o}C, which indicates the presence of Ni metal available to provide active hydrogen to gasify the AC support. The reduction process increases the micropore volume by 20% and gives a 3-fold increase of the mesopore volume (Table 4-1). The knee broadening in the N_2 isotherm at P/Po <0.2 indicates broadening of the pore size distribution towards larger pores, which could be explained by the catalytic gasification of the supports creating new pores and/or the enlarging of existing ones in the dimension of the Ni particle sizes (Fig. 4-1b). Because AC is composed of microcrystalline graphite rich in curvature with possible cross-linking between the graphite microcrystals, the catalytic gasification is likely to occur in three dimensions of the carbon matrix, creating voids thus increasing the porosity. Such gasification is different from that of graphite that forms two- and three-dimensional channels in specific directions.[23,28,29,20,30,31] Figure 4-1b also shows that catalytic gasification remains a dominant process even after CNF growth, especially for composite grown at 550^{o}C. The preservation of microporosity in the composites, suggests that micropores were not involved in the growth process. Indeed, no filaments of ~2 nm in diameter were observed in the TEM images for any of the composites. This is very likely due to the sintering of Ni nanoparticles to form bigger particles during the gasification and ramping to growth temperature. Indeed, the catalyst size distributions measured for samples after reduction (red300) and after subsequent treatment at

550°C (T550) show a slight shift towards a higher value, indicating a tendency for the Ni particles to sinter after treatment at 550°C (Fig. 4-9). In an earlier study on Ni-catalyzed carbon gasification Tomita et al. reported the gradual increase of Ni particle size after the gasification in hydrogen atmosphere.[19]

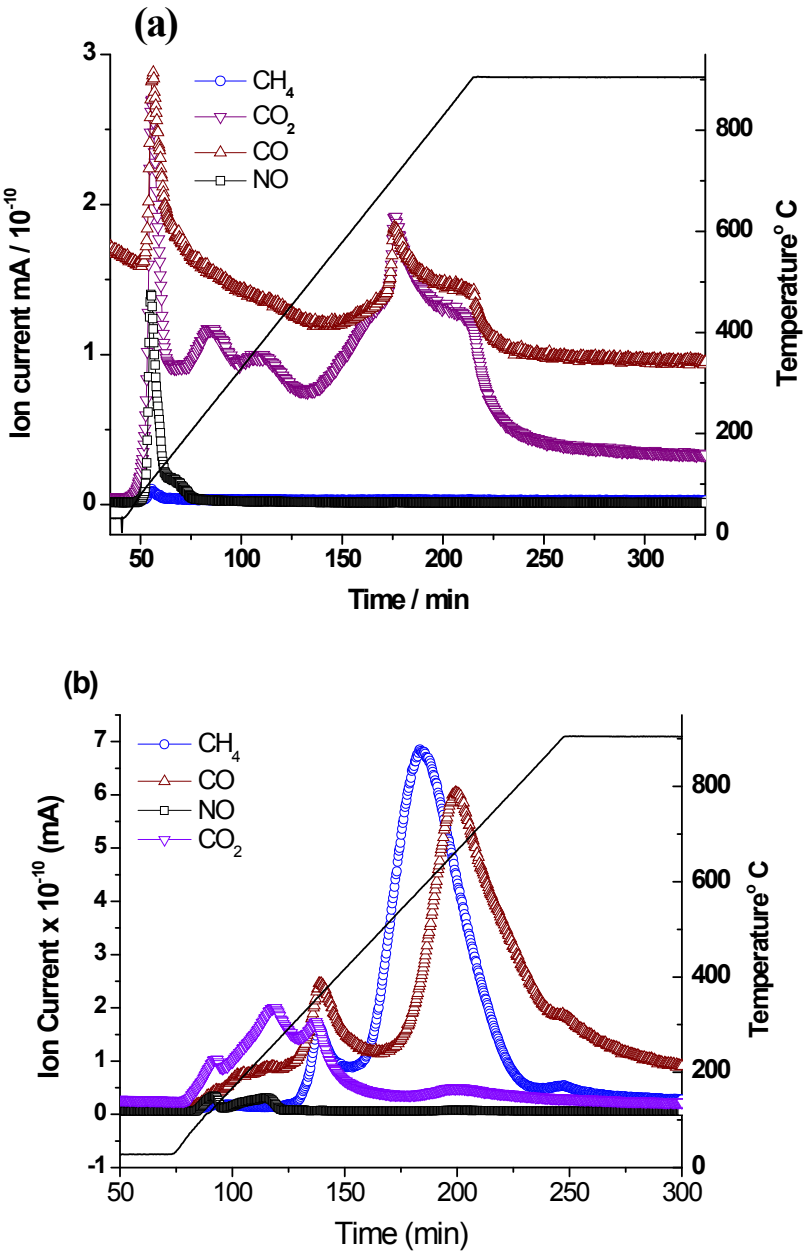

Figure 4-8. Gasses evolved during the heat treatment in Ar (a) and 5% H_2 in Ar (b) of 1wt% Ni/AC. The evolution of CH_4 under H_2 atmosphere indicates catalytic gasification of the carbon support by Ni catalyst.

Gasification produces two prominent CH_4 peaks, the first in the low temperature region with a peak maximum at 300°C and a second peak with higher intensity and a maximum around 670°C. The methane production is strongly correlated with the surface functionalities of the carbon support.[19] Figure 4-8b shows that the CH_4 and CO peaks overlap at the low temperature region and deviated from the overlaps for the second CH_4 peak at the higher temperature region. Note that CO_2 evolution under reducing atmosphere was suppressed dramatically for the high temperature region. CH_4 production decreased at around 750°C, as shown in Figure 4-8b. The minimum is also illustrated in the N_2 isotherms after reduction at 300°C and subsequent treatment at 550°C in Figure 4-1b. The isotherms show a more moderate increase in micropore adsorption due to gasification for samples after subsequent treatment at 550°C when compared with that after reduction at 300°C. Several arguments have been proposed from earlier studies to explain the catalytic gasification deactivation, which includes catalyst encapsulation by carbon, H_2 diffusion problems, and catalyst-carbon surface contact loss.[17,19,22,24]

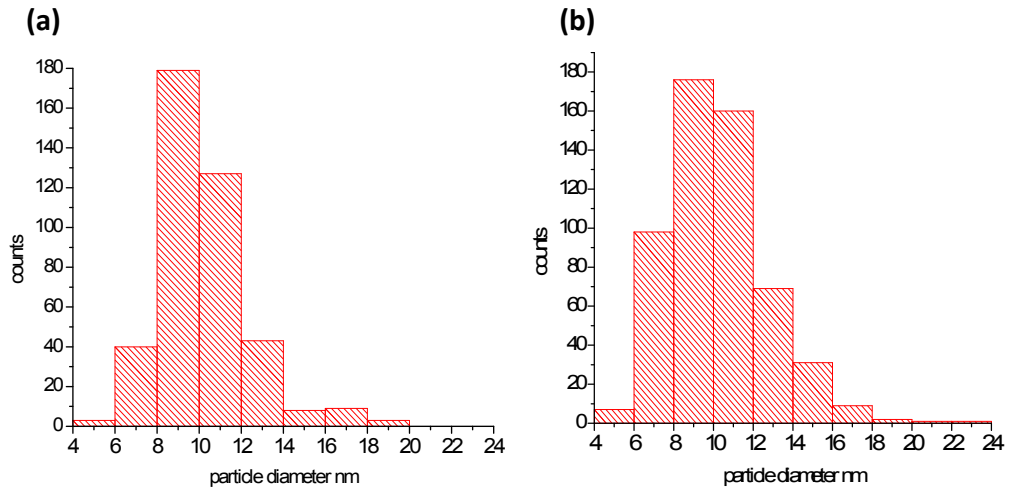

Figure 4-9. Particle size counts for the Ni/AC catalyst after reduction (Red300) (a, c) and after subsequent treatment (T550) (b, d). The average particle sizes are 10±2.5 nm and 10±2.1 nm for reduced and after subsequent treatment sample respectively.

4.1.3. The effect of the subsequent treatment to the CNF/AC composite

Interestingly, the CNF growth increased dramatically with subsequent reduction treatment at 500^{o}C (NCT500) or 550^{o}C (NCT550), compared to when the composites were synthesized without the treatment (NC500 and NC550) as represented in the SEM images shown in Figure 4-10. For CNF synthesis with subsequent treatment, the reduced Ni/AC was subsequently exposed to 5% H_2/Ar at the growth temperature for 1 h prior to the exposure with ethylene/hydrogen. CNF was not observed under SEM analysis for sample grown at 500^{o}C without the subsequent treatment (NC500). The effect of the treatment is reflected in the increased weight change, the development of the hysteresis in the N_2 isotherm and thus higher mesoporosity after CNF growth (Table 4-1 and Fig. 4-1b).

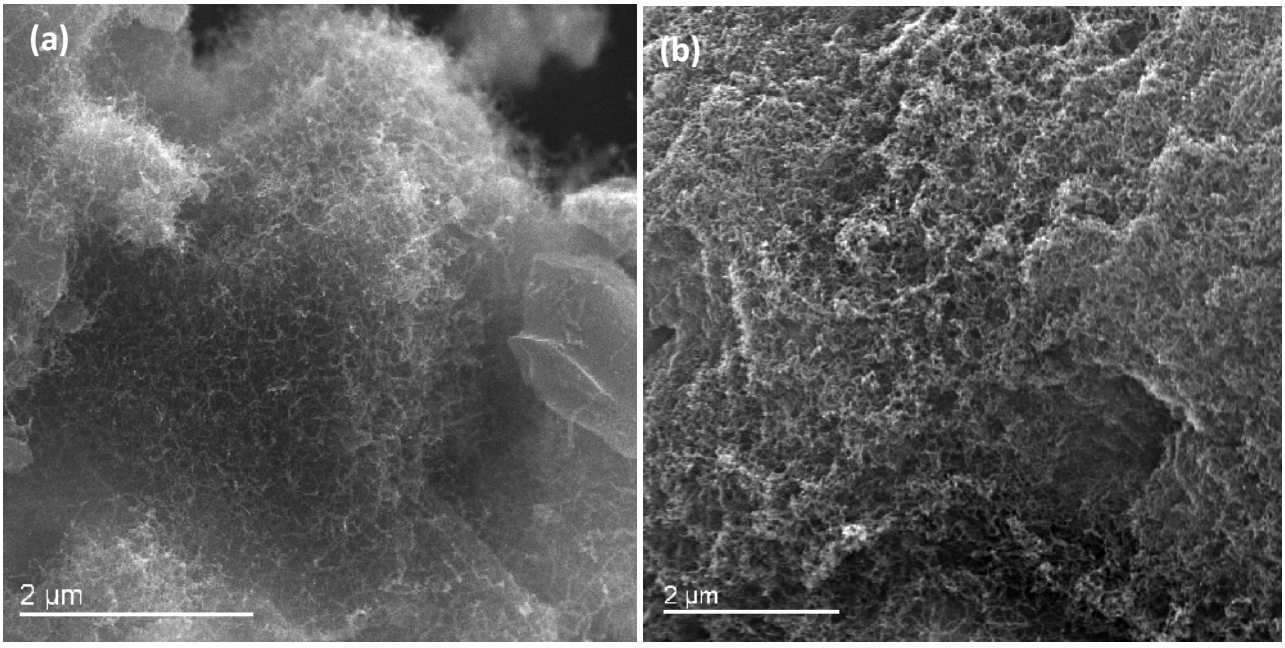

Figure 4-10. SEM images of CNF/AC composites synthesized after treatment in 5% H_2/Ar for 1 h at 500^{o}C (NCT500) (a) and 550^{o}C (NCT550) (b). The CNFs growth density is significantly enhanced after the treatment prior to C_2H_4 exposure.

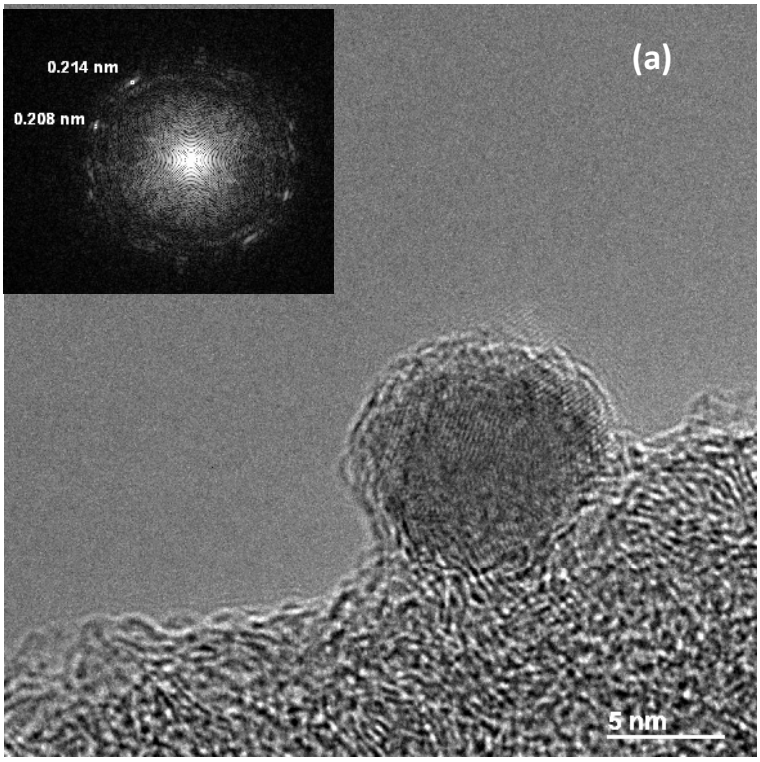
0.214 nm
0.208 nm
(a)
5 nm

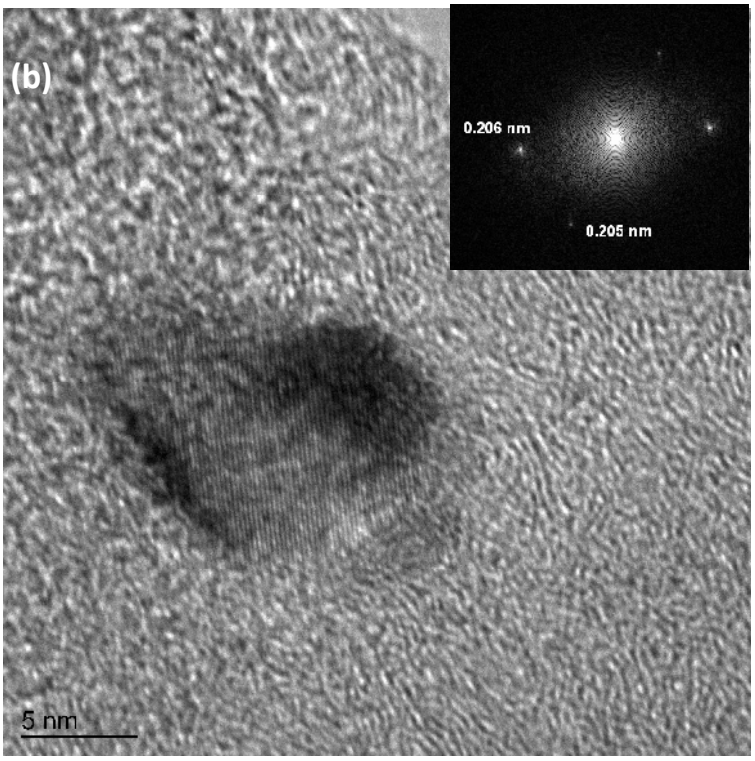
(b)
0.206 nm
0.205 nm
5 nm

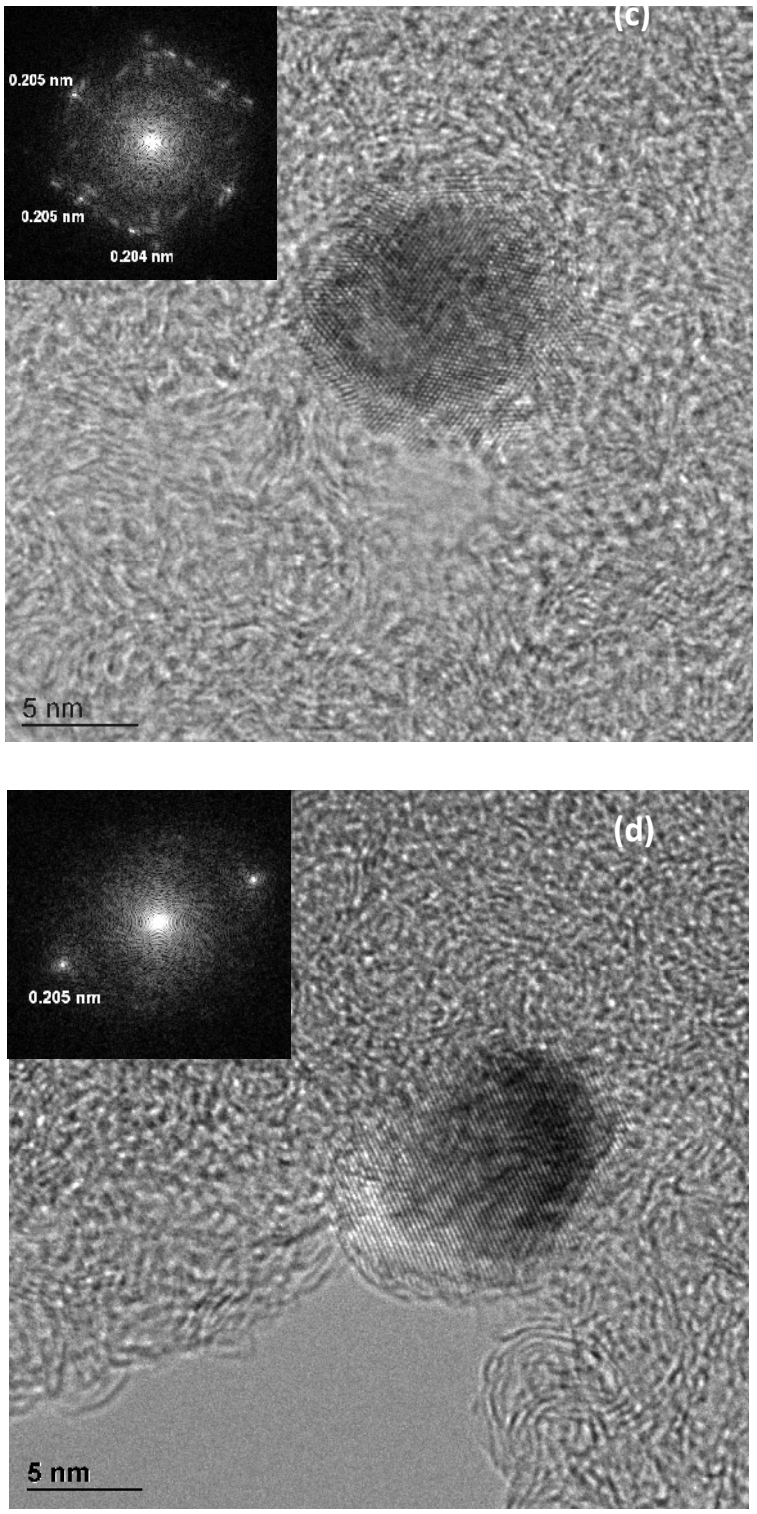

Figure 4-11. HRTEM images for the Ni/AC catalyst after reduction (Red300) (a, b) and after subsequent treatment (T550) (c, d). The Ni nanoparticle exhibit metallic fcc structure showing mostly the (111) lattice spacing. Occasionally the (111) spacing deviates to higher value (a).

In an attempt to understand the improved activity after the subsequent treatment, HRTEM investigations were carried out for Ni/AC samples after reduction at 300^{o}C (Red 300) and after subsequent treatment at 550^{o}C (T550) for their catalyst size distribution (Fig. 4-9) and microstructure (Fig. 4-10). Both size distributions and microstructure of Ni particles failed to show significant differences after either treatment. Within the resolution of the HRTEM used, the d spacing of the Ni particles show values that can be assigned to metallic Ni of face-centered cubic (fcc) structure. d spacings of 0.203 and 0.176 nm assigned to (111) and (200) lattice planes respectively are frequently observed in HRTEM investigations. Albeit a small shift in the catalyst size distribution after the subsequent treatment, it is unlikely that such small difference can cause the dramatic activity for CNF growth.

However, we have yet to take into consideration that the shape of Ni particle may change after each treatment. Pioneering works with controlled atmosphere electron microscope (CAEM) by Baker in the 1970s clearly showed the mobility of metal particles on graphite under different atmospheres.[16,23,30,31,32] Later on equipped with better resolution, Anton[33,34] also reported the liquid-like mobility of Ni nanoparticles on thin amorphous carbon films subjected to heating in inert and reducing atmospheres under in situ TEM observations at temperatures similar to the current study. The mobile Ni particles were observed to wet the carbon surface and spread out randomly leaving behind graphitic tracks. Thus, reshaping the Ni particles during reduction and subsequent treatment is very likely to occur in the current study. To elucidate on the mobility of catalyst metal particles, Baker has shown the relationship between mobility of metal particles on graphite surface with the Tammann temperature ($0.5T_{melting}$) of the metal. For 10nm size Ni metal particles it was observed that the mobility starts at 640^{o}C under hydrogen atmosphere.[30,31,32] Due to smaller average size of Ni nanoparticles (Fig 4-9) and the defective and functionalized nature of the AC support, it is very likely that the nanoparticle starts the mobility at lower temperature.[17,19,22] Thus there is every reason to believe that the mobility will have a pronounced effect in the orientation of the metal particles on the carbon surface.

In the previous in situ TEM study of Ni-catalyzed amorphous carbon gasification, Ni particles encapsulated with several graphitic layers were also observed. Indeed earlier works have shown

under inert atmosphere Fe and Ni films supported on amorphous carbon films precipitated graphite films after heating.[35,36] However Ni particles encapsulated by graphitic layers or carbon layers were not observed by HRTEM investigation of samples in the current investigation.

In addition, there is also a possibility for surface reconstruction of the Ni catalyst to occur due to the adsorption-desorption dynamics of CH_4 and CO molecules during the two treatments.[37,38,39,40] The CO profile changed dramatically when the atmosphere was changed from Ar to 5% H_2/Ar, which strongly suggest that the decomposition is altered in the presence of active hydrogen. TPR was carried out in a temperature program to simulate the reduction at 300^{o}C and subsequent treatment at 550^{o}C under 5% H_2/Ar atmosphere (Fig. 4-12). The subsequent treatment at 550^{o}C produced a significantly higher CH_4 peak. Nevertheless, the catalyst particles are still in a metallic state after subsequent reduction at 550^{o}C, and no Ni carbide phase was evident in the HRTEM images (Fig. 4-11c and d). The absence of carbidic phase is expected, as Ni carbide is not stable at 550^{o}C.[41,42] Similarly the presence of metallic state and the absence of carbidic phase of Ni catalyst were previously reported after deactivation from the catalytic carbon support gasification, after graphitization of the amorphous carbon film, and during and after CNT growth.[7,24,34,43,44,45,46,47] Catalytic gasification, CNT and CNF growth, and catalytic graphitization presumably involve a similar general mechanism of carbon atoms dissolutions, diffusion and precipitation from the catalyst Ni particles.[22,34] Such relationship was first proposed by Holstein et al in their work with Pd-catalyzed conversion of amorphous carbon to graphitic carbon.[48]

Several works have claimed the presence of dissolved carbon[7,49] or carbide-like compounds[47] in Ni catalyst particles after CNF growth. Such dissolved carbon or carbon contamination has also been reported in works involving metal catalyst supported on non-graphitic carbons.[50,51,52] Gandia and Montes[53] speculated the influence of carbon contamination in carbon-supported Ni catalyst for the hydrogenation of acetone after thermal treatments in inert and H_2 atmospheres.

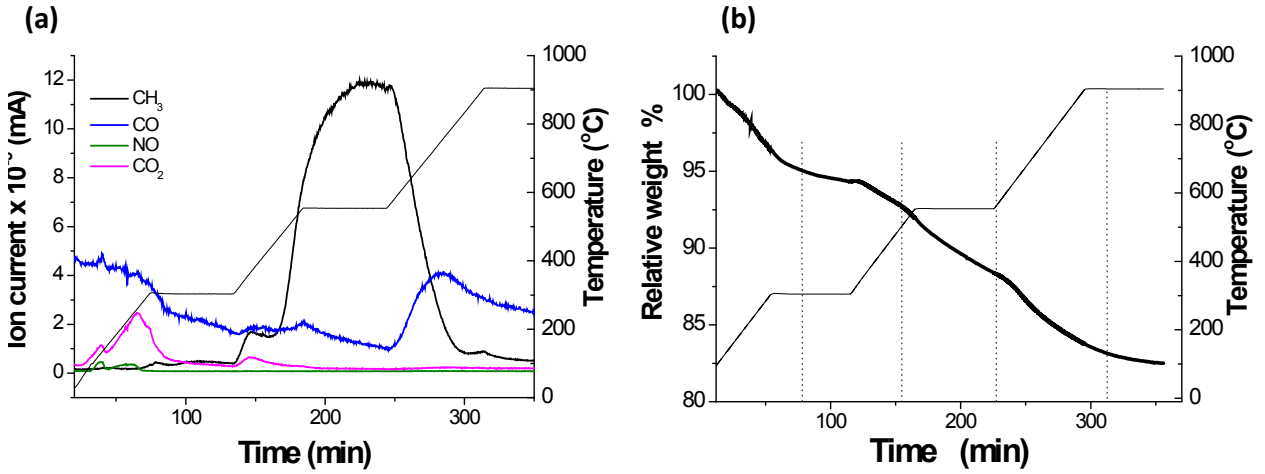

Figure 4-12. Gasses evolved (a) and weight loss profile (b) during TPR experiment under 5%H_2/Ar simulating reduction at 300°C and subsequent treatment at 550°C. The temperature ramp is at 5 K/min. The Ni catalyst gasifies the AC support under the reduction and subsequent treatment steps.

Based on the TPR profiles in Figures 4-8b and 4-12, CH_4 and CO evolution may be interdependent on the surface of the Ni catalyst. It is likely that the CO participate in the catalytic gasification reaction. The gasification can take place via re-adsorption of CO onto Ni surface and/or spillover reaction by hydrogen. Indeed, several surface carbon species have been identified from the CO hydrogenation reactivity of Ni catalysts at conditions similar to those in the current study.[54] Such surface carbons or surface carbidic species that may be present in the current study may cause electronic perturbations[39,55] and geometrical modifications[38] and thus affecting the activity of the Ni catalyst.[51,52,56] Based on the literature mentioned above, *we propose the possibility of dissolved carbons in the bulk and/or surface of Ni particles after reduction and/or after the subsequent treatment that may contribute to the change of Ni catalyst activity for CNF growth.*

In addition to the already complicated dynamics of the catalyst for CNT and CNF synthesis, the fact that Ni may be supplied with carbon from three different sources (*C_2H_4, carbon support and CO from the surface functionalities*) further complicates the process. There are still no conclusive arguments on how gasification and/or carbon support contamination can change the catalyst activity to grow CNFs. Nevertheless, we showed experimentally that subsequent treatment

of Ni/AC under reducing atmosphere for 1 h prior to C_2H_4 and H_2 exposure increases the ability of the system to grow CNFs significantly.

There are several scenarios suggested in this thesis to explain the additional activity of the Ni catalyst after the subsequent treatment process: the presence of dissolved carbon, surface carbon, surface carbide, catalyst faceting and reconstruction, which may all contribute to the increase in Ni catalyst activity in growing CNFs under the current conditions. Such activity enhancement may also be relevant for the study of other reactions involving CO and/or hydrocarbons.

To summarize, CNFs and CNTs have been synthesized using a Ni/AC catalyst. By varying the growth temperature, the microstructure and the texture of the CNF/AC composite have been successfully controlled. Catalytic gasification was experimentally shown to change the texture of the CNF/AC composites via the development of microporosity. For composites synthesized at low temperatures, the activity of the Ni/AC catalyst was increased significantly after treatment with 5% H_2/Ar prior to C_2H_4/H_2 exposure. However, the particle size distribution and the microstructure of the Ni catalyst after the treatment did not show appreciable changes.

4.2. Carbon nanofilament growth on Ni/Graphite catalyst

To further investigate the Ni-carbon catalyst interaction for the growth of carbon nanofilament, a graphitic support was used. As-received graphite sample was impregnated with 0.1M $Ni(NO_3)_2$ acetone solution to achieve ~1wt% Ni content. The impregnated graphite was then dried at room temperature overnight. Acetone was chosen as solvent considering the hydrophobicity of the graphite surface. Calcination, reduction and growth conditions were of similar temperatures, gas compositions, reactor and swinging speed with that of nanofilament synthesis on Ni/AC. The ethylene/Hydrogen exposures were performed for 2, 5, 60 and 120 min.

The as-received graphite sample was obtained from TIMCAL with average grain size of 150 microns and surface area of 1.6 m^2/gram. SEM images of the sample after 5 min ethylene/hydrogen exposure at 700^oC demonstrate the activity of Ni/graphite catalyst (Figure 4-

13). Ni/graphite is significantly more active than that Ni/AC catalyst. Most of the graphite surfaces are homogeneously covered with nanofilaments. Some of the surfaces however are not covered probably due to the SEM sample preparation that scratched away the nanofilament aggregates. The length of the nanofilaments reaches several micrometers. The nanofilaments are smoother and exhibit more straight texture as compared to that grown from activated carbon.

The activity of the Ni catalyst to grow carbon nanofilament is demonstrated by the development of the N_2 isotherm profile with ethylene/hydrogen exposure time. The hysteresis of the nanofilament-graphite composite developed with increasing growth time indicating more entanglement per gram of material (Fig. 4-14). The development of the entanglement due to the progressing nanofilament growth is reflected in the surface area that increases gradually with growth time (Fig 4-14). From SEM images and N_2 isotherm data it is obvious that the growth is significantly enhanced when Ni is supported on Graphite as compared to Ni/AC.

The nanofilaments grown are quite uniform with external diameter ranging from 10-40 nm. As depicted in Fig 4-15 the particle size of the Ni catalyst after reduction show quite narrow distribution ranges from 4-20 nm. These observations of reduced catalyst and the nanofilaments diameter suggest the catalyst to sinter prior and/or during the growth period (Fig 4-15).

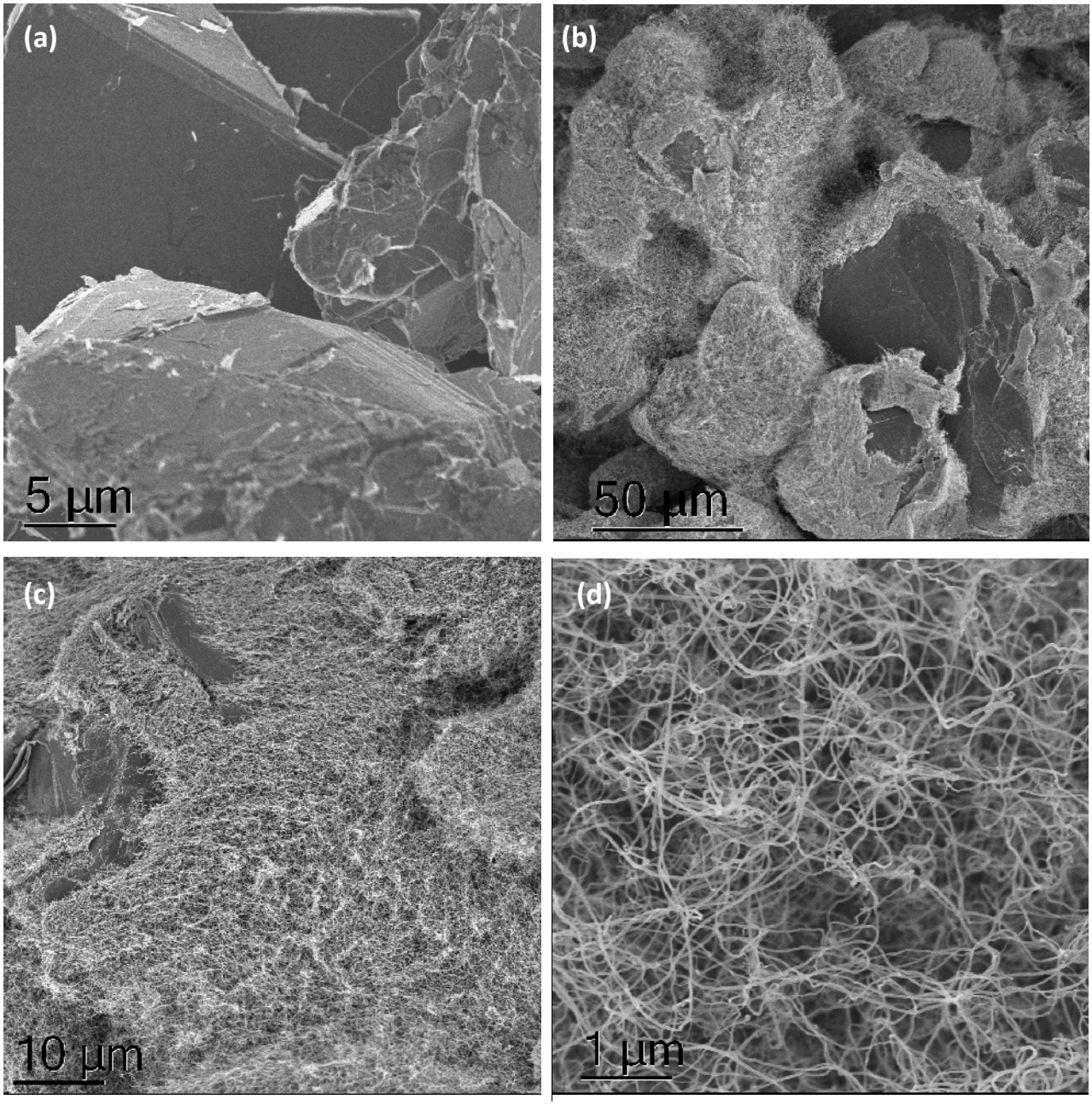

Figure 4-13. SEM images of graphite support (a) and carbon nanofilaments grown on 1 wt% Ni/graphite catalyst synthesized for 2 min (b-d). The reactivity of Ni on graphite for CNF reaction is clearly obvious as compared to Ni/AC. After 2min of growth the CNFs almost cover the entire surface of the graphite support, the entangled CNFs may have been scratch-off from the graphite surface during the SEM sample preparation. The texture of CNFs is smoother and exhibit entirely of single directional growth.

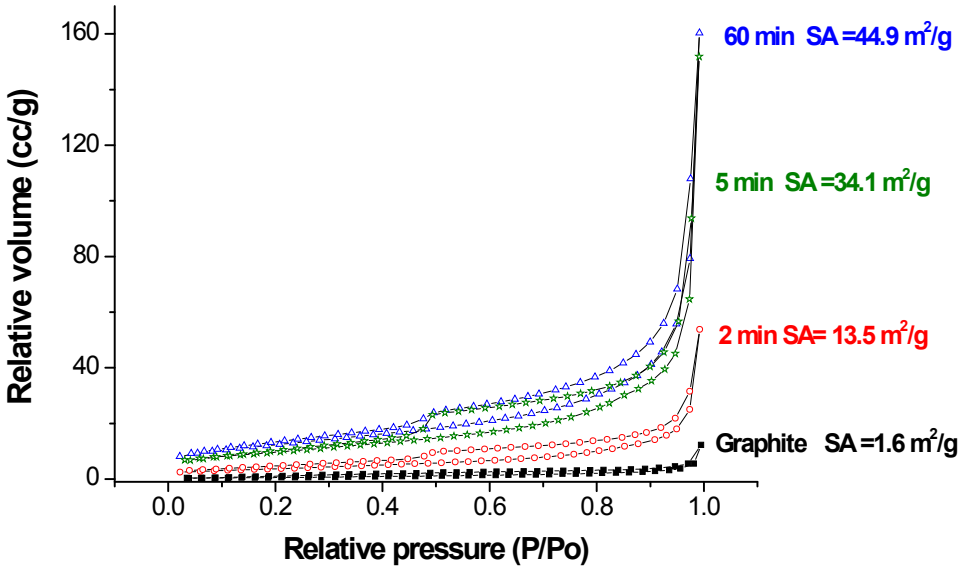

Figure 4-14. N_2 adsorption isotherm of graphite support, and Ni/graphite after 2, 5, and 60 min of carbon nanofilament growth. The CNF/graphite composite develops mesoporosity with higher CNF growth density.

The carbon nanofilaments grown from Ni/graphite catalyst have different arrangement of graphene planes from multiwalled nanotube, graphitic herringbone with hollow channel and defective herringbone with poorly developed hollow channel (Fig. 4-16). The angle distribution of the graphene arrangements relative to the filament axis of the filaments is presented in Fig 4-17. The nanofilaments grown in the sample are mostly herringbone CNFs with broad distribution of graphene angle orientation relative to the filament axis with the average value of 12^{o}. The smaller diameter herringbone CNFs are more defective than that of bigger ones (Fig 4-16b &c). This is probably due to different diffusion pathways and the stability of the Ni catalyst during growth. At the moment there is no conclusive explanation to why some catalyst appears to be less active than the other on the graphite surface. It is not clear from TEM and SEM images collected in this work whether there are difference in the catalyst sitting in basal plane of the graphite surface and prismatic edges. In general the CNFs grown from Ni/graphite are single directional growth with no octopus mode observed. The CNFs show more graphitic character than that grown from Ni/AC.

There are two types of inactive Ni catalysts in the after growth sample. One type is of encapsulated particles of random shapes in the range of 30-100 nm (Fig 4-18a). The second type is of finely dispersed particles in the range of 1.5-2.5 nm (inset Fig 4-18a). The small Ni nanoparticles are arranges in a regular array along the step edges of the surface. These Ni nanoparticles demonstrate high stability under hydrogen exposure at 700^{o}C. This type of small particles has the same features as that of mechanically fixed Ru nanoparticles supported on graphite.[57] Similarly the Ru nanoparticles supported on the graphite edges were reported to be inactive to grow CNTs in contrast to the Ru on basal plane of graphite.[58] The metals on the edges were reported to have stronger metal-carbon interaction as revealed form the wetting and spreading nature of the nanoparticles onto the graphite surface.

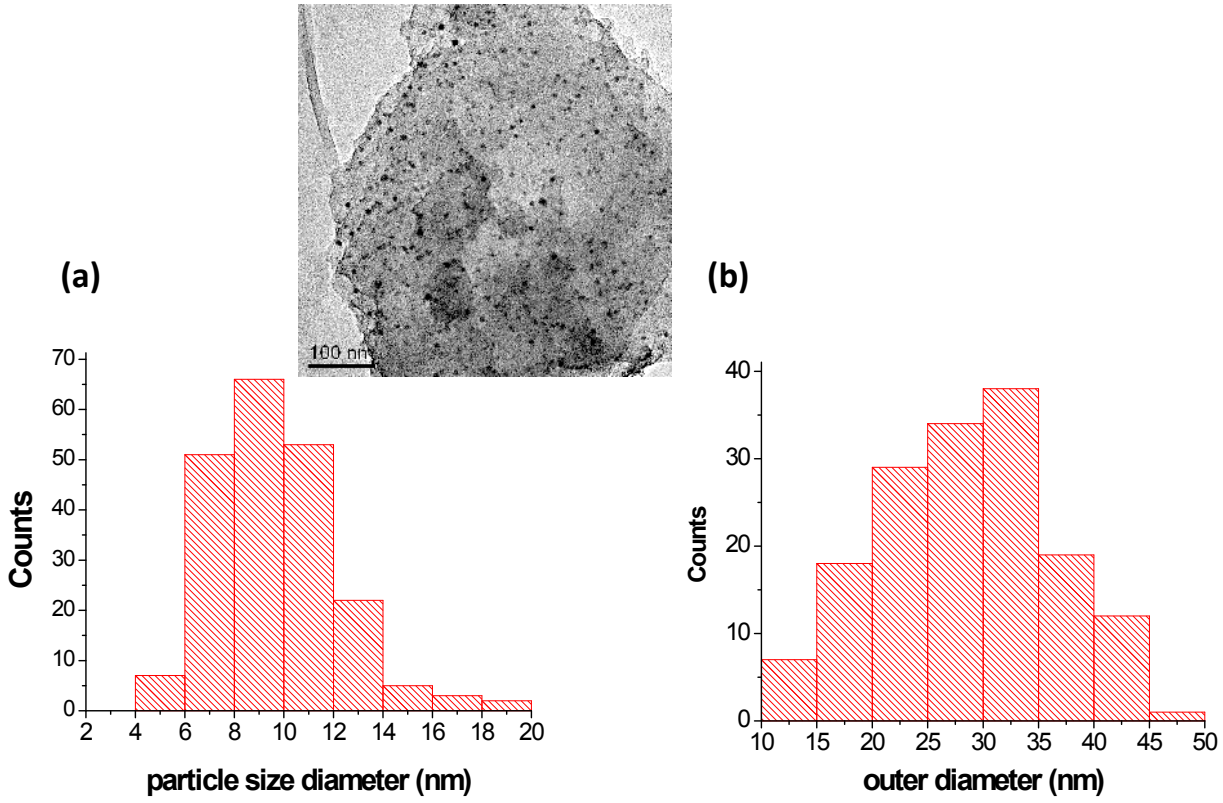

Figure 4-15. Ni particle size distribution on graphite support (a) and CNFs diameter distribution on CNF/graphite after 2 min of growth (b). (inset: show the TEM image of Ni particles on graphite support). The higher outer diameter value suggest that the catalyst particle sinters during ramping and/or at growth temperature prior to CNF growth.

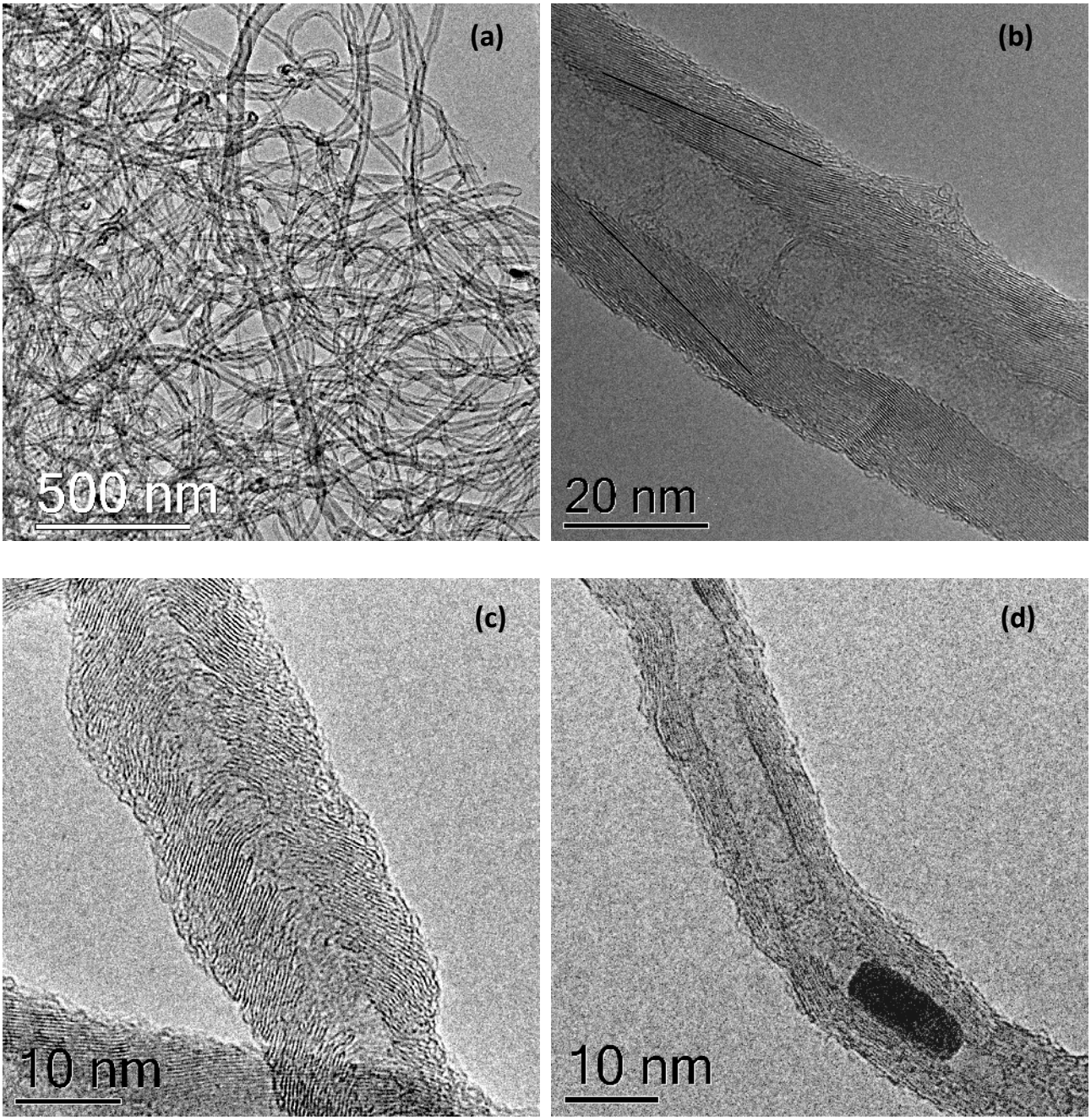

Figure 4-16. TEM images of CNFs (a) exhibiting graphene arrangement with herringbone structure (b & c) and tubular structure of parallel graphene walls (d). The majority of CNFs show herringbone structure.

For the encapsulated particles it is not clear whether the encapsulation occurs during cooling and/or during growth period. Nevertheless there is a similarity between the encapsulated

particles and catalyst at the tip of CNFs after growth that there is inhomogeneous thickness of encapsulation within a particle (Fig 4-8b &c). Such observation supports the argument of concentration gradient in a particle as the driving force for the CNF growth. The general proposed mechanism is that there are two types of Ni facets, one that is active in decomposing ethylene and another face active in precipitating the solid carbon. It is believed that larger catalyst possesses lower curvature and thus lowering the energy barrier to form graphene sheet on the metal surface, and thus making it more active than catalyst with smaller size. However this does not explain to why smaller catalyst grow more defective herringbone CNF.

A characteristic of this sample is that the metal particles are located at the tip and occasionally along the hollow channel of the CNFs or CNTs (Fig. 4-18c & d). This may be one of the possible reasons of deactivation for carbon nanofilament growth, as there would be then less Ni metal amount to dissolve, diffuse and precipitate carbon under similar chemical potential.

TEM investigation of the catalyst particle at the tip of the filaments reveals the catalyst shape and graphene defects/bending correlation as shown in Fig 4-19. The lattice spacing observed in the cold catalyst exhibit values of ~0.2 nm and ~0.176 nm corresponding to Ni (111) and Ni (200) of metallic fcc structure respectively. The bump in the catalyst projection in Fig. 4-19b deposited graphene layers with more defects and/or more bending (in parallel to the beam direction, so that it loses the focus) as compared to the graphene layers precipitate from a flat surface. This suggests that the surface microstructure of the Ni catalyst active in the deposition of graphenes was constant throughout the entire period of the graphene layer precipitation. It is however plausible to argue that similar structural consistency is required to precipitate a smooth graphitic CNTs or CNFs. It is tempting to consider that the total encapsulation of the catalyst (Fig 4-19) occurred during the cooling, as it is required to have a clean Ni surface to continuously adsorb ethylene during the growth process.

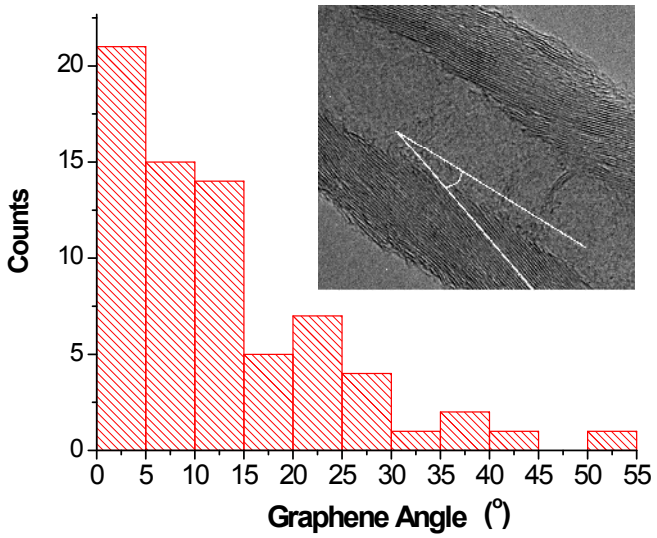

Figure 4-17. The graphenes stacking angle distribution of CNFs grown on Ni/graphite.

Figure 4-20 show the Raman spectra of the carbon materials of as-received graphite and after 120 min of CNF growth. The graphite sample exhibit first order G band corresponding to an ideal graphitic lattice vibration at around 1573 cm^{-1} and first order defect bands at 1325 cm^{-1} arising from edges of graphene layers (D1), and a very small contribution at 1611cm^{-1} assigned to lattice vibration similar to G band but involving graphene layers at the surface of graphitic crystals (D2).[59] After CNF growth the relative intensity of G band decreases relative to the D band that indicates increasing degree of disorder to the sample. Similar to the as-received graphite spectra, the Raman spectra of the CNF-graphite composite can be fitted with only three Lorentzian line shape peaks exhibiting much higher intensity of the first order defect bands. Unlike commercial CNT samples e.g. Baytubes and Nanocyls, the CNF-graphite sample does not show another first order defect band at around 1500 cm^{-1} assigned to soot-like fragments. The Raman investigation is in agreement with TEM data showing carbon nanofilament without the presence of amorphous carbon on their surface.

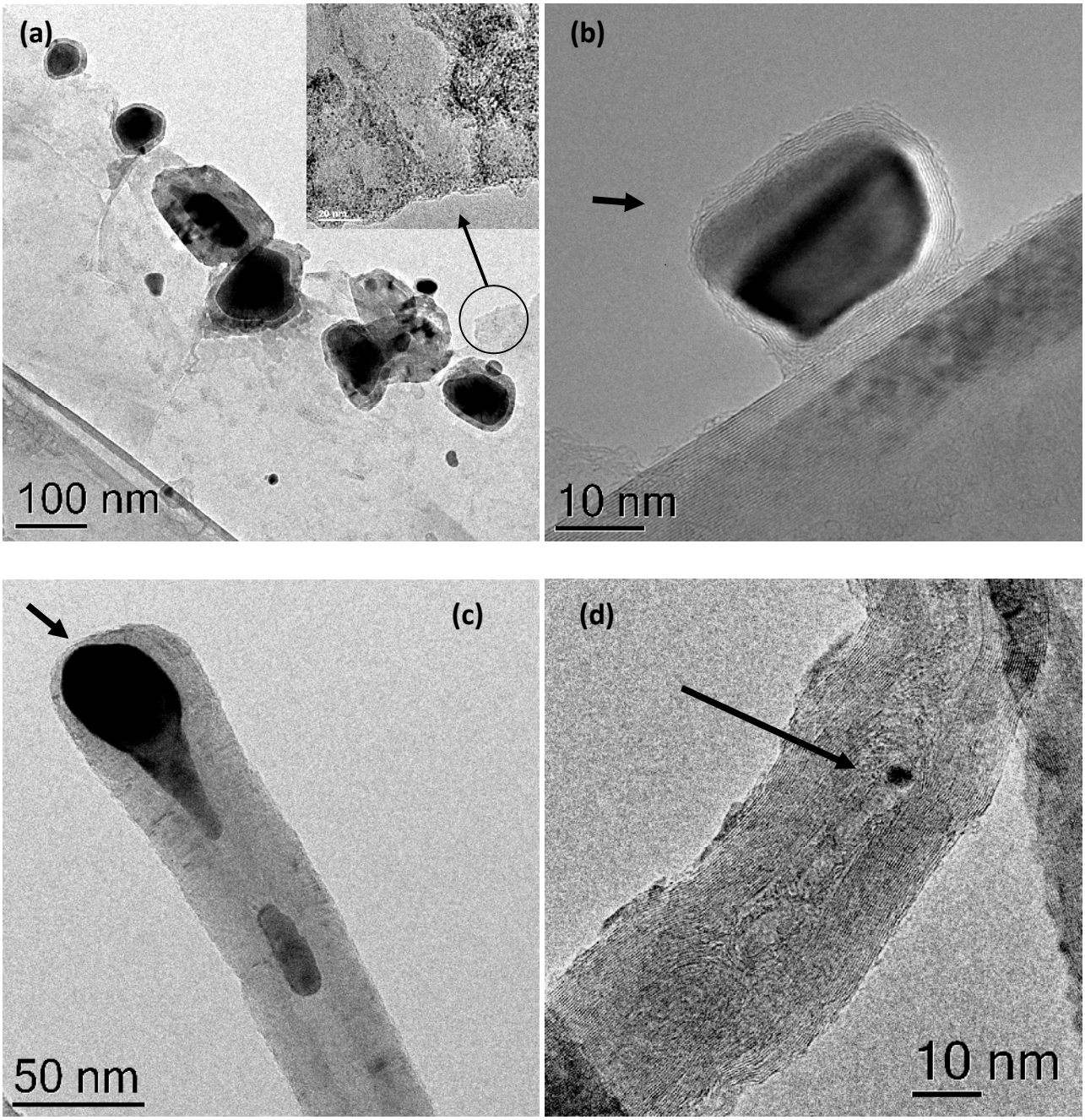

Figure 4-18. Ni catalyst particles after 2 min of C_2H_4/H_2 exposure at 700^{o}C. Some of the Ni particles are encapsulated with some part of the particle showing thinner carbon layer (a & b). The Ni particles are observed to be fragmented during growth leading to smaller fragments of Ni particles encapsulated inside the hollow channel of the CNFs (c & d). Finely dispersed Ni catalyst particles are also observed on the graphite surface with no observed encapsulation (inset a).

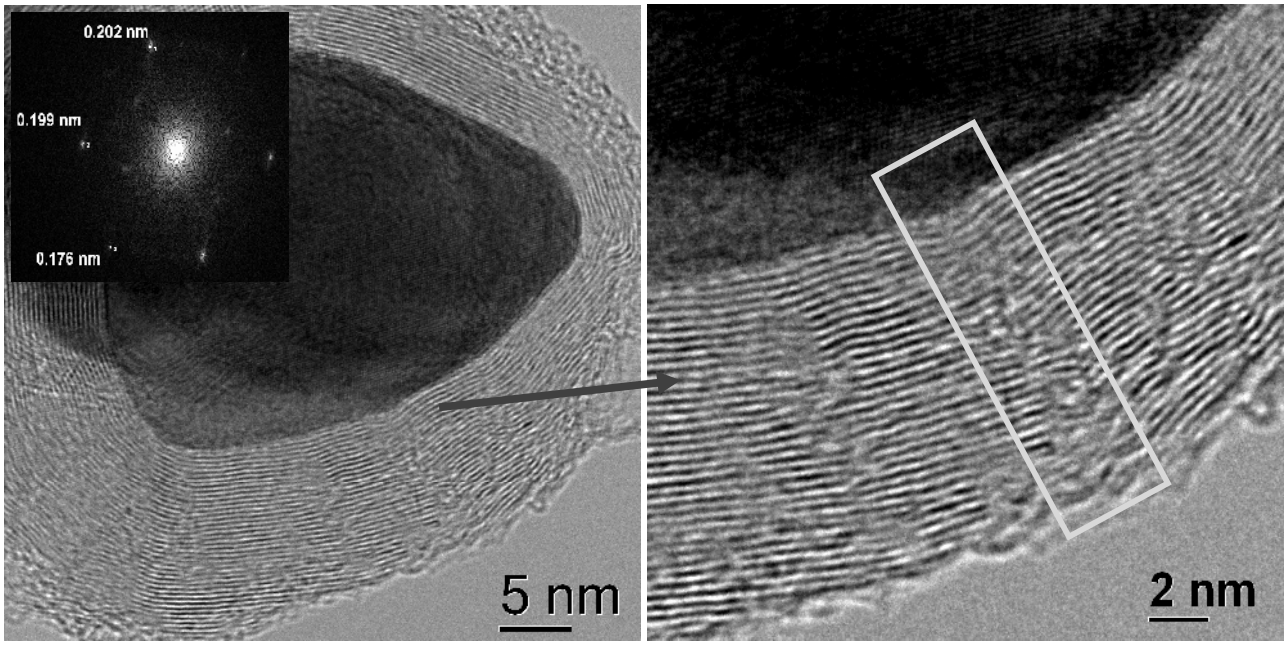

Figure 4-19. TEM image of Ni particle at the tip of CNFs grown from graphite support grown for 5 min. The catalyst exhibit fcc structure showing Ni(111) and Ni(100) lattice planes.

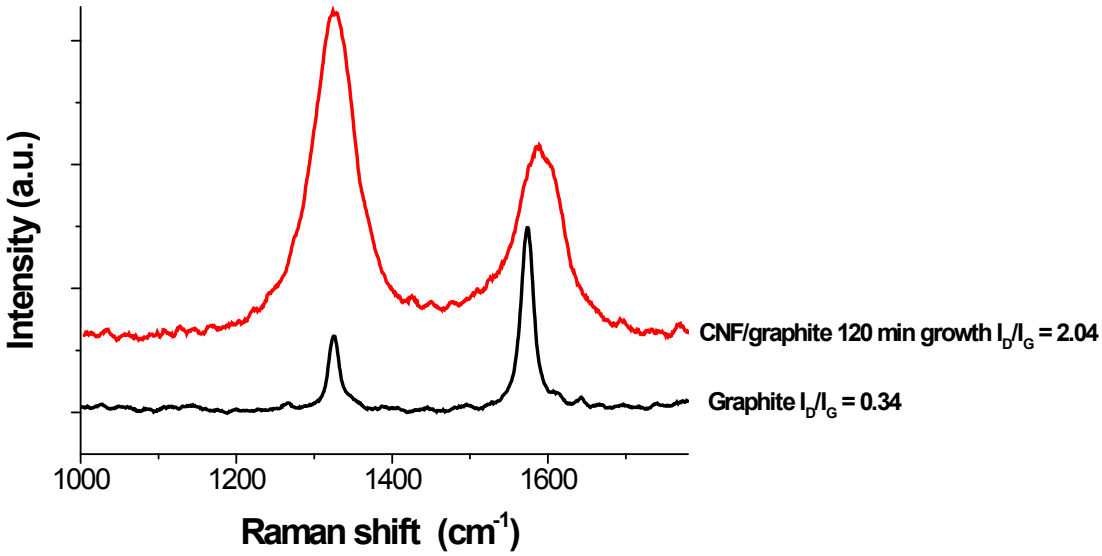

Figure 4-20. Raman spectrum depicting I_D/I_G band ratio for graphite, Ni/graphite after 120 min of filament growth (spectra normalized by the G band height).

The Ni nanoparticles catalyze the gasification of the graphite support in hydrogen atmosphere to a much lesser amount compared to activated carbon (Fig 4-21). This is expected as the C-C is more stable in the crystalline graphitic support as compared to C-C bond in defective carbons. The catalytic gasification was suggested to follow mechanism where the carbon is first activated by the metal to break the C-C bonds. The "activated" carbon then diffuse on the metal surface or through the bulk of the metal to either react with other adsorbed species (in this case adsorbed hydrogen) to form methane and/or combine with other carbon atoms to form graphene islands finally leading to encapsulation that deactivate the catalyst. Indeed SEM images of the sample after TPR experiment (Fig 4-21b-d) clearly demonstrated channels formed as result of catalytic gasification by Ni nanoparticles. The nanoparticles are seen at the end of the channels. There are also finer patches or channels probably formed from a smaller sized catalyst that later sintered into bigger ones (Fig 4-21d). Monolayer channels have been reported to form on the graphite after Ni-catalyzed gasification. The two dimensional produces channels with a soft contrast.[30,60]

HRTEM investigation was performed on reduced Ni/graphite catalyst sample to identify the catalyst microstructure to see possible carbide formation (Fig. 4-18). The sample was reduced at 300^{o}C for 1 h in 5% H_2 in helium and ramp to the growth temperature (700^{o}C) and directly cooled to room temperature in helium. The Ni particles appear to have round shapes with no graphene layer encapsulation on their surface. Similarly to Ni/AC catalyst, the reduced Ni/graphite exhibit metallic Ni with fcc structure. Selected area measurements of Ni particles lattice spacing at near surface and metal-carbon interface conclusively demonstrate that the crystal exhibit (111) and (200) lattice planes with spacing of ~0.2 nm and ~0.176 nm respectively (Fig. 4-18a-f). However lattice spacing of ~0.24 nm is occasionally observed in the particles as shown in Fig 4-18b, c, and f. The lattice fringes with a periodicity of ~0.24 nm cannot be attributed to hexagonal nickel carbide (Ni_3C) as it would not survive the temperature above ~400^{o}C. Alternative argument is the presence of interstitial carbon in the Ni particles dissolved during reduction and thus expanding the Ni fcc lattice planes. Unfortunately the current HRTEM investigation cannot conclusively confirmed the preferential area of the ~0.24 nm lattice fringes within a particle.

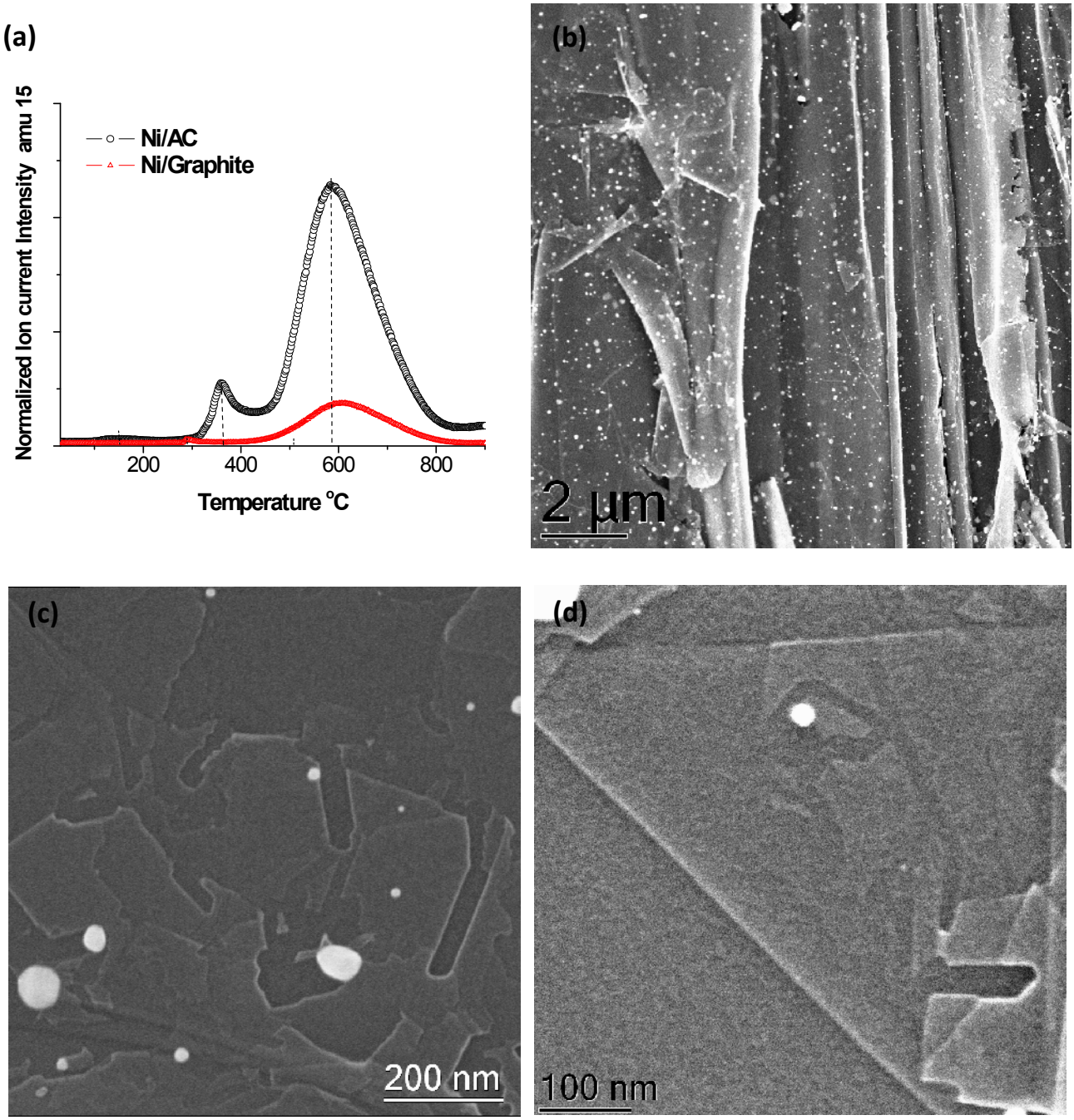

Figure 4-21. TPR profile of 1wt% Ni catalyst supported on AC and graphite under (5°C/min & 5%H_2 in Argon) (a) and SEM images of Ni/graphite samples after TPR experiments (b-d). The catalytic gasification of graphite support by Ni nanoparticles proceeds via channeling.

Several publications have reported the absence of Ni carbide phase in the catalyst after CNT growth.[61-64] However several authors have also suggested the formation of carbide-like compound in the Ni catalyst as a cause for catalyst deactivation of CNT growth.[49,65]

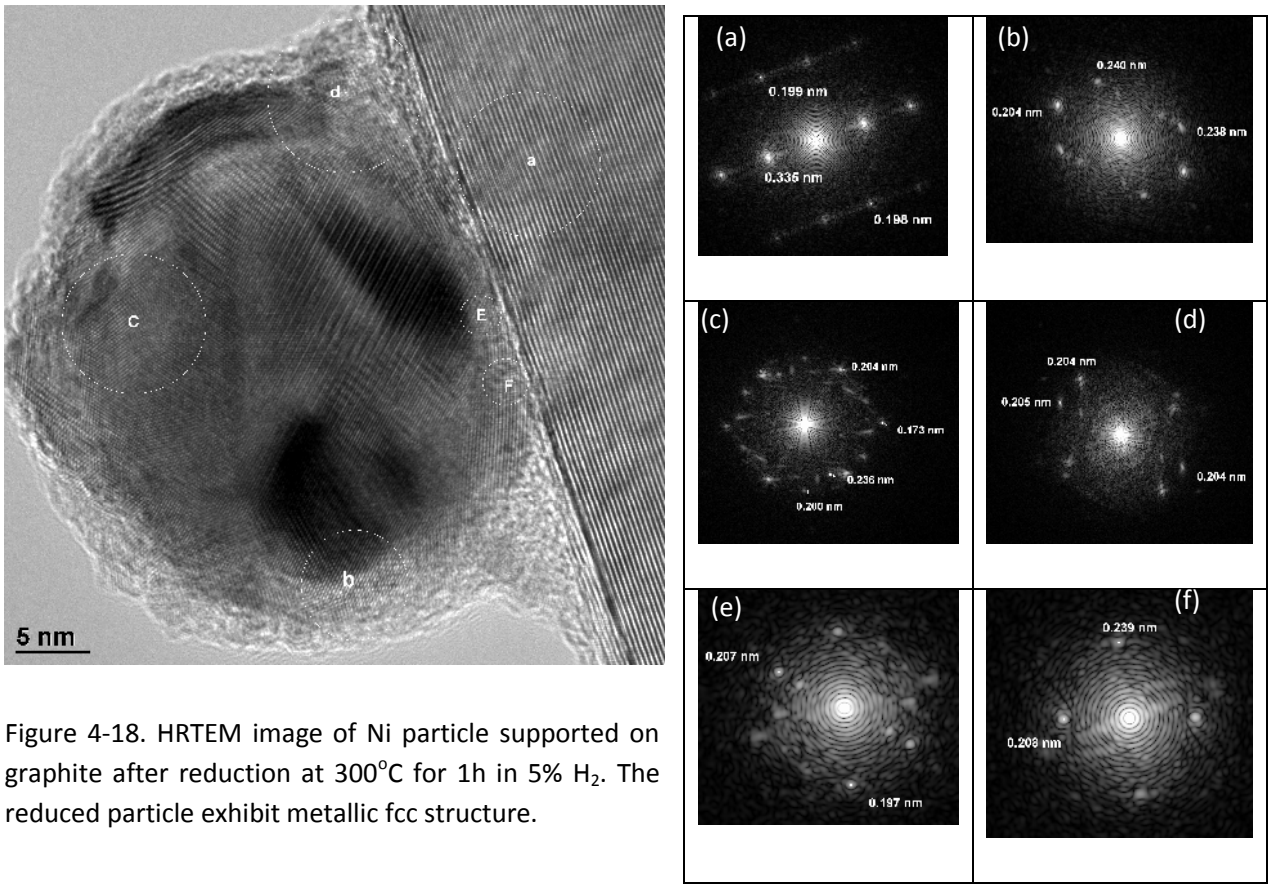

Figure 4-18. HRTEM image of Ni particle supported on graphite after reduction at 300°C for 1h in 5% H_2. The reduced particle exhibit metallic fcc structure.

Thus it is uncertain whether some sort of Ni carbide phase was present in the bulk or surface during and/or after reduction of the catalyst. The absence of an observable graphene layer and the presence of metallic fcc Ni particles suggest either the amount of carbide was too low and/or the carbide was very stable even after ramping to 700°C and cooling to room temperature.

In the current investigation Ni nanoparticles show different activity to grow carbon nanofilament when supported on AC and graphite. The latter show more activity and produced

nanofilament with more graphitic character. The superiority of graphitic support over disordered support has been reported previously. In one of the early application of CNFs as catalyst support Rodriguez et al. have clearly shown the superiority of graphitic filament over disordered carbon support.[66] Various arguments were proposed previously to explain the intrinsic activity difference between metal catalyst supported on disordered and graphitic carbon. They include carbon contaminations, carbon encapsulation and faceting of the catalyst particles. Savva et al[67] reported that Ni supported on CNTs showed activity for CNF production with C_2H_4 at 400^oC, whereas Otsuka et al[68] showed that Ni supported on carbon fiber could grow herringbone CNFs after exposure to C_2H_4 at 500^oC. Other authors have also reported the production of CNFs by Ni supported on various carbon supports with C_2H_4 in similar temperature ranges as those used in our study.[14,23] Pham-Huu et al[3] reported that CNF-supported Ni catalysts could grow CNFs with C_2H_6 in similar temperature ranges. Against that Fe catalyst supported on AC resulted the growth of defective CNFs.[69,70]

4.2.1. Carbon nanofilament growth from Ni catalyst supported on CNF/Graphite

The as-grown carbon nanofilaments from Ni/graphite catalyst composed mainly of hollow CNFs with herringbone microstructure. The carbon filament was impregnated with Ni catalyst to investigate the effect of the exposed prismatic edges to the catalyst activity for CNT growth. In general herringbone CNFs and graphite represent two graphitic materials with different basal to prismatic edges ratio. The CNF-graphite composite was used as is without pretreatment. Impregnation, calcinations, reduction and growth condition were consistent with previous experiments of Ni/AC and Ni/graphite.

Any pretreatment was avoided to preserve the physical integrity of the CNFs and to avoid introducing functional groups that would make the prismatic edges in the CNTs less comparable to that in as received graphite.

After 5 min of ethylene/hydrogen exposure at 700^oC no morphological difference can be observed from the SEM indicating no growth of the second-generation filaments (Fig 4-19a). Indeed overview TEM images only show catalyst particles with slightly elongated shapes of 10-25

nm in size supported on the surface and hollow channels of herringbone CNFs. Higher resolution images further revealed that most of the catalyst particles are encapsulated with mono to several layers of graphitic carbon (Fig 4-19c &d). There are however catalyst particles active in growing CNTs or depositing more carbons in the inner channel of the hollow CNF support (Fig 4-19e &f).

This simple experiment pictured the reactivity difference between Ni particles supported on basal plane and prismatic edges for the activity to grow carbon nanofilament in the case of graphite and CNFs as the carbon supports respectively. The differences have been suggested to be the result of different spreading action of Ni particles on prismatic edges and basal plane surface as what was reported in the case of Ru on graphite by Baker et al.[58] The degree of carbon contamination from the support in the catalyst particle can also lead to reactivity difference between the two systems. As it has been reported those active metals gasify graphites via edge recession and/or channel formation from the active edge surface.[30] It is not clear however on why the catalyst inside the hollow channel show more activity than the ones on surface. Geometrical constraints and particle size difference could play a role in the activity difference between the Ni particles.

At this point there are clear indications that Ni catalyst behaves differently when supported on activated carbon, graphite and herringbone CNFs. The three supports represent carbon supports with different basal/prismatic plane ratios. Graphitic support is shown to be the support on which Ni particles show the highest activity to grown graphitic nanofilaments with multiwalled and herringbone microstructure. The kinetic of the carbon nanofilament growth and the microstructure of the nanofilament are highly affected by the choice of support. Carbon contamination from the support to Ni particles is suspected to be responsible for the change of activity to grow carbon nanofilaments. However other factors such as porosity, support texture and surface functional groups cannot be excluded. Thus it is of paramount importance to design an experiment that would only isolate the effect of the support's graphitic character.

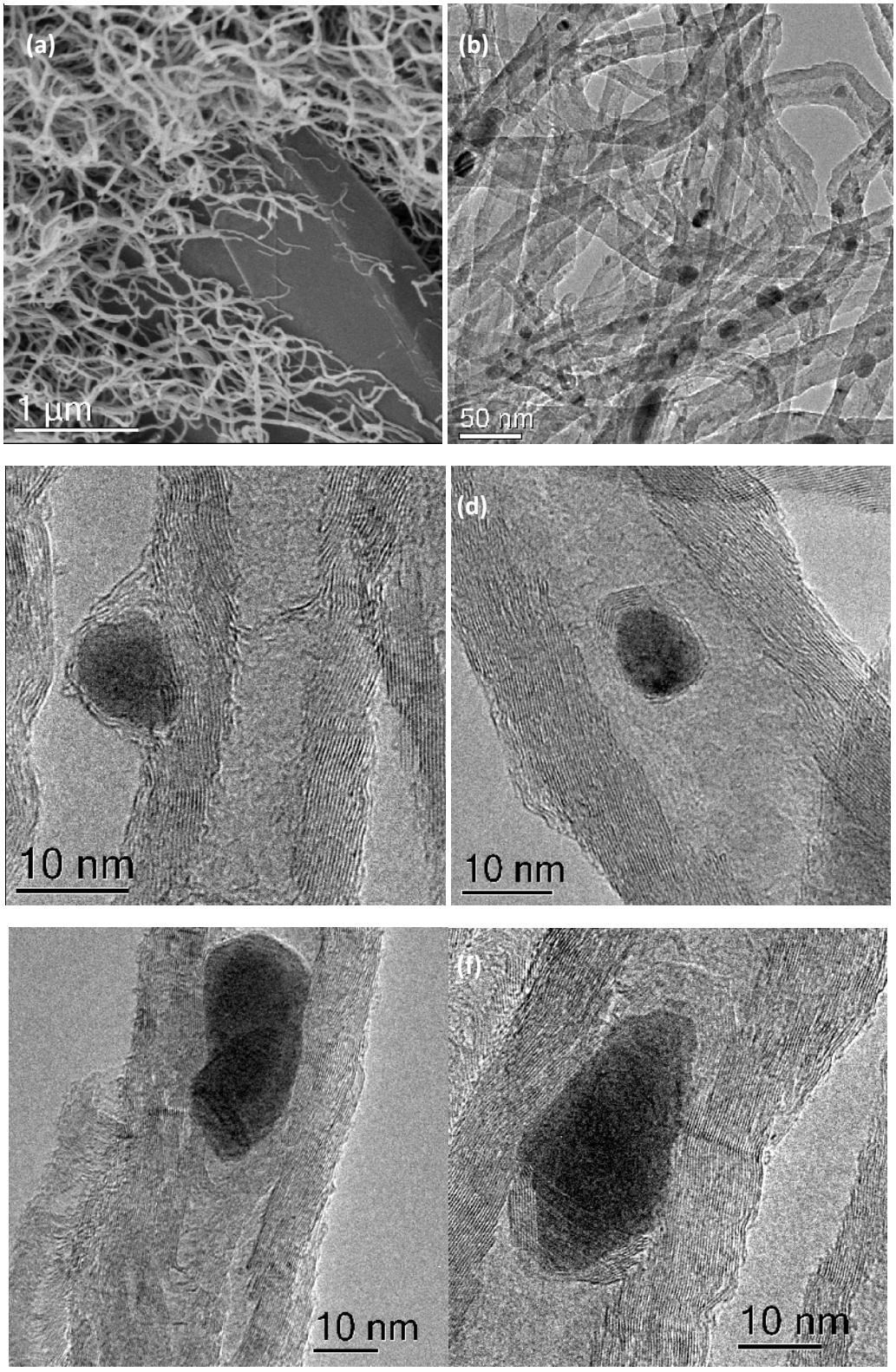

Figure 4-19. SEM and TEM images of Ni on CNF/graphite after 5 min of C_2H_4/H_2 exposure at 700°C. The Ni catalyst is not as active as Ni/graphite; however the deposited carbon structure is still graphitic.

References

(1) Vander Wal, R. L.; Ticich, T. M.; Curtis, V. E. Substrate-support interactions in metal-catalyzed carbon nanofiber growth. *Carbon* **2001**, *39*, 2277-2289.

(2) Aoki, K.; Yamamoto, T.; Furuta, H.; Ikuno, T.; Honda, S.; Furuta, M.; Oura, K.; Hirao, T. Low-Temperature Growth of Carbon Nanofiber by Thermal Chemical Vapor Deposition Using CuNi Catalyst. *Jpn. J. Appl. Phys.* **2006**, *45*, 5329-5331.

(3) Pham-Huu, C.; Keller, N.; Roddatis, V. V.; Mestl, G.; Schlogl, R.; Ledoux, M. J. Large scale synthesis of carbon nanofibers by catalytic decomposition of ethane on nickel nanoclusters decorating carbon nanotubes. *Phys. Chem. Chem. Phys.* **2002**, *4*, 514-521.

(4) Monthioux, M.; Noe, L.; Dussault, L.; Dupin, J.; Latorre, N.; Ubieto, T.; Romeo, E.; Royo, C.; Monzon, A.; Guimon, C. Texturising and structurising mechanisms of carbon nanofilaments during growth. *J. Mater. Chem.* **2007**, *17*, 4611-4618.

(5) Fenelonov, V. B.; Derevyankin, A. Y.; Okkel, L. G.; Avdeeva, L. B.; Zaikovskii, V. I.; Moroz, E. M.; Salanov, A. N.; Rudina, N. A.; Likholobov, V. A.; Shaikhutdinov, S. K. Structure and texture of filamentous carbons produced by methane decomposition on NI and NI-CU catalysts. *Carbon* **1997**, *35*, 1129-1140.

(6) Ledoux, M.; Pham-Huu, C. Carbon nanostructures with macroscopic shaping for catalytic applications. *Catalysis Today* **2005**, *102-103*, 2-14.

(7) Avdeeva, L. B.; Goncharova, O. V.; Kochubey, D. I.; Zaikovskii, V. I.; Plyasova, L. M.; Novgorodov, B. N.; Shaikhutdinov, S. K. Coprecipitated Ni-alumina and Ni---Cu-alumina catalysts of methane decomposition and carbon deposition. II. Evolution of the catalysts in reaction. *Applied Catalysis A: General* **1996**, *141*, 117-129.

(8) Pham-Huu, C.; Ledoux, M. Carbon nanomaterials with controlled macroscopic shapes as new catalytic materials. *Topics in Catalysis* **2006**, *40*, 49-63.

(9) Louis, B.; Vieira, R.; Carvalho, A.; Amadou, J.; Ledoux, M.; Pham-Huu, C. Carbon nanofibers grown over graphite supported Ni catalyst: relationship between octopus-like growth mechanism and macro-shaping. *Topics in Catalysis* **2007**, *45*, 75-80.

(10) Pham-Huu, C.; Vieira, R.; Louis, B.; Carvalho, A.; Amadou, J.; Dintzer, T.; Ledoux, M. J. About the octopus-like growth mechanism of carbon nanofibers over graphite supported nickel catalyst. *Journal of Catalysis* **2006**, *240*, 194-202.

(11) Chen, D.; Christensen, K. O.; Ochoa-Fernández, E.; Yu, Z.; Tøtdal, B.; Latorre, N.; Monzón, A.; Holmen, A. Synthesis of carbon nanofibers: effects of Ni crystal size during methane decomposition. *Journal of Catalysis* **2005**, *229*, 82-96.

(12) Dupuis, A. The catalyst in the CCVD of carbon nanotubes--a review. *Progress in Materials Science* **2005**, *50*, 929-961.

(13) Toebes, M. L.; Bitter, J. H.; van Dillen, A. J.; de Jong, K. P. Impact of the structure and reactivity of nickel particles on the catalytic growth of carbon nanofibers. *Catalysis Today* **2002**, *76*, 33-42.

(14) Anderson, P. E.; Rodriguez, N. M. Influence of the Support on the Structural Characteristics of Carbon Nanofibers Produced from the Metal-Catalyzed Decomposition of Ethylene. *Chemistry of Materials* **2000**, *12*, 823-830.

(15) Rodríguez-reinoso, F. The role of carbon materials in heterogeneous catalysis. *Carbon* **1998**, *36*, 159-175.

(16) Baker, R. T. K.; Harris, P. S. In *Chemistry and Physics of Carbon*; Thrower, P., Ed.; Marcel Dekker Inc.: New York, 1978; Vol. 14, pp. 83-165.

(17) Lund, C. R. F. Nickel catalyst deactivation in the steam-carbon reaction. *Journal of Catalysis* **1985**, *95*, 71-83.

(18) Matos, J.; Brito, J. L.; Laine, J. Activated carbon supported Ni---Mo: effects of pretreatment and composition on catalyst reducibility and on ethylene conversion. *Applied Catalysis A: General* **1997**, *152*, 27-42.

(19) Tomita, A.; Sato, N.; Tamai, Y. Hydrogenation of carbons catalyzed by nickel, platinum and rhodium. *Carbon* **1974**, *12*, 143-149.

(20) Tomita, A.; Tamai, Y. Optical microscopic study on the catalytic hydrogenation of graphite. *The Journal of Physical Chemistry* **1974**, *78*, 2254-2258.

(21) Figueiredo, J. L.; Bernardo, C. A.; Chludzinski, J. J.; Baker, R. T. K. The reversibility of filamentous carbon growth and gasification. *Journal of Catalysis* **1988**, *110*, 127-138.
(22) Lund, C. R. Staged carbon gasification with nickel catalysts. *Carbon* **1987**, *25*, 337-341.
(23) Baker, R. T. K.; Sherwood, R. D. Catalytic gasification of graphite by nickel in various gaseous environments. *Journal of Catalysis* **1981**, *70*, 198-214.
(24) Wigmans, T.; van Doorn, J.; Moulijn, J. A. Deactivation of nickel during gasification of activated carbon, studied by X-ray photoelectron spectroscopy. *Surface Science* **1983**, *135*, 532-552.
(25) Haydar, S.; Moreno-Castilla, C.; Ferro-García, M. A.; Carrasco-Marín, F.; Rivera-Utrilla, J.; Perrard, A.; Joly, J. P. Regularities in the temperature-programmed desorption spectra of CO2 and CO from activated carbons. *Carbon* **2000**, *38*, 1297-1308.
(26) Nam, Y.; Lee, J. Metal-catalyzed gasification of carbon. *Korean Journal of Chemical Engineering* **1995**, *12*, 466-471.
(27) Holstein, W. L.; Boudart, M. Hydrogenolysis of carbon and its catalysis by platinum. *Journal of Catalysis* **1981**, *72*, 328-337.
(28) Baker, R. T. K.; Sherwood, R. D.; Derouane, E. G. Further studies of the nickel/graphite-hydrogen reaction. *Journal of Catalysis* **1982**, *75*, 382-395.
(29) Baker, R. T. K.; Sherwood, R. D. Catalytic action of iron on graphite in a hydrocarbon/steam environment. *Journal of Catalysis* **1985**, *95*, 101-107.
(30) Baker, R. T. K. In Situ Electron Microscopy Studies of Catalyst Particle Behavior. *Catalysis Revs.* **1979**, *19*, 161-209.
(31) Baker, R. T. K. In *Carbon and coal gasification: science and technology*; Figueiredo, J.; Moulijn, J., Eds.; NATO ASI; Springer: Dordrecht, 1986; pp. 231-268.
(32) Baker, R. T. K. The relationship between particle motion on a graphite surface and Tammann temperature. *Journal of Catalysis* **1982**, *78*, 473-476.
(33) Anton, R. In situ transmission electron microscopy study of the growth of Ni nanoparticles on amorphous carbon and of the graphitization of the support in the presence of hydrogen. *J Mater Res* **2005**, *20*, 1837-1843.
(34) Anton, R. On the reaction kinetics of Ni with amorphous carbon. *Carbon* **2008**, *46*, 656-662.
(35) Derbyshire, F.; Presland", A.; Trimm, D. The formation of graphite films by Precipitation of Carbon from Nickel Foils. *Carbon* **1972**, *10*, 114, IN21, 115.
(36) Omori, M.; Hirai, T.; Yajima, S. Electron microscope observations of carbon layers around iron particles dispersed in a glasslike carbon matrix. *Carbon* **1974**, *12*, 474-476.
(37) Nakano, H.; Nakamura, J. Carbide-induced reconstruction initiated at step edges on Ni(1 1 1). *Surface Science* **2001**, *482-485*, 341-345.
(38) Zdansky, E. O.; Nilsson, A.; Mårtensson, N. CO-induced reversible surface to bulk transformation of carbidic carbon on Ni(100). *Surface Science* **1994**, *310*, L583-L588.
(39) Alstrup, I.; Chorkendorff, I.; Ullmann, S. Interaction of hydrogen with carbidic carbon on Ni(100). *Surface Science* **1993**, *293*, 133-144.
(40) Nakano, H.; Ogawa, J.; Nakamura, J. Growth mode of carbide from C2H4 or CO on Ni(1 1 1). *Surface Science* **2002**, *514*, 256-260.
(41) Smith, M. A.; Sinharoy, S.; Levenson, L. L. Thermal decomposition of nickel carbide: an Auger lineshape study. *J. Vac. Sci. Technol.* **1979**, *16*, 462-465.
(42) Nagakura, S. Study of Metallic Carbides by Electron Diffraction Part I. Formation and Decomposition of Nickel Carbide. *J. Phys. Soc. Jpn.* **1957**, *12*, 482-494.
(43) Lamber, R.; Jaeger, N.; Schulz-Ekloff, G. Electron microscopy study of the interaction of Ni, Pd and Pt with carbon : I. Nickel catalyzed graphitization of amorphous carbon. *Surface Science* **1988**, *197*, 402-414.
(44) Krivoruchko, O. A new phenomenon involving the formation of liquid mobile metal-carbon particles in the low-temperature catalytic graphitisation of amorphous carbon by metallic Fe, Co and Ni. *Mendeleev Communications* **1998**, *8*, 97-100.
(45) Gur'yanova, O.; Kukovitsky, E.; L'vov, S.; Sainov, N.; Shustov, V. Electron diffraction investigation of catalytic particles at the tips of carbon nanotubes. *Physics of the Solid State* **2002**, *44*, 473-474.
(46) Ermakova, M. A.; Ermakov, D. Y. Ni/SiO2 and Fe/SiO2 catalysts for production of hydrogen and

filamentous carbon via methane decomposition. *Catalysis Today* **2002**, *77*, 225-235.
(47) Ermakova, M.; Ermakov, D.; Plyasova, L.; Kuvshinov, G. XRD studies of evolution of catalytic nickel nanoparticles during synthesis of filamentous carbon from methane. *Catalysis Letters* **1999**, *62*, 93-97.
(48) Holstein, W.; Moorhead, R.; Poppa, H.; Boudart, M. In *Chemistry and Physics of Carbon*; Marcel Dekker Inc.: New York.
(49) Takenaka, S.; Ogihara, H.; Otsuka, K. Structural Change of Ni Species in Ni/SiO2 Catalyst during Decomposition of Methane. *Journal of Catalysis* **2002**, *208*, 54-63.
(50) Schlögl, R. In *Handbook of Heterogeneous Catalysis*; Ertl, G.; Knözinger, H.; Schüth, F.; Weitkamp, J., Eds.; Wiley-VCH, 2008; pp. 357-427.
(51) Krishnankutty, N.; Vannice, M. A. The Effect of Pretreatment on Pd/C Catalysts : I. Adsorption and Absorption Properties. *Journal of Catalysis* **1995**, *155*, 312-326.
(52) Krishnankutty, N.; Li, J.; Albert Vannice, M. The effect of Pd precursor and pretreatment on the adsorption and absorption behavior of supported Pd catalysts. *Applied Catalysis A: General* **1998**, *173*, 137-144.
(53) Gandia, L. M.; Montes, M. Effect of Thermal Treatments on the Properties of Nickel and Cobalt Activated-Charcoal-Supported Catalysts. *Journal of Catalysis* **1994**, *145*, 276-288.
(54) McCarty, J. G.; Wise, H. Hydrogenation of surface carbon on alumina-supported nickel. *Journal of Catalysis* **1979**, *57*, 406-416.
(55) Abild-Pedersen, F.; Lytken, O.; Engbæk, J.; Nielsen, G.; Chorkendorff, I.; Nørskov, J. K. Methane activation on Ni(1 1 1): Effects of poisons and step defects. *Surface Science* **2005**, *590*, 127-137.
(56) Viñes, F.; Loschen, C.; Illas, F.; Neyman, K. M. Edge sites as a gate for subsurface carbon in palladium nanoparticles. *Journal of Catalysis* **2009**, *266*, 59-63.
(57) Schlögl, R. In *Preparation of Solid Catalysts*; Ertl, G.; Knözinger, H.; Weitkamp, J., Eds.; Wiley-VCH Verlag GmbH & Co. KGaA, 1999.
(58) Baker, R. T. K.; Chludzinski, J. J. In-situ electron microscopy studies of the behavior of supported ruthenium particles. 2. Carbon deposition from catalyzed decomposition of acetylene. *The Journal of Physical Chemistry* **1986**, *90*, 4734-4738.
(59) Sadezky, A.; Muckenhuber, H.; Grothe, H.; Niessner, R.; Pöschl, U. Raman microspectroscopy of soot and related carbonaceous materials: Spectral analysis and structural information. *Carbon* **2005**, *43*, 1731-1742.
(60) Goethel, P. J.; Yang, R. T. Platinum-catalyzed hydrogenation of graphite: Mechanism studied by the rates of monolayer channeling. *Journal of Catalysis* **1986**, *101*, 342-351.
(61) Helveg, S.; Lopez-Cartes, C.; Sehested, J.; Hansen, P. L.; Clausen, B. S.; Rostrup-Nielsen, J. R.; Abild-Pedersen, F.; Norskov, J. K. Atomic-scale imaging of carbon nanofibre growth. *Nature* **2004**, *427*, 426-429.
(62) Hofmann, S.; Blume, R.; Wirth, C. T.; Cantoro, M.; Sharma, R.; Ducati, C.; Hävecker, M.; Zafeiratos, S.; Schnoerch, P.; Oestereich, A.; Teschner, D.; Albrecht, M.; Knop-Gericke, A.; Schlögl, R.; Robertson, J. State of Transition Metal Catalysts During Carbon Nanotube Growth. *J. Phys. Chem. C* **2009**, *113*, 1648-1656.
(63) Lin, M.; Ying Tan, J. P.; Boothroyd, C.; Loh, K. P.; Tok, E. S.; Foo, Y. Direct Observation of Single-Walled Carbon Nanotube Growth at the Atomistic Scale. *Nano Letters* **2006**, *6*, 449-452.
(64) Lin, M.; Tan, J. P. Y.; Boothroyd, C.; Loh, K. P.; Tok, E. S.; Foo, Y. Dynamical Observation of Bamboo-like Carbon Nanotube Growth. *Nano Letters* **2007**, *7*, 2234-2238.
(65) Shaikhutdinov, S.; Avdeeva, L.; Novgorodov, B.; Zaikovskii, V.; Kochubey, D. Nickel catalysts supported on carbon nanofibers: structure and activity in methane decomposition. *Catalysis Letters* **1997**, *47*, 35-42.
(66) Rodriguez, N. M.; Kim, M.; Baker, R. T. K. Carbon Nanofibers: A Unique Catalyst Support Medium. *The Journal of Physical Chemistry* **1994**, *98*, 13108-13111.
(67) Savva, P.; Olympiou, G.; Costa, C.; Ryzhkov, V.; Efstathiou, A. Hydrogen production by ethylene decomposition over Ni supported on novel carbon nanotubes and nanofibers. *Catalysis Today* **2005**, *102-103*, 78-84.
(68) Otsuka, K.; Abe, Y.; Kanai, N.; Kobayashi, Y.; Takenaka, S.; Tanabe, E. Synthesis of carbon nanotubes on Ni/carbon-fiber catalysts under mild conditions. *Carbon* **2004**, *42*, 727-736.
(69) Su, D. S.; Chen, X.; Weinberg, G.; Klein-Hofmann, A.; Timpe, O.; Hamid, S. B. A.; Schlögl, R. Hierarchically Structured Carbon: Synthesis of Carbon Nanofibers Nested inside or Immobilized onto Modified Activated Carbon. *Angewandte Chemie International Edition* **2005**, *44*, 5488-5492.

(70) Chen, X.; Su, D. S.; Hamid, S. B.; Schlögl, R. The morphology, porosity and productivity control of carbon nanofibers or nanotubes on modified activated carbon. *Carbon* **2007**, *45*, 895-898.

Chapter 5:

Probing metal-carbon interaction by growing CNTs

In heterogeneous catalysis, the nature of the support influences the catalytic activity through its interaction with the (transition metal) active phase. Carbon is a special case as its structure (graphitic character) also plays a significant role. This characteristic remains an unresolved scientific issue of crucial importance for material science, catalysis and nanotechnology. In this study model supports of vapor grown carbon fibers annealed at different temperatures were used to represent carbon support with a different degree of graphitic character. The use of model supports aims to control the experiments by focusing on the graphitic character of the support by excluding other factors such as surface functionality, porosity and textures. Using in-situ methods to investigate the process of carbon nanofilament growth on carbon-supported Ni nanoparticles, the results show that atomic carbon from defective supports is already incorporated in the Ni nanoparticles at relatively low temperatures. This is observed before exposure to the reaction feed to grow nanofilaments. The dissolved carbon not only modifies the electronic properties of the metal but it also leads to a reconstruction of the nanoparticles. The idea of carbon contamination proposed earlier based on the experiments with Ni/AC and Ni/graphite was confirmed in this study. The findings here may explain many of the differences in catalytic activity observed when supporting metals on carbon and contribute to the general understanding of the CNT and CNF growth mechanism(s). The concept of controlling the microstructure of the grown nanofilaments by pre-contaminating the Ni catalyst by carbon was tested by a pre-dosing experiment with ethylene. The results are in agreement and support the hypothesis proposed.

5.1. Carbon nanofilament synthesis by Ni catalyst supported on carbon of different graphitization

Vapor grown carbon nanofibers produced by Pyrograph were used as the "model" supports to investigate the effect graphitic character of the support to the activity of Ni catalyst. The nanofibers are synthesized by decomposition of CH_4 with $Fe(CO)_5$ catalyst precursor at 1100^{o}C. The carbon nanofibers grown from the iron catalyst was kept in the reactor to allow CH_4 to thermally crack on the nanofibers surface overtime. The thermal cracking of CH_4 resulted in the thickening of the nanofibers surface with highly disordered carbon coatings. This pyrolytic carbon homogenously covers the nanofibers surface. Details of the material have been investigated elsewhere.[1] The as-grown fibers were later treated at different annealing temperature by the Pyrograph manufacturer to produce PS-grade (annealed at 700^{o}C) LHT-grade (annealed at 1500^{o}C) and HHT-grade (annealed at 3000^{o}C). The average outer diameter of the nanofibers material from PR24 series is 100 nm.

The PR24-PS and PR24-HHT were selected as the model carbon support that represents two systems with significant difference in the degree of graphitization. The outer surface of the two materials has different graphitic character. HRTEM and Raman spectra demonstrate the graphitic character of the two supports (Fig. 5-1 and Fig. 5-2).

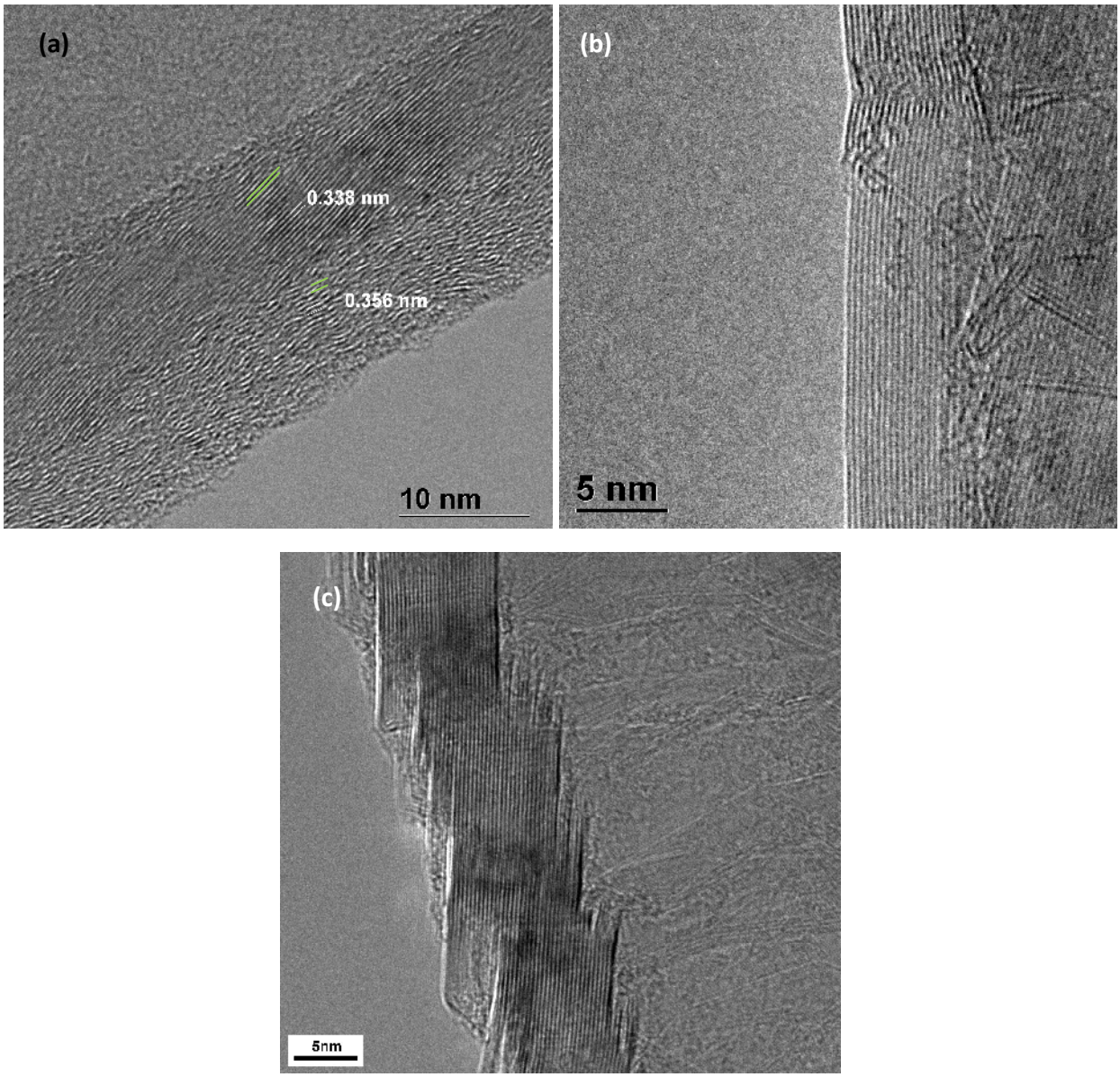

Figure 5-1. Microscopy images of VGCNFs used in this study as catalyst supports; defective carbon support PR24-PS (a) and graphitic carbon support PR24-HHT (b,c).The shape of the two supports are similar in macro dimension. In the defective carbon support (a) the pyrolytic layer produces a disordered surface with higher interlayer spacing (0.356 nm). Whereas the graphitic carbon support (b&c) shows highly ordered surface.

Later in the text PR24-PS and PR24-HHT will be labeled “defective carbon” and “graphitic carbon” supports respectively. SEM images show that the defective carbon support

has smooth surface whereas the graphitic has a faceted surface (Fig. 3-2c, d). The faceting of the VGCNFs surface was reported after high temperature annealing resulted in graphite-like structure. The defective carbon support exhibit short graphene sheets stacked along the filament with turbostratic arrangements. The inner core of the nanofiber show graphitic herringbone hollow microstructure. *d* spacing value for (002) planes of the core and outer layer of the defective nanofiber are 338 pm and 356 pm respectively. The outer layer is rich in structural and topological defects e.g. bending that give its surface roughness and distorted texture (Fig.5-1c). The degree of disorder in the PS nanofiber is characterized by the low *La* (in plane coherence length) and *Lc* (c-axis crystalline coherence length) showing short range order in plane and c-axis directions respectively. On the basis of HRTEM observations, the outer layer of PS nanofiber show short parallel layers forming distorted columnar structures of varying heights. After annealing at high temperature the support developed a smooth graphitic surface with long range order in the in-plane and c-axis orientations (Fig. 5-1d). Raman spectra of the two carbon nanofibers are in agreement with TEM observations demonstrating broad G and D bands typical of disordered carbon materials for the PS nanofiber.[2,3] Fitting procedure performed for the Raman spectra further revealed a contribution of bands at around 1150cm^{-1} and 1490cm^{-1} attributed to polyene-like structure and molecular amorphous carbon. After annealing the nanofibers exhibit a sharp G band with a drastic decrease of the D band with the absence of 1150 and 1490cm^{-1} contribution, characteristic of graphitic carbon material.[4]

The defective carbon contain 1.47 wt% of Fe catalyst impurity encapsulated in graphitic layers. After annealing at 3000^{o}C the graphitic carbon nanofiber is free from metallic impurities.[1]

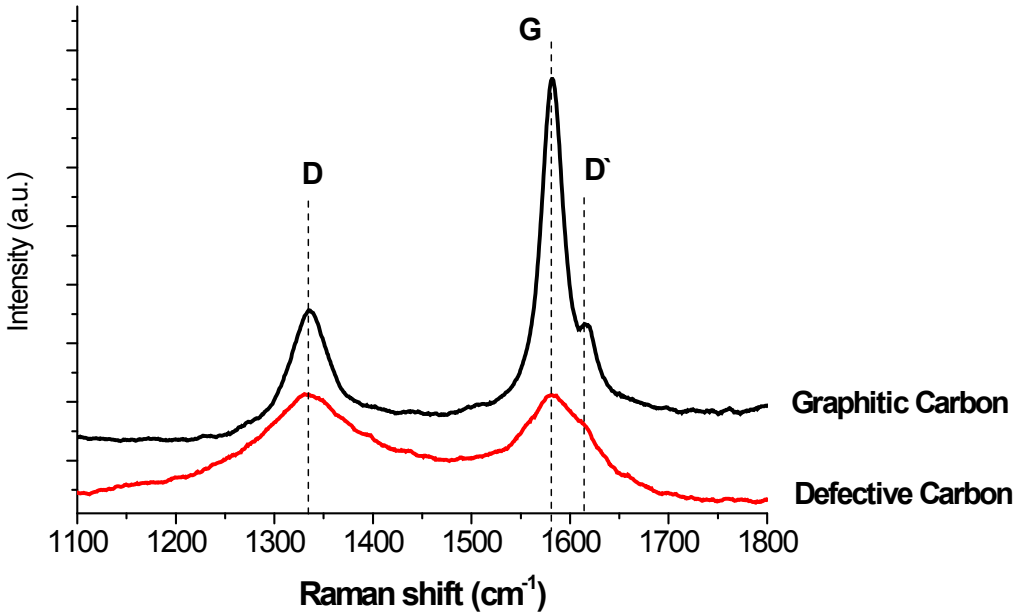

Figure 5-2. Raman spectra of VGCNF supports used in this study. The G band in the graphitic support has sharper peak shape with much higher intensity.

The VGCNFs supports were deposited with $Ni(NO_3)_2$ in an acetone solution using wet impregnation method and were later dried in a fume hood overnight (25^{o}C). The carbon supports were used directly without further treatment. Calcinations, reduction and growth conditions used in this set of experiments were similar to above-mentioned experiments with AC and graphite as supports. The catalyst was calcined at 250^{o}C in 5% O_2 for 1 h, reduced at 300^{o}C in 5% H_2 for 1 h and ramped up to 700^{o}C in helium and exposed to C_2H_4/H_2 mixture for 5 min before cooling down in helium.

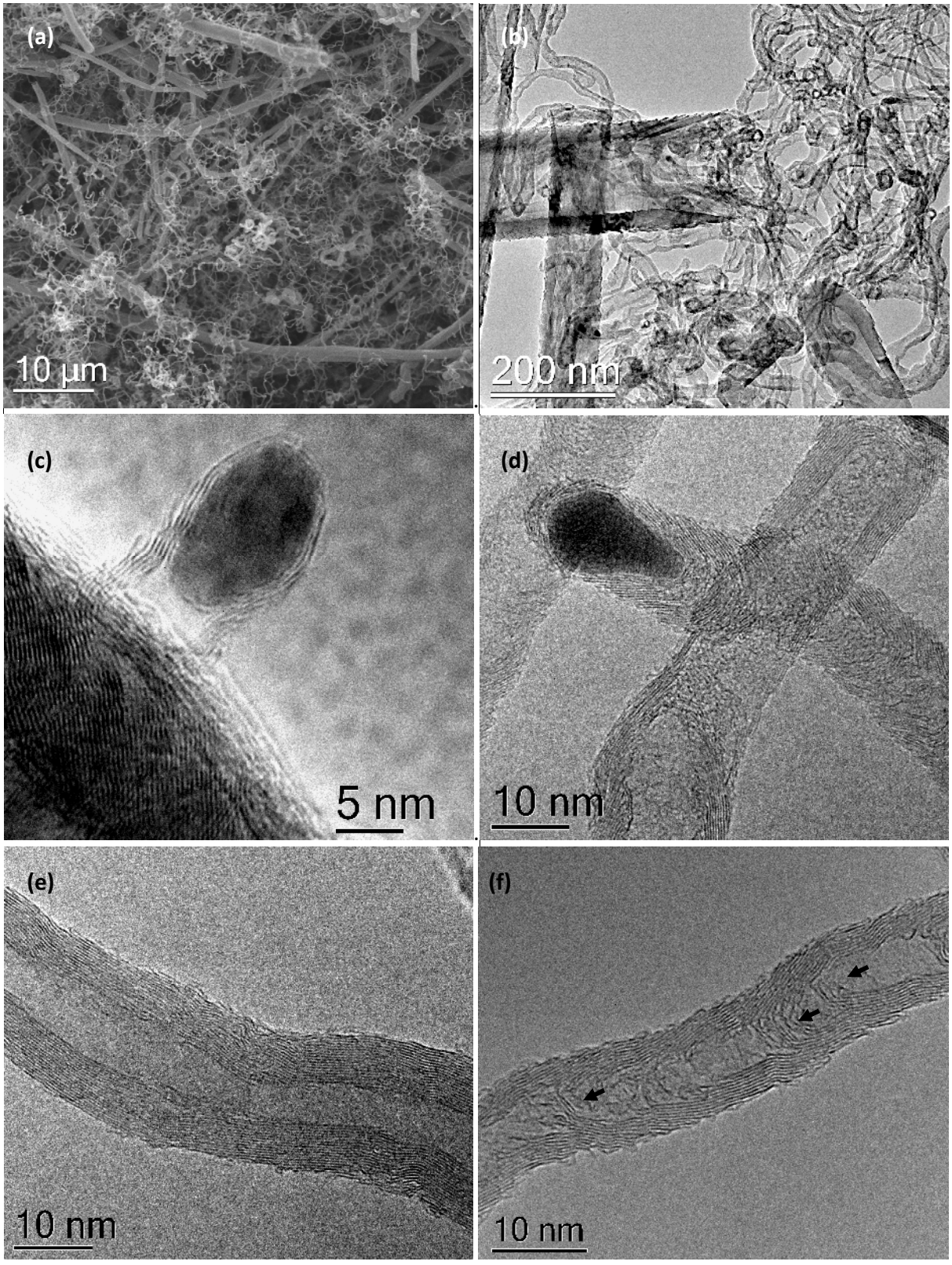

Figure 5-3. Carbon nanofilaments grown from Ni supported on Graphitic carbon.

The carbon nanofilaments synthesized from Ni/graphitic and Ni/defective catalyst systems are presented in Fig. 5-3 and Fig. 5-4 respectively. After 5 min of growth the as-grown nanofilaments form a web-like network covering the VGCNF supports (Fig.5-3a & Fig. 5-2a). TEM investigations demonstrate significant difference in the as grown nanofilaments microstructure from the two supported Ni catalysts. Nanofilaments grown from Ni/graphitic carbon have graphitic tubular multiwall structure with hollow channel (CNTs) and graphitic herringbone with hollow channel (CNFs). The CNTs show equivalent number of walls on both sides of the filaments observed from the projection images (Fig 5.3c &e). The nanofilament growth follows a tip-growth mechanism showing the catalyst moving away from the support. After 5 min of growth the catalyst particles exhibit "pear" or "teardrop" shape with the end pointing to the direction of carbon diffusion and fully encapsulated with several graphitic layers (Fig. 5-3c & d). The interplanar distance of the graphitic layers for multiwall CNTs and herringbone CNFs are in the range of 3.3 to 3.5Å. Especially for herringbone CNFs the hollow channels exhibit occasional thin layer of graphitic layer perpendicular to the tube axis forming a bamboo-like structure. Along the tube axis, the distance between the layers forming the bamboo like structure is quite random (Fig 5-3f). In the literature it was suggested that a change in the steady-state diffusion of carbon atoms in bulk and/or surface of a catalyst particle caused interruptions to the growth process thus allowing the formation periodic compartment bamboo structures.[5,6]

The carbon nanofilaments grown from Ni/defective carbon however show disordered microstructures. They are composed of single directional and octopus-like filaments grown from small and bigger catalyst particles respectively (Fig. 5-4d & e). The Ni catalysts were observed at the top of the filament suggesting a tip growth mechanism. The filaments have no hollow channel along the filament axis. They demonstrate a broad distribution of graphene arrangements relative to the filament axis within the sample. Some of the filaments exhibit platelets arrangements of defective character showing a lot of bending and/or shorter in-plane length (*La*). Whereas some filaments exhibit arrangements of disordered orientation relative to axis and with low interlayer stacking length (Lc) rich in bending (Fig 5-4c & e). Fig 5-4e presents the contrast-adjusted TEM image of a short filament to highlight the degree of disorder in the

sample. Complete carbon encapsulation was not observed for the catalyst particles after 5 min of nanofilament growth on the defective supported system. The front face of the catalyst which is generally accepted to be the area where carbon-containing gas decomposition reaction takes place is only partially covered with a monolayer of distorted carbon. Especially for bigger particles active in growing octopus–like filaments, some facets appear to be free from carbon deposition.

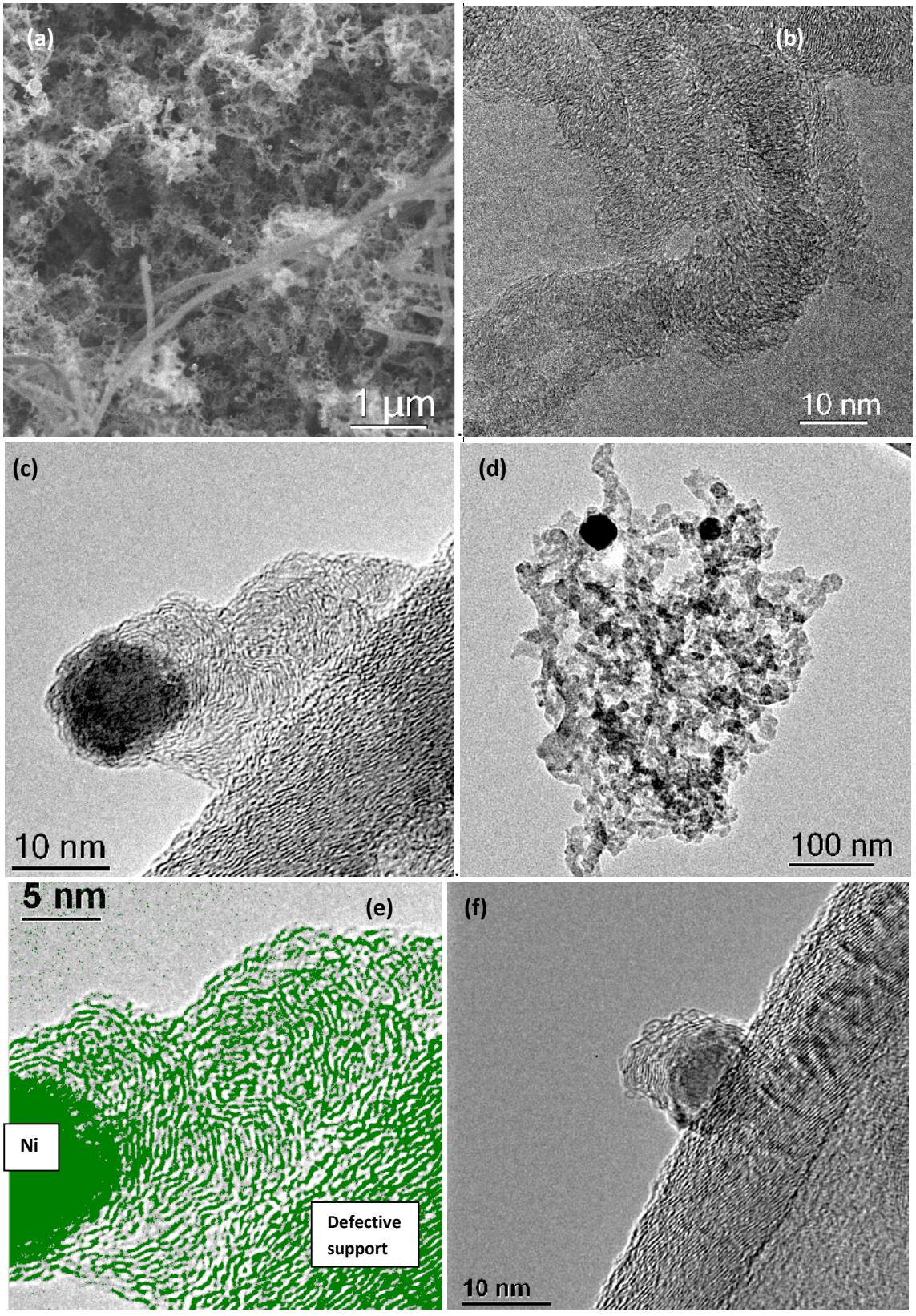

Figure 5-4. Carbon nanofilaments grown from Ni catalyst supported on defective carbon.

A general character of carbon support exerting weak metal-substrate interaction is demonstrated by the tip-growth mechanism of the filaments in both cases. A general observation from the two systems is that smaller catalyst particles (5-10 nm) precipitated shorter filaments after 5 min of ethylene/hydrogen exposure. It was suggested that there is a size limit for catalyst particles to facilitate the formation of graphene islands on the surface to allow CNT nucleation to occur.[7,8,9] In addition the high energy strain from curved graphene sheets increases the energy required to nucleate CNTs from smaller catalyst.

The experiments clearly demonstrate the effect exerted by the carbon support to the Ni catalyst for the synthesis of Carbon nanofilaments. There are several scenarios on how one can explain the origin of the effect exerted by the carbon supports. One is from the perspective of support-induced catalyst particle reconstruction. It has been reported that catalyst particles adopted different morphology when supported on different carbon supports. On basal plane of graphite Ni particles exhibit faceted shapes whereas on carbon black support the particles show a featureless shape. [10] Experimental and theoretical investigations have also reported the epitaxial growth of graphite layers on Ni(111) surfaces.[11,12,9] It was calculated that the Ni atoms on the surface of Ni(111) face has almost perfect registry with graphene layer. Thus it is plausible to consider that the same forces apply for the epitaxial growth of Ni crystal on graphitic carbon surfaces. The two carbon supports under investigation also represent two conditions whereby the carbon materials have different electronic properties. There are claims in the literature where graphitic support influences the activity of a catalyst via increasing the electronic density of the metal.[13] However as the filaments grown from both systems exhibit tip-growth mechanism the significance of the electronic and/or structural-induced effect from the supports to the catalyst is ambiguous and debatable.

(a)

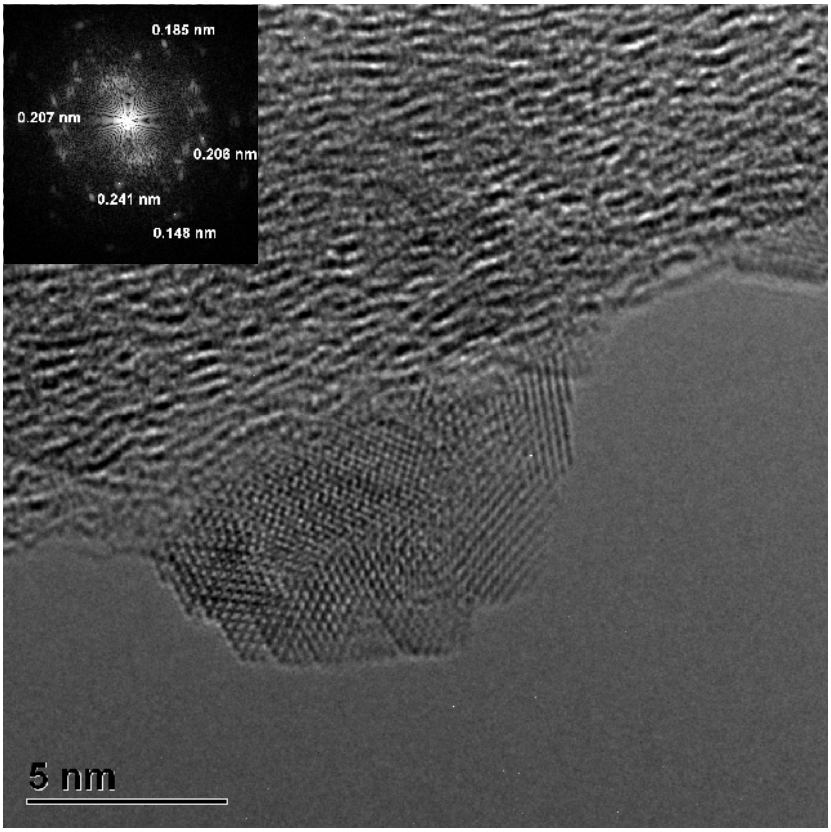
0.185 nm
0.207 nm
0.208 nm
0.241 nm
0.148 nm
5 nm

(b)

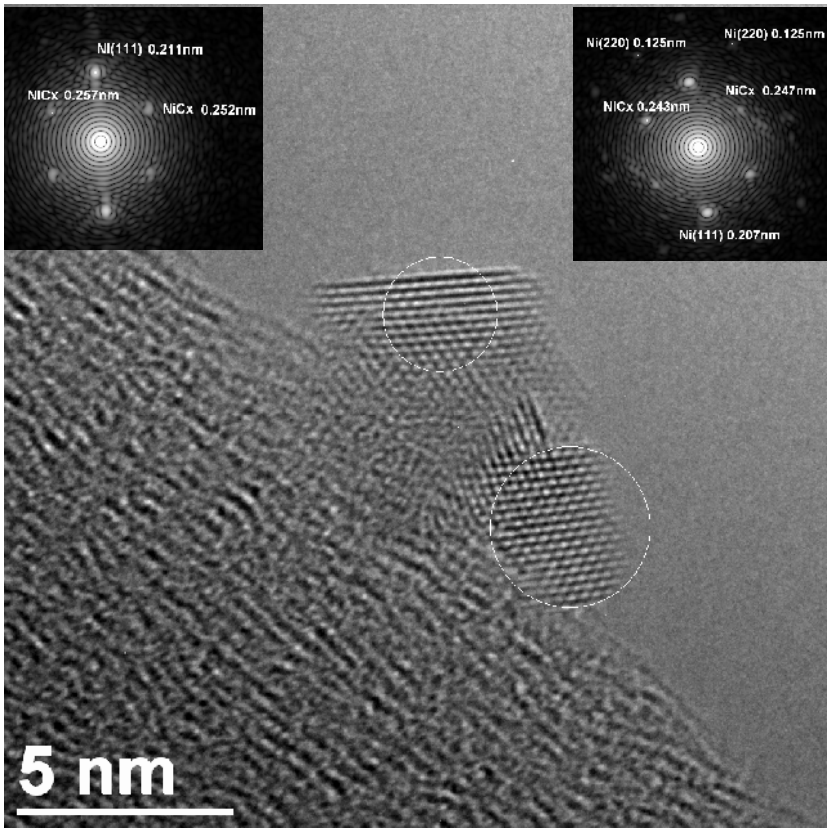
Ni(111) 0.211nm
NiCx 0.257nm
NiCx 0.252nm
Ni(220) 0.125nm
Ni(220) 0.125nm
NiCx 0.247nm
NiCx 0.243nm
Ni(111) 0.207nm
5 nm

(c)

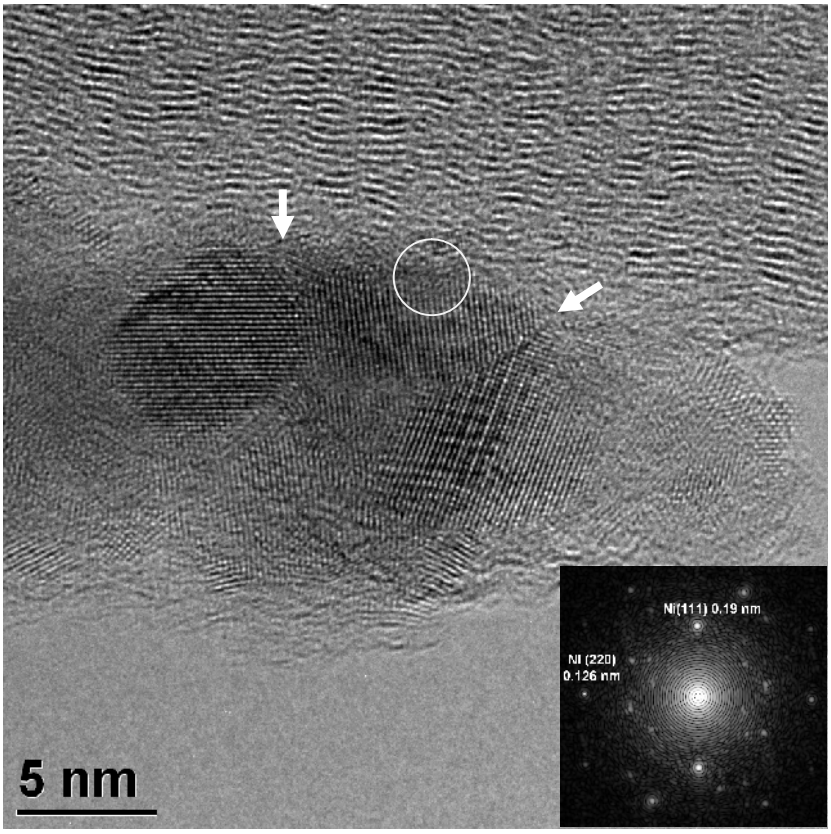

(d)

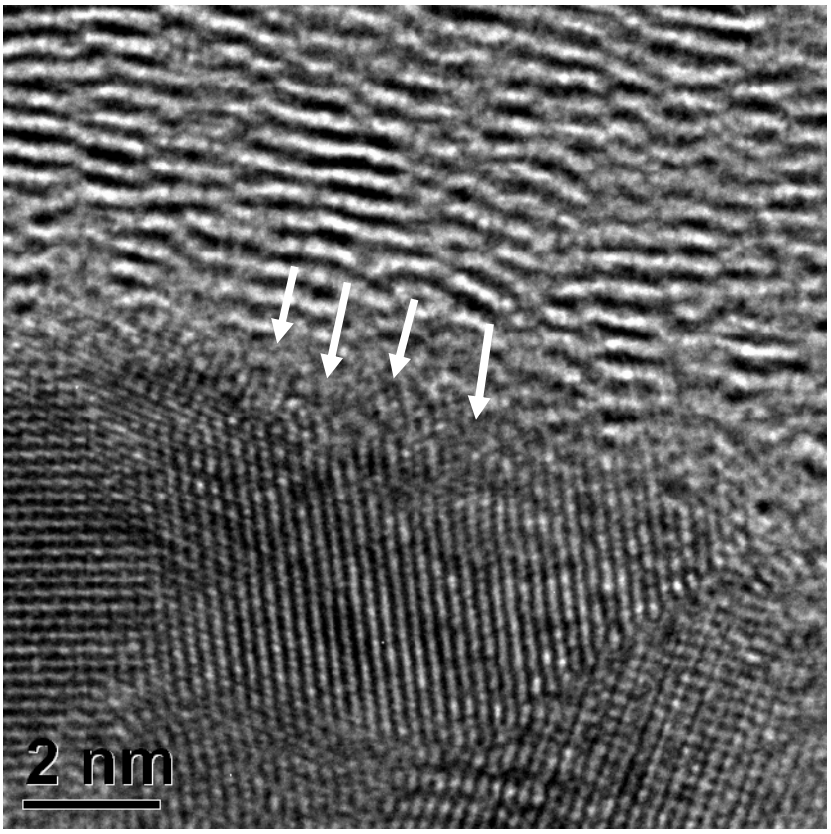

(e)

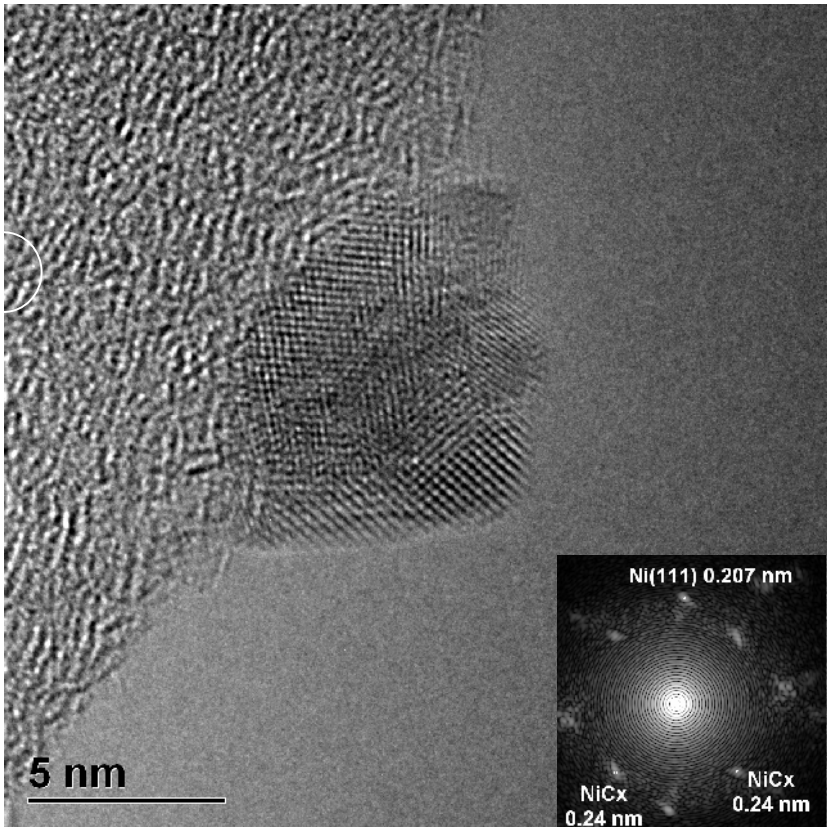

(f)

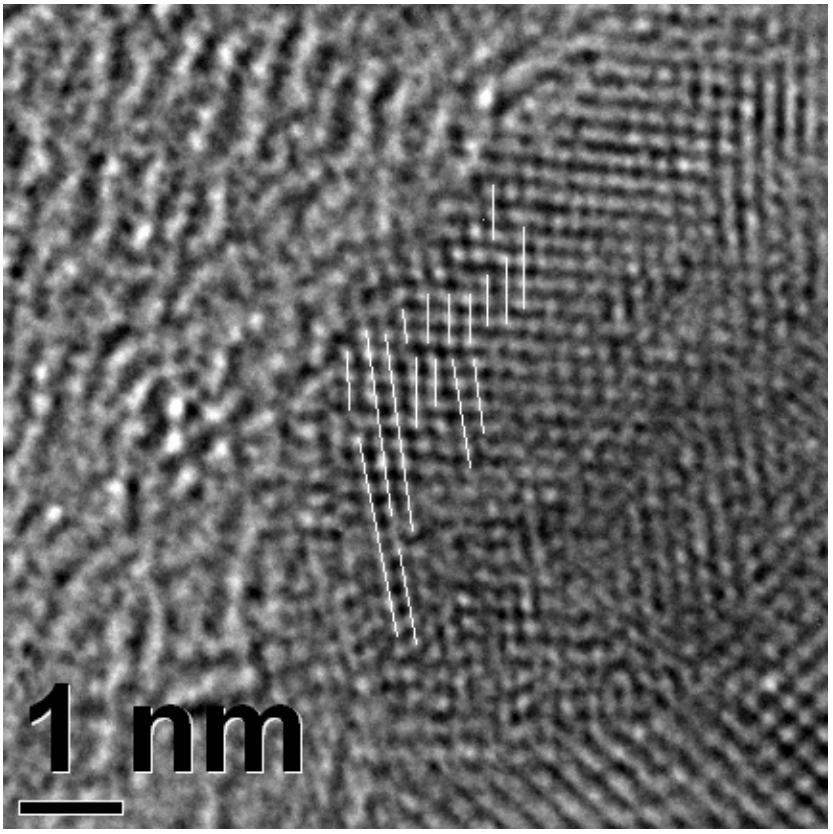

(g)

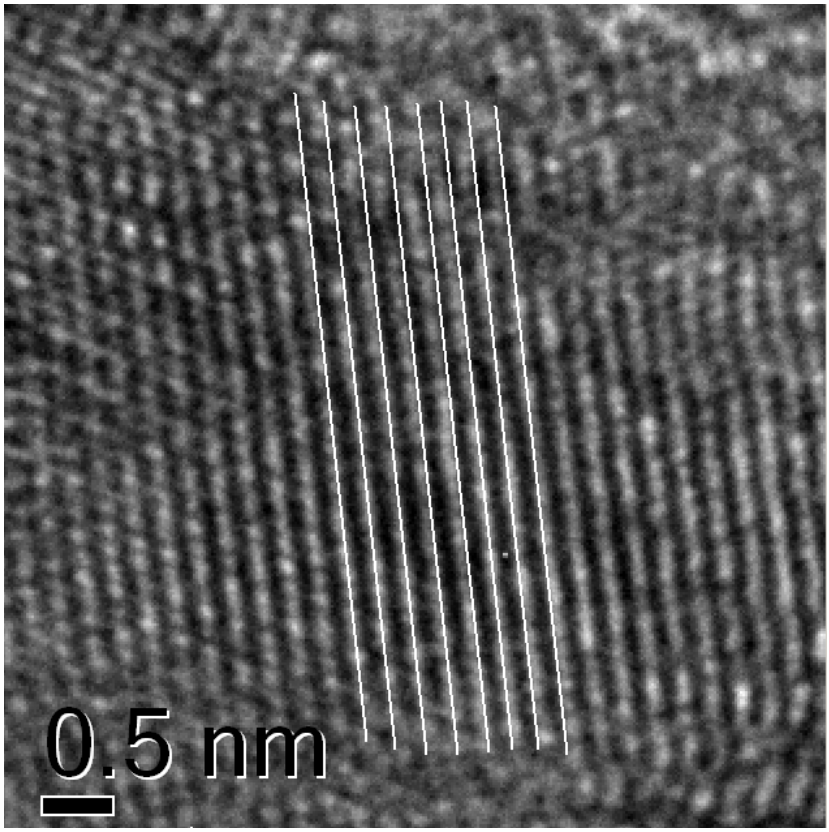

Figure 5-5. HRTEM images of Ni nanoparticles supported on defective carbon after reduction at 300^{o}C, ramping 5 K/min in helium to 700^{o}C and cooled down in helium. The Ni nanoparticles show fcc structure with lattice spacings deviated from the ideal Ni fcc. The interfacial region between Ni nanoparticle and carbon is rich in dislocations, lattice defect, and lattice strain.

Another plausible scenario about the origin of the support effect is the contamination of Ni particles with carbon from the support during nucleation and/or prior to the growth period. As has been suggested in the previous chapter, catalytic gasification occurred by first introducing carbon into the surface and/or bulk of metal catalyst particles. Similarly, under heating in inert atmosphere catalytic graphitization requires the catalyst first to break the C-C bond and later dissolution and diffusion of the carbons via surface and/or bulk of the particle. Catalytic synthesis of CNTs or CNFs is considered to follow similar mechanism where carbon containing gasses are first decomposed on the metal nanoparticle surface followed by diffusion of carbon atoms and finally deposites into graphitic filaments at the other side of the nanoparticle. The diffusion of carbon atoms in the catalyst particles is said to involve bulk and

surface pathways. Evidences presented from state of the art in situ TEM works suggested the latter.

The issue of carbon diffusion, its pathways and energy as the origin or consequence of the catalyst structure are thus of crucial importance to the growth process. It may not be surprising if carbon contamination prior to the exposure of carbon containing gasses can have significant consequences on the growth process.

It is well established from fundamental surface science studies and catalysis that metal particles undergo reconstruction as a result of adsorption and subsurface absorption.[14] For example it has been investigated that Ni film show different carbide advancement under the exposure of ethylene and carbon monoxide.[15] And it is well reported in the vast literature of CNT synthesis that different carbon source resulted in CNT with different microstructures.[16] An interesting analogy can then be deduced to suggest additional carbon dissolved from the support able to change the equilibrium structure of the catalyst prior to the exposure of gaseous carbon source.

The idea that solid carbons can affect CNT growth due to carbon contamination is not far-fetched. Solid carbons have been demonstrated to act as carbon source for a given catalyst system to grow CNTs. Kanzow et al reported the formation of graphitic filaments by heating fullerene blacks covered with thin Ni films at 1000^{o}C.[17] Studies of single wall CNTs production using laser ablation method suggested the solid-state mechanism model where the growth occurs in the latter stage when the carbons are in the condensed phase. Gorbunov et al and Kataura et al demonstrated the production of SWNT after heating soot obtained from laser ablation of Ni-Co graphite target in inert atmosphere at temperatures <1000^{o}C.[18,19,20] Their reports clearly demonstrate the conversion of disordered carbons into nanotubes promoted by metal particles. Due to the high temperature applied for the experiments above it is believed that the metal nanoparticles are in the molten state. An interesting work by Ichihashi et al of amorphous carbon nanofilament conversion into graphitic CNT by Fe catalyst suggests the solid-quasi liquid-solid mechanism of CNT synthesis.[21] They demonstrated the conversion process by annealing experiment inside a TEM instrument. The resolution however was not

high enough to notice the Fe atoms arrangements during the nanoparticle movement in the amorphous filament.

Dissolution of carbon atoms into metal nanoparticles as interstitial compound will result in the perturbation and even rearrangement of the metal crystal lattice spacing.[22,23,24] One can expect that this would have consequences in the catalyst surface adsorption affinity and thus decomposition rate of the carbon containing gas into atomic carbons.

Indeed such arguments require strong supporting evidences. Bulk and surface sensitive characterization methods have been performed to acquire evidences of the following:

1. Whether carbon dissolve into the catalyst
2. When do the carbon atoms start to dissolve
3. Do the carbon atoms dissolve on the surface and/or the bulk?
4. Does the crystal microstructure change with carbon dissolution
5. Do the electronic properties change with carbon dissolution?
6. Does the carbon dissolution change the Ni nanoparticle's shape or faceting?
7. Whether the dissolved carbons participate in the Ni-carbon dynamics during filament growth?

HRTEM, XRD, and XPS characterization methods used in this study will try to address the questions forwarded.

Microstructural investigation with HRTEM and XRD techniques were carried out for Ni/defective and Ni/graphitic systems. For HRTEM, the measurements were performed after the catalyst was reduced at 300^{o}C in diluted hydrogen and ramp to 700^{o}C in helium. HRTEM images and free Fourier transform analysis of Ni/defective system are presented in Fig. 5-5. The micrographs show that the Ni nanoparticles are highly faceted with multiple steps and edges (Fig 5-5a & b). Most of the Ni nanoparticles exhibit polycrystalline structure with crystal

domains of random orientations. Fig 5-5c demonstrates the typical grain boundaries in the Ni nanoparticles when supported on defective carbon. Lattice fringes measurements revealed that the Ni nanoparticles are of metallic fcc structure. Other set of lattice spacings attributed to other Ni phases such as NiO or Ni_3C were not observed and thus their presence can be excluded in the sample. Most of the nanoparticles show lattice spacings of 0.202 nm and 0.176 nm consistent with fcc Ni (111) and Ni (200) spacings respectively with the latter showing lower frequency of occurrence. From total of 462 lattice fringes measurements, 23% deviate from the ideal value of fcc Ni (111) (0.203 nm) resulting in 10 to 40% of expansion (Fig 5-7a). Half of the lattice spacing expansion measurements are spread in the bulk of the nanoparticles and the other half are localized within the metal-carbon interfacial region. The carbon dissolution is very likely to start at the metal-carbon interfacial region. As a consequence, the carbon-rich interfacial regions of Ni nanoparticle exhibit more structural defects. Previous investigations report the occurrence of lattice dislocations and strains upon carbon incorporation in Ni metal.[25,23] Fig 5-5d-f shows the dislocations and strains commonly present in the interfacial region between Ni particles and defective carbon support. Typical examples of faults and lattice defects commonly present in the interface region are shown in Fig 5-5g. There is no preferred Ni lattice orientation relative to defective basal plane in the interface observed. The Ni lattice fringes have random orientation relative to the carbon support. The TEM investigation shows no graphitic tracks in the vicinity of the Ni nanoparticle that would suggest catalytic graphitization during reduction and/or ramping to 700^{o}C. The Ni nanoparticles show no encapsulation albeit the cooling down step to ambient temperature from 700^{o}C prior to TEM investigation. This suggests that the Ni-C compound is relatively stable and that the dissolved carbon is not ejected from the nanoparticle. The Ni-C compound observed in this system does not exist as a stoichiometric compound. The Ni-C compound can therefore be described as a solid solution. Later in the text the solid solution will be referred as NiC_x , and the Ni in this phase will be referred as “carbidic Ni”.

Ni nanoparticles supported on graphitic carbon have smoother features than the Ni/defective carbon. The nanoparticles are more crystalline forming large quasi defect-free domains (Fig 5-6a-d). Some of the Ni nanoparticles even exhibit single crystal orientation as

presented in Fig 5-6d. The lattice fringes measurements show that the Ni nanoparticles are of metallic fcc structure exhibiting Ni (111), Ni (200) and Ni (220) lattice planes with ideal distances of 0.202, 0.176 and 0.12 nm respectively. Similar to Ni/defective carbon, other set of lattice spacings attributed to NiO or Ni_3C was not observed and thus their presence can be excluded in the Ni/graphitic carbon sample. For the most frequently observed lattice planes Ni (111), only 5% of the measurements significantly deviate from the ideal value. The metal-carbon interface region in this case exhibits crystalline lattice arrangements of Ni atoms (Fig 5-6e). The Ni nanoparticles in the Ni/graphitic carbon system are also free from carbon encapsulation and no sign of graphitization of the support by Ni nanoparticles. And there is no preferred orientation of Ni lattice planes relative to the (002) planes of the graphitic carbon support.

The lattice expansion of Ni atoms in the nanoparticle is a strong indication of carbon incorporation within the fcc crystal lattice of Ni. Fig. 5-7 presented the distribution of lattice spacing of Ni (111) for Ni/defective and Ni/graphitic catalyst system. Bimodal distribution of the Ni (111) lattice spacing is observed for Ni/defective carbon. Whereas a single log normal distribution is observed for Ni/graphitic carbon system. This observation strongly suggests that Ni nanoparticles dissolved more carbons from the defective carbon support than the graphitic carbon. Thus Ni/defective carbon contains more NiC_x fraction than Ni/graphitic carbon.

Earlier works in carbon supported metal catalysts have highlighted the difference in shapes adopted by transition metal catalyst when supported on different carbon supports. In the study of metal-catalyzed gasification of graphite, Baker suggested that the channeling and edge recession modes of gasification are the result of different metal-carbon interaction.[26,27] The former is the result of catalyst wetting the graphite edges/steps while the latter is the result of catalyst with stronger metal-carbon interaction spreading along the graphite edges. Interestingly in an earlier publication Baker also reported that Ru particles dispersed on the graphite edges are incapable to grow carbon nanofilament, in contrast to highly active Ru nanoparticle on the basal plane.[28] In this current study however no conclusive observation can be offered from TEM investigation on the shape difference between Ni supported on defective

and graphitic carbon. The inconsistency with extensive works of previous authors may originate from the different conditions of observation. The extensive works of Baker were performed on environmental TEM under reaction temperature and with the presence of reactive gases.[27] Later work by Hansen et al with the use of better resolution environmental TEM has shown the sensitivity of the catalyst shape and structure under the exposure of different gas environments.[29,30]

To put this argument into perspective a simple and brief experiment was conducted in the LaB6 Philips TEM instrument equipped with a heating stage. Ni/graphitic carbon catalyst was heated from 25^{o}C to 290^{o}C under high vacuum. Between 25^{o}C to 143^{o}C the catalyst particle shows almost no changes. Increasing the temperature further resulted in changes of the catalyst shape (Fig 5-8). During heating the catalyst first adopted a more faceted shape and later at 290^{o}C a more spherical shape. The last image acquired at 290^{o}C however can be considered of having a much poorer contrast thus making the interpretation ambiguous. Nevertheless one would expect that at 700^{o}C the catalyst would be more mobile. In accordance with the work of Baker that observed graphite supported Ni particle to become mobile at 640^{o}C under hydrogen or acetylene.[27]

(a)

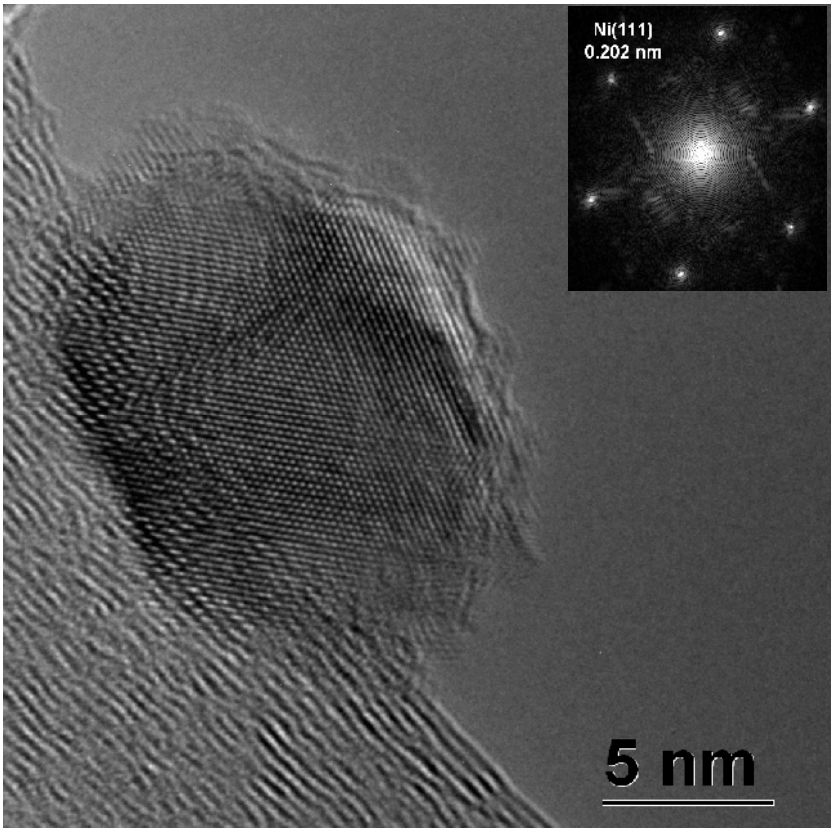

(b)

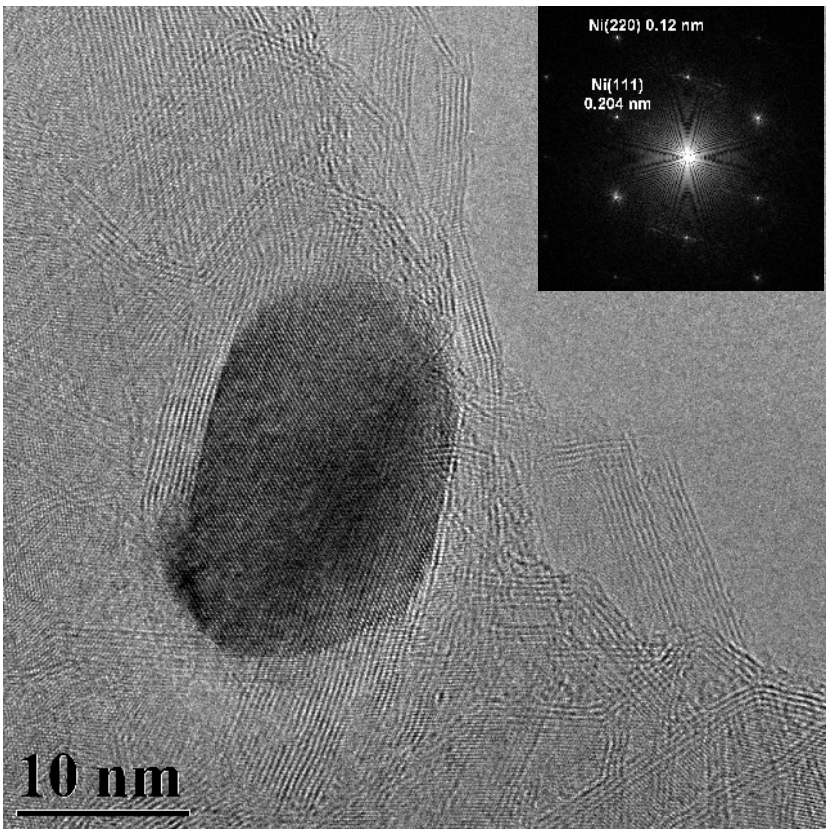

(c)

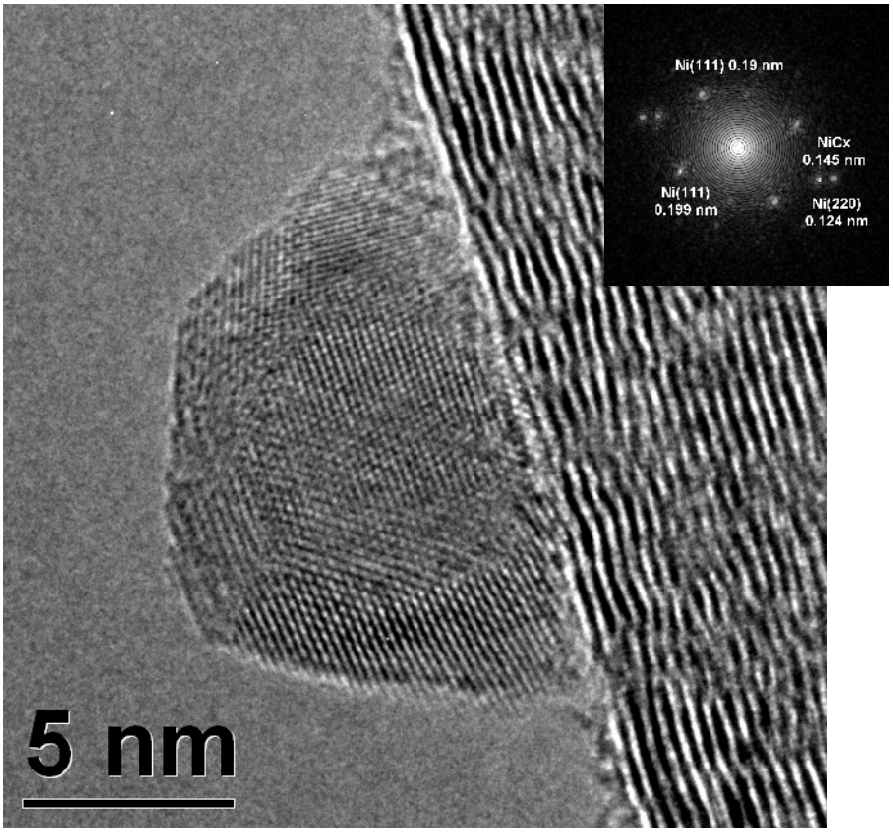
Ni(111) 0.19 nm
NiCx
0.145 nm
Ni(111)
0.199 nm
Ni(220)
0.124 nm
5 nm

(d)

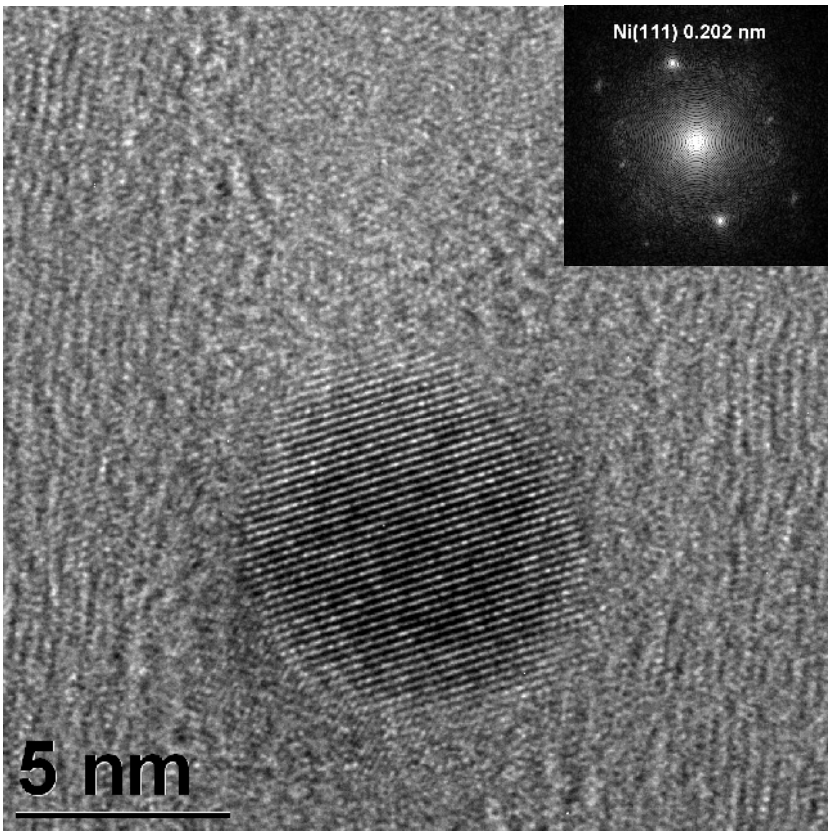
Ni(111) 0.202 nm
5 nm

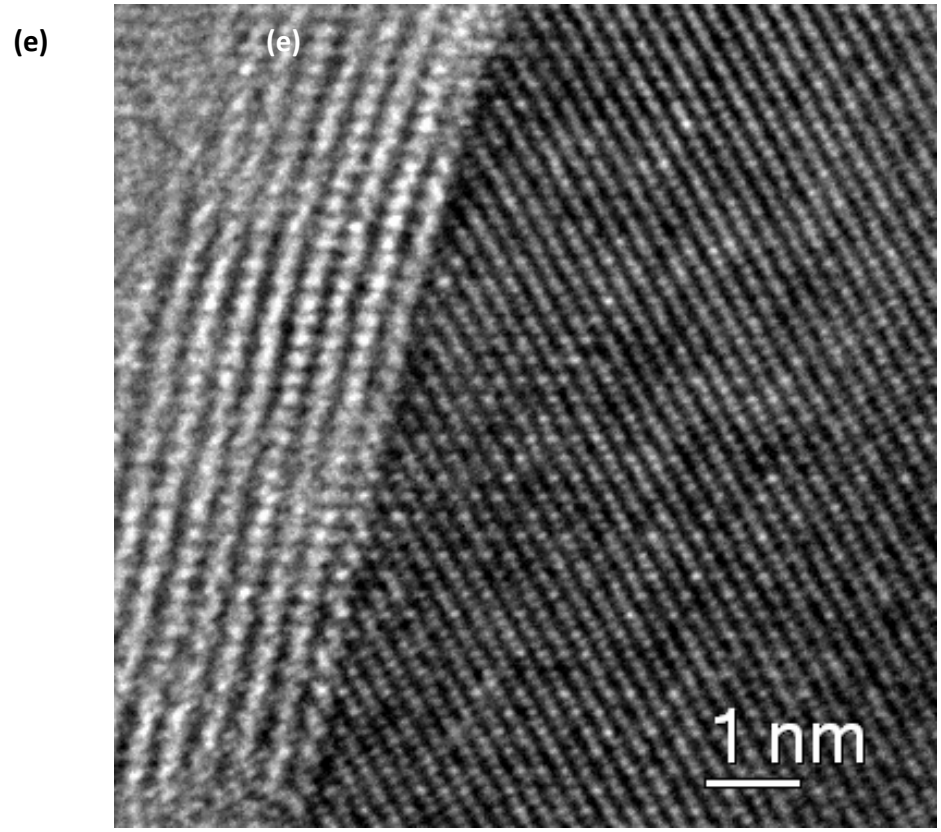

Figure 5-6. HRTEM images of Ni nanoparticles supported on graphitic carbon after reduction at 300°C, ramping in helium to 700°C and cooled down in helium. The Ni nanoparticles are of metallic fcc structure with minimum dislocations and strains.

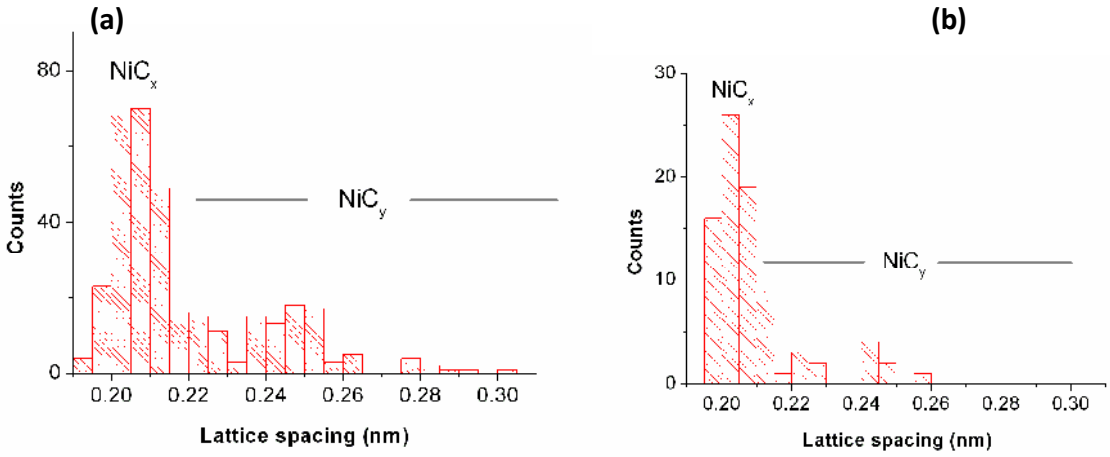

Figure 5-7. Statistic distribution of fcc Ni (111) lattice spacing for Ni/defective (a) and Ni/graphitic carbon (b). $0 \leq x < y$.

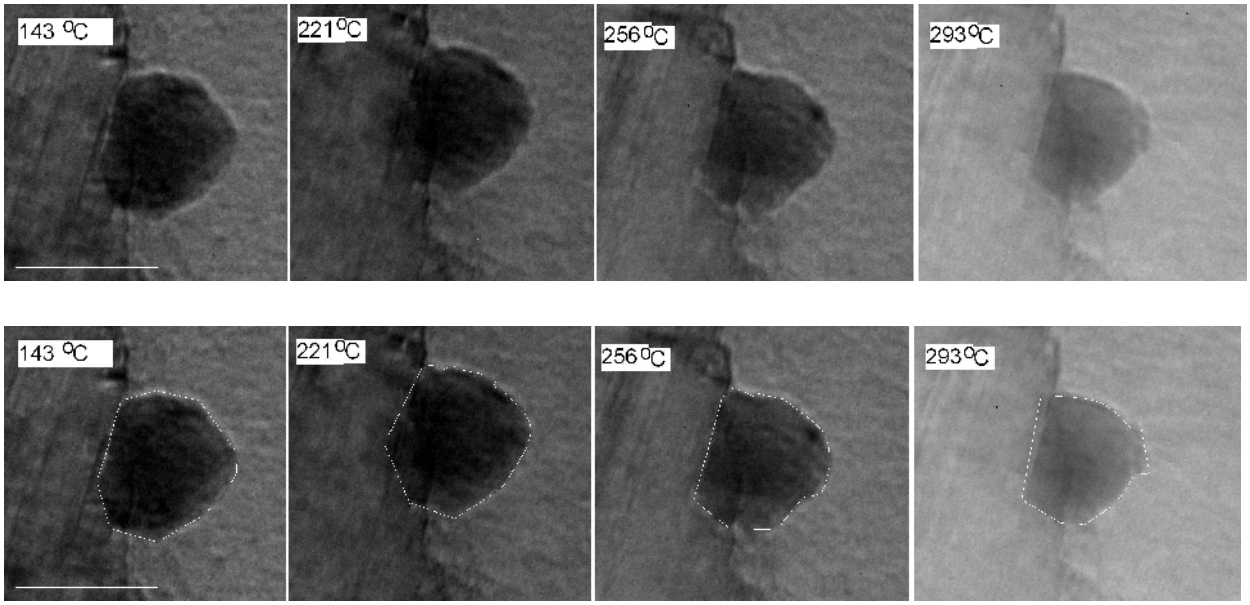

Figure 5-8. TEM images of reduced Ni nanoparticle shape evolution with increasing temperature in vacuum. Lower part is of similar image with guided lines for clarity (Scale bar 20 nm).

For bulk characterization, X-ray diffraction patterns were collected for both systems subsequently after reduction, ramping to 700°C and nanofilament growth (Fig. 5-9 and 5-10). The diffraction peaks from the carbon supports were used as an "internal standard" to monitor diffraction peaks position and intensity change after the respective steps. As expected the background and diffraction peaks for the Carbon supports remain constant throughout the entire steps. Thus it is proven that the carbon supports remain unchanged and undisturbed. Thus other factors that cause displacement errors in the measurement such as sample height and packing density that would bring about to the overall shift of the diffraction pattern can be excluded. Indeed throughout the experiments for every step for both of the samples the position of the carbon support reflections remain fixed in their position and intensity. The XRD patterns agree with the observation from HRTEM in the presence of fcc metallic Ni for the reduced sample. The XRD patterns show diffraction peaks at ~44.5°, ~51.8 ° and 76.37° assigned for diffraction lines of fcc Ni (111), (200) and (220) respectively. In agreement with HRTEM investigation no Ni_3C, hexagonal metallic Ni and NiO reflections was observed in the diffraction pattern of the reduced samples. The Ni diffraction peaks in Ni/graphitic sample show slightly

sharper and more intense peaks as compared to Ni/defective carbon, which is consistent with HRTEM observation. The line broadening in the XRD pattern is known to arise from various reasons such as crystallite size effect, occurrence of strain and lattice defects. HRTEM investigation in Fig 5-5 and Fig 5-6 clearly suggest that the broadening is not only caused by smaller crystallite size, but also due to the presence of more strains, defects and dislocations in the Ni particles supported on defective carbons.

The reduced Ni/defective carbon sample shows Ni reflections with asymmetric peak shape exhibiting a shoulder at lower 2θ (Fig 5-9a). This is especially obvious for the (111) line at ~44.5^{o} and (200) at ~51.8^{o}. The (220) reflection for Ni/defective carbon however is too broad and the intensity is too low to notice any substantial differences after each consecutive step. When the reduced sample was ramped to 700^{o}C, the position of Ni (111) reflection slightly shifted to lower 2θ and the Ni reflections become sharper and more intense (Fig 5-9a). The Ni reflections are still asymmetric with a shoulder at lower 2θ. The peaks evolution after ramping to 700^{o}C suggests that Ni crystals become more ordered and/or sintered into larger domains and that at the same time the Ni lattice slightly expanded. After ethylene/hydrogen exposure at 700^{o}C the peaks for Ni (111) and Ni (200) reflections further shifted to lower 2θ and the shoulders became better resolved. The shoulders shifted to 43.7^{o} and 50.7^{o} after the growth (Fig 5-9b & c). There is no known phase to match with these peaks. The fact that Ni (111) and Ni (200) reflections shifted in a similar manner suggest that the shoulder is very likely caused by carbon dissolving into the Ni fcc lattice resulting in its expansion as already observed in earlier metallurgy studies for carbon dissolution in bulk Ni metal. [22]

The Ni-C compound here cannot be assigned to a typical Ni_3C crystalline structure, as this carbide is known to decompose into Ni metal and graphitic carbon at temperature exceeding 300^{o}C.[31-33] HRTEM and in situ XRD observations are in good agreement to support the interpretation that carbon from defective carbon diffused and dissolved into the *bulk* of Ni metallic lattice as interstitial compound (NiC_x). The observations suggest that the carbon dissolution start during the reduction step at 300^{o}C in hydrogen and continue further during ramping to 700^{o}C in inert atmosphere.

Against that, the Ni/graphitic carbon shows constant Ni reflections after each consecutive step (Fig 5-10). The peaks however are slightly sharper after CNT growth. The Ni reflections fixed at their position and remain symmetric from the reduction step to CNT growth. This however does not mean that the Ni nanoparticles supported on graphitic carbon do not contain any dissolved carbon at all. Minute amount of interstitial carbon and/or in the form of surface carbidic Ni that are invisible to XRD are still possible to be present in the Ni/graphitic carbon system prior to CNT growth step.

The evolution of crystallite size and lattice parameter of the Ni compounds after each treatment is shown in Table 5-2. The values are acquired from simultaneous fitting of three difference patterns. The difference diffraction patterns are each acquired from subtracting diffraction patterns of *reduced-calcined*, after *growth-calcined* and *after growth-reduced* (Fig 5-11). This approach cancels out the contribution of the background and the carbon supports. This approach works under several assumptions of the following: (i) the background and support is not influenced or changed throughout the set of experiments, and (ii) fcc *NiO* present in calcined sample, fcc *Ni* present in reduced sample and fcc NiC_x, NiC_y present in the after growth sample. The simultaneous fittings of NiO, Ni and NiC_x, NiC_y are then applied to the difference patterns with a combination of positive and negative fit as displayed in Fig 5-11. The fitting parameters performed on all the difference patterns are similar. The fits are in a good agreement with the difference pattern (Fig 5-11). The lattice parameter of Ni, NiC_x and NiC_y are then extracted from the fit as displayed in Table 5-2. The lattice parameters are not to be compared between the two samples as they have different sample packing density and height that can cause dislocation errors. The lattice parameters however are valid to be compared in one set of the in situ experiments (in the same row of Table 5-2). Especially for the Ni/defective carbon system, the Ni lattice parameter "*a*" increases after growth into NiC_x and NiC_y.

Zwell et al. have proposed the formula explaining the relationship between the amounts of carbon dissolved in fcc Ni with dilation of the lattice parameter (Equation 5-1). With "a" is the observed lattice parameter, 3.5238 Å is the lattice parameter with almost no carbon detected and "x" is the calculated atomic percentage of dissolved carbon. The absolute value of

Ni lattice parameter varies in the literature, probably due to varying impurities; including carbon impurities prepared from different routes. Thus in the diffraction patterns and fits acquired in this investigation, it is uncertain whether the lattice parameter of fcc Ni after reduction for both samples are pure Ni (free from dissolved carbon) or already contain some amount of dissolved carbon. (Later in the investigation with XPS it is revealed that already reduced-Ni/defective contains more dissolved carbon than reduced-Ni/graphitic carbon). Nevertheless only the shift of the fcc Ni peak that represent the different amount of dissolved carbon between reduced step and after nanofilament growth can be approximated with the formula by Zwell et al. For Ni/defective carbon, after CNF growth there are 2at % and 9at% more carbon dissolved in to the fcc lattice forming NiC_x and NiC_y respectively. As the fit acquired for after CNT growth sample for Ni/graphitic system are poor, no meaningful lattice parameter can be obtained. However one can notice that the Ni (100) peak after CNT growth remain constant without any significant shift, suggesting no carbon or minimum amount of carbon dissolved after CNT growth as compared to the reduced sample.

$$a\ (Å) = 3.5238 + 0.0074x \qquad \text{Equation 5-1}$$

The carbon percentages in the samples are an approximation, especially as the validity of the formula was only proven for carbon concentration up to 1.5 at%. The values for higher carbon concentration may be debatable.

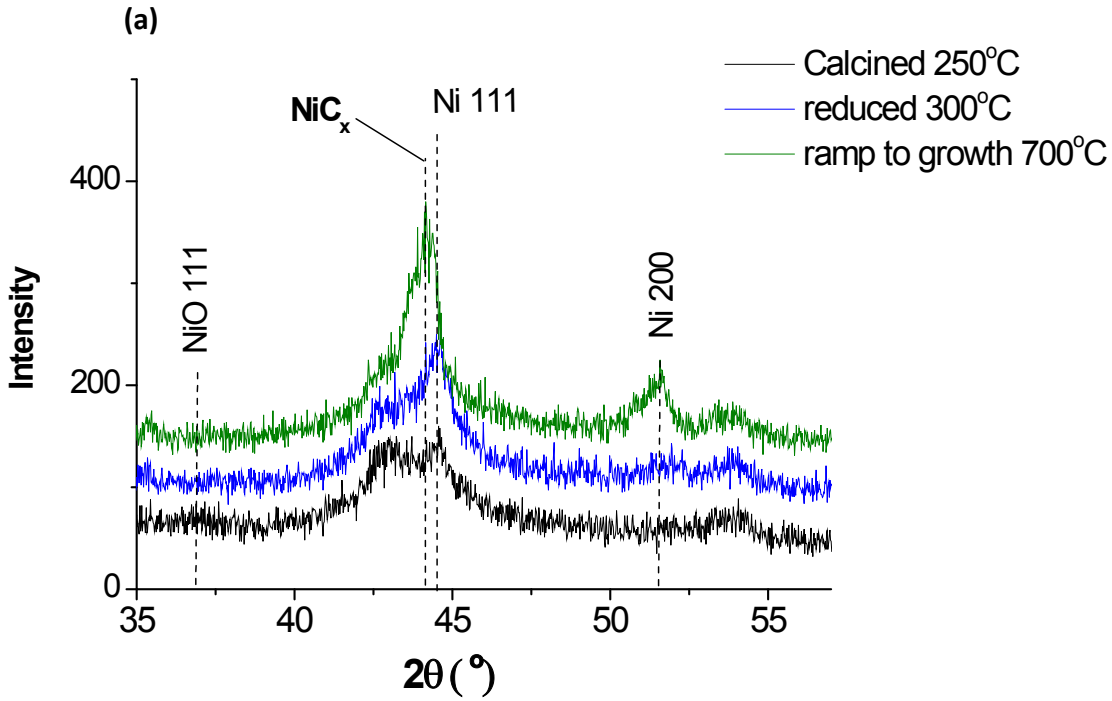
(a)
Calcined 250°C
reduced 300°C
ramp to growth 700°C
NiC$_x$
Ni 111
NiO 111
Ni 200
Intensity
400
200
0
35
40
45
50
55
2θ (°)

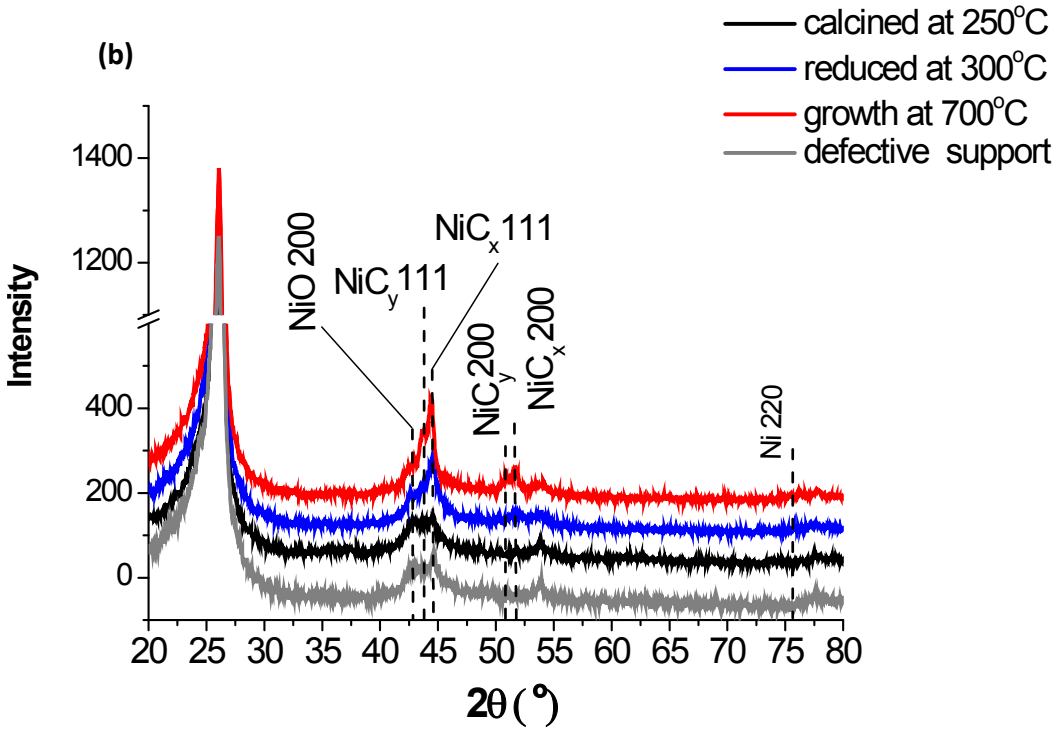
(b)
calcined at 250°C
reduced at 300°C
growth at 700°C
defective support
NiO 200
NiC$_y$ 111
NiC$_x$ 111
NiC$_y$ 200
NiC$_x$ 200
Ni 220
Intensity
1400
1200
400
200
0
20
25
30
35
40
45
50
55
60
65
70
75
80
2θ (°)

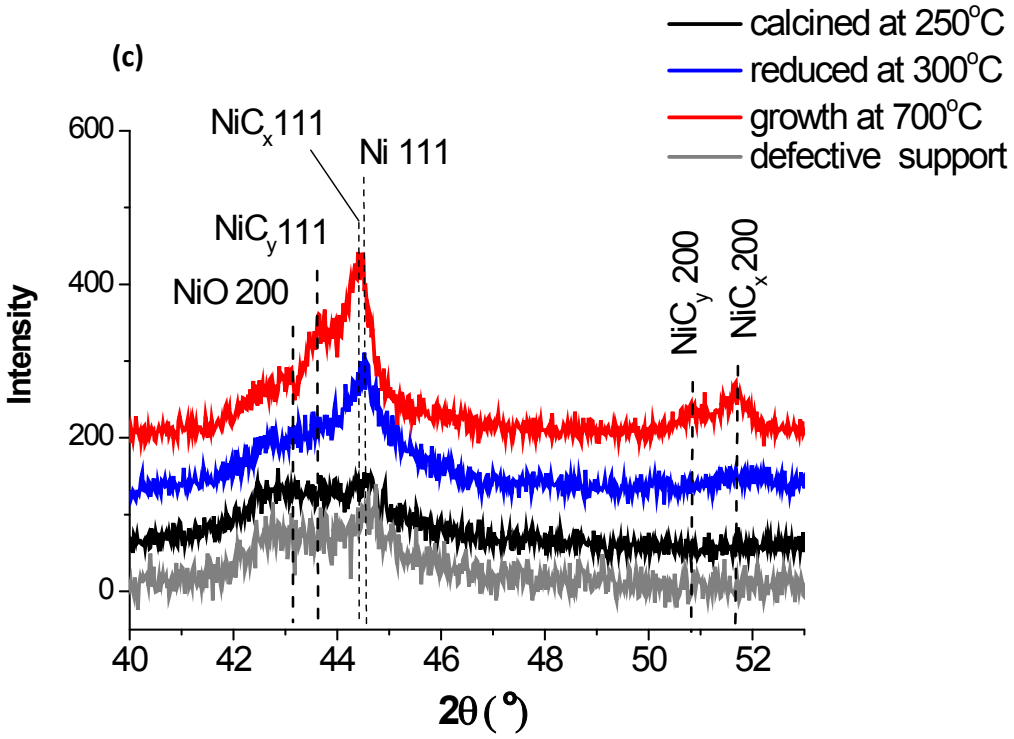

Figure 5-9. *In situ* XRD patterns of Ni/defective carbon for one set of experiments showing pattern for calcined, after reduction and after ramping to growth temperature (a). *In situ* XRD patterns of defective carbon support and Ni/defective carbon for another set of experiments showing calcined, after reduction an after CNF growth (b) and zoom in of XRD patterns highlighting Ni (111) and Ni (200) reflections (c).

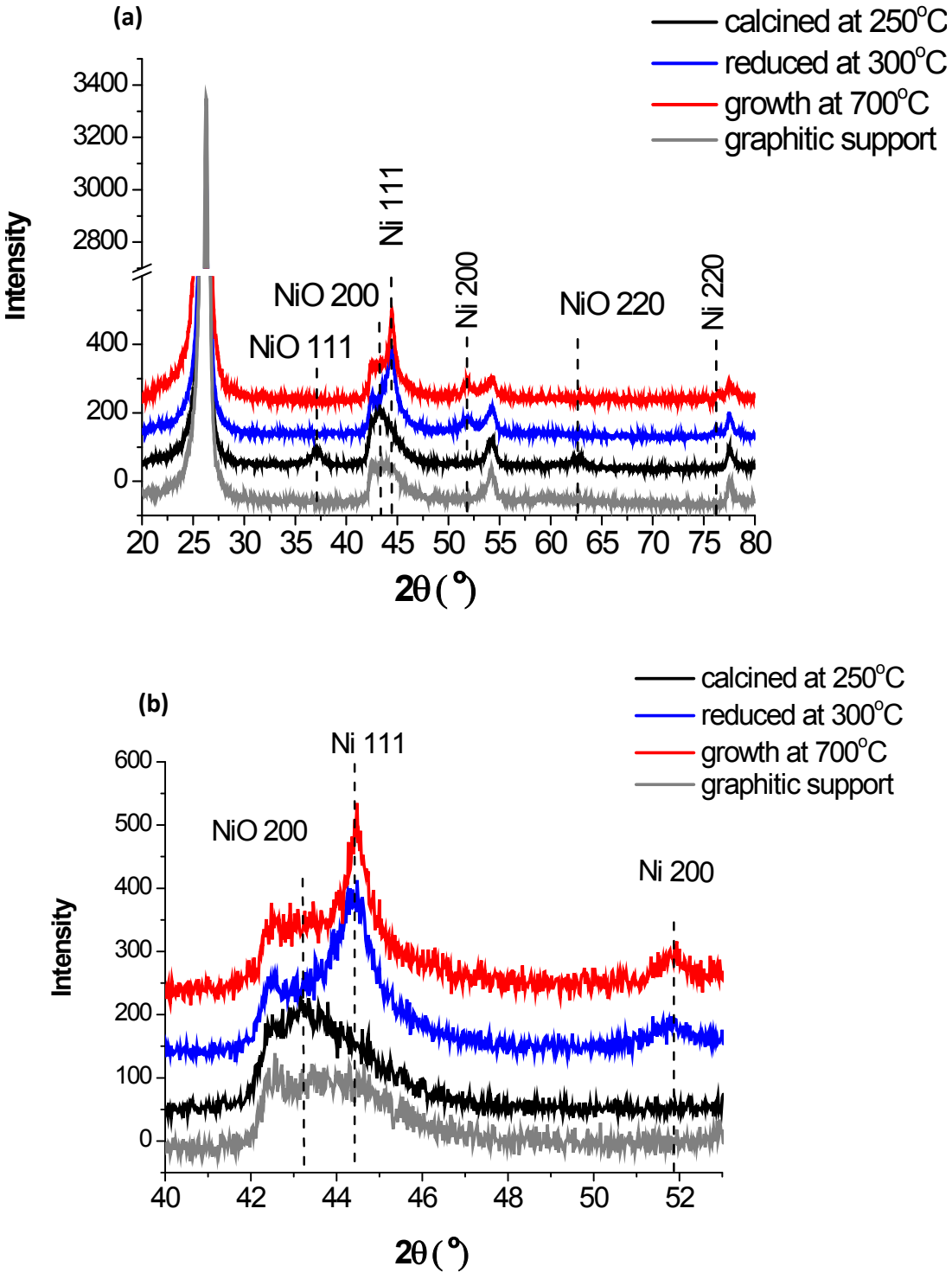

Figure 5-10. *In situ* XRD patterns of Ni/graphitic carbon set for one set of experiments showing calcined, after reduction an after CNT growth (a) and zoom in of XRD patterns highlighting Ni (111) and Ni (200) reflections (b).

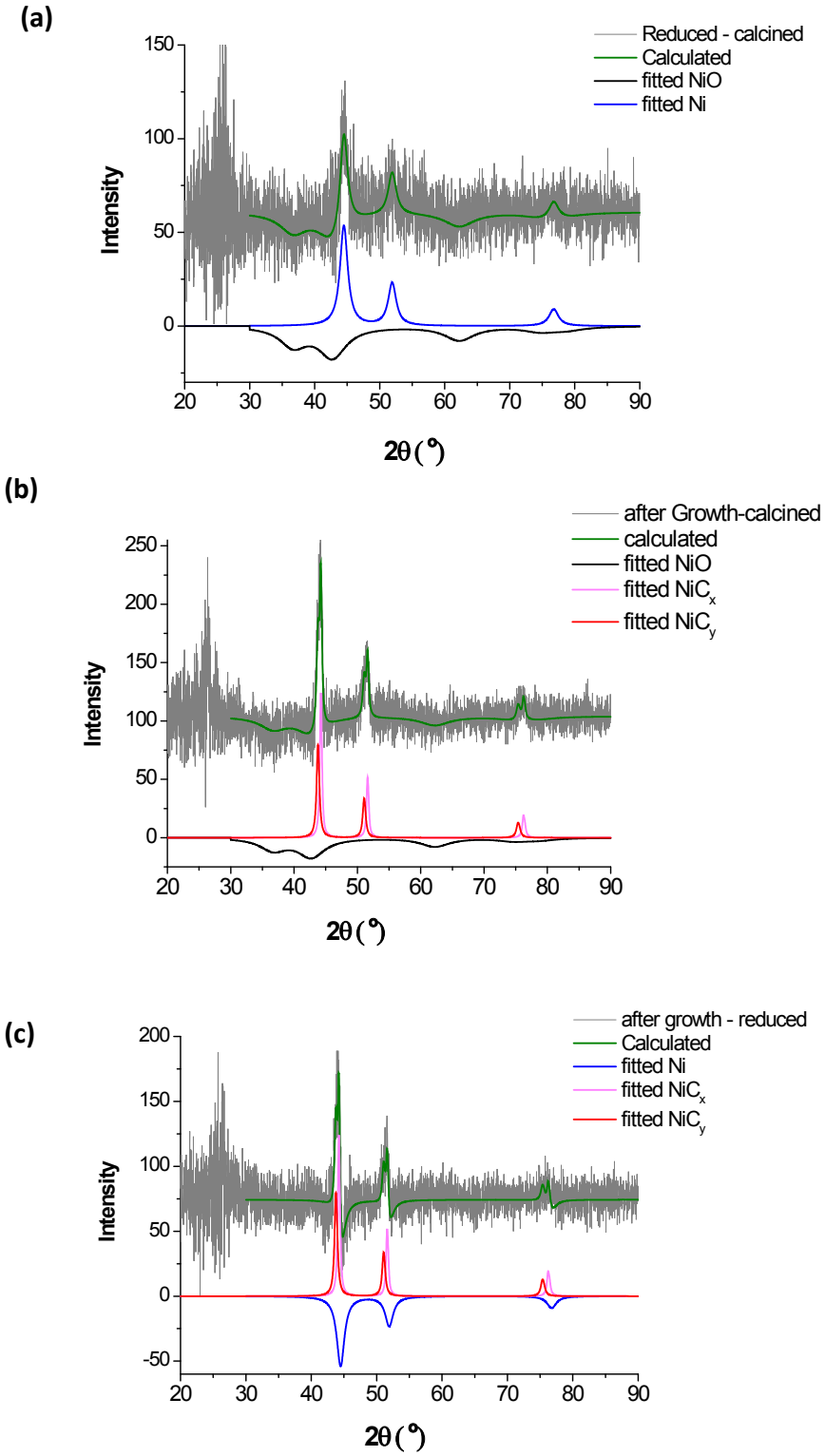

Figure 5-11. Simultaneous fitting of difference diffraction patterns from Ni/defective carbon obtained from subtraction of reduced – calcined (a), growth-calcined (b) and growth – reduced patterns(c).

Table 5-2. Calculated lattice parameter *a* and crystallite size L_{vol} from XRD pattern of Ni/carbon*

System	Calcined sample**		Reduced sample (nm)		After nanofilament growth	
	a (Å)	L_{vol} (Å)	a (Å)	L_{vol} (Å)	a (Å)	L_{vol} (Å)
Ni/defective	4.266	9	3.516	45	3.533 3.576[+]	150 130[+]
Ni/graphitic	4.199	30	3.531	100	-[++]	-[++]

*volume weighted of averaged crystal domain size

**NiO

[+] NiC_x and NiC_y respectively

[++] No good fit is achieved

In order to gain insight into the carbon incorporation, especially to the surface of Ni catalyst, *in situ* XPS measurements were performed on both systems. The measurements were acquired from the calcined sample, after reduction at 300^{o}C, ramping to 700^{o}C and after nanofilament growth at 700^{o}C. The spectra were collected after each treatment at the corresponding temperature in vacuum. The objective of the measurements was to confirm the presence of surface carbidic Ni and the evolution after each treatment.

The Ni2p XP spectra for Ni/defective carbon and Ni/graphitic carbon are presented in Fig 5-12a and Fig 5-12b respectively. The freshly calcined samples exhibit heavily oxidized Ni on both samples. The line shapes of the main intensity at 855 eV and the satellite region >858 eV suggest a mixture of NiO and hydrated Ni oxide, the latter being more pronounces on the Ni/defective carbon support. This observation is in agreement with the XRD pattern of the freshly calcined samples showing NiO with less crystalline character on defective carbon than

on graphitic carbon (Fig 5-9). This resulted in the fitting of the XP spectra as follows: NiO at 854 and for $Ni(OH)_2$ or NiOOH at 855.3 as well as 856.5 eV. The calcined samples exhibit the oxidic state of the Ni catalyst. The oxide phase is not the active state for ethylene cracking and hence carbon nanofilament growth. Thus it is not the interest of this work to further investigate the oxide state. However it is worth mentioning that the defective carbon support can also be responsible for the poor crystallinity of the NiO phase or the incomplete NiO formation from the nitrate source as compared to graphitic carbon support.

A difference in the evolution of Ni2p signal between the two support starts after reduction in hydrogen at 300^{o}C. The Ni/graphitic carbon exhibit mainly two contribution corresponding to metallic Ni at 852.6 eV and carbidic Ni (NiC_x) at 853.5 eV. Furthermore three minor components located at 854.5, 856.5 and 858.4 eV attributed to residual oxides and a Ni metal satellite feature respectively. For the Ni/defective carbon however, the residual oxide contribution is slightly higher and the NiC_x peak is already quite pronounced after the reduction step. After heating to 700^{o}C the $Ni2p_{3/2}$ changes are more pronounced for the Ni/defective carbon system showing the loss of residual oxide contribution and considerable increment of NiC_x peak. The carbidic Ni becomes the dominant feature of the spectrum after heating to 700^{o}C exceeding the intensity of metallic Ni (Fig 5-10a). After exposure to ethylene at 700^{o}C the intensity of NiC_x advances further suggesting diffusion and dissolution of more carbon from the gaseous carbon source. The $Ni2p_{3/2}$ changes for Ni/graphitic carbon however are barely visible. The spectrum revealed only a slight increase of the NiC_x contribution after heating to 700^{o}C while still showing a dominant metallic Ni feature in the spectrum. After ethylene exposure the spectra remains highly metallic and showing slight increase in the NiC_x contribution (Fig 5-10b).

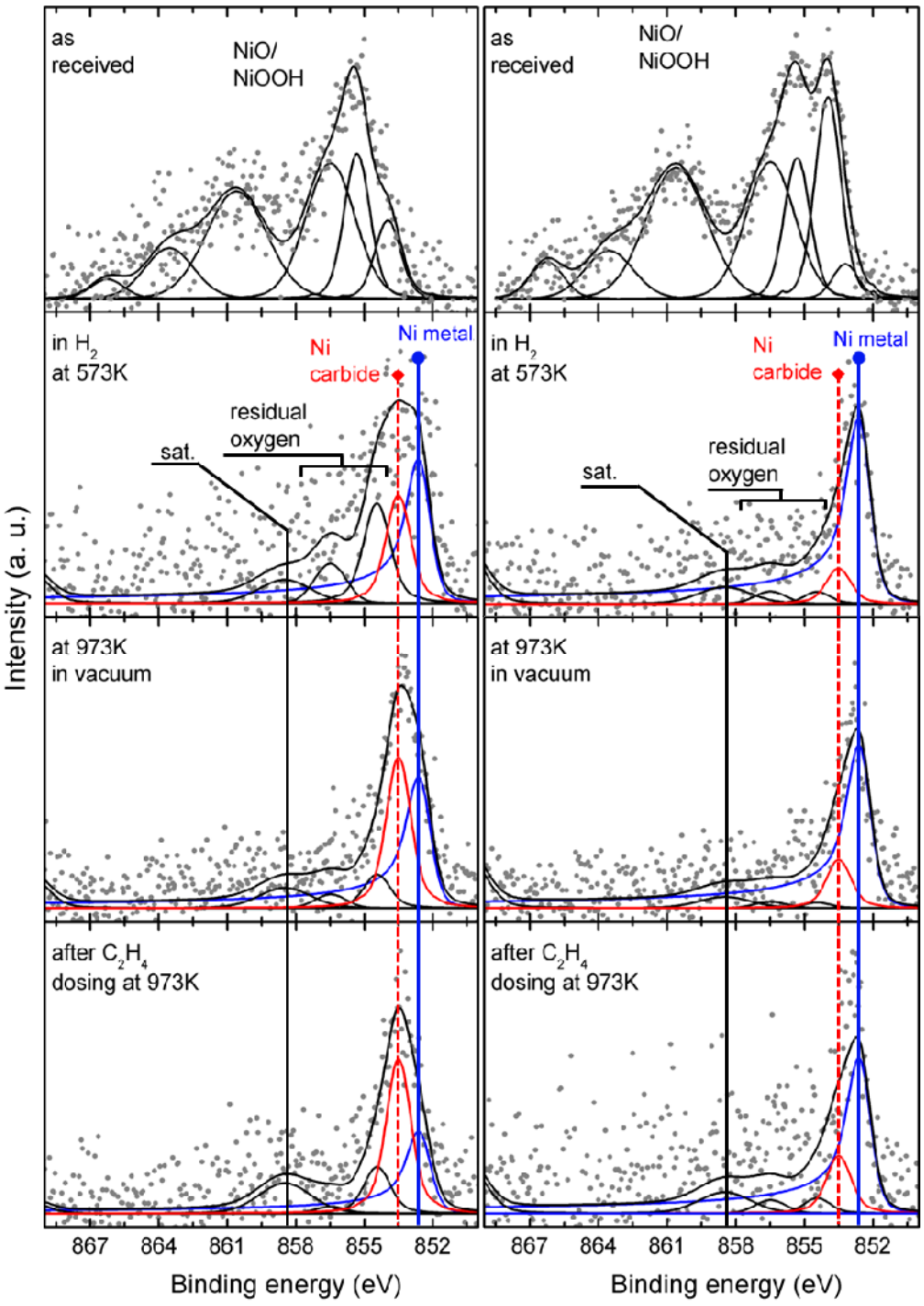

Figure 5-12. Evolution of the Ni2p XP spectra for Ni/defective carbon (a) and for Ni/graphitic carbon (b) before and after reduction, heating to growth temperature in inert gas and exposure to ethylene.

In agreement with XRD and HRTEM observations, *in situ* XPS spectra confirms that prior to the exposure to ethylene at 700^{o}C, the *surface* of Ni catalyst is highly populated with carbidic Ni for Ni/defective carbon while it is metallic for Ni/graphitic carbon system. The *in situ* XPS further reveals the presence of minor amount of carbidic Ni on the *surface* of Ni nanoparticles when supported on graphitic carbon. The gradual carbon dissolution from the support was also observed especially for Ni supported on defective carbon after reduction in hydrogen, and further progressed after heating to growth temperature in inert. In general, a clear distinction was observed between the state of Ni nanoparticles (before the ethylene exposure) that resulted in the growth of defective CNFs and graphitic CNTs. The former is Ni nanoparticle with its *surface* and *bulk* rich in carbidic Ni, while the latter has a *bulk* metallic Ni with small carbidic concentration on its *surface*.

In situ XPS measurements demonstrate that Ni dissolves different amount of carbon atoms from the solid carbon when supported on defective and graphitic support, with the latter accounts for the minimum. The Ni2p$_{3/2}$ XP spectra clearly show that supported Ni nanoparticles has a *different reduction profile* when supported on defective and graphitic carbons. Ni/defective carbon is more difficult to reduce into metallic Ni than Ni/graphitic carbon. At a given reduction time there are three visible phases detected by XPS at the surface of the nanoparticles on the Ni/defective carbon system. They are NiO (or hydroxides), metallic Ni and carbidic Ni. Whereas for Ni/graphitic carbon system, the metallic Ni phase is already the dominant phase. Such changes in the kinetic of NiO reduction can be partly explained by the presence of NiC_x phase. It has been reported that the reduction of bulk NiO follows the nucleation model.[34] The model explains as follows: in the first stage, oxygen in the NiO lattice is first removed by hydrogen thus forming vacancies. After a certain concentration of vacancies the lattice will rearrange into eventual formation of metal nuclei. The NiO and Ni metal interface will begin to increase by growth of the nuclei and by the formation of new ones. Overtime as the oxide is consumed the interface decreases. Especially for Ni metal, known to dissociate and activate hydrogen, the reduction is autocatalytic. The Ni metal nuclei will catalyze the reduction of the remaining oxide. In the case of supported metal oxide the reduction can be hindered due to the metal-support interaction e.g. the formation of metal

aluminates or metal silicates in the case of alumina or silica supported catalysts. For carbon support known to have weak metal-support interaction (at least as it is traditionally defined), it is very likely that the formation of NiC_x is responsible for hindering the reduction process. In accordance with the mechanism proposed by Boudart, Baker and Houlstein et al for the metal-catalyzed gasification and graphitization of carbons, the C-C bond is first dissociated by metal catalyst as a preliminary step prior to the diffusion onto the surface and/or into the bulk of the metal.[35,26,37,38,36] In this case the formation of NiC_x from metal nuclei interaction with the defective carbon support (very likely on the interface) will result in the loss of sites to provide active hydrogen to autocatalyze the reduction. In addition the mobility of active hydrogen in a given particle (with crystal domains) will also be restricted.

An artistic impression is presented in Scheme 5-1 to represent the nucleation model for the reduction of Ni/defective carbon with significant NiC_x phase and Ni/graphitic with minimum NiC_x phase.

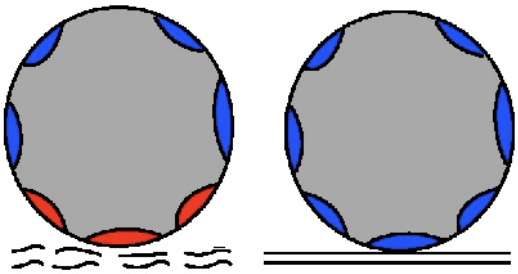

Scheme 5-1. NiO reduction by nucleation mechanism model in the case of Ni/defective carbon (i) and Ni/graphitic carbon (ii). Gray, blue and red refers to NiO, Ni^0 and NiC_x respectively.

There is another possibility that the reduction of Ni oxides is carried out by the carbon support itself, producing CO_x. This mechanism however should help the kinetic of reduction instead of hindering it (at least in the beginning before the formation of substantial NiC_x phase).

Figure 5-13 show the microstructure of carbon deposited after *in situ* XPS experiments from Ni/defective carbon (Fig 5-13 a & b) and Ni/graphitic carbon (Fig 5-13 c-f). Consistent with the result at atmospheric condition (Fig 5- 3 & 5-4) the carbon filaments deposited from Ni/defective carbon have defective platelet-like CNF structure whereas Ni/graphitic carbon led to the growth of CNTs with graphitic tubular structure. The low-pressure condition in the *in situ* XPS cell only affects the kinetic of the nanofilament growth; the microstructure of the deposited carbon however was barely affected. This observation is of significant importance because it highlights the followings: (1) with different chemical potential between atmospheric and low-pressure conditions, the ethylene and hydrogen flux in the gas phase (and thus adsorbing onto the Ni surface) are substantially different. Nevertheless the microstructures of the carbon nanofilaments, as an indication of atomic carbon diffusion pathways in a catalyst, are consistent. This observation suggests that the effect exerted by carbon support changes the thermodynamic of the Ni catalyst to grow carbon nanofilaments. In other words the carbon introduced into the bulk or onto the surface of the Ni nanoparticles prior to ethylene exposure altered the carbon diffusion pathways during nanofilament growth. (2) The initial concentration of carbon (prior to the ethylene exposure) in the Ni catalyst is of crucial importance to determine the final microstructure of grown nanofilaments.

From the data presented above, especially that of *in situ* XRD and *in situ* XPS, one can clearly notice the different carbon diffusion pathways microscopically between the two Ni supported catalysts, after the reduced samples were exposed to ethylene at 700^{o}C. The Ni on defective carbon incorporated more carbon into the bulk whereas Ni on graphitic carbon remains metallic with only slight increase in its surface/subsurface carbon concentration. The origin of this different carbon diffusion pathway remains dubious. The involvement of bulk carbon and surface/subsurface carbon in the carbon nanofilament growth mechanism invoke an essential question to whether the dissolved carbon from the support remains *static* or *dynamic* throughout the nanofilament growth process. One approach to find some explanation from the analogous debate within the Fischer- Tropsch catalysis study on whether the carbide phase of the catalyst is dynamically involved in the reaction mechanism. A study using a pre-carbided Fe catalyst with radioactive ^{14}CO show that only a small fraction of the hydrocarbon

products obtained in the Fischer-Tropsch synthesis using unlabelled CO contained the radioactive label. The study indicates that the carbide phase might be dynamically involved, but the carbon products do not solely originate from the carbide.[39]

For smaller particle the growth rate seems to be slower as some Ni nanoparticles only exhibit several layers of graphitic cap formation pointing out to a nucleation stage (Fig 5-13f). From the smaller particle, one can observed that several layer of graphitic carbon covers the front face while the rear face is free from carbon encapsulation (Fig 5-32f). This observation is consistent with the concept of the concentration gradient as being the driving force for the carbon nanofilament growth. One can also see from the micrograph that the graphene layers terminates on the Ni step edges in accordance with the observation made by Helveg et al from their *in situ* TEM experiments. [40]

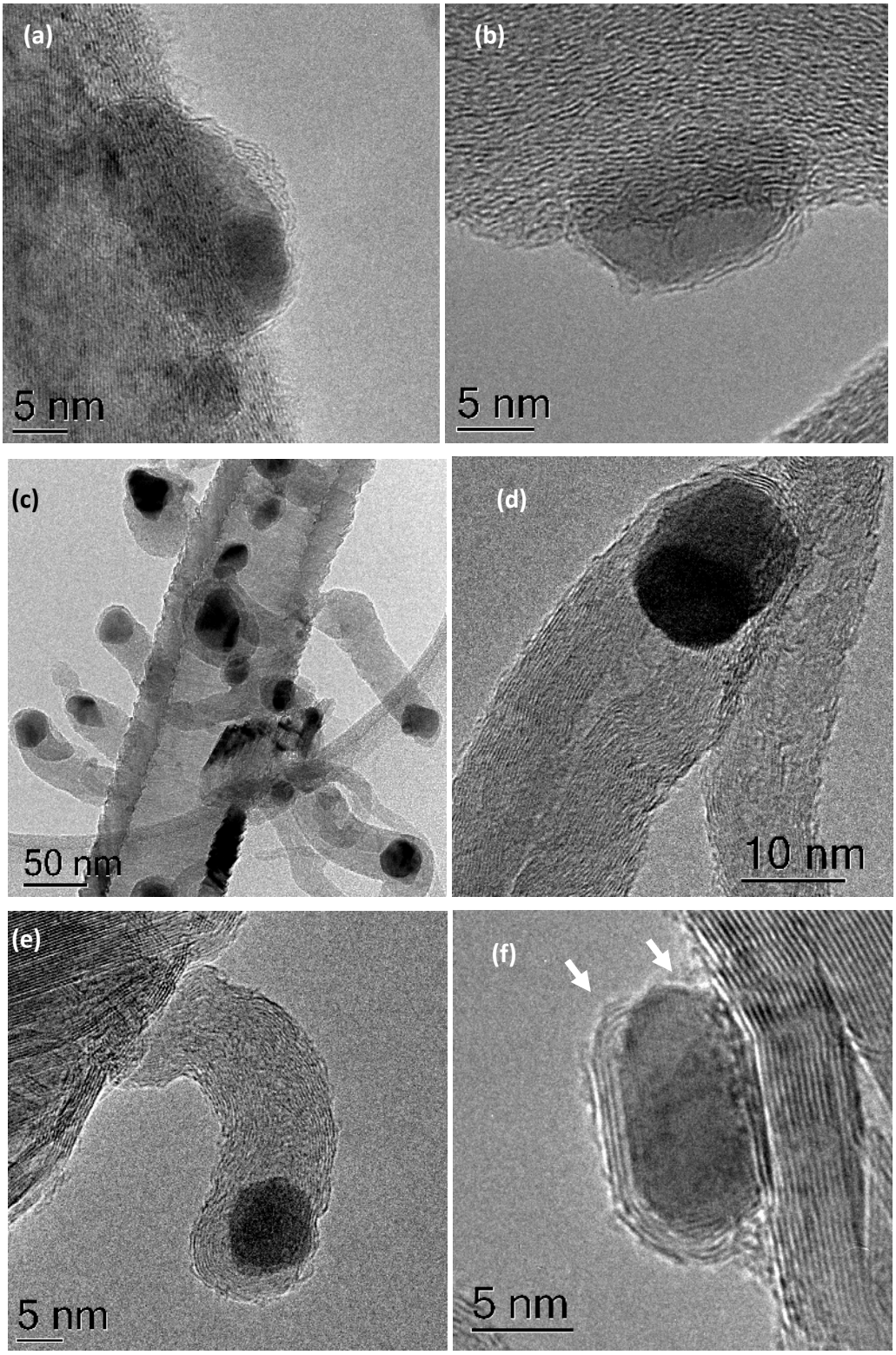

Figure 5-13. Carbon deposited after *in situ* XPS experiments after subsequent steps of reduction – ramp to 700°C – ethylene exposure for Ni/defective carbon (a & b) and for Ni/graphitic carbon (c-f).

There are abundant examples in the catalysis literature on the ambiguous characteristic of carbon supported metal particles or the suspected presence of carbon atoms in metal particle. In the investigation of CNF supported Ni catalyst, Shaikhutdidov et al reported the formation of carbide-like Ni phase after annealing at 350^{o}C in inert atmosphere when the Ni nitrate was impregnated on the reactive CNF support.[41] They suggested that the carbon support interact with the NiO phase via carbon atoms dissolution into the NiO lattice. Gandia and Montes also reported the reducing activity of carbon support to the supported NiO nanoparticles.[42] They reported that the reduction of NiO on activated charcoal proceed at much lower temperature than on graphite support. Also in the preparation of Pd catalyst on meso and microporous carbon, Okhlopkova et al reported that the catalyst dispersion based on CO chemisorption decreases with reduction temperature.[43] The dispersion however did not relate linearly with the catalytic activity data. Although the authors postulated the hampered accessibility of reactant to reactive site as the cause for the loss of activity, it may well be that there is already carbon from the high surface area support introduced into the Pt catalyst during the reduction treatment. In the case of Pd/carbon catalyst Khrisnakutty et al suggested the formation of carbon contamination from acetyl-acetonate precursor and the subsequent contamination from the carbon support after reduction at 300^{o}C in hydrogen.[44] The contamination resulted in the suppression of hydrogen and carbon monoxide chemisorptions and beta-hydride forming ability of the Pd catalyst. In accordance with the result of Khrishnakutty et al., Teschner et al observed a PdC_x signal by *in situ* XPS on a freshly prepared Pd/CNT catalyst that gave a higher selectivity in the pentyne hydrogenation reaction than Pd/Al_2O_3.[45] For carbon-supported Ru catalyst, the choice of support may lead to different activity as it was reported in the case of Ru/graphite and Ru/AC for n-hexane conversion.[13] Although Ruthenium is not known to form carbides, the existence of surface carbon (or carbide-like) species have been measured to be quite stabile.[46] In the study of carbon nanofilament growth on Ni/diamond catalyst, Higashi et al reported that after annealing to 1000^{o}C the catalyst was encapsulated with carbon and shows no activity to grow carbon nanofilaments. They postulated that the carbon from the support diffused and precipitated into graphitic layers that blocked the active sites.[47]

In the field of catalytic CNT synthesis identifying the active and deactivated state of the catalyst have been a major issue and challenge. Takenaka et al investigated the deactivated Ni/SiO_2 catalyst after long-term reaction to grow CNTs.[48] From EXAFS measurements they suggested that the deactivated Ni catalyst was in a form of carbide-like state. They excluded the presence of Ni_3C. The XRD pattern of deactivated catalyst showed a broad and diffuse band with shifted position to low angle as compared to fresh and active catalyst with sharp and defined position of fcc Ni metal. They referred the catalyst to have amorphous-like structure. In accordance to the findings in this thesis, it is very likely that the deactivated state in their study is highly defective fcc Ni with significant amount of dissolved carbon atoms (NiC_x). Equipped with in situ XRD instrument, Ermakova studied the evolution of Ni catalyst during the exposure with methane to grow carbon filaments.[49] After several hours of reaction, the fcc Ni reflections started to show broadening. With respect to the active state of catalyst, Hoffman and Helveg et al have elegantly showed that the metallic Ni is the active phase to growth CNT or CNF.[50,40] However the possibility that there is carbon diffusing into subsurface or even bulk during the nucleation or towards the deactivation of the catalyst was not discussed in their work.

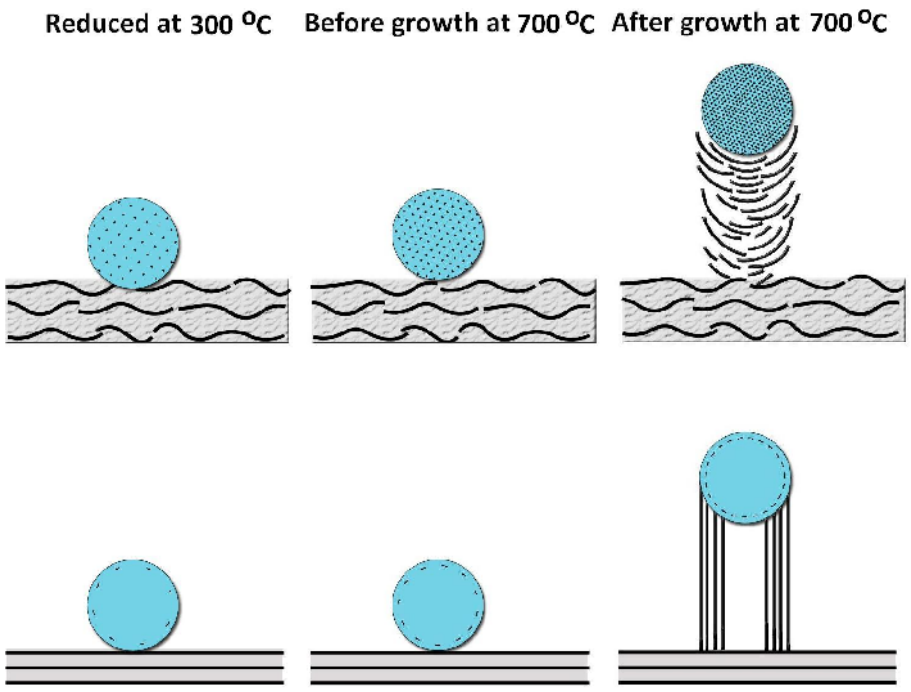

Scheme 5-2. The carbon nanofilament growth summary from Ni/defective and Ni/graphitic carbon.

To summarize, HRTEM, *in situ* XRD and *in situ* XPS give conclusive evidences over the presence of dissolved carbon into the bulk of Ni catalyst especially if supported on defective carbon. Defective carbon with more disordered structure has higher free energy than well-graphitized carbon support leading to weaker C-C bond and more favorable to be broken and the carbon atoms dissolved into bulk Ni.[51] The Ni catalysts under the current investigation condition are expected to be still in its solid state. The temperature used in this study, 700^{o}C is much too low for Ni or NiC_x solid solution to liquefy.[52] In general this work highlights the way carbon supports influence the catalytic activity of transition metal particles.

So far, the role of surface oxygen-containing functional groups and geometric-induced effect by carbon microstructure were used to explain the observed differences in catalytic activity of carbon supported metal catalyst. The preferred adsorption orientation of cinnamaldehyde molecules onto CNF-supported metal catalyst was reported to be influenced by the surface functionality of the CNF support. The different adsorption was suggested to be responsible for the change in activity and selectivity of cinnamaldehyde hydrogenation.[53,54] It has been demonstrated that the catalytic performance of Ni supported CNFs for the hydrogenation of alkenes and dienes at moderate temperatures is sensitive to microstructure of the CNFs. [55] It was proposed that the Ni crystals to form epitaxial relationship with carbon atoms on the surface of the CNFs. The interaction of Ni particles with the carbon support dictates the crystallographic faces of Ni exposed to the reactant gas. Adding to these flexible and complex natures of carbon support, its role as a source to form dissolved carbon in transition metal particles and its effect in catalysis is proposed. The current study established the evidences for the presence and the effect of dissolved carbons on carbon-supported transition metal catalyst for carbon nanofilament synthesis as the probe reaction.

The growth of CNFs instead of multiwall CNTs on Ni particles, in which carbon has been incorporated at low temperature, can be explained by both electronic and structural effects. In addition, the dissolution of carbon in the Ni particles induced their reconstruction. The particles became polycrystalline, with faces oriented in various directions. During growth,

short graphene sheets most likely formed on each of the faces and interconnected in a random way, thus leading to a soot-like structure.

The idea proposed about the concept of carbon introduction at pre-growth temperature to change the microstructure of a catalyst was tested. The experiments were design as follows: reduced-Ni/graphitic carbon was pre-dosed with known minute amount of ethylene at temperatures <700^{o}C and continue to growth temperature and exposed to ethylene for 5 min. The aim of these experiments is to mimic the condition in Ni/defective carbon where significant amount of carbon is present in the bulk of Ni after reduction (before nanofilament growth). The pre-dosing experiments with ethylene have profound influence on the microstructure of the grown nanofilaments and its consistency throughout the filament length (Fig 5-14 & 5-15). The pre-dosing experiments especially performed at higher ethylene amount resulted in the total encapsulation of the Ni nanoparticles with several layers of graphitic carbon. There is no clear pattern between the microstructure of the filaments, pre-dosing amount and temperature. In general the microstructure of grown nanofilament starts to developed defects and especially for nanoparticles of 5-10 nm in diameter, the microstructure is clearly defective platelet-like CNFs. Whereas for filaments with diameter >10 nm the microstructure in a given filament is alternating between herringbone CNFs and platelet-like CNFs (Fig 5-14e-f). In general the experiment is consistent with the idea that carbon incorporation into the Ni catalyst prior to the growth step modifies the microstructure of the grown carbon nanofilaments. The modification of the microstructure suggests that the pre-dosing with ethylene disrupt the diffusion pathways of carbon in the bulk and/or on the surface of Ni nanoparticle.

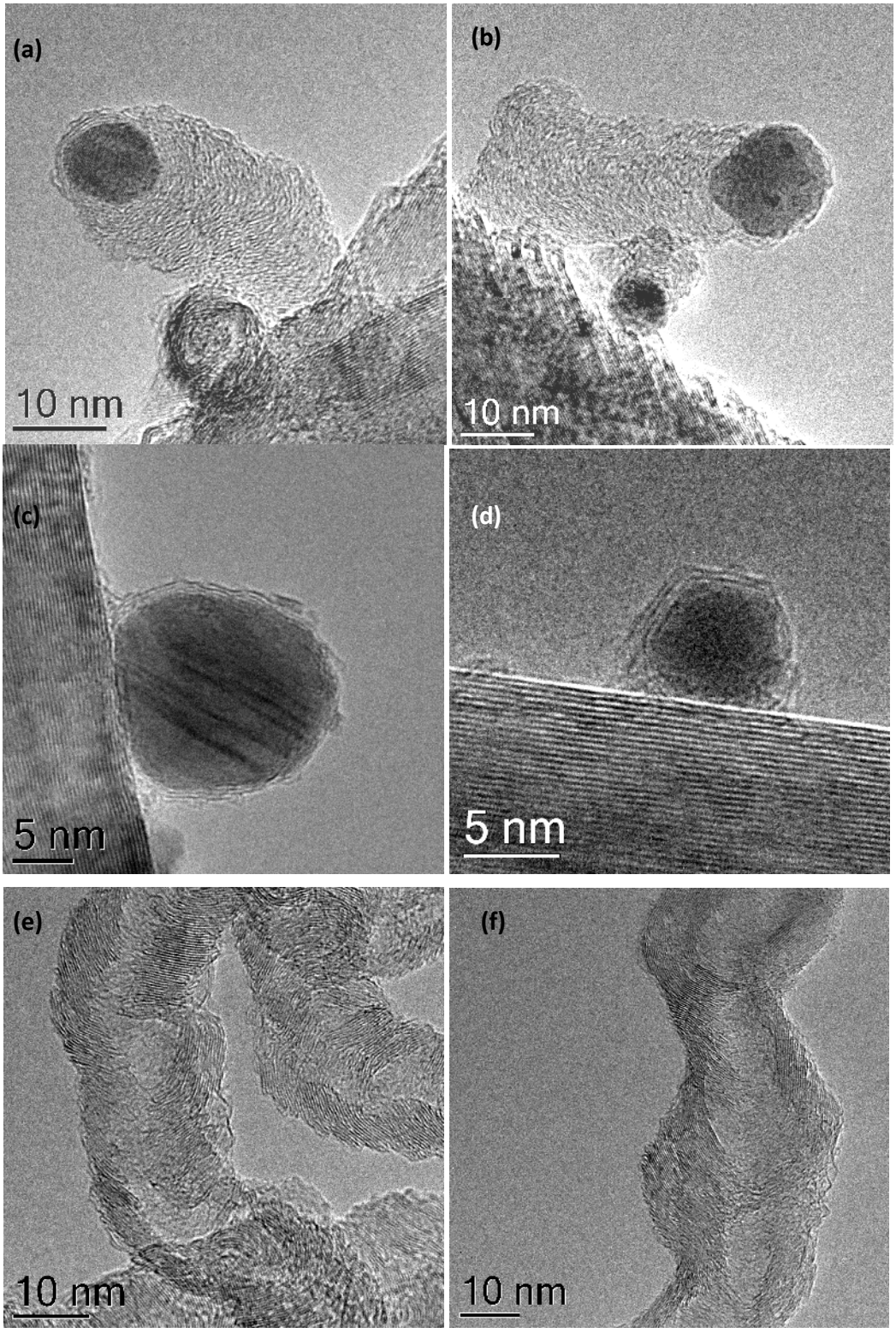

Figure 5-14. Defective CNFs and encapsulated Ni nanoparticles as a result of pre-dosing experiment with ethylene prior to the second exposure (growth) at 700^{o}C.

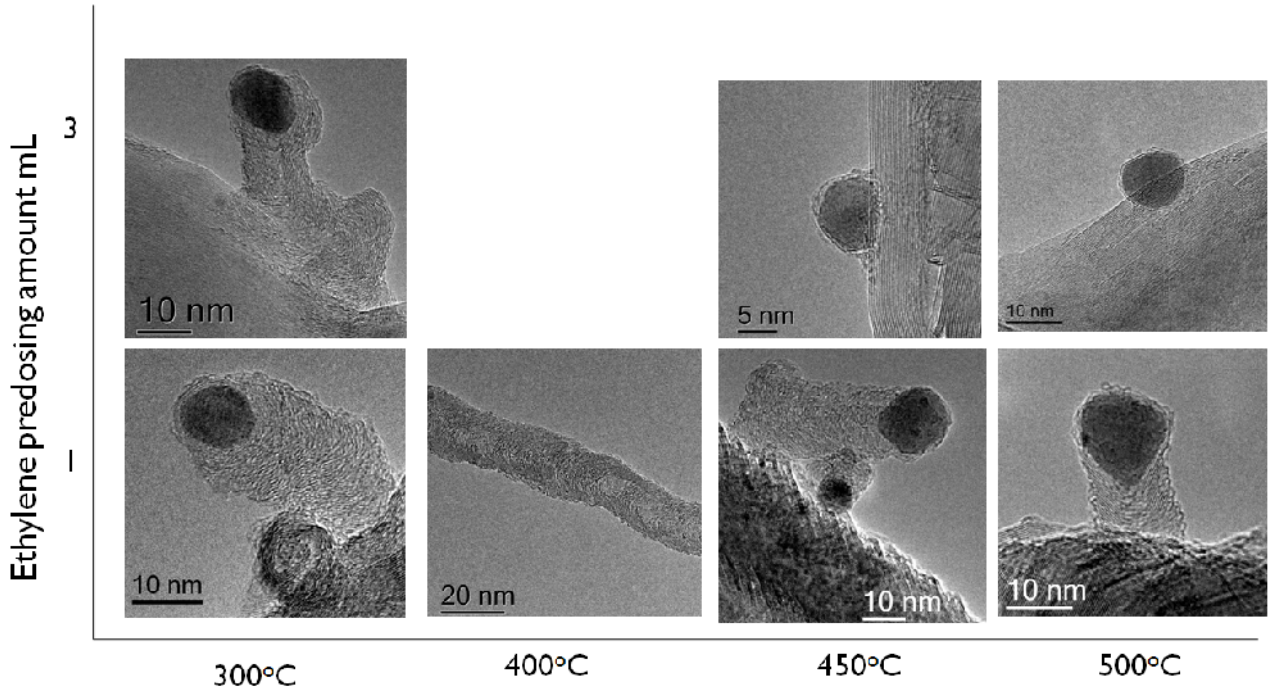

Figure 5-15. Summary of the pre-dosing experiments with ethylene with a certain volume and at a certain temperature resulting in defective CNFs and encapsulated Ni nanoparticles.

The pre-dosing experiments with ethylene were also carried out in the *in situ* XRD and *in situ* XPS cell to investigate the electronic and structural change of the catalyst during the carbon nanofilament growth. The pre-dosing with ethylene at 400^{o}C resulted almost no change in the bulk structure of Ni nanoparticles (green line Fig 5-16). The fcc Ni reflections remain constant with respect to its position and breadth after the dosing. However there is a slight shift of the Ni reflections to lower angle after nanofilament growth at 700^{o}C, suggesting that there is an increase of dissolved carbon amount in the Ni catalyst after growth, as compared to growth without pre-dosing (Fig 5-10). The *in situ* XP spectra showed that carbon was incorporated in the Ni subsurface and/or bulk instantly after pre-dosing at 400^{o}C (Fig 5-17). The contribution of the Ni metal and carbidic Ni remains constant. They however change after the system was ramp to 700^{o}C. The carbon atoms started to diffuse into the subsurface during heating to 700^{o}C. The observation from in situ XRD and XPS are consistent suggesting that there are more carbons in

the bulk and sub-surface of the Ni nanoparticle with the pre-dosing experiment. These observations suggest that it is possible to grow CNTs or CNFs by simply introducing C into the catalyst prior to the growth step. The carbon atoms can either be provided by the support or by exposing the catalyst to hydrocarbons at a relatively low temperature.

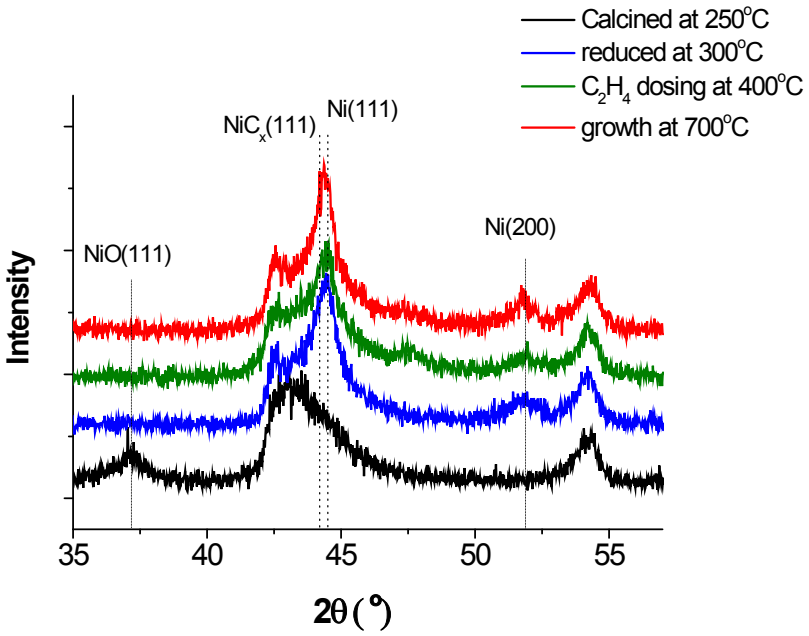

Figure 5-16. in situ XRD pattern of Ni/graphitic carbon after reduction, pre-dosing and growth.

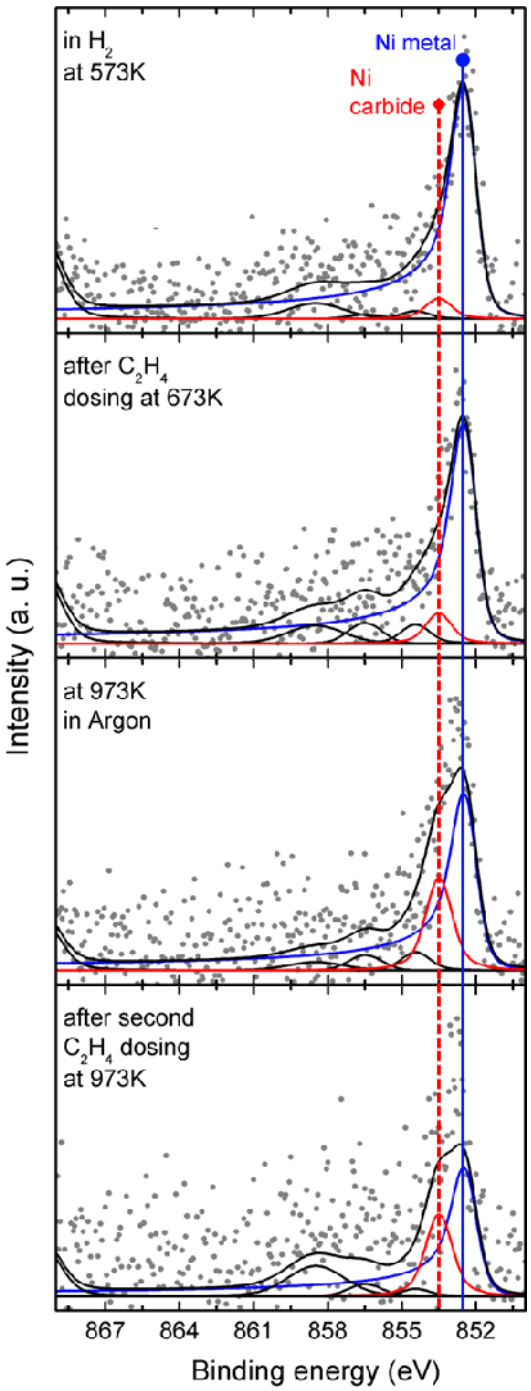

Figure 5-17. Evolution of the Ni2p XP spectra for Ni/graphitic carbon after reduction, after ethylene pre-dosing, after heating to 700°C and after growth.

These experiments lead to three major conclusions. First, it is now clear that differences in catalytic activity observed in the literatures for metals supported on various carbons can be partially explained by carbon incorporation from the support. The electronic and structural properties of metallic particles supported on carbon are chemically modified by carbon incorporation. The amount of introduced carbon remains relatively low and might only be observed with highly sensitive *in-situ* techniques, which explains why such an effect has not been demonstrated before. Secondly, it is observed that carbon incorporation already during reduction at 300^{o}C, which is an activation condition typical for catalysts. Therefore, carbon incorporation may also play a role for reactions occurring at low temperatures. Finally, it is possible to also introduce sub-surface carbon by exposing the active metal to hydrocarbons at low temperature. This offers new possibilities to control the catalytic activity of metal particles and might open new routes for the rational design of heterogeneous catalysts.

5.2. Contribution of the current work with the general understanding of the mechanism of Carbon nanofilament growth

The first significant study on the mechanism of carbon filaments came from Baker et al on the study of acetylene decomposition on Ni particles using controlled atmosphere electron microscopy.[56,57] It provides the first direct evidence that the formation of the filament took place by the build up behind the metal particle. Their work also revealed the presence of an induction period before a liner rate growth of filament. They showed that the deactivated catalyst no longer have free surface exposed to the gas phase but rather encapsulated by carbon layers. The similarity between the activation energy of filament growth with the carbon diffusion in solid metal suggests them to postulate bulk diffusion of carbon to be the rate-determining step. They further postulate that the temperature gradient in the particle to be the driving force of filament synthesis. In a later publication Baker et al proved that carbide is not the active state for carbon filament growth.[58] These pioneering works by Baker et al. provide a strong foundation for the understanding of carbon nanofilament synthesis.

Decades after that, several research groups equipped with atomic resolution environmental TEM demonstrate that the metal catalyst are in a crystalline state with frequent shape changes. [6,40,59,50,60,61] Under lower resolution in situ TEM reported in previous literature, such shape changes lead authors to suggest the liquid state of the catalyst during carbon nanofilament growth. For Ni the catalyst remains metallic during the CNT growth whereas for Fe, both carbide and metallic state coexist during the growth.[59] However it is obvious that carbide is not prerequisite for carbon nanofilament growth, as other metal such Ru not known to have stabile carbide can still grow carbon filaments.[28]

This chapter has several major findings that contribute to the general understanding of the carbon nanofilament growth mechanism. They are:

- This investigation provides direct evidence that carbon diffusion control the microstructure of the grown carbon filaments. This investigation gives direct evidence for the presence of bulk and surface dissolved carbon in Ni nanoparticle during the growth of CNFs and CNTs respectively. Finally this investigation demonstrates that dissolved carbon is an important parameter to control the growth of carbon nanofilaments. A Model to explain the role of dissolved carbon is shown in scheme 5-2. The dissolved carbon exerted electronic and structural changes to the Ni catalyst.

- It is not clear whether the amount of dissolved carbon alter the time for graphene nucleation (induction period). In this investigation it has been proven that Ni catalyst containing more dissolved carbon (up to the bulk level) resulted in slower growth with poorly crystalline carbon. However Ni catalyst with much less dissolved carbon especially on the surface (and maybe also in the bulk) produces long CNTs with graphitic structure. The idea that nucleation occur once the catalyst reach supersaturation amount of dissolved carbon is not supported by the current investigation. The same metal catalyst with different percentage of dissolved carbon resulted CNT with different microstructure. Thus these observations indicate that dissolved carbon change the kinetic and thermodynamic of the carbon nanofilament growth.

- The carbon dissolved at lower temperature (pre-dissolved carbon from the support or from ethylene pre-dosing experiments) facilitates the dissolution of more carbon into the bulk during carbon nanofilament growth. Under this condition/behavior the grown filament has a defective CNF structure. In contrast if there are no or only minute amount of dissolved carbon in the Ni catalyst, there is barely more carbons dissolved during the CNT growth.

- There seem to be a relation between the percentage of dissolved carbon, the temperature at which the carbon dissolved and the final microstructure of the grown nanofilaments. The first set of experiments show that pre-dissolved carbon changes the microstructure of grown nanofilaments. The second set of experiments involving pre-dosing ethylene demonstrates that dissolved carbon change the dynamic of carbon deposition. The carbon filaments grown from pre-dosed Ni/graphitic catalyst show that the graphene arrangement varies along the filament. In contrast the experiment without pre-dosing ethylene resulted in a constant graphitic tubular structure along the filaments. This observation proves that indeed pre-dissolved carbon change how carbon diffuse through and precipitate from a metal catalyst. The pre-dissolved carbon alters the orientation of graphene arrangements during growth relative to the filament axis. The history of the catalyst shape during nanofilaments growth can be traced by the structure of the deposited carbon. The observation suggests that the pre-dissolved carbon changes the equilibrium state of catalyst structure/shape, and thus modifying the way carbon is deposited.

- In situ TEM investigations of CNT growth demonstrate that the shape of the catalyst is responsible for the alignment of graphene layers.[6,40,60] Abrupt shape changes precede the formation of defects and bending during CNT growth. Smooth, straight and quasi-defect free CNTs comes from catalyst with constant shape during growth.[59] Helveg et al have suggested that the reshaping of Ni nanoparticles involves the movement of Carbon and Ni atoms on the surface during the CNT growth.[40] The catalyst deformation caused by Ni and C flux is not limited to the surface. The breakup of catalyst particle during CNT

growth supports this argument. The breakup suggests that the deformation takes place in the middle of the catalyst, away from gas-adsorbing and carbon-precipitating surface of the catalyst. To fit this scenario, highly defective CNFs such as that grown from catalyst rich in pre-dissolved carbon, should grow from catalyst with continuous reshaping. It is intuitive to assume that flux of Ni atoms deforming the crystals occurred at sites where carbon is actively diffusing and precipitating away. A steady state of low percentage of carbon diffusing through the bulk/surface will not significantly deform the crystals. However as more carbon is dissolved, the crystal is significantly deformed[23,24] and the registry reported between certain facets of Ni crystal and basal plane of graphene is lost.[9,11] As a result, deformed graphene is precipitated instead. There are reports in the field of material science dealing with metal/graphite interaction claiming that when a critical amount of carbon dissolved in metal particles, abrupt change from wetting to non-wetting takes place at the metal/graphite interface.[63,62] Similar analogy can be taken into consideration when dealing with carbon nanofilament growth.

5.3. Relationship between Carbon nanofilament growth and Catalyzed Gasification and Catalyzed Graphitization of carbon.

Several phenomena observed during growth of carbon nanofilaments show striking similarities to the phenomena reported during catalytic gasification and catalytic graphitization of carbon materials.[37] These include fluid-like behavior or reshaping of catalyst particles, encapsulation of deactivated catalyst particles and catalyst break-up or re-dispersion. [21,26,64,27,37,65] It has also been shown that the active state for these reactions involving Ni catalyst is the metallic state.[40,48,66,64] The involvement of dissolved carbon into the Ni particle during these reactions has also been suggested in previous studies. However no direct evidence has been presented yet. It has been demonstrated that once the catalyst is encapsulated it was no longer active for nanofilaments growth and catalytic graphitization presumably because there is no longer contact between metal surface and carbon source. It was suggested that encapsulation first start with an increase of dissolved carbon content in the metal catalyst.[48,62,65]

Another mode of deactivation suggested to occur during Ni-catalyzed hydrogenation of graphite is the gradual break-up of metal particles to re-disperse on the graphite edges in the channels.[65] The disappearance of Pd during catalytic graphitization of amorphous carbon has also been suggested to be the result of particle re-dispersion or Pd evaporation.[37] The disappearance contributed to the loss of activity over time. An analogy can be extrapolated for the break-up of the catalyst particle to be partially responsible for the deactivation of catalyst during CNT growth. The break-up may lead to re-dispersion of metal particles along the inner channel of the tube within the range of cluster to nanometer scale (probably containing different amount of dissolved carbon). The lack of metal atoms in the catalyst will eventually lead to over saturation of the bulk with dissolved carbon thus leading to encapsulation. The validity of scenario need to be further investigated and tested.

Interestingly the fluid-like behavior of metal particles was also observed during Pd-catalyzed oxidation of graphite and amorphous carbon.[67,68] The similarities between these reactions invoke one to rationalize that they involve similar fundamental reaction mechanism. The reactions involve first the breaking of C-C bond from solid carbon or gaseous carbon. The second step involves the transfer of carbon either through the surface and/or the bulk of the metal particle. The dissolved carbon atoms will finally reappear on the metal surface to react with adsorbed hydrogen or oxygen for hydrogenation or oxidation respectively. For carbon nanofilament synthesis and catalytic graphitization, C-C bonds are formed on the other side of the metal particles. Frames of TEM images acquired from in situ studies of catalytic graphitization of amorphous carbon[21,69,64] and CNT synthesis[6,40,59] demonstrate that the change of catalyst particle's morphology during reaction strongly correlate with the imperfections of the precipitated graphitic carbon microstructure. Catalyst with constant/stabile morphology resulted in a quasi-defect free CNTs or CNFs.[6,59] For catalytic graphitization, distinct changes of the catalyst morphology are related to the wetting of metal particles to the amorphous carbon substrate with random orientation. In accordance with that observation, graphitization of amorphous carbon with tubular texture resulted in the precipitation of graphitic tubular CNTs. With tubular amorphous carbon substrate, the wetting and thus the graphitization are geometrically constrained. In contrast to amorphous carbon, the Ni-catalyzed hydrogenation of

graphite takes place forming straight channels with occasional 60^{o} and 120^{o} bends. The channels align along <11$\underline{2}$0> orientation of graphite indicating preferential wetting action of the metal with the armchair faces of the graphite throughout the reaction. [71,70,6571] The interconnecting influence between the catalyst faces, microstructure of carbon and the hydrogenation reactivity in this example is evident. In accordance with this observation, due to different wetting behavior of the catalyst on the more reactive amorphous carbon and on graphite[51], it can be speculated that the precipitation of graphite from the other side of the catalyst will itself contribute to the changes of the metal catalyst morphology.

It was suggested by Lamber et al that the wetting is accompanied by carbon diffusion forming some kind of a metal-carbon solid solution in the interface. Indeed in later publications they observed interface defects[72] and increase of lattice constant[73] for Ni and Pd when supported on amorphous carbon after heat treatment at 400^{o}C. No argument was clearly established in the literature whether the initial amount of dissolved carbon in the catalyst differs between the gasification of amorphous carbon and graphite. However based from the results obtained in the current investigation, it can be deduced that Ni particles to contain more dissolved carbon when gasifying amorphous carbon, as oppose to graphite where only subsurface dissolved carbon is expected.

These clear and direct examples acquired earlier studies in accord with the current investigation support the idea that the change of catalyst morphology as the result of catalyst wetting onto the carbon substrate or different dissolved carbon content or different gaseous carbon potential have a direct impact to the structure of precipitated graphitic carbons.

5.4. Carbon supported metal catalyst.

Metal-carbon support interaction has been exploited to modify the activity of a catalyst material. The interaction has been proven to modify the geometry[55] of the catalyst and presumably also its electronic character.[13] The anchoring of catalyst particles are classically carried out by the available surface functionalities or on surface defects such as steps in the

graphite basal plane. Such approach of attachment is limited to mild catalyst pretreatments and reaction conditions in order to avoid reducing the anchoring sites. A new strategy of geometric fixation was later proposed to create a stabile attachment of metal particle on carbon.[74] The strategy is based on the assumption that the carbon support provides edge sites as geometric barrier and possibly to the extent of creating metal-carbon bond with the dangling terminating edges of the graphene layers. In a review by Schlögl this concept is discussed and the mechanism of its formation is proposed as follows.[74] The metal nanoparticles can be mechanically fixed on the structural defects of the graphitic surface or by creating unique pits by selective etching achieved under high temperature reduction. Another mode of fixation with supposedly stronger metal-carbon interaction is the combination of selective etching with a redeposition of carbon in the interface between carbon support and metal particles. It is suggested that under this chemical fixation a metal-carbon covalent bond is formed acting as binder between the metal and carbon support.

There are several examples in the literature that are suggested to demonstrate the mechanical fixation mode of attachment.[75-77] For smaller particles and/or more reactive carbon supports/sites, the interaction resulted in depleting the electron charge of the metal nanoparticles.[78,79] In the discussion of the articles, the authors suggested that electron deficiency represent the catalyst of different phases or charge transfer with the carbon support. Based from the result in the current study and that of earlier single crystal studies[80] it is very likely that the electron deficient behavior of the catalyst is due to strong metal-carbon bond forming carbidic metal.

Baker & Sherwood pictured the etching and chemical fixation mode in the investigation of Fe-graphite interaction under hydrocarbon-steam environment.[81] The catalyst first gasifies the graphite forming channels, and switching to carbon deposition at higher temperature propagating in the opposite direction. The carbon deposition is suggested to occur in the same mechanism as carbon filament synthesis. Again, in accordance with the result obtained in the current investigation, depending on the microstructure of the deposited carbon, different amount of dissolved carbon either bulk and/or subsurface may present.

The current investigation proves and demonstrates that the metal-carbon support interacting via the dissolution of carbon atoms from catalytic dissociation of C-C of the support. Depending to the reactivity of the metal and the carbon supports, different amount dissolved carbon can have dramatic consequences to catalytic reactions. The involvement of this dissolved carbon either bulk or subsurface in the reaction is however not yet proven in the current work.

Heterogeneous catalysis is considered classically to be surface phenomena. However evidences for the role of bulk species are now presented in the literatures. The importance of subsurface and bulk dissolved carbon has also been studied with theoretical calculations. Theoretical and experimental investigations have shown the favorable formation of subsurface carbon over on-surface carbon in Ni catalyst.[14,83,84,82] It has also been proposed that the presence of subsurface and dissolved carbon to have similar importance as surface adsorbed species for the role in catalytic activity.

In the study of Ni single crystal, the presence of dissolved carbon is shown to be responsible for the deposition of carbon monolayer on the metal surface. The deposition is accompanied with the rearrangement of metal facets leading to the development of (111) faces. [82,85] Bulk and subsurface dissolved carbon have been theoretically and experimentally observed to cause crystal strains, lattice expansion and defects in the solvent metal catalyst. The electronic properties of the catalyst were also modified after carbon dissolution.[80,83] In addition to the perturbation caused by subsurface or bulk carbon, it is not surprising for reactions that involve subsurface pathways to be affected by the dissolved carbon during or prior to the reaction.

Fischer-Tropsch synthesis, catalytic hydrogenation and steam-reforming reaction are several key examples where evidences have been presented to support the notion that subsurface or bulk carbon affects catalytic behavior. It is suggested that there is a relationship between the dissolved carbon and the probability for carbon chain growth for FT synthesis. [86,87] Another study by other authors for FT synthesis argues that the critical step for chain-lengthening processes is the reaction of surface methyl group with bulk dissolved carbon. From

theoretical calculation and kinetic investigation, the involvement of subsurface carbon and bulk-dissolved carbon as intermediates in CNT growth has been proposed. [86,82,84] These observations suggest that carbon atoms in the subsurface sites is involved in the reaction. However a study using pre-carbided Fe catalyst with radioactive label showed that only a small fraction of the product contains the isotope label.[39] This indicates that the involvement of bulk carbon (in this case carbide) is not dominant for Fischer-Tropsch synthesis. Teschner et al provided the evidences for the role of dissolved carbon on the selectivity of alkyne hydrogenation in Pd catalyst.[88] The dissolved carbon limits the amount of dissolved hydrogen in Pd thus affecting the selectivity of the hydrogenation reaction. The work demonstrates that the subsurface sites in Pd catalyst occupied by either H or C is affected by the chemical potential of the gas phase. These experiments establish the nature of the subsurface sites with the surface events. The current investigation support this argument, the phenomena of carbon dissolving into the catalyst from the carbon support have been demonstrated. Indeed in an earlier work by Teschner et al. presented the data that Pd supported on commercial CNT showed more Pd-C contribution in the XP spectra and a more selective hydrogenation of 1-pentyne as compared to Pd on Al_2O_3.[45] It is very likely that some carbon from the CNT support dissolved into the Pd particles.

Thus especially in catalysis, catalyst preparation requires the selection of condition for pretreatments to control the presence of dissolved carbon. Reduction in hydrogen in particular is of significant importance as it is a common method to reduce transition metal oxide. In addition to modifying the reduction progress, the presence of dissolved carbon is crucial for altering the catalyst reactivity.[44,89,90] The evidences presented in the current investigation and that of from other authors on the role of subsurface or bulk species for catalysis, are of crucial importance toward rational catalyst preparation and design.

The amount of dissolved hydrogen present in the Ni particles was not be measured and not the focus in this work. The amount of dissolved hydrogen in the two carbon supported Ni catalyst may probably be different and contribute to the different carbon growth. However, theoretical calculations have shown that the stability of subsurface carbon in Ni catalyst

exceeds that of subsurface hydrogen. [82] Experimental work with Ni particles show that it requires high pressure to achieve for appreciable amount of dissolved hydrogen. [87,91] In addition in the current investigation, the effect exerted by the carbon support and thus the dissolved carbon under atmospheric and low pressure synthesis condition; with and without hydrogen in the ethylene feed show consistent results. They both resulted in defective platelet CNFs and graphitic CNTs for Ni/defective carbon and Ni/graphitic carbon respectively. Having said that, it is safe to say that dissolved hydrogen play no significant role in the carbon nanofilament synthesis on carbon supported Ni catalyst within the experimental conditions set in the current study.

References

(1) Tessonnier, J.; Rosenthal, D.; Hansen, T. W.; Hess, C.; Schuster, M. E.; Blume, R.; Girgsdies, F.; Pfänder, N.; Timpe, O.; Su, D. S.; Schlögl, R. Analysis of the structure and chemical properties of some commercial carbon nanostructures. *Carbon* **2009**, *47*, 1779-1798.

(2) Sadezky, A.; Muckenhuber, H.; Grothe, H.; Niessner, R.; Pöschl, U. Raman microspectroscopy of soot and related carbonaceous materials: Spectral analysis and structural information. *Carbon* **2005**, *43*, 1731-1742.

(3) Darmstadt, H.; Sümmchen, L.; Ting, J. -.; Roland, U.; Kaliaguine, S.; Roy, C. Effects of surface treatment on the bulk chemistry and structure of vapor grown carbon fibers. *Carbon* **1997**, *35*, 1581-1585.

(4) Dresselhaus, M. S.; Dresselhaus, G. *Graphite Fibers and Filaments*; Springer-Verlag, 1988.

(5) Zhao, N.; He, C.; Ding, J.; Zou, T.; Qiao, Z.; Shi, C.; Du, X.; Li, J.; Li, Y. Bamboo-shaped carbon nanotubes produced by catalytic decomposition of methane over nickel nanoparticles supported on aluminum. *Journal of Alloys and Compounds* **2007**, *428*, 79-83.

(6) Lin, M.; Tan, J. P. Y.; Boothroyd, C.; Loh, K. P.; Tok, E. S.; Foo, Y. Dynamical Observation of Bamboo-like Carbon Nanotube Growth. *Nano Letters* **2007**, *7*, 2234-2238.

(7) Bezemer, G. L.; Bitter, J. H.; Kuipers, H. P. C. E.; Oosterbeek, H.; Holewijn, J. E.; Xu, X.; Kapteijn, F.; van Dillen, A. J.; de Jong, K. P. Cobalt Particle Size Effects in the Fischer−Tropsch Reaction Studied with Carbon Nanofiber Supported Catalysts. *Journal of the American Chemical Society* **2006**, *128*, 3956-3964.

(8) Bengaard, H. S.; Nørskov, J. K.; Sehested, J.; Clausen, B. S.; Nielsen, L. P.; Molenbroek, A. M.; Rostrup-Nielsen, J. R. Steam Reforming and Graphite Formation on Ni Catalysts. *Journal of Catalysis* **2002**, *209*, 365-384.

(9) Rostrup-Nielsen, J.; Sehested, J.; Norskov, J. K. In *Advances in Catalysis*; 47; Elsevier, 2002; pp. 65-139.

(10) Lund, C. R. F. Nickel catalyst deactivation in the steam-carbon reaction. *Journal of Catalysis* **1985**, *95*, 71-83.

(11) Yang, R. T.; Chen, J. P. Mechanism of carbon filament growth on metal catalysts. *Journal of Catalysis* **1989**, *115*, 52-64.

(12) Hong, S.; Shin, Y.; Ihm, J. Crystal Shape of a Nickel Particle Related to Carbon Nanotube Growth. *Jpn.*

J. Appl. Phys. **2002**, *41*, 6142-6144.
(13) Guerrero-Ruiz, A.; Bachiller-Baeza, B.; Rodríguez-Ramos, I. Catalytic properties of carbon-supported ruthenium catalysts for n-hexane conversion. *Applied Catalysis A: General* **1998**, *173*, 231-238.
(14) Somorjai, G.; Van Hove, M. Adsorbate-induced restructuring of surfaces. *Progress in Surface Science* **1989**, *30*, 201-231.
(15) Nakano, H.; Nakamura, J. Carbide-induced reconstruction initiated at step edges on Ni(1 1 1). *Surface Science* **2001**, *482-485*, 341-345.
(16) See, C. H.; Harris, A. T. A Review of Carbon Nanotube Synthesis via Fluidized-Bed Chemical Vapor Deposition. *Industrial & Engineering Chemistry Research* **2007**, *46*, 997-1012.
(17) Kanzow, H.; Ding, A.; Nissen, J.; Sauer, H.; Belz, T.; Schlögl, R. Formation of chains of graphitic nanoparticles by heating fullerene blacks covered with thin metal films **2000**.
(18) Gorbunov, A.; Jost, O.; Pompe, W.; Graff, A. Solid-liquid-solid growth mechanism of single-wall carbon nanotubes. *Carbon* **2002**, *40*, 113-118.
(19) Sen, R.; Suzuki, S.; Kataura, H.; Achiba, Y. Growth of single-walled carbon nanotubes from the condensed phase. *Chemical Physics Letters* **2001**, *349*, 383-388.
(20) Harris, P. J. Solid state growth mechanisms for carbon nanotubes. *Carbon* **2007**, *45*, 229-239.
(21) Ichihashi, T.; Fujita, J.; Ishida, M.; Ochiai, Y. In situ observation of carbon-nanopillar tubulization caused by liquidlike iron particles. *Phys. Rev. Lett* **2004**, *92*, 215702.
(22) Zwell, L.; Fasiska, E.; Nakada, Y.; Keh, A. Dilation of Nickel Lattice by Dissolved Carbon. *Trans. Metall. Soc. AIME* **1968**, *242*, 765-766.
(23) Boah, J.; Winchell, P. Dislocation configurations developed during carburization of nickel. *Metall. Mater. Trans.A* **1975**, *6*, 717-724.
(24) Portnoi, V. K. Formation of nickel carbide in the course of deformation treatment of Ni-C mixtures. *Phys. Met. Metall.* **2010**, *109*, 153-161.
(25) Cribb, W.; Reed-Hill, R. The initial development of a yield point due to carbon in nickel 200 during static strain aging. *Metall. Mater. Trans.A* **1978**, *9*, 887-890.
(26) Baker, R. T. K. In *Carbon and coal gasification: science and technology*; Figueiredo, J.; Moulijn, J., Eds.; NATO ASI; Springer: Dordrecht, 1986; pp. 231-268.
(27) Baker, R. T. K. In Situ Electron Microscopy Studies of Catalyst Particle Behavior. *Catalysis Revs.* **1979**, *19*, 161-209.
(28) Baker, R. T. K.; Chludzinski, J. J. In-situ electron microscopy studies of the behavior of supported ruthenium particles. 2. Carbon deposition from catalyzed decomposition of acetylene. *The Journal of Physical Chemistry* **1986**, *90*, 4734-4738.
(29) Hansen, T. W.; Wagner, J. B.; Hansen, P. L.; Dahl, S.; Topsoe, H.; Jacobsen, C. J. H. Atomic-Resolution in Situ Transmission Electron Microscopy of a Promoter of a Heterogeneous Catalyst. *Science* **2001**, *294*, 1508-1510.
(30) Hansen, P. L.; Wagner, J. B.; Helveg, S.; Rostrup-Nielsen, J. R.; Clausen, B. S.; Topsoe, H. Atom-Resolved Imaging of Dynamic Shape Changes in Supported Copper Nanocrystals. *Science* **2002**, *295*, 2053-2055.
(31) Nagakura, S. Study of Metallic Carbides by Electron Diffraction Part I. Formation and Decomposition of Nickel Carbide. *J. Phys. Soc. Jpn.* **1957**, *12*, 482-494.
(32) Sinharoy, S.; Levenson, L. The formation and decomposition of nickel carbide in evaporated nickel films on graphite. *Thin Solid Films* **1978**, *53*, 31-36.
(33) Smith, M. A.; Sinharoy, S.; Levenson, L. L. Thermal decomposition of nickel carbide: an Auger lineshape study. *J. Vac. Sci. Technol.* **1979**, *16*, 462-465.
(34) Hurst, N. W.; Gentry, S. J.; Jones, A.; McNicol, B. D. Temperature Programmed Reduction. *Catalysis Reviews: Science and Engineering* **1982**, *24*, 233.
(35) Holstein, W. L.; Boudart, M. Hydrogenolysis of carbon and its catalysis by platinum. *Journal of Catalysis* **1981**, *72*, 328-337.
(36) Holstein, W. L.; Boudart, M. Transition metal and metal oxide catalysed gasification of carbon by oxygen, water, and carbon dioxide. *Fuel* **1983**, *62*, 162-165.

(37) Holstein, W.; Moorhead, R.; Poppa, H.; Boudart, M. In *Chemistry and Physics of Carbon*; Marcel Dekker Inc.: New York.
(38) Holstein, W. L.; Boudart, M. Uncatalyzed and platinum-catalyzed gasification of carbon by water and carbon dioxide. *Journal of Catalysis* **1982**, *75*, 337-353.
(39) Kummer, J. T.; DeWitt, T. W.; Emmett, P. H. Some Mechanism Studies on the Fischer-Tropsch Synthesis Using C14. *Journal of the American Chemical Society* **1948**, *70*, 3632-3643.
(40) Helveg, S.; Lopez-Cartes, C.; Sehested, J.; Hansen, P. L.; Clausen, B. S.; Rostrup-Nielsen, J. R.; Abild-Pedersen, F.; Norskov, J. K. Atomic-scale imaging of carbon nanofibre growth. *Nature* **2004**, *427*, 426-429.
(41) Shaikhutdinov, S.; Avdeeva, L.; Novgorodov, B.; Zaikovskii, V.; Kochubey, D. Nickel catalysts supported on carbon nanofibers: structure and activity in methane decomposition. *Catalysis Letters* **1997**, *47*, 35-42.
(42) Gandia, L. M.; Montes, M. Effect of Thermal Treatments on the Properties of Nickel and Cobalt Activated-Charcoal-Supported Catalysts. *Journal of Catalysis* **1994**, *145*, 276-288.
(43) Okhlopkova, L. B.; Lisitsyn, A. S.; Likholobov, V. A.; Gurrath, M.; Boehm, H. P. Properties of Pt/C and Pd/C catalysts prepared by reduction with hydrogen of adsorbed metal chlorides: Influence of pore structure of the support. *Applied Catalysis A: General* **2000**, *204*, 229-240.
(44) Krishnankutty, N.; Li, J.; Albert Vannice, M. The effect of Pd precursor and pretreatment on the adsorption and absorption behavior of supported Pd catalysts. *Applied Catalysis A: General* **1998**, *173*, 137-144.
(45) Teschner, D.; Vass, E.; Hävecker, M.; Zafeiratos, S.; Schnörch, P.; Sauer, H.; Knop-Gericke, A.; Schlögl, R.; Chamam, M.; Wootsch, A.; Canning, A. S.; Gamman, J. J.; Jackson, S. D.; McGregor, J.; Gladden, L. F. Alkyne hydrogenation over Pd catalysts: A new paradigm. *J. Catal.* **2006**, *242*, 26-37.
(46) Wise, H.; McCarty, J. G. Thermodynamic properties of surface carbon on ruthenium. *Surface Science* **1983**, *133*, 311-320.
(47) Higashi, N.; Ichi-oka, H.; Miyake, T.; Suzuki, T. Growth mechanisms of carbon nanofilaments on Ni-loaded diamond catalyst. *Diamond and Related Materials* **2008**, *17*, 283-293.
(48) Takenaka, S.; Ogihara, H.; Otsuka, K. Structural Change of Ni Species in Ni/SiO2 Catalyst during Decomposition of Methane. *Journal of Catalysis* **2002**, *208*, 54-63.
(49) Ermakova, M.; Ermakov, D.; Plyasova, L.; Kuvshinov, G. XRD studies of evolution of catalytic nickel nanoparticles during synthesis of filamentous carbon from methane. *Catalysis Letters* **1999**, *62*, 93-97.
(50) Hofmann, S.; Blume, R.; Wirth, C. T.; Cantoro, M.; Sharma, R.; Ducati, C.; Hävecker, M.; Zafeiratos, S.; Schnoerch, P.; Oestereich, A.; Teschner, D.; Albrecht, M.; Knop-Gericke, A.; Schlögl, R.; Robertson, J. State of Transition Metal Catalysts During Carbon Nanotube Growth. *J. Phys. Chem. C* **2009**, *113*, 1648-1656.
(51) Yudasaka, M.; Tasaka, K.; Kikuchi, R.; Ohki, Y.; Yoshimura, S.; Ota, E. Influence of chemical bond of carbon on Ni catalyzed graphitization. *J. Appl. Phys.* **1997**, *81*, 7623.
(52) Singleton, M.; Nash, P. The C-Ni (Carbon-Nickel) system. *Journal of Phase Equilibria* **1989**, *10*, 121-126.
(53) Toebes, M. L.; Prinsloo, F. F.; Bitter, J. H.; van Dillen, A. J.; de Jong, K. P. Influence of oxygen-containing surface groups on the activity and selectivity of carbon nanofiber-supported ruthenium catalysts in the hydrogenation of cinnamaldehyde. *Journal of Catalysis* **2003**, *214*, 78-87.
(54) Toebes, M. L.; Zhang, Y.; Hájek, J.; Alexander Nijhuis, T.; Bitter, J. H.; Jos van Dillen, A.; Murzin, D. Y.; Koningsberger, D. C.; de Jong, K. P. Support effects in the hydrogenation of cinnamaldehyde over carbon nanofiber-supported platinum catalysts: characterization and catalysis. *Journal of Catalysis* **2004**, *226*, 215-225.
(55) Park, C.; Baker, R. T. K. Catalytic Behavior of Graphite Nanofiber Supported Nickel Particles. 2. The Influence of the Nanofiber Structure. *The Journal of Physical Chemistry B* **1998**, *102*, 5168-5177.
(56) Baker, R. T. K.; Barber, M. A.; Harris, P. S.; Feates, F. S.; Waite, R. J. Nucleation and growth of carbon deposits from the nickel catalyzed decomposition of acetylene. *Journal of Catalysis* **1972**, *26*, 51-62.
(57) Baker, R. T. K.; Harris, P. S. In *Chemistry and Physics of Carbon*; Thrower, P., Ed.; Marcel Dekker Inc.:

New York, 1978; Vol. 14, pp. 83-165.
(58) Baker, R. T. K.; Yates, D. J. C.; Dumesic, J. A. In *Coke Formation on Metal Surfaces*; American Chemical society, 1982; Vol. 202, pp. 1-21.
(59) Yoshida, H.; Takeda, S.; Uchiyama, T.; Kohno, H.; Homma, Y. Atomic-Scale In-situ Observation of Carbon Nanotube Growth from Solid State Iron Carbide Nanoparticles. *Nano Letters* **2008**, *8*, 2082-2086.
(60) Sharma, R.; Rez, P.; Treacy, M. M. J.; Stuart, S. J. In situ observation of the growth mechanisms of carbon nanotubes under diverse reaction conditions. *J Electron Microsc (Tokyo)* **2005**, *54*, 231-237.
(61) Sharma, R.; Iqbal, Z. In situ observations of carbon nanotube formation using environmental transmission electron microscopy. *Appl. Phys. Lett.* **2004**, *84*, 990.
(62) Weisweiler, W.; Mahadevan, V. Wettability Characteristics of Metal Melts on Graphite and glasslike Carbon Substrates and their Relation to catalytic Graphitization. *High Temp.-High Pressures* **1972**, *4*, S27-38.
(63) Owens, W. T.; Rodriguez, N. M.; Baker, R. T. K. Carbon filament growth on platinum catalysts. *The Journal of Physical Chemistry* **1992**, *96*, 5048-5053.
(64) Anton, R. On the reaction kinetics of Ni with amorphous carbon. *Carbon* **2008**, *46*, 656-662.
(65) Terry, R.; Baker, K. A Review of In-Situ Electron Microscopy Studies of Metal/Metal Oxide-Graphite Interactions. *The Journal of Adhesion* **1995**, *52*, 13.
(66) Wigmans, T.; van Doorn, J.; Moulijn, J. A. Deactivation of nickel during gasification of activated carbon, studied by X-ray photoelectron spectroscopy. *Surface Science* **1983**, *135*, 532-552.
(67) Anton, R.; Reetz, O.; Schmidt, A. A. In Situ TEM Investigation of Processes Catalyzed by Pd-Ni Alloy Particles on Carbon Substrates in the Presence and Absence of Oxygen. *Journal of Catalysis* **1994**, *149*, 474-485.
(68) Baker, R. T. K.; France, J. A.; Rouse, L.; Waite, R. J. Catalytic oxidation of graphite by platinum and palladium. *Journal of Catalysis* **1976**, *41*, 22-29.
(69) Krivoruchko, O. A new phenomenon involving the formation of liquid mobile metal-carbon particles in the low-temperature catalytic graphitisation of amorphous carbon by metallic Fe, Co and Ni. *Mendeleev Communications* **1998**, *8*, 97-100.
(70) Tomita, A.; Tamai, Y. Optical microscopic study on the catalytic hydrogenation of graphite. *The Journal of Physical Chemistry* **1974**, *78*, 2254-2258.
(71) Baker, R.; Chludzinski Jr., J.; Sherwood, R. A comparison of the catalytic influence of nickel, iron and nickel-iron on the gasification of graphite in various gaseous environments. *Carbon* **1985**, *23*, 245-254.
(72) Lamber, R.; Jaeger, N. I. Electron microscopy study of the interaction of Ni, Pd and Pt with carbon : III. Formation of a substitutional Pt-C carbide in ultrafine platinum particles. *Surface Science* **1993**, *289*, 247-254.
(73) Lamber, R.; Jaeger, N.; Schulz-Ekloff, G. Electron microscopy study of the interaction of Ni, Pd and Pt with carbon: II. Interaction of palladium with amorphous carbon. *Surface Science* **1990**, *227*, 15-23.
(74) Schlögl, R. In *Preparation of Solid Catalysts*; Ertl, G.; Knözinger, H.; Weitkamp, J., Eds.; Wiley-VCH Verlag GmbH & Co. KGaA, 1999.
(75) Kalucki, K.; Morawski, A. W. Iron intercalated in graphite as catalysts for ammonia synthesis. *Journal of Chemical Technology & Biotechnology* **1990**, *47*, 357-363.
(76) Chen, A. A.; Vannice, M. A.; Phillips, J. Effect of support pretreatments on carbon-supported iron particles. *The Journal of Physical Chemistry* **1987**, *91*, 6257-6269.
(77) Jones, V. K.; Neubauer, L. R.; Bartholomew, C. H. Effects of crystallite size and support on the carbon monoxide hydrogenation activity/selectivity properties of iron/carbon. *The Journal of Physical Chemistry* **1986**, *90*, 4832-4839.
(78) Hegenberger, E.; Wu, N. L.; Phillips, J. Evidence of strong interaction between iron particles and an activated carbon support. *The Journal of Physical Chemistry* **1987**, *91*, 5067-5071.
(79) Jung, H.; Vannice, M. A.; Mulay, L. N.; Stanfield, R. M.; Delgass, W. N. The characterization of carbon-supported iron catalysts: Chemisorption, magnetization, and Mössbauer spectroscopy. *Journal of Catalysis* **1982**, *76*, 208-224.
(80) McCarty, J. G.; Madix, R. J. The adsorption of CO, H2, H2, CO2 and H2O on carburized and graphitized

Ni(110). *Surface Science* **1976**, *54*, 121-138.
(81) Baker, R. T. K.; Sherwood, R. D. Catalytic action of iron on graphite in a hydrocarbon/steam environment. *Journal of Catalysis* **1985**, *95*, 101-107.
(82) Xu, J.; Saeys, M. First Principles Study of the Stability and the Formation Kinetics of Subsurface and Bulk Carbon on a Ni Catalyst. *The Journal of Physical Chemistry C* **2008**, *112*, 9679-9685.
(83) Wiltner, A.; Linsmeier, C.; Jacob, T. Carbon reaction and diffusion on Ni(111), Ni(100), and Fe(110): Kinetic parameters from x-ray photoelectron spectroscopy and density functional theory analysis. *J. Chem. Phys.* **2008**, *129*, 084704.
(84) Moors, M.; Amara, H.; Visart de Bocarmé, T.; Bichara, C.; Ducastelle, F.; Kruse, N.; Charlier, J. Early Stages in the Nucleation Process of Carbon Nanotubes. *ACS Nano* **2009**, *3*, 511-516.
(85) Kikowatz, R.; Flad, K.; Horz, G. Effects of carbon and sulfur on the decomposition of hydrocarbons on nickel. *J. Vac. Sci. Technol. A* **1987**, *5*, 1009-1014.
(86) Nolan, P. E.; Lynch, D. C.; Cutler, A. H. Carbon Deposition and Hydrocarbon Formation on Group VIII Metal Catalysts. *The Journal of Physical Chemistry B* **1998**, *102*, 4165-4175.
(87) Barbier, A.; Brum Pereira, E.; Martin, G. The role of bulk H and C species in the chain lengthening of Fischer-Tropsch synthesis over nickel. *Catalysis Letters* **1997**, *45*, 221-226.
(88) Teschner, D.; Borsodi, J.; Wootsch, A.; Revay, Z.; Havecker, M.; Knop-Gericke, A.; Jackson, S. D.; Schlogl, R. The Roles of Subsurface Carbon and Hydrogen in Palladium-Catalyzed Alkyne Hydrogenation. *Science* **2008**, *320*, 86-89.
(89) Cerro-Alarcón, M.; Bachiller-Baeza, B.; Guerrero-Ruiz, A.; Rodríguez-Ramos, I. Effect of the reduction-preparation method on the surface states and catalytic properties of supported-nickel particles. *Journal of Molecular Catalysis A: Chemical* **2006**, *258*, 221-230.
(90) Krishnankutty, N.; Vannice, M. A. The Effect of Pretreatment on Pd/C Catalysts : I. Adsorption and Absorption Properties. *Journal of Catalysis* **1995**, *155*, 312-326.
(91) Johnson, A. D.; Daley, S. P.; Utz, A. L.; Ceyer, S. T. The Chemistry of Bulk Hydrogen: Reaction of Hydrogen Embedded in Nickel with Adsorbed CH3. *Science* **1992**, *257*, 223-225.

Chapter 6:

Purification of CNTs

CNTs are a promising nanocarbon material with many applications. Basic science combined with technical research in CNT production provides the backbone for these applications which is discussed in subsequent chapters. One of the challenges in producing CNTs is the control and homogeneity of their microstructure. The current research shows satisfying results in producing multiwalled CNTs with uniform microstructure.[1,2] Other factors in producing uniform CNTs in batches also involve the diameter, number of graphene walls, distribution of defects and minimizing the presence of pyrolytic carbon. In this chapter, the focus is the presence of pyrolytic carbon on the surface of commercial CNTs and methods to remove it without damaging the parent CNTs. It also considers and discusses the removal of oxidation debris as the by-product of CNT oxidative functionalization.

6.1. Commercial CNTs sample

The extensive studies of CNTs for several applications, such as catalysis require CNTs to be free from impurities. Catalyst particles and pyrolytic carbons are the most common impurities present in CNT samples synthesized using the CCVD method.

As mentioned in Chapter 1 the purpose of this investigation is to approach the purification method from different points of view as such that the physically or chemically attached carbon chains is considered as polyaromatic hydrocarbons (PAHs), fullerene-like carbons or as short defective graphene-like carbons. The methods used in this research include:

1. solvent extraction

2. gaseous oxidation with diluted O_2
3. liquid phase oxidation with mild HNO_3, and
4. ultrasonic irradiation.

The starting material for this study is the commercial multiwalled CNTs produced by Bayer, Germany. The product known simply as Baytubes CNTs has 95 wt% of carbon purity and average outer diameter of 10 nm. The impurities of this sample composed mainly of Co and Mn from the catalyst. These metal particles are encapsulated with graphitic carbon either at the tip or in the channel of the CNTs. The microstructures of the Baytubes sample most often show graphitic walls parallel to the tube axis (exposing the basal plane to the surface). However, CNTs with fishbone-like arrangements are also observed in the sample exposing prismatic edges on the CNT surface. Physical and chemical details of this material have been described elsewhere.[3] TEM analysis clearly show there is a broad distribution of defects over an individual CNT. Some CNTs show straight textures with smooth straight graphene layers while some show curvy textures with defective graphene stacking. Most of the CNT surface is coated with thin layers of pyrolytic carbon, ranging from one to several layers of amorphous carbon (Fig 6-1).

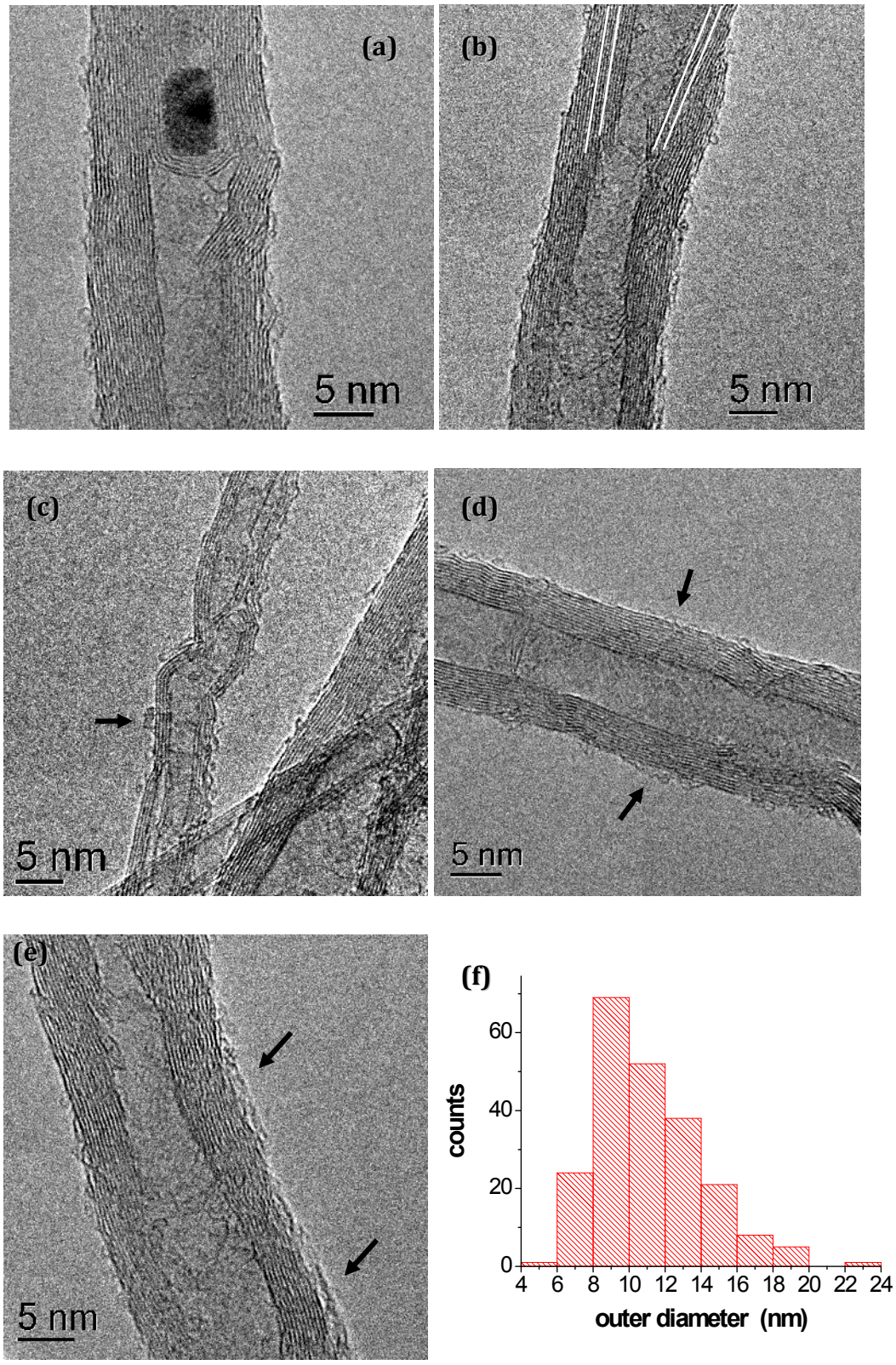

Figure 6-1. TEM images of Baytubes CNTs showing parallel walls with encapsulated catalyst particle in the channel (a), CNT with fishbone structure (b), typical coatings of pyrolytic carbon on the CNTs outer surface of single and multilayers (c-d). The Baytubes CNTs shows an outer diameter distribution from 4-20 nm (e). The white lines are guide for the eye to see the herringbone structure and the black arrows point to pyrolytic carbon.

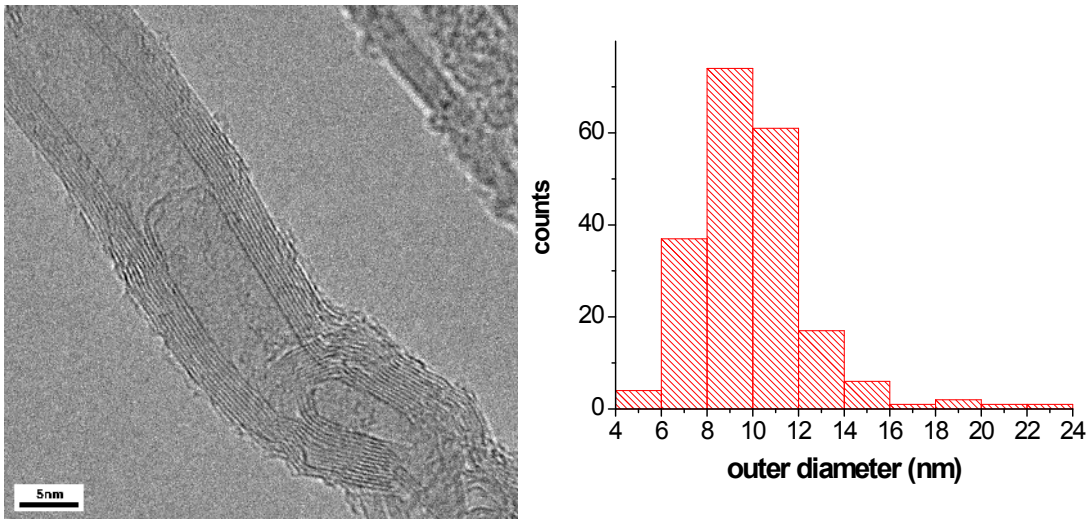

Figure 6-2. TEM image and outer diameter distribution of NC3100 CNT sample.

Another commercial sample that was also investigated in this chapter is NC3100 sample (Nanocyl Belgium). Raman analysis illustrate that the sample has a more graphitic character than the Baytubes sample (Fig. 6-3).[3] The overview from the TEM images suggests that the NC3100 sample contain less pyrolytic carbon than Baytubes sample. The differences between the two commercial CNT samples are best described in the TG profiles and Raman spectra as depicted in Fig. 6-3. The higher T_{50} and the asymmetric shape of the DTG curve suggest that there are less amount of active sites (number of defects) and higher activation energy for the NC3100 sample respectively (Appendix 6-1 & 7-1). This is in agreement with the less amount of catalyst and a more graphitic character of NC3100 as compared to Baytubes sample revealed from Raman and TEM investigations. The higher BET surface area of NC3100 (334m^2/g) over Baytubes (288 m^2/g) further demonstrate the NC3100 stability towards combustion reaction. The inhomogeneous nature of the Baytubes sample is also reflected in the TG profile, better demonstrated by the shoulder in the DTG profile (Fig 6-3b). The shoulder presumably is the combustion of more graphitic CNTs in the sample. This is in agreement with the Raman investigations displaying CNTs with defective and more graphitic character in the Baytubes sample (Fig 6-3). For oxidation catalysis application e.g. ODH reaction of ethyl benzene later shown in Chapter 7, the NC3100 sample was chosen due to their superior oxidative stability over the Baytubes sample.[4]

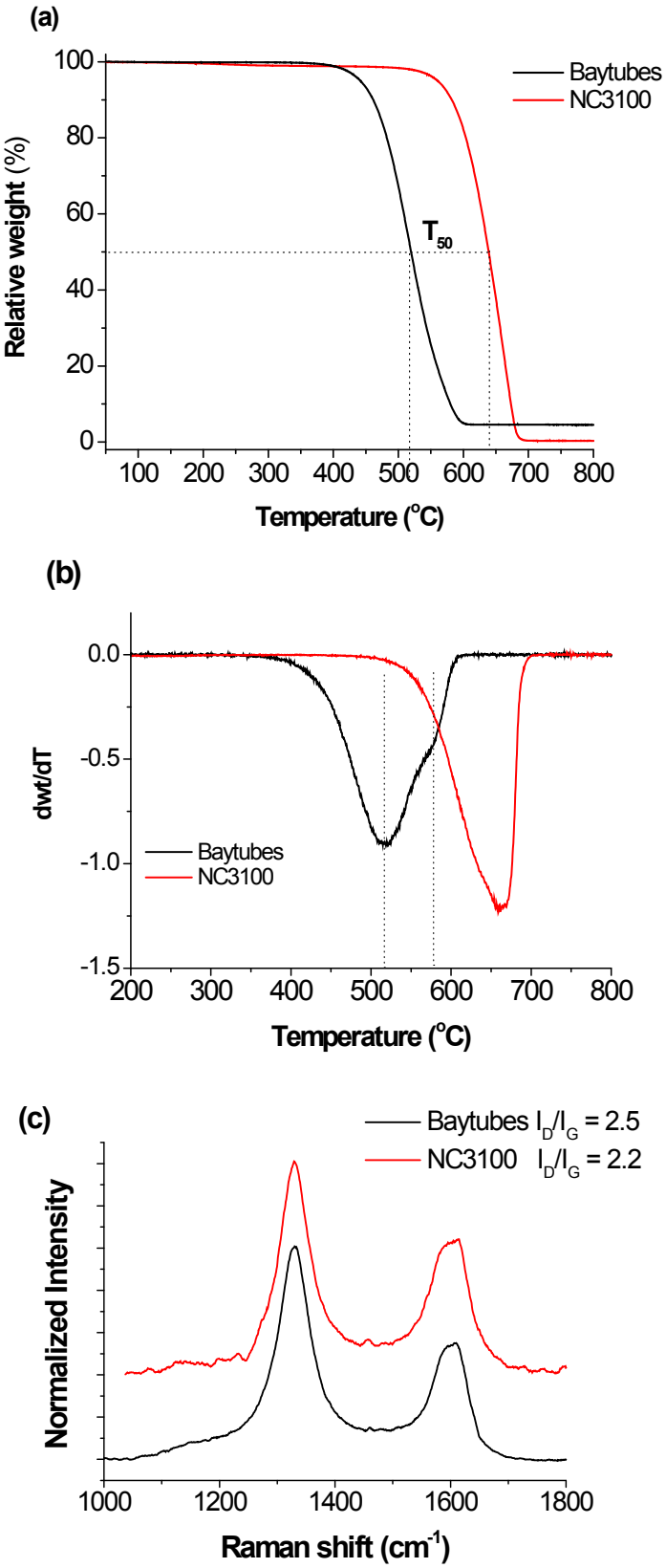

Figure 6-3. Thermal analysis (a,b) and Raman spectra (c) of two commercial as-received CNT samples from Baytubes and NC3100.

6.2. Removal of pyrolytic carbon from CNT surface

6.2.1. Solvent Extraction

With this method it was assumed that the pyrolytic carbon present on the CNT surface has fullerene-like carbon,[5] and/or undeveloped PAHs character. A similar approach was reported for the surface cleansing of carbon fibers from pyrolytic tarry residues.[6] Toluene was chosen as the solvent due to its appreciable solubility for PAHs and fullerenes.[7,8] Soxhlet extraction experiments were performed up to 120 h on the as-received Baytubes sample.

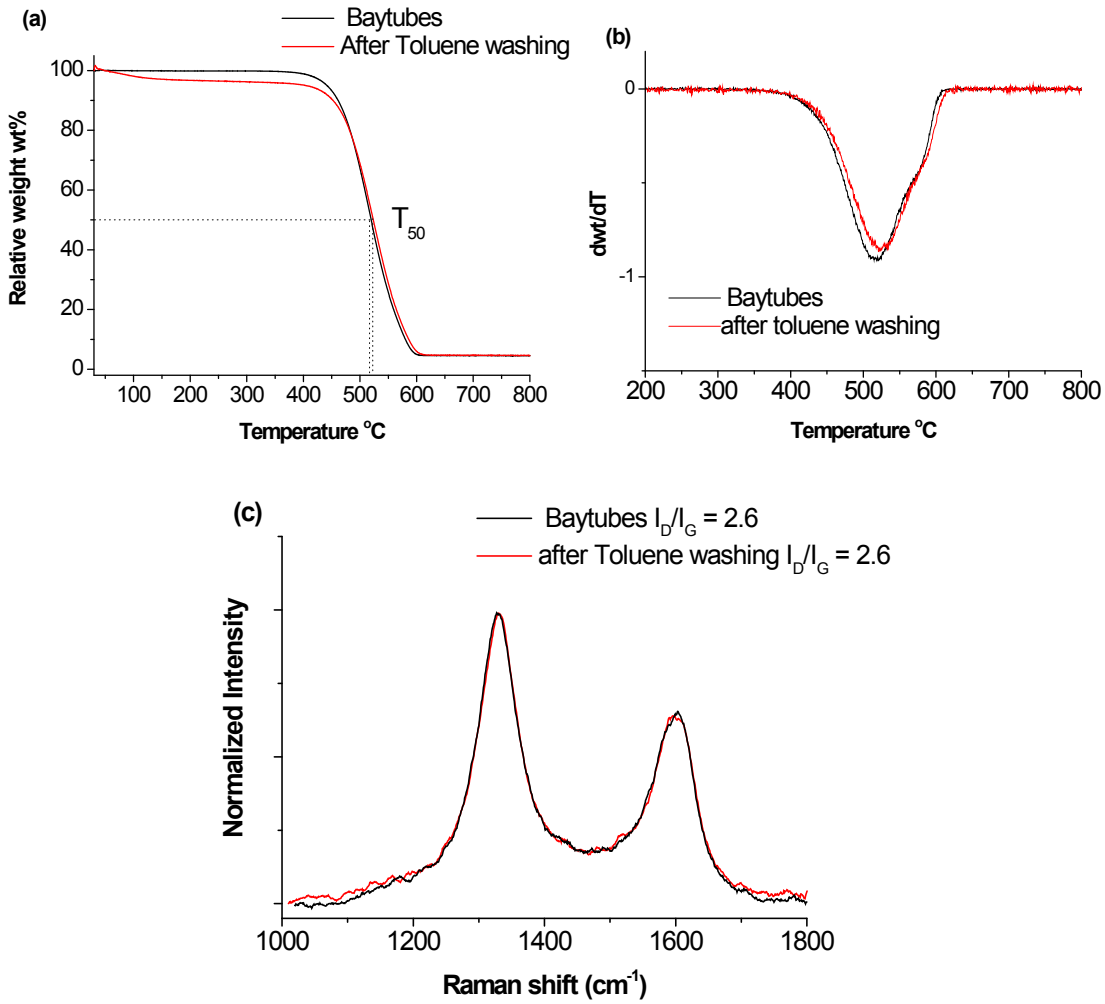

Figure 6-4. Oxidation profile (a) and Raman spectra (b) of Baytubes CNT before and after toluene soxhlet extraction. The Raman spectra are normalized with respect to the D band.

After 120 h of extraction, the sample only exhibits minimum changes in the oxidation profile as shown in Fig 6-4a. The onset of combustion does not change after the toluene washing. The T_{50} however shifted 10 K to a higher temperature presumably due to less thermal runaway. This decrease can be the result of the dissolution of fullerene-like pyrolytic carbons. Raman spectra of the samples reveal a slight decrease in the I_D/I_G value after the toluene extraction treatment (Fig 6-3c) probably within errors of measurements and the fitting procedure. The toluene extraction method may have removed some PAH compounds but not enough to improve the oxidation stability. There are no changes observed in the D2 and D3 bands assigned for amorphous carbon and polyene-like materials respectively.[9] This may be due to more developed chains of carbon network observed in the Baytubes sample. Not surprisingly, no changes were observed for a short treatment time. Careful mild oxidation of such carbon networks may shorten the pyrolytic carbon chains, thus making it easier for dissolution in organic solvents.

6.2.2. Gaseous oxidation with air

The experiments were performed in the UTP setup with quartz reactor type II (Appendix 2-1) which was allowed to swing at half of the maximum speed. For each experiment 2 g of CNT sample was heated to 400^{o}C under flowing air. The temperature was set at 400^{o}C in accordance with the onset of combustion for the Baytubes sample (Fig. 6-3). Pyrolytic carbon, as the most reactive carbon material, should be the first to combust. The reason for applying the mild oxidation temperature is to avoid the autocatalytic combustion of CNTs by hotspots from exothermic combustion of pyrolytic carbons.[10]

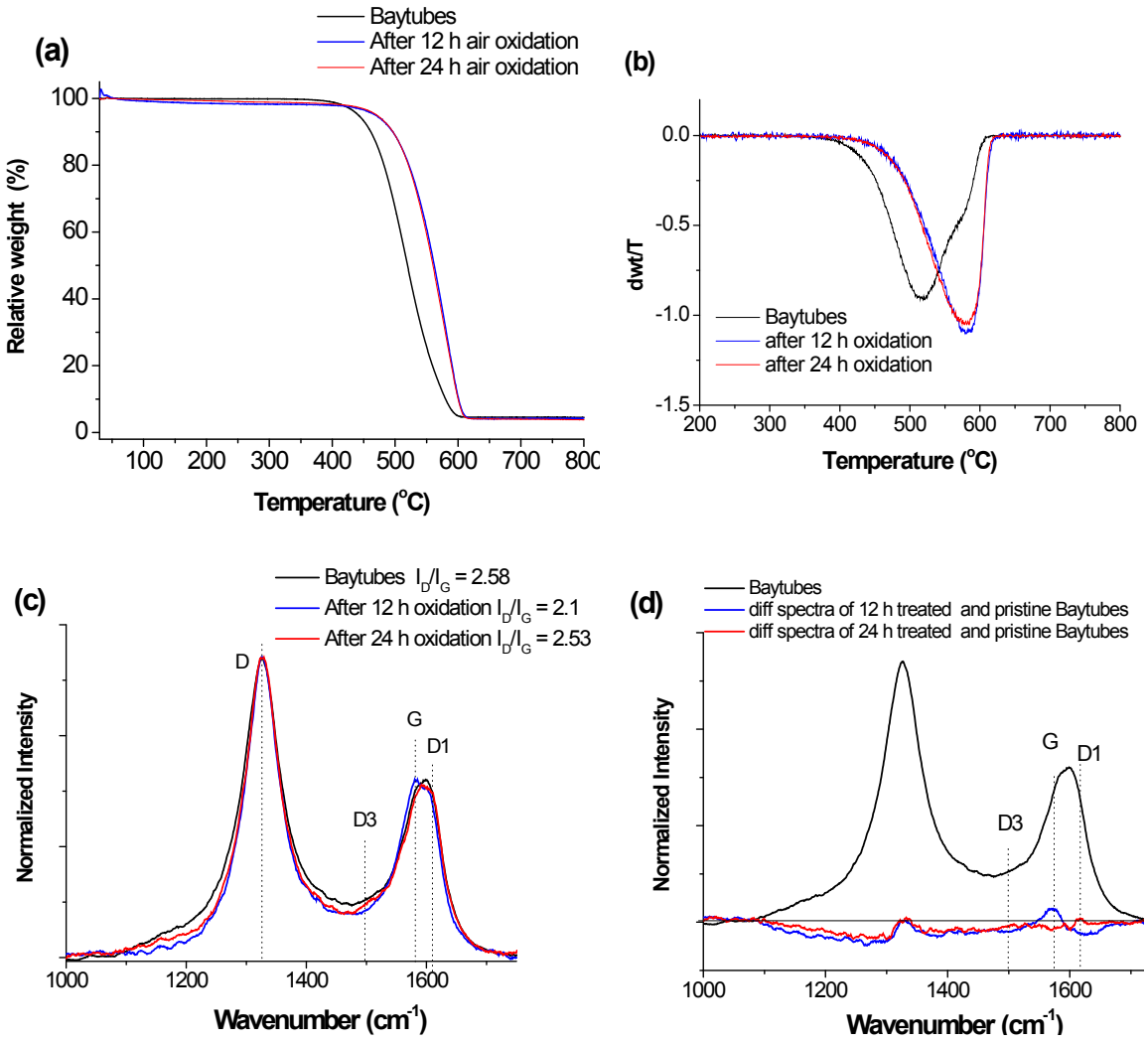

Figure 6-5. TG, DTG oxidation profiles (a, b) and Raman spectra analysis (c, d) of Baytubes CNT before and after oxidation treatment at 400°C. The Raman spectra are normalized with respect to the D band.

The oxidation stability of the sample improves after the treatment as shown in the TG experiments (Fig 6-5a). The onset temperature shifted from 400°C to 460°C after 12 h of air-oxidation treatment suggesting a decrease in the number of active sites. The thermal analysis indicates that the treatment increases the combustion activation energy observed from the change in the DTG shape. The sample after 12 h of air oxidation exhibits more graphitic character demonstrated by the decreasing I_D/I_G value which is consistent with the TG result. The spectrum after 12 h of treatment reveals a narrowing of the D band and a lowering of the D1 and D3 peaks suggesting a change in the concentration and distribution of defects in the amount in

the CNT sample after the air oxidation treatment (Fig 6-5c & d). The increase in the activation energy and the decrease in the number of defects observed from the TG combustion profile strongly indicate that the oxidation treatment selectively oxidizes the defective carbon material resulting in a more graphitic sample afterwards. The role of the catalyst impurities can also change the activation energy; in this case the loss of contact between catalyst and the carbon can lead to decreasing role of catalytic combustion thus increasing the activation energy.

The difference Raman spectra in Fig 6-5d reveal the evolution of the defects and graphitic peaks as a result of the oxidation treatments. The intensity of G band increases after the first 12 h of oxidation and later decreases after 24 h relative to the intensity of D and D1 bands. Against that the D band decreases and narrowed in the 12 h of the treatment and slightly broadened after 24 h treatment. The broadening of the D peak after 24 h however still shows a narrow width as compared to the pristine Baytubes sample.

Prolonging the oxidation treatment however barely change the oxidation profile of the sample (Fig 6-5a & b). The Raman spectra suggest that prolonging the treatment to 24 h generate more defects and degradation of the CNT structure.

Consistent with TG and Raman analysis, TEM investigations (Fig 6-6) reveal cleaner and smoother surface after the oxidation treatment indicating the removal of pyrolytic carbon. There are no pits or holes observed in the sample to indicate hotspots-induced combustion in the sample.[10] However there are clear indications that the catalyst impurities participate in the CNT combustion (Fig 6-6b & c).

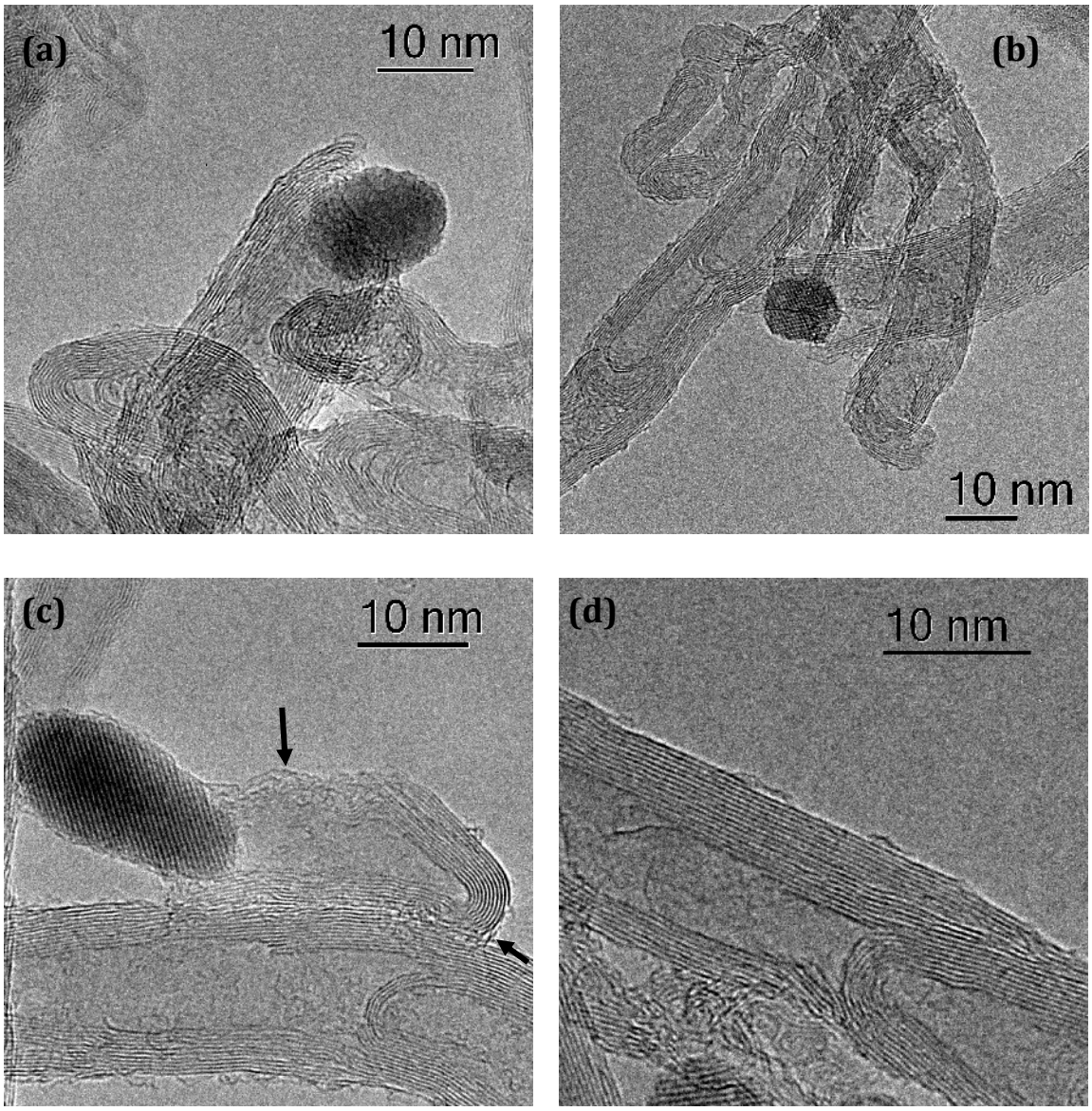

Figure 6-6. TEM images of Baytubes CNTs after 12 h of oxidation treatment.

The catalytic combustion seems to propagate along the tube axis and the rate seems to vary in a complex manner for individual catalyst-CNT pair. TEM image in Fig 6-6c shows the extreme case where the CNT was catalytically combusted leaving only the CNT cap. There are several speculations proposed here to explain such behaviour, for example difference in catalyst-CNT contact, difference in catalyst composition and difference in density of defects of a particular CNT. It is plausible that the differences mentioned may play a role in the catalytic combustion of CNTs. Some of the CNT caps still remain closed while other CNTs are already partially

oxidized giving open tubes. Figure 6-6b & c demonstrate the integrity of small-diameter CNTs (outer diameter of 6-8 nm) with preserved caps and tubular structure after 12 h of oxidation. It is reported that sites with topological defects such as caps and bending have more strains and thus are more reactive towards the attack of oxygen as compared to the perfect graphene walls.[11] In the case of Fig 6-6c where the cap is preserved, catalytic combustion is the dominant process. The cap in Fig 6-6c shows only minor combustion at the tip (highlighted by an arrow for clarity). This figure also reveals the presence of oxidation debris (highly defective, amorphous structure) in the remaining edges of the cap (pointed with arrow for clarity). The origin of this debris cannot be confirmed whether it is the result of catalytic or non-catalytic oxidation or consecutive process of both during the treatment.

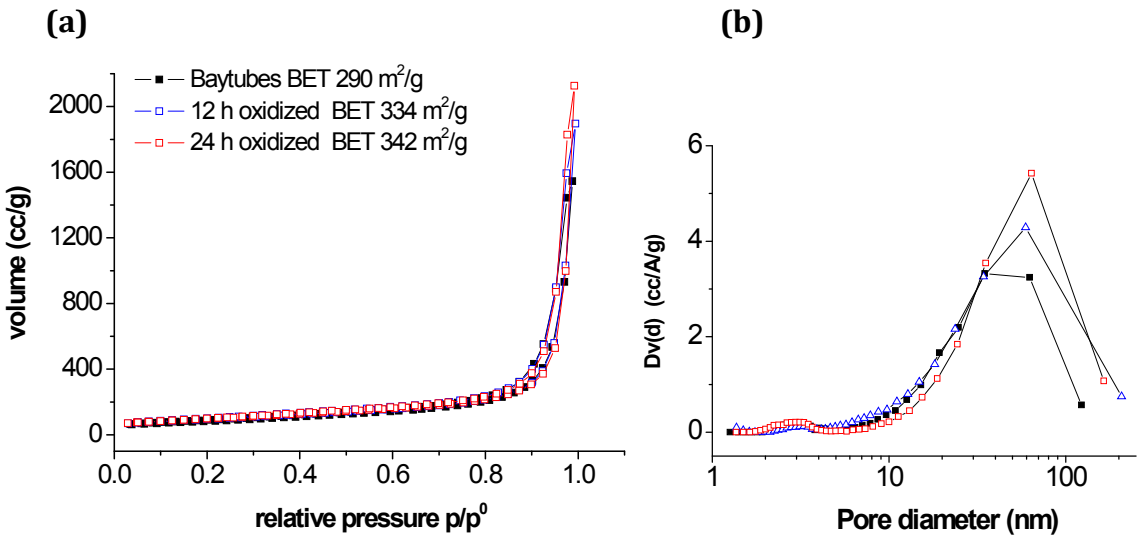

Figure 6-7. N_2 adsorption isotherms profile (a) and pore size distributions calculated from the BJH method (b) of Baytubes samples before and after air-oxidation at 400°C.

The 12 h oxidation treatment resulted in the decrease of pyrolytic carbon and defective CNTs amount from the Baytubes sample. However based on TEM observation, minute amount of oxidation debris (Fig 6-6c) was also detected in the oxidized sample. Aside from the removal reactive carbons such as pyrolytic carbon and defective CNTs, the loss of contact between catalyst and CNTs also contribute to

increase in the oxidation stability. These effects contribute to the increase in energy of activation as shown in the TG profile (Fig 6-5a & b).

CNT shortening as a result of combustion is revealed by the evolution of the N_2 isotherms after the oxidation treatment (Fig 6-7). The CNT shortening should create voids within the CNT network. The shape of the hysteresis in the isotherm and the pore size distribution plot suggested more open CNT entanglements after the oxidation treatments. As the Baytubes sample was only mildly fluidized by the swinging reactor, the treatment is not expected to create re-dispersion or re-distribution of the CNTs that would modify the entanglements.

It is reported that the strain caused by the high curvature of the graphene sheet in small diameter CNTs can be a dominant factor for the initiation of oxidation.[12,13] In contrast to that argument, TEM images of the oxidized Baytubes sample show small diameter of CNTs with only minimum signs of oxidation. There are no pits, holes[10], and visible thinning[14,15] observed in the treated sample. The diameter distribution of the CNTs measured from TEM images, however, reveals a shift to lower value suggesting wall-thinning pathway for the non-catalytic CNT combustion (Fig.6-8).[15] This observation points out that for the Baytubes sample the initiation of combustion is not limited to high strain sites such as tips, bending and small curvatures but is more preferably to start at structural defects in the CNTs. Structural defects, prismatic edges and pyrolytic carbon present on the CNT surface are more susceptible towards combustion than the basal plane of defect-free CNTs.[16,17] Hence these sites can initiate the combustion and in the case of pyrolytic carbon can further create hotspots to propagate onto the graphitic CNT surface.[10]

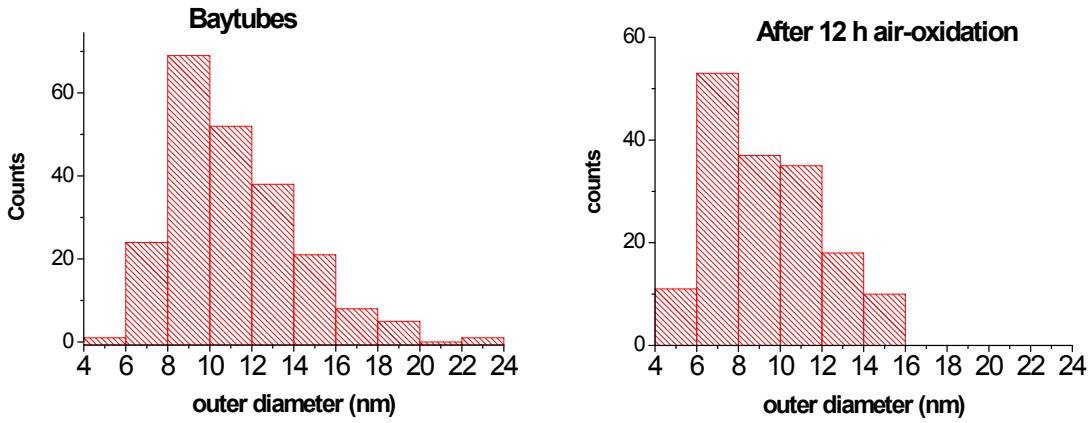

Figure 6-8. Diameter distribution of Baytubes CNT after 12 h of air-oxidation at 400 °C.

The bulk of the weight loss after the air-oxidation treatment can thus be attributed to the catalytic and non-catalytic combustion of CNTs. The high burn-off (~25 wt% and ~40 wt% for 12 h and for 24 h of treatment respectively) clearly suggest that the pyrolytic carbon cannot be the only carbon material being burned during the oxidation treatment. TEM investigation of the as-received Baytubes sample (Fig 6-1) demonstrates that the pyrolytic carbon coatings should not be as high as 25 wt%. With an exaggerated assumption of a uniform *monolayer* pyrolytic carbon coating of the CNT outer surface, the weight fraction is only ~8 wt% (Baytubes BET surface area 288 m^2/g from N_2 isotherm, with benzene cross-sectional area of 0.423nm^2 and a monolayer adsorption onto the CNTs surface). Thus it is obvious that the bulk of the burn-off could not have originated from the combustion of pyrolytic carbon alone but also from the CNTs. The CNT combustion in the pristine Baytubes sample can occur through several pathways; from the combustion of the highly defective CNTs, initiated by the hotspots created by the combustion of pyrolytic carbon, and from the catalytic combustion of CNT by the metal impurities.

A similar experiment was also performed on the NC3100 sample at 400°C for 24 h. The NC3100 sample having less metal impurities and more graphitic character than Baytubes sample shows more stability towards the air oxidation. The TG analysis however showed insignificant changes in the oxidation profiles after the treatment (Fig 6-9a & b). The Raman spectra collected after the treatment exhibit

only a minimum change (Fig 6-9c). The width of D band after the treatment increases suggesting creation of defects after the treatment.

TEM investigations show less pyrolytic carbon on the CNT surface with no significant signs of wall thinning. TEM investigation also reveals that CNTs with small diameter are still stable after the oxidation treatment with only minimum signs of combustion even on the high strain sites. The total burn-off after the treatment is 20 wt%. There were however holes occasionally observed in the CNT projections from the TEM images as displayed in Figure 6-10c & d. The holes/pits created by the combustion have a uniform size in all layers. Successive and simultaneous gasification of all layers in the CNTs reflects the various defects present in the sample that can initiate the combustion.[10,4] It is plausible to argue that the holes are induced by hotspots from combustion of pyrolytic carbon, as other high strain sites in the CNT are still preserved. However the distribution of pits/holes does not correspond to the distribution of the pyrolytic carbon in the pristine NC3100 sample. TEM investigation shows no sign of tube shortening in the oxidized sample.

The treatment resulted in the decrease of micropore adsorption in the N_2 isotherm giving lower surface area (Fig 6-11). The capillary condensation however increases after the treatment. The increase can be attributed to the loosening of CNT entanglement and/or the opening of the CNT hollow channel as the result of the oxidation. However pore size distributions in Fig 6-11b reveal the formation of mesopores in the range of 2-4 nm and a removal of the pores in macropore region. The mesopore region nicely fits with the CNT hollow channel and the size of the holes observed in the TEM images. Thus, TEM and N_2 isotherm investigations are in agreement suggesting the creation of pits and holes in the CNTs as a result of oxidation. There is no strong evidence of CNTs shortening that would result in the observable change of entanglement. The different response of combustion in the CNT microstructure and texture between Baytubes and NC3100 is a clear reflection of their structural differences.

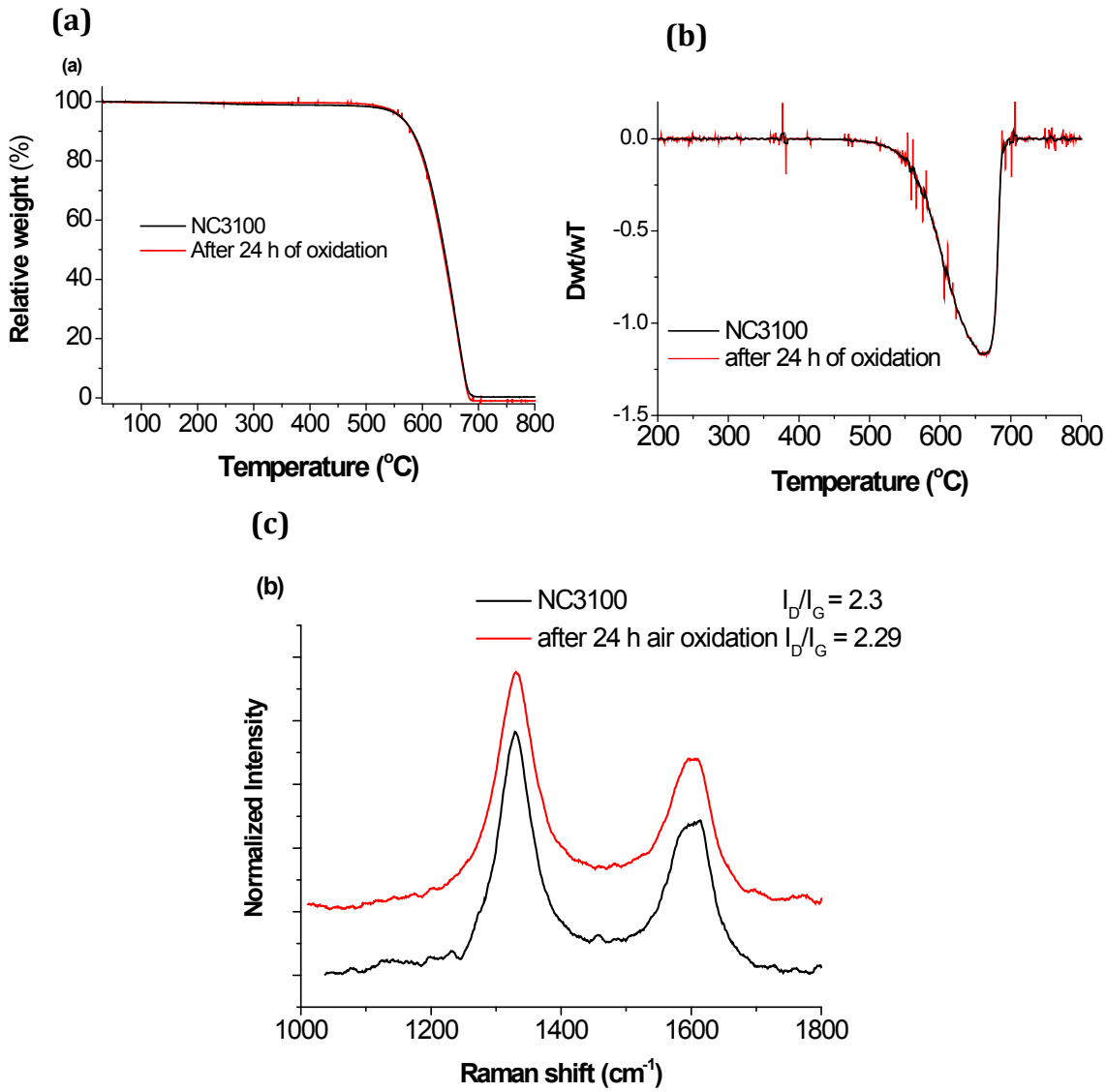

Figure 6-9. TG, DTG oxidation profiles (a, b) and Raman spectra of NC3100 CNT before and after air oxidation treatment at 400°C (c). The Raman spectra are normalized with respect to the D band.

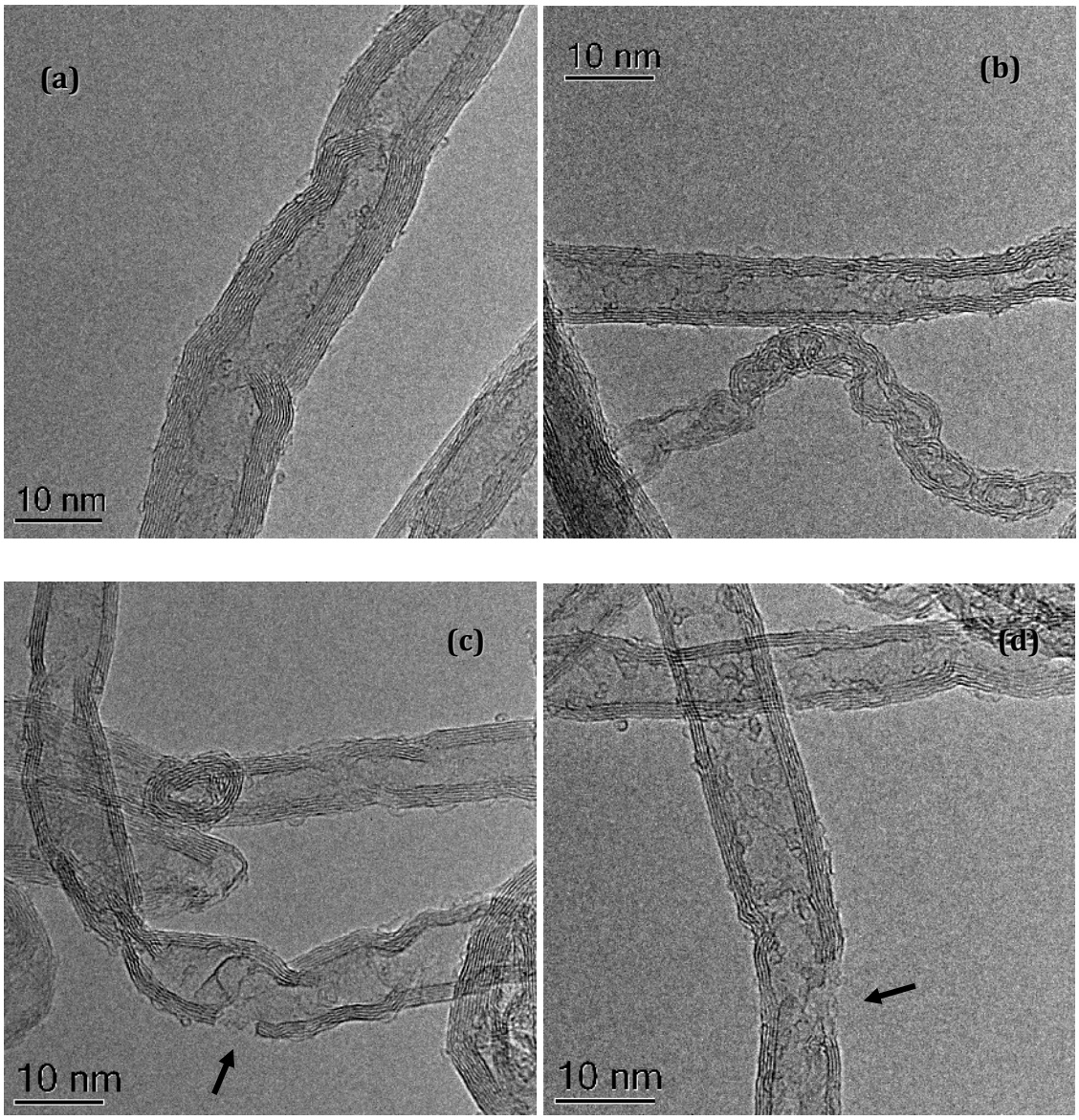

Figure 6-10. TEM images of NC3100 CNTs after 24 h air-oxidation at 400^{o}C.

The differences can be attributed to different distribution of structural and topological defects in the CNTs of each sample. In addition there may be a possibility that the pyrolytic carbon present in the two samples have different microstructure that reflects different chemical reactivity towards oxidation. Selective oxidation by air creates significant loss of the CNTs although it removes some pyrolytic carbon. Thus a more moderate and controllable method is required to achieve selective and efficient way to remove the pyrolytic carbon impurities from the CNT surface.

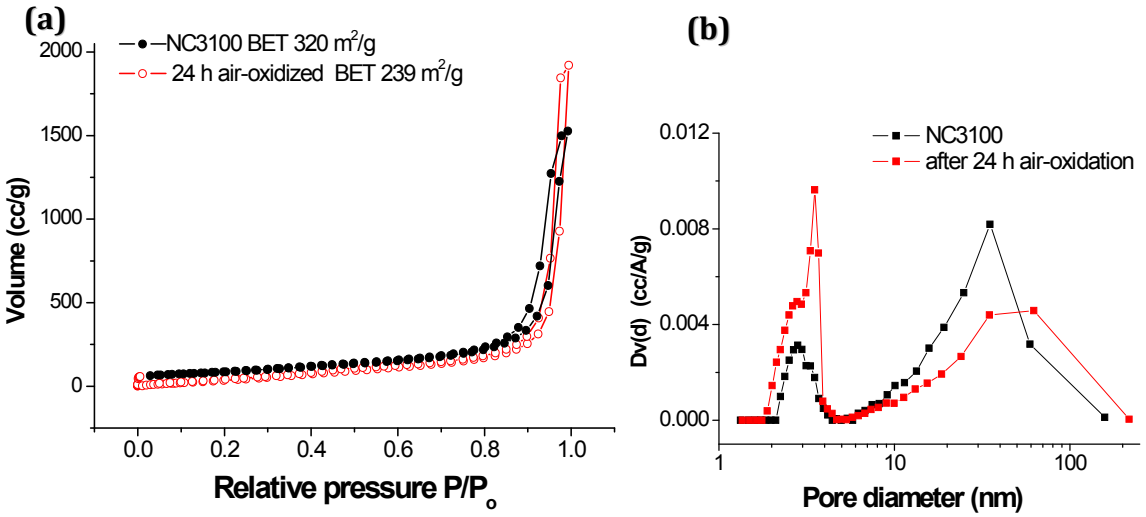

Figure 6-11. N_2 adsorption isotherm profiles of NC3100 samples before and after air-oxidation at 400°C.

6.2.3 Mild oxidation with HNO_3

Treatment with HNO_3 is a common method to remove metal and pyrolytic carbon impurities from CNT samples.[18,19,20] HNO_3 treatment is also frequently used to functionalize CNTs to improve CNT dispersion in polar solvents and provide anchoring centres for metal salts precursors in catalyst support applications. [21,22,23]

Often the conditions applied for the purification and/or functionalization of single-walled and multiwalled CNTs with HNO_3 were harsh, involving boiling and concentrated solutions. Previous authors have highlighted the issue of oxidation debris as a result of over oxidation from HNO_3 treatment.[19,24] Hence optimum/mild HNO_3 treatment condition and careful investigation are prerequisite to the removal of thin layer pyrolytic carbon deposits on CNT samples and to avoid/minimize oxidation debris. Based from previous investigations performed on Baytubes sample, it is reasonable to consider that the highly defective CNTs have comparable reactivity as that of pyrolytic carbon.

1 g of CNT sample was mixed with 400 mL of 3M HNO_3 for 24 h at room temperature under mechanical stirring at 400 rpm. The suspension was filtered and further washed with 3M NaOH for 2 h. The suspension after NaOH washing was

again filtered and the black solid was put in a thimble. The thimble was then installed inside a soxhlet system for sequential washing with water and acetone for 24 h each.

After 6M and 3M HNO_3 treatments the Baytubes samples demonstrate an increase in oxidative stability as depicted in the TG profile (Fig 6-12). The ash content of the sample decreased after the acid treatment. 60 wt% of the metal impurities was removed by 3M HNO_3 while complete removal was achieved by 6M HNO_3 treatment. It has been reported previously that the treatment conditions such as duration, concentration and temperature determine the effectiveness of the removal of catalyst particles. [19,20,25] The increase in oxidation stability can then be attributed to the removal of metal catalyst impurities and/or removal of reactive carbon materials, e.g., pyrolytic carbon. One can observe the evolution of the sample's oxidation profiles after HNO_3 treatments in the DTG peaks presented in Fig 6-12b. They suggest that the improved oxidation stability is a combination of less defects sites and higher energy of activation as a result of the treatment. The shift of the oxidation onset in the HNO_3 -treated Baytubes can be attributed to the decrease of number of available defects for combustion. Whereas the change of the TG curve slopes especially after 6M HNO_3 treatment is the result of higher activation energy, presumably due to ash removal and/or removal of reactive carbons. Thermal analysis suggests that the treatment removes some highly defective carbons and also resulted in the gradual removal of metal catalyst. There is already a slow weight loss at $<400^{o}C$ due to the decomposition of surface functional groups as a result of acid treatment. This initial weight loss is proportional with the acid concentration applied (inset Fig 6-12a).

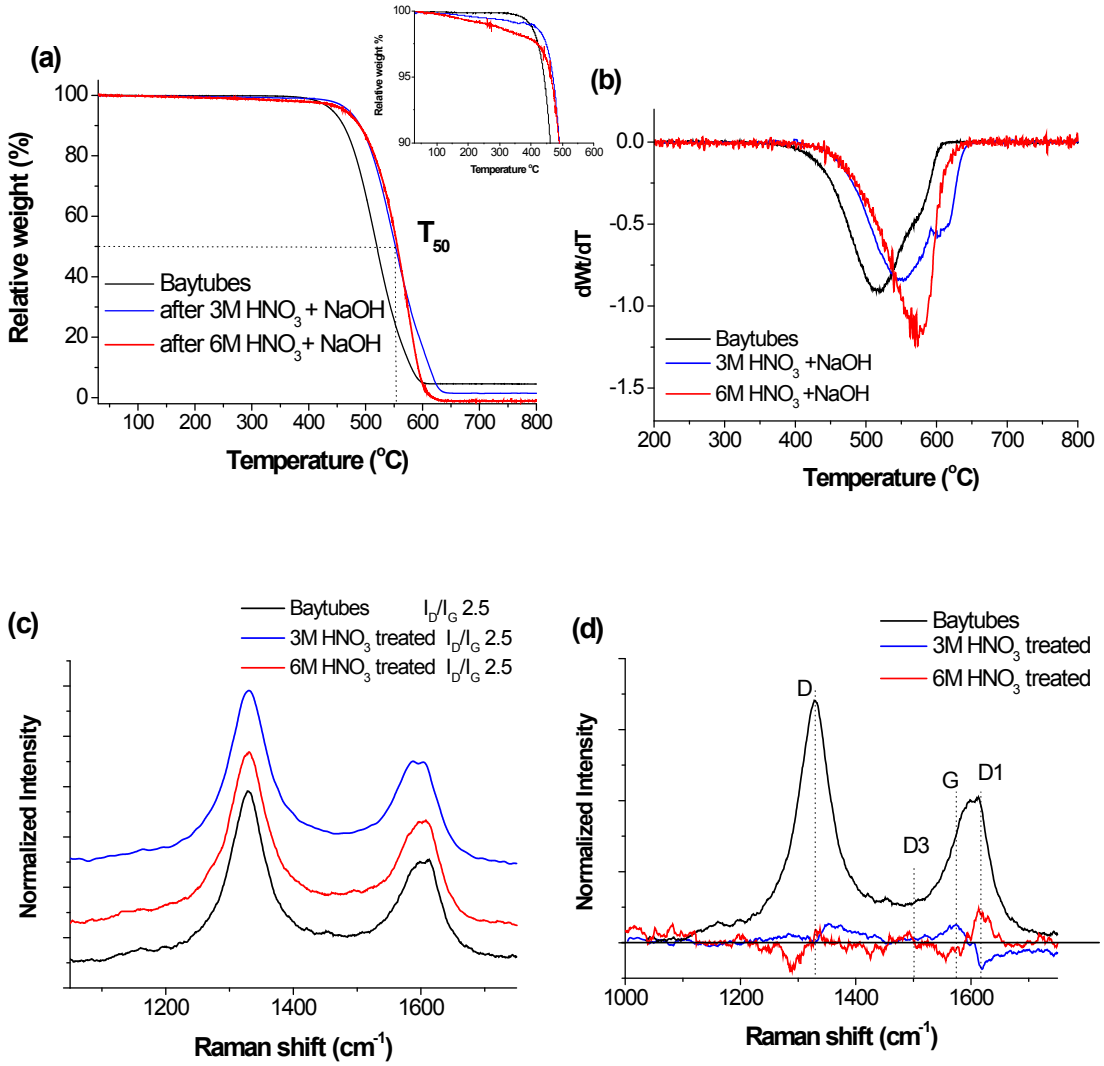

Figure 6-12. Oxidation profiles (a&b) and Raman spectra (c&d) of Baytubes CNT before and after HNO_3-NaOH at 25°C. The Raman spectra are normalized with respect to the D band.

An overview of TEM images in Figure 6-13 show that the HNO_3-treated CNTs have cleaner /smoother surface, almost free from the single or multi layer pyrolytic carbon. Raman spectra show the decrease of D1 peak and increase of G and D peaks after 3M HNO_3 treatment. On the contrary after 6M HNO_3 the G peak decreases while the D1 peak increases. Raman and TG investigations indicate that the treatment with 6M HNO_3 resulted in a more surface modification (damage) than 3M HNO_3. Diameter distribution measurements of the sample after the HNO_3 treatment reveal slight shift to lower values, pointing to thinning of the CNT as a result of oxidation (Fig 6-14). The complete loss of metal impurities after 6M HNO_3 is

compensated by the creation of more defects and thus moderating the oxidation stability of the sample.

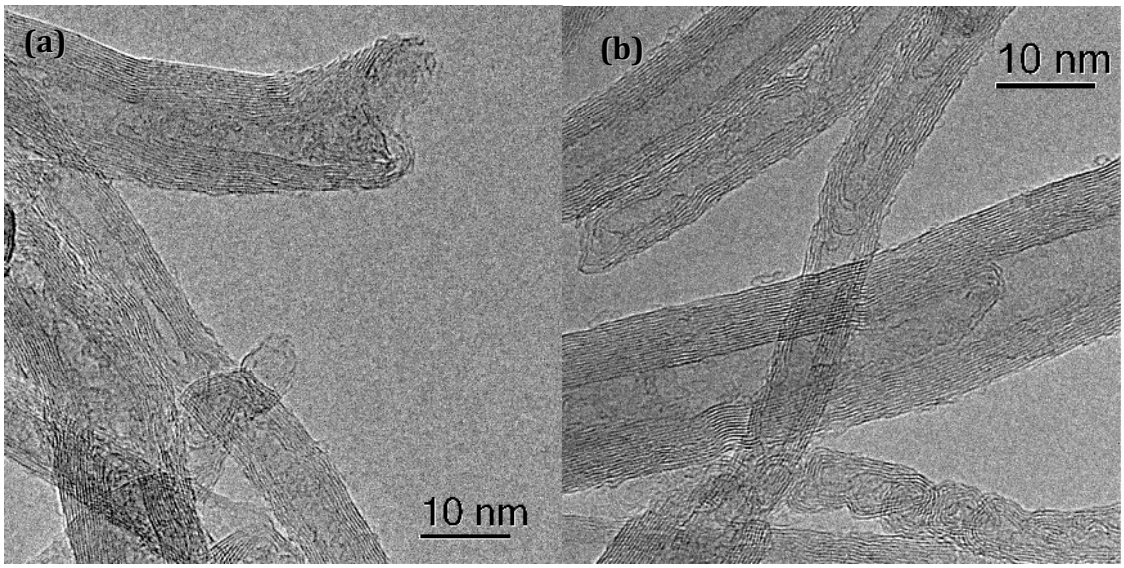

Figure 6-13. TEM overview images of Baytubes CNT after 6M (a) and 3M HNO_3 (b).

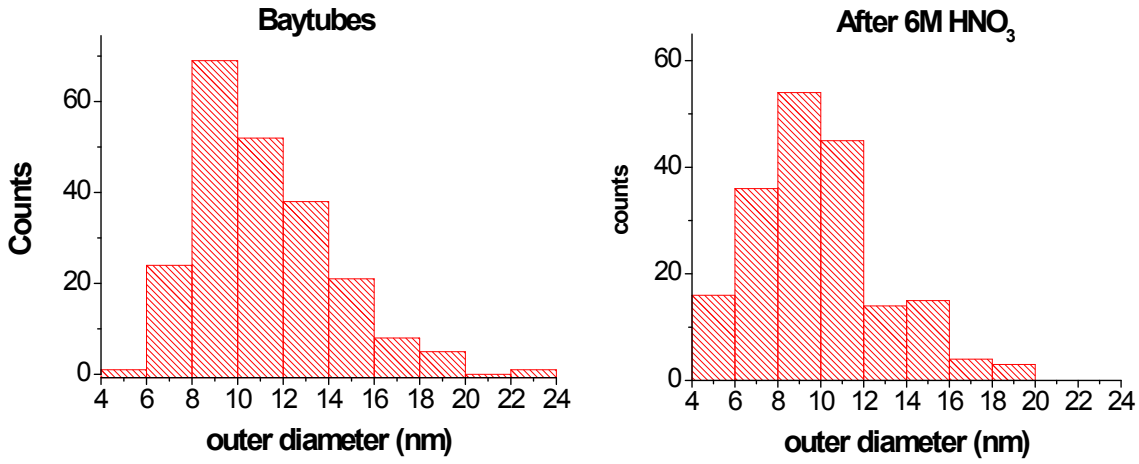

Figure 6-14. Diameter size distributions of as-received Baytubes CNTs and after HNO_3-NaOH treatment.

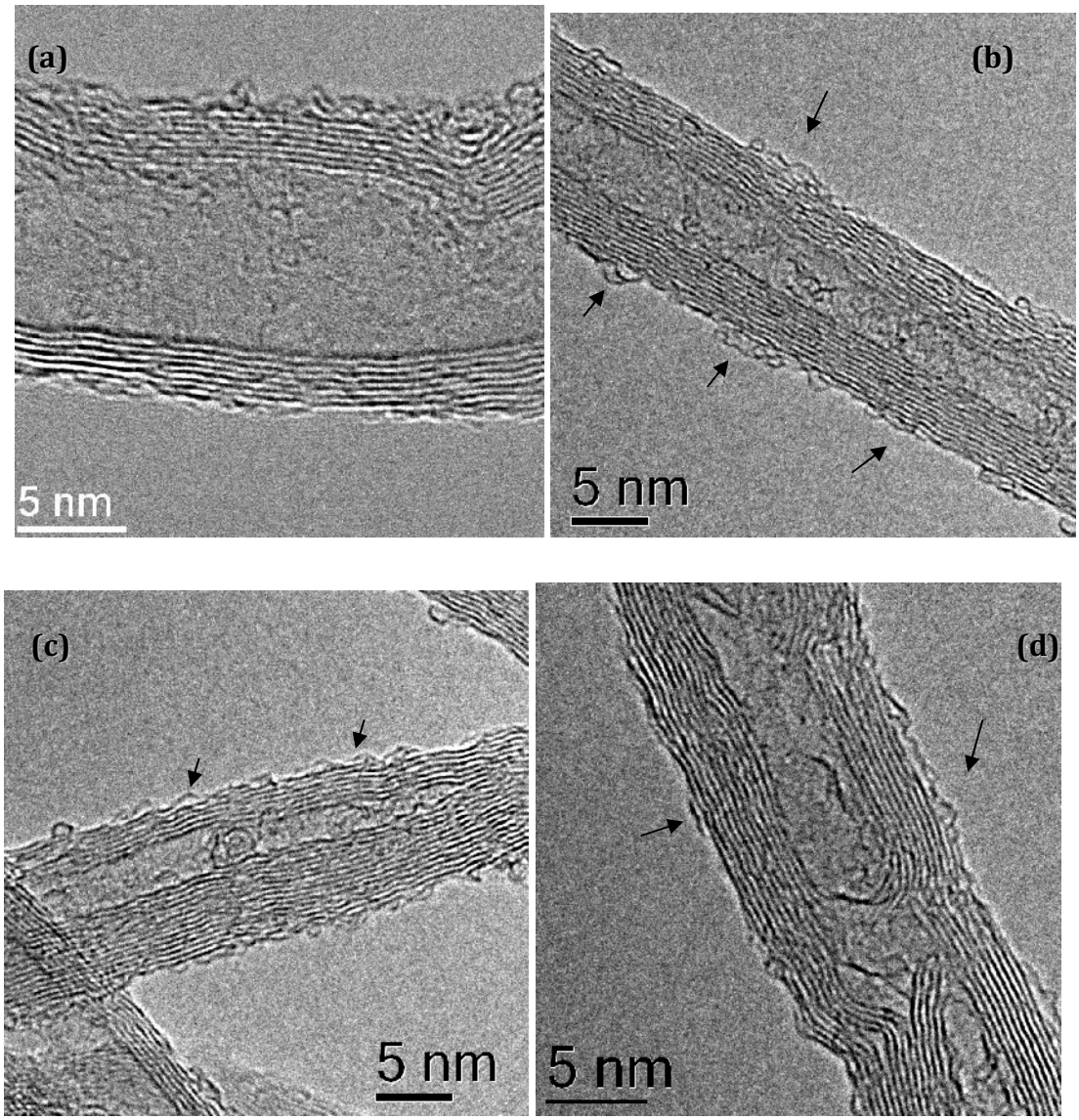

Figure 6-15. TEM images of as-received Baytubes CNTs (a) and after 3M HNO_3 at 25°C (b-d). Arrows point out the bent/curved prismatic edges and short graphene layer as a result of over oxidation of the CNT surface.

Careful TEM observation however points out the presence of various structural modification or damage to the CNT surface after the treatment with 3M HNO_3 (Fig 6.15). Most of the prismatic edges in CNTs are curved/bent, inclined from the flat basal plane. Short single graphene layers of ~ 2 nm in length still attached to the CNT are also observed (Fig 6-15b & d). The appearance of such graphene fragments is a strong indication of the extensive oxidation of the CNT surface under the mild treatment. The short graphene layers is also indicative to the gradual wall

thinning of the CNTs as observed in the diameter distribution measurements in Fig 6-14. The focus of TEM investigation in Fig 6-15 is for the treatment with 3M HNO_3. Hence as suggested earlier with a more aggressive HNO_3 treatment, the damage to the CNTs' microstructure especially to the surface will be more severe.

In agreement with TEM investigation the TPD profile of the Baytubes samples was modified after mild 3M HNO_3 treatment suggesting chemical and structural modifications to the CNT surface (Fig 6-16). The amount of surface functional groups decomposing as CO and CO_2 doubles after the acid treatment (Tab 6-1 and Fig 6-16).

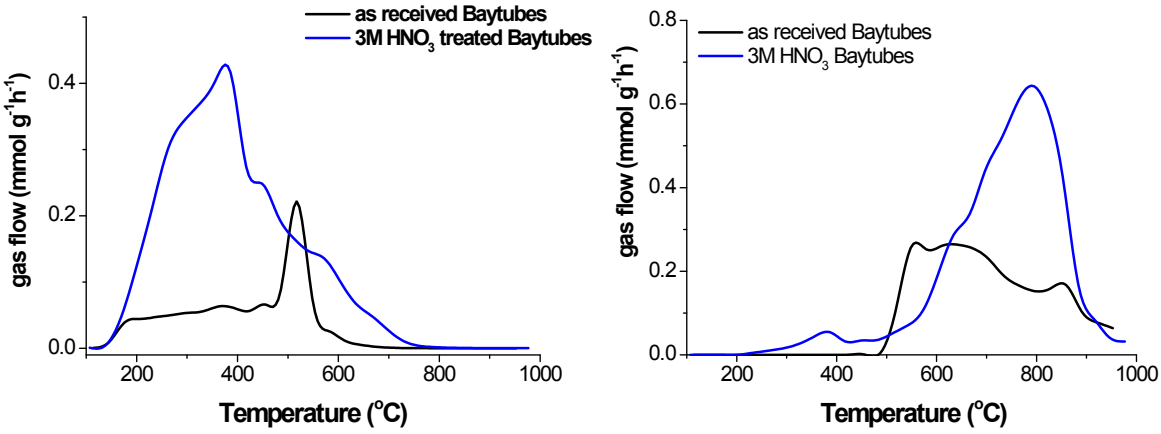

Figure 6-16. TPD of Baytubes before and after HNO_3 treatment at 25°C for 24 h; CO_2 signal (a) and CO signal (b).

The TPD signals can be tentatively assigned to different surface functionalities by comparison from the data reported in the literature.[26, 27,28]

The effect of the HNO_3 treatment is apparent in the desorption profiles. The spike for both CO_2 and CO is no longer observed for the HNO_3-treated samples. The acid treatment shows a clear maximum at 380°C with a shoulder at 300°C. The first CO_2 peak can be ascribed to the decomposition of carboxylic acids. While the higher temperature CO_2 peaks at 450°C and 600°C can be the result of anhydrides ad lactones decompositions. The CO desorption is ascribed to anhydrides at 400-450°C, phenols, hydroquinone at 600-700°C and carbonyls, quinones at 800-900°C.

Table6-1. Physiochemical properties of as-received, acid washed and sonicated Baytubes samples.

Sample Treatment	solvent	T_{50}[a] / C	I_D/I_G	Ash content / wt%[a]	CO_2 released[c] / mmol g^{-1}	CO released[c] / mmol g^{-1}
pristine	-	519	2.58	4.3	0.051	0.155
ultrasonic 1 h	water	538	2.45	3.54	0.098	0.244
ultrasonic 2 h	water	545	2.40	3.6	0.097	0.246
ultrasonic 3 h	water	550	2.20	0.037	0.097	0.247
3M HNO_3-NaOH	-	553	2.47	1.48	0.159	0.256
ultrasonic 2 h	water	571	2.64	1.47	0.121	0.195
ultrasonic 3 h	water	585	2.30	0.77	0.136	0.197
ultrasonic 2 h	Ethanol		2.56	1.7	0.138	0.326
ultrasonic 2 h	THF		2.44	2.5	0.13	0.336

The degradation products from the HNO_3 treatment were detected in the filtrate by UV-Vis and FTIR spectroscopic analyses. UV-Vis spectra in Fig. 6-17a show strong and broad absorption in the range of 200–350 nm. This observation is consistent with previous studies on carbon black. Here, the treatment with concentrated HNO_3 resulted in the dissolution of polynuclear aromatic compounds rich in functional groups.[8] Stretching vibrations of aromatic C=C and C=O bonds were also detected in the FTIR spectra of the filtrate in the present study (Fig 6-17b-c). The filtrate from HNO_3 treatment throughout the entire period is clear and colourless.

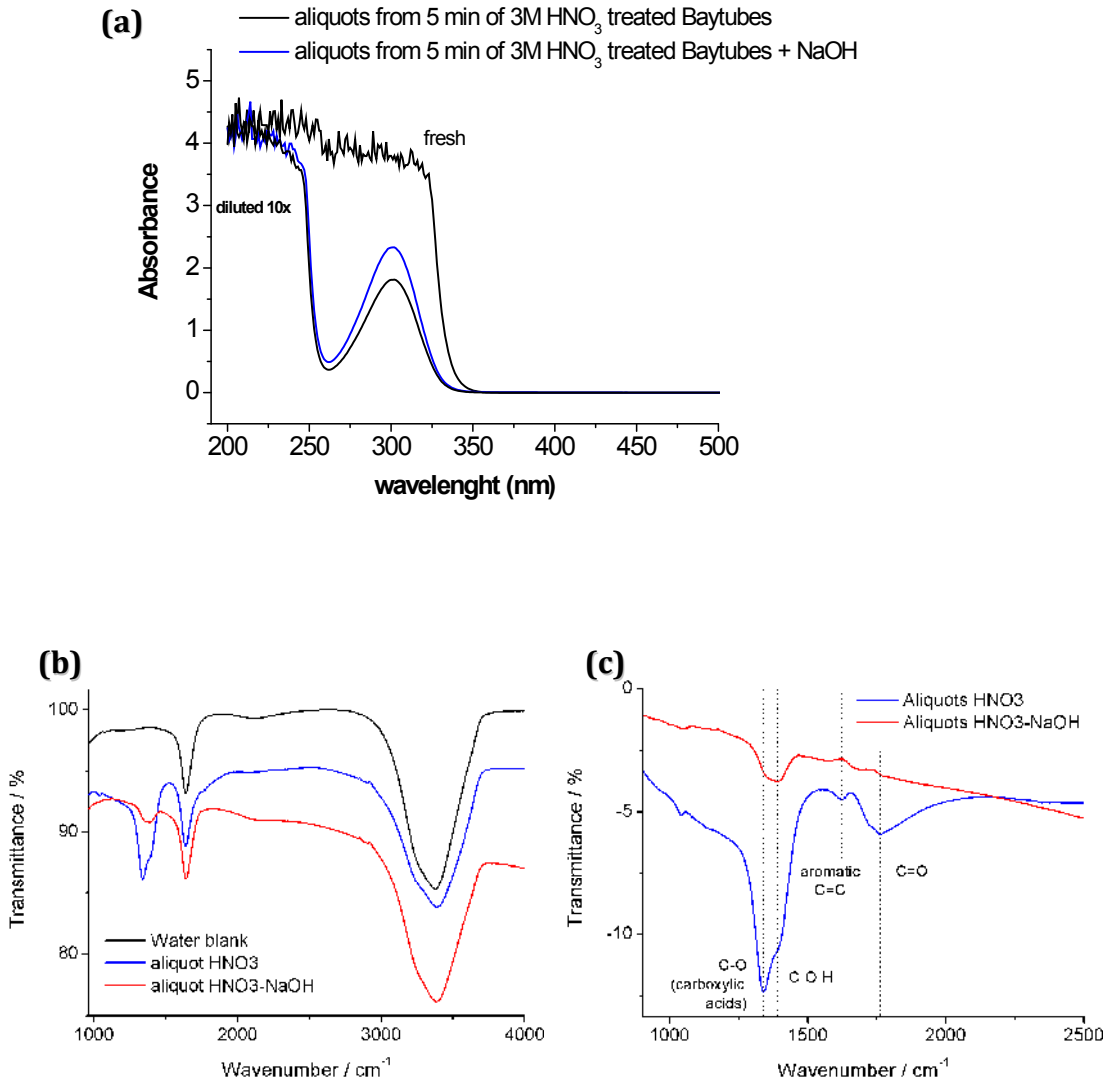

Figure 6-17. UV-Vis spectra (a), FTIR spectra (b) of aqueous solutions collected after filtration of the 3M HNO_3 and successive NaOH treatments; (c) difference FTIR spectra with water.

In this work it is shown that the mild HNO_3 treatment removes some pyrolytic carbon by oxidation and also extensively oxidizes the CNT surface resulting in surface damage and the dissolution of functionalized polyaromatic fragments. The remaining pyrolytic carbon and the new defects sites created by the HNO_3 treatment contribute to the surface functionalization of the sample. The remaining disordered carbons can be attributed to original pyrolytic carbon and/or from the oxidation debris as a result from the over oxidation of the CNTs. The damage in the carbon surface microstructure is clearly apparent for the HNO_3-treated sample. As a

comparison the air-oxidation treatment with significant sample burn-off however resulted in a smoother and cleaner CNT surface. The advantage of HNO_3 treatment over the air-oxidation treatment is the minimum loss of sample with respect to the removal of impurities. However, severe surface damage caused demand a post treatment, e.g. annealing in inert atmosphere to heal these defects.

Similar mild HNO_3 treatment was performed on the NC3100 sample. The treatment show slight decrease in the I_D/I_G value, this however can be due to errors from the fitting procedure. There seem to be some indication of removal of pyrolytic carbon. Nevertheless, similar to that from the Baytubes experiment, short graphene layer on the CNT surface is observed. This observation suggests that the treatment damages the CNT surface. Nevertheless the oxidation stability of HNO_3-treated NC3100 is still much better compared to HNO_3-treated Baytubes. This stability is very likely caused by the more graphitic and less pyrolytic content of NC3100 sample in comparison to the Baytubes sample.[3,29]

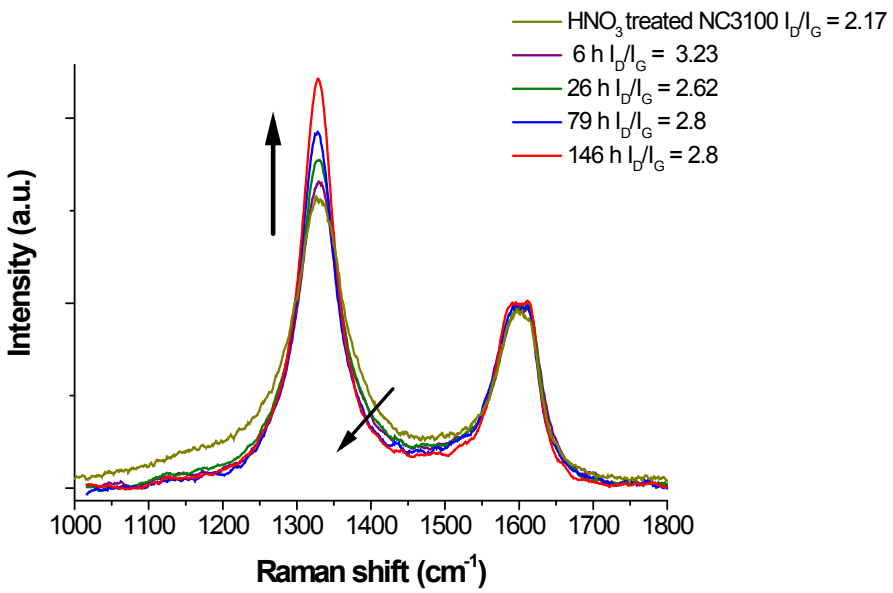

Figure 6-18. Raman spectra of HNO_3-treated NC3100 after combustion at different time, intensity normalized at the G-band.

Long term study of NC3100 combustion with 20% O_2/He was performed to investigate the oxidation stability and to monitor the microstructural evolution of this material. The oxygen conversion was kept below 3% to avoid thermal runaway and autocatalytic of the combustion process. The combustion experiment was frequently interrupted for Raman and TEM investigation after 7, 26, 79 and 146 h.

During the first 7 h time on stream a peak sharpening of the D band can be observed which indicates the initial cleaning of the CNT from pyrolytic and/or oxidation carbon debris (Fig. 6-18). After this process the peak width remains constant, however, the D band intensity increases relative to the G band pointing at the continuous generation of defects and the stepwise degradation of the graphitic CNT structure during oxidation.

The structural transformation is well confirmed by TEM analysis. Fig. 6-19 illustrates the structural damage inflicted on the CNTs as a result of combustion. The discontinuity of the graphene fringes in the TEM micrographs represents the most obvious indication of combustion in the CNTs. The formation of pits and wall thinning are frequently observed. It is reported that sites with topological defects such as the caps contain bond strain and thus are more reactive towards oxygen attack than smooth graphene walls along the CNT axis.[11] However, from the TEM micrographs it is evident that this cannot be generalized for this sample. After the first 7 h of combustion some CNTs still retain the close cap structure and some oxidation pits are located away from the topological defect site (Fig. 6-19a & b). These observations point out that the initiation of the combustion is not limited to the strongly curved sites such as tips and bendings but is also located at the (defective) cylindrical regions of the CNTs.[30] Oxidation carbon debris, steps and prismatic edges present at the CNT surface are more susceptible towards combustion than the basal plane of defect-free CNTs. Hence these sites can initiate the combustion and create hotspots to propagate to the graphitic CNT surface.[10]

In addition the broad distribution of topological and structural defects in the CNTs with varying diameters are very likely to contribute to the various combustion patterns observed in HNO_3-treate NC3100 CNT samples. At least there are three

distinct combustion propagation modes observed in the oCNT sample: (i) layer-by-layer mode resulting in thinner CNTs (Fig 6-19g), (ii) successive formation of pits in each graphene layer giving smaller holes in deeper layers (Fig 6-19e), and (iii) formation of pits with uniform size in all layers (Fig 6-19f). Successive and simultaneous gasification of all layers in the CNTs reflects the various defects present in the sample that can initiate the combustion.[10]

The typical combustion features in the carbon microstructure become more obvious after the longer period of combustion. Here, pit holes of varying sizes are observed on the CNTs together with indications that oxidation debris is formed as the combustion progresses (Fig 6-19i).[31] The TEM analysis does not allow to distinguish whether the disordered structures attached to the CNTs surfaces originate from the highly oxidized graphene layers as oxidation debris or from remaining pyrolytic carbon. However, the presumption that pyrolytic carbon has a higher reactivity towards oxygen than the graphitic basal plane clearly points out that the disordered carbon deposits (oxidation debris) are intermediates of CNT combustion. Thus these controlled-combustion experiments demonstrate the limit for selective oxidation to remove the disordered carbon from the CNT surface.

At the sites where extensive combustion takes place, short remaining graphene stacks or unzipped graphene layers were also observed (Fig 6-19c, f & g). A trace amount of remaining catalyst particles attached to the edges of CNTs was also observed by TEM indicating their participation in catalytic combustion (Fig 6-19j).

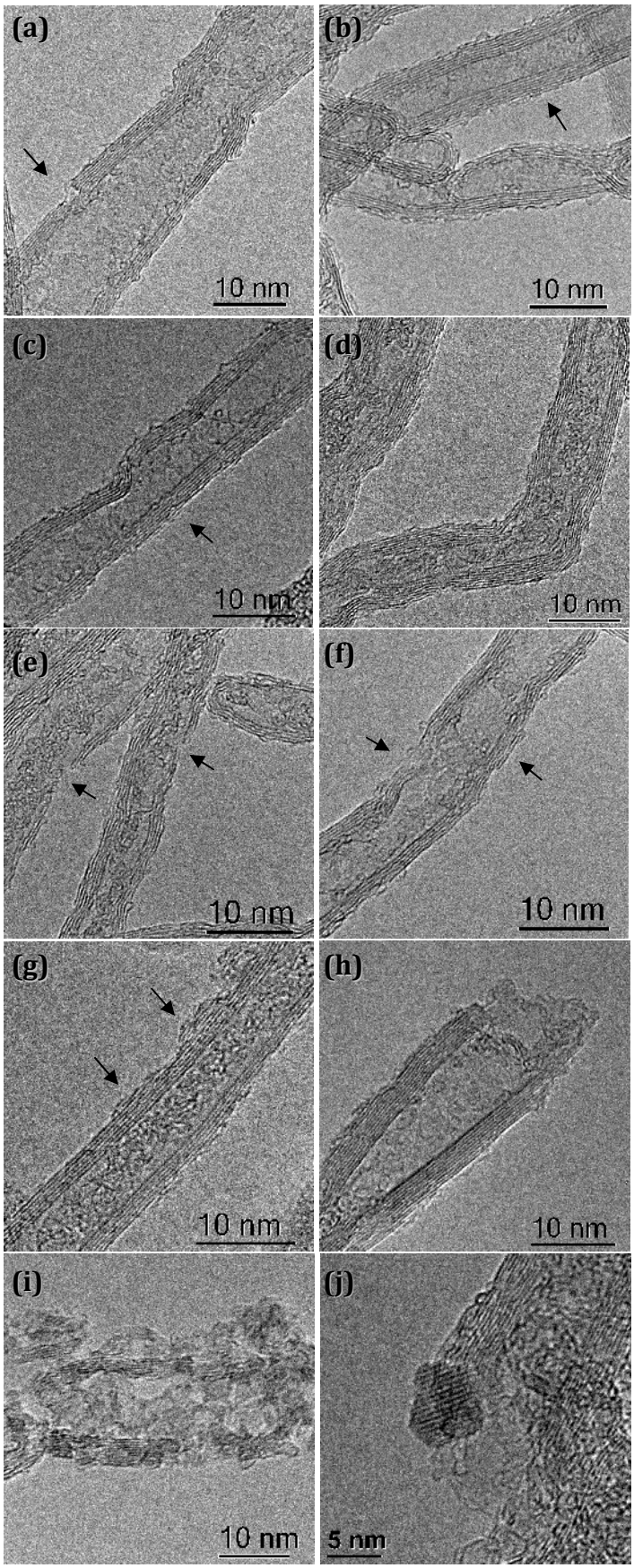

Figure 6-19. TEM images of HNO_3-treated NC3100 after combustion for 7 h (a, b), 26 h (c, d), 79 h (e, f) and 146 h (g-j).

6.2.4. Ultrasonication treatment

In the case of carbon materials ultrasonic irradiation has been utilized for the preparation of nanocarbons e.g. the preparation of carbon nanosheet from carbon black and graphene nanoribbon from exfoliated graphite.[32,33] The synthesis C_{60} by ultrasonic irradiation of liquid benzene was reported by Katoh et al.[34] Recently a novel method to prepare CNTs by ultrasonic irradiation on the mixture of aromatic hydrocarbons and catalyst have been reported. [35]

In a paper by Cataldo it was shown that aromatics and naphthenic hydrocarbons undergo cracking and pyrolysis under intense ultrasonic irradiation. It was shown that the sonocation of benzene yields acetylene accompanied by insoluble dark coke-like matter.[36] Earlier investigations on the effect of ultrasonic irradiation to benzene reported the polymerization of benzene and formation of tars.[37,38] It is suggested that the carbonization of the aromatic hydrocarbons to occur inside the micro bubble during the ultrasonic implosion that provided the extreme conditions.

Sonocation was mainly used as dispersing method and functionalizations in works involving CNTs.[39] The ultrasonic-assisted functionalization of CNTs with oxidizing agents such as HNO_3 or H_2SO_4 was reported to improve the nanoparticles dispersion on the CNT support.[40] In the literature the functionalization of CNTs with ultrasonic irradiation involves the creation of oxygen functional groups, *in situ* polymerization and attachment of organic molecules onto the CNT surface.[41,40,42,43]

It is reasonable to assume that depending on the ultrasonic irradiation condition the extent of damage caused to the CNTs will vary. High-energy ultrasound was reported to have caused severe damage to the CNTs such as tube shortening, striping of the outer graphitic layer resulting in CNTs wall thinning.[44,45] The microstructure of CNTs will also play a role in the final functionalization or damage caused by the ultrasonic irradiation.

Within the context of removing pyrolytic carbon from CNT surfaces, the ultrasonic irradiation will provide acoustic streaming and jet pulses onto the CNT

surface that would potentially allow the loosely attached amorphous carbon to detach from the CNT surfaces. With the radicals produced as the result of sonolysis of water (scheme 6-1), the pyrolytic carbon attached on the surface and the ones already detached can be further oxidized. In addition with the presence of dissolved O_2 the radical can react to produce peroxyl radical (scheme 6-2). The preferred functionalization of defective carbons allow for the dissolution of oxidized pyrolytic carbon and/or the fragments from the pyrolytic carbon from the CNT surface. It is expected that the two effects of agitation and oxidation will have an effect in the removal of pyrolytic carbon from CNT surfaces.

$$H_2O = H\bullet + \bullet OH$$

Scheme 6-1. Sonochemical decomposition of water inside the microbubbles as the result of local high temperature and high pressure during the collapse of the bubbles.

$$H\bullet + O_2 = HOO\bullet$$

Scheme 6-2. The production of peroxyl radical from the reaction of hydrogen radical with dissolved oxygen.

The approach has been exploited in the environmental application of ultrasonic irradiation, where organic pollutants such as chlorinated hydrocabons aromatic hydrocarbons, and PAHs, were mineralized into CO_2, short organic chains and inorganic ions.[46,47] The contaminants destruction can proceed via pyrolysis and/or oxidation in the microbubbles and/or oxidation by radical species on the interface or outside of the bubble as a result of water sonolysis. Depending on the volatility of the organic contaminants the destruction will occur at different sites and will follow different pathways. A more volatile organic molecule will tend to be decomposed inside of the bubble.

6.2.4.1. Ultrasonic irradiation of Baytubes CNT

For the ultrasonic irradiation experiments the CNTs were suspended in a 10 vol% of ethanol/water solution. A probe-type Ultrasonic Homogenizer GM2200 (Bandelin) with the sound frequency of 20 kHz was used. The ultrasonic treatment was performed at 10% power in pulse mode with an active interval of 0.5 sec. The temperature of the suspension was kept constant at $0^{o}C$ in an icebath. The obtained solid was subsequently washed with warm 1 mol L^{-1} NaOH followed by Soxhlet extraction with water and acetone, respectively, each for 24 h.

The ultrasonic irradiation resulted in the gradual improvement of the oxidation stability as shown in Fig 6-20. The effect is clearly visible in the parallel shift of profile with sonication time. In the first hour T_{50} shifted $20^{o}C$ to higher temperature, followed by milder shift for the next following hours (Tab 6-1). The shift can be attributed to the decrease of active sites. However the steep slope of the TG profile especially after 1hour of irradiation suggests that energy activation may have also increased. After longer irradiation time the slope or the DTG peak shape almost bear a resemblance to that of pristine Baytubes with a shift to higher temperature. The ultrasonic irradiation also resulted in functionalization of the CNT surface observed from the initial wt loss at temperature $<400^{o}C$. The mild sonication treatment exhibits the ability to remove metal impurities from the Baytubes sample. To our knowledge this effect has not yet been reported in literature so far. Raman analyses presented in Fig. 6-20c & d demonstrate gradual improvement of the graphitic (G) signal after the treatments (lower I_D/I_G) which suggest the removal of disordered pyrolytic carbons. The D-band around 1320 cm^{-1} of the sonicated samples is slightly sharper than the pristine material and, especially after ultrasonic treatment for 3 h, the G-band located at around 1600 cm^{-1} appears slightly intensified. Thus the improvement in the oxidation stability of the treated samples can be attributed to the removal metal impurities and pyrolytic carbon.

The TEM show smoother surface with less surface damages in comparison

with sample after 3M HNO_3 treatment (Fig. 6-21). However there are still amorphous carbons observed even after 3 h of sonication as presented in Figure 6-21e. Fragments of small graphene layer were also observed for the sonicated sample but with fewer occurrences than that observed for HNO_3-treated CNT. The graphene fragments give the indication that the ultrasonic irradiation functionalize and damages the CNT surface (to a lesser extent than that of HNO_3 treatment).

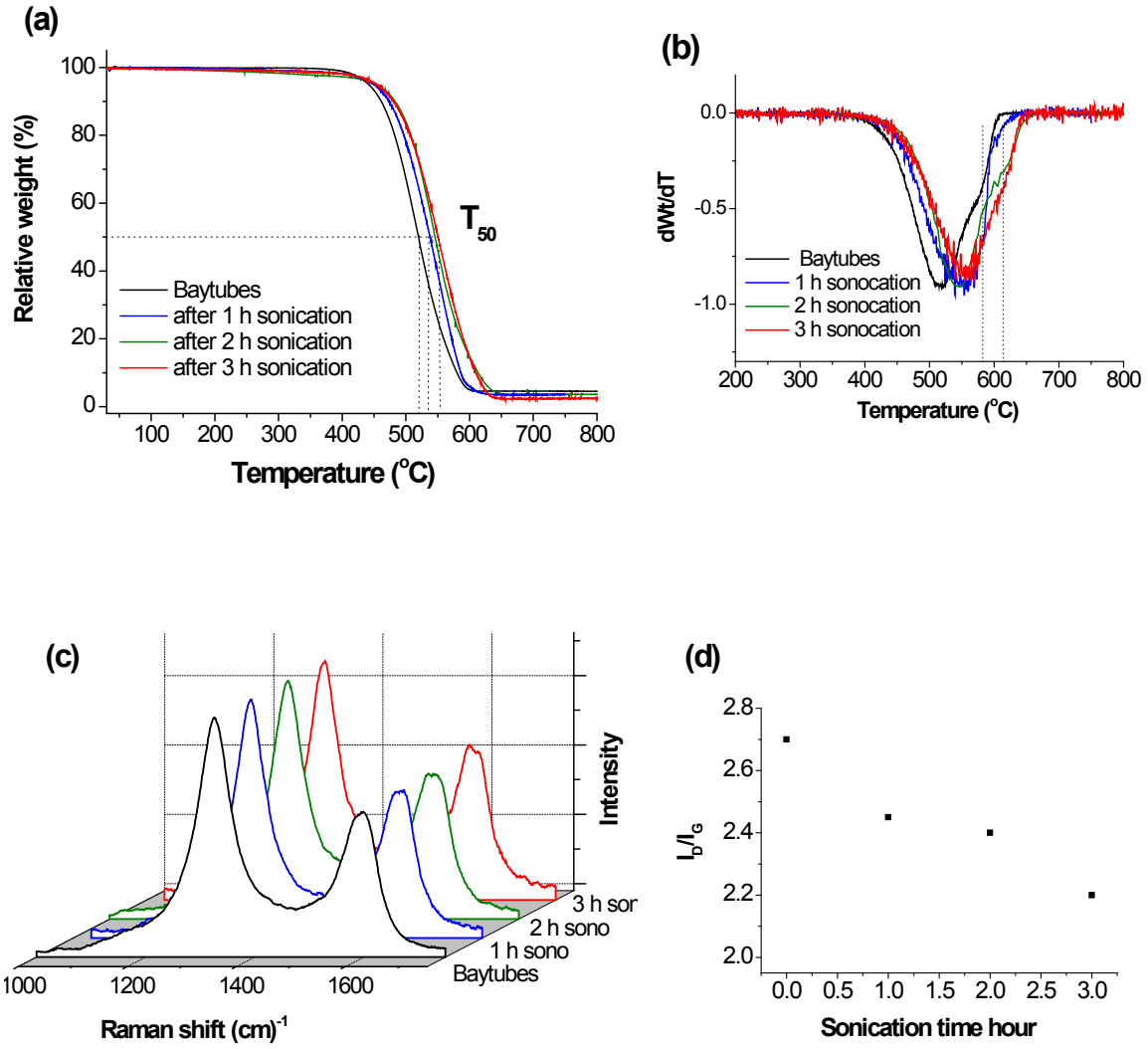

Figure 6-20. Oxidation profiles (a, b) and Raman analysis (c, d) of Baytubes CNT before and after ultrasonic irradiation in water. The Raman spectra are normalized with respect to the D band.

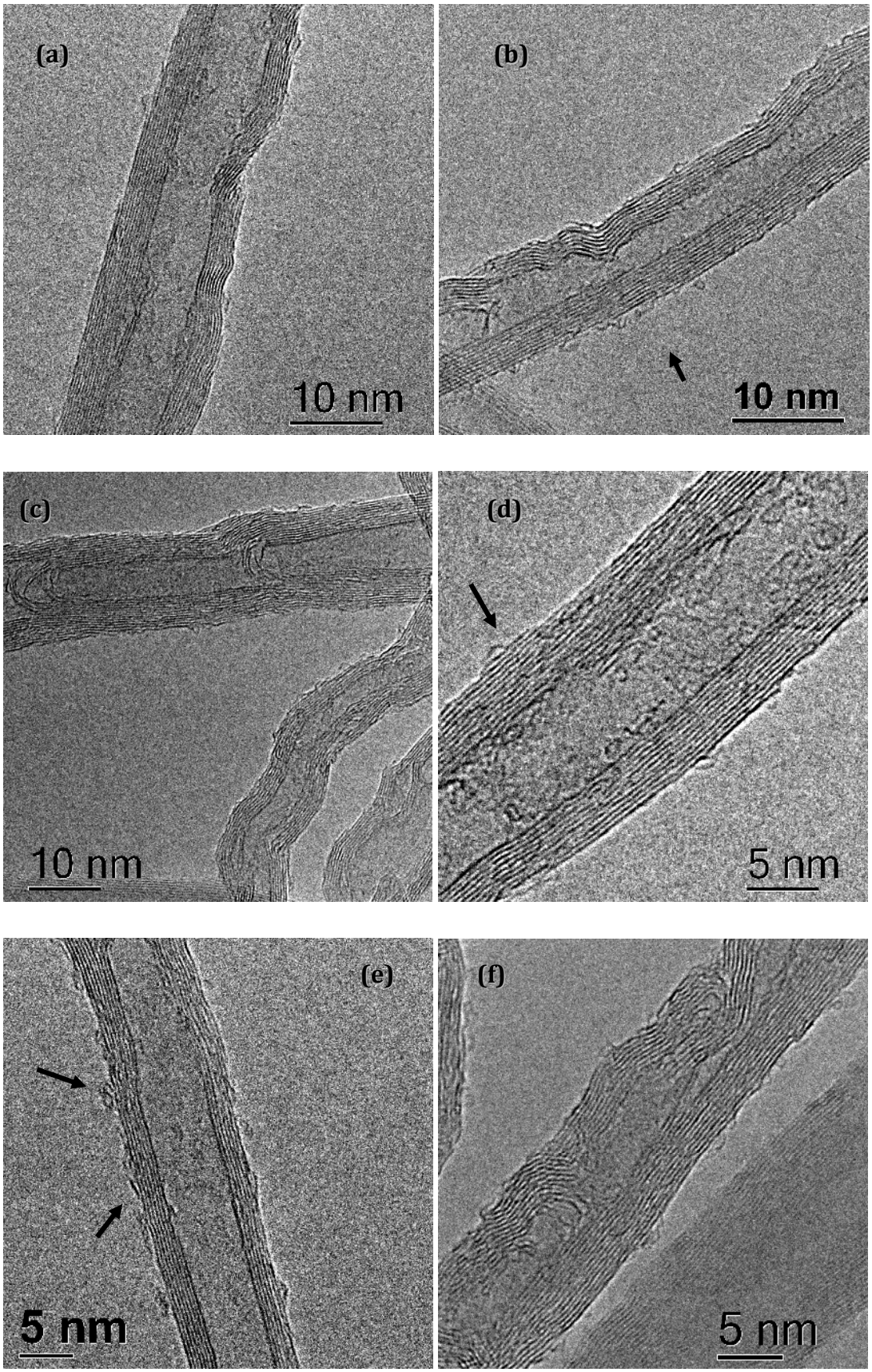

Figure 6-21. TEM images of Baytubes samples after sonication in water for 1 h (a,b) 2 h (c,d) and 3 h (e, f).

In contrast to mild HNO_3 treatment, the ultrasonic treatments avoid rigorous damage to the CNT surface while removing pyrolytic carbon as verified by TEM investigation (Fig. 6-21). The functionalization of the CNTs due to ultrasonic irradiation is moderate as compared to the HNO_3 treatment resulting in a modest increase in the amount of CO and CO_2 from TPD experiments (Tab 6-1 and Fig 6-22). The moderate oxidation process exerted from the ultrasonic treatment is demonstrated by the higher enhancement of CO amount as comparison to the CO_2 amount. The ultrasonic treatment preferably introduced functional groups of anhydrides, phenols and hydroquinones types. One can notice the difference of surface functionalization between the HNO_3-treated CNT and sonicated-CNT, where the former resulted in higher enhancement of CO_2 signal from carboxylic functionalities.

TPD experiments were performed with gas-phase analysis by MS and GC in parallel. Slight differences between the m/e 28 trace and the actual CO desorption profile for the sonicated samples indicate the presence of further species. Indeed the evolution of methane, ethane, ethylene, methanol, ethanol, acetone, and other hydrocarbons with and without functional groups were observed during the TPD of sonicated samples (Fig. 6-23). The intensity of these hydrocarbons increases with sonication time. Guittonneeau et al. performed ultrasonic treatment on aqueous suspension of graphite and observed graphite nanosheets, and dissolved organic compounds of narrow mass composition mainly of aromatics, alkenes, and carboxylic acids compounds.[48] The authors proposed a mechanism of graphite degradation by ultrasonic irradiation in water (Fig. 6-24). However it is very likely also that ethanol added in the CNT suspension contribute to the hydrocarbon functionalization during irradiation.

UV-Vis spectroscopy investigations were performed to analyze the aqueous filtrate after different sonication time (Fig. 6-25a-b) and from the subsequent NaOH and soxhlet treatments (Fig. 6-25c). The spectrum reveals absorption in the range of 200–350 nm with much lower intensity at higher wavelengths. The absorption is by far weaker than in the solution of HNO_3 treatment (Fig. 6-17a). The absorption is attributed to organic molecules of broad

possibilities such as PAHs, benzenes, alkenes and their derivatives as a result of destructive radical reactions and/or subsequent pyrolysis reactions under the extreme conditions.[46,47,49,50,48]

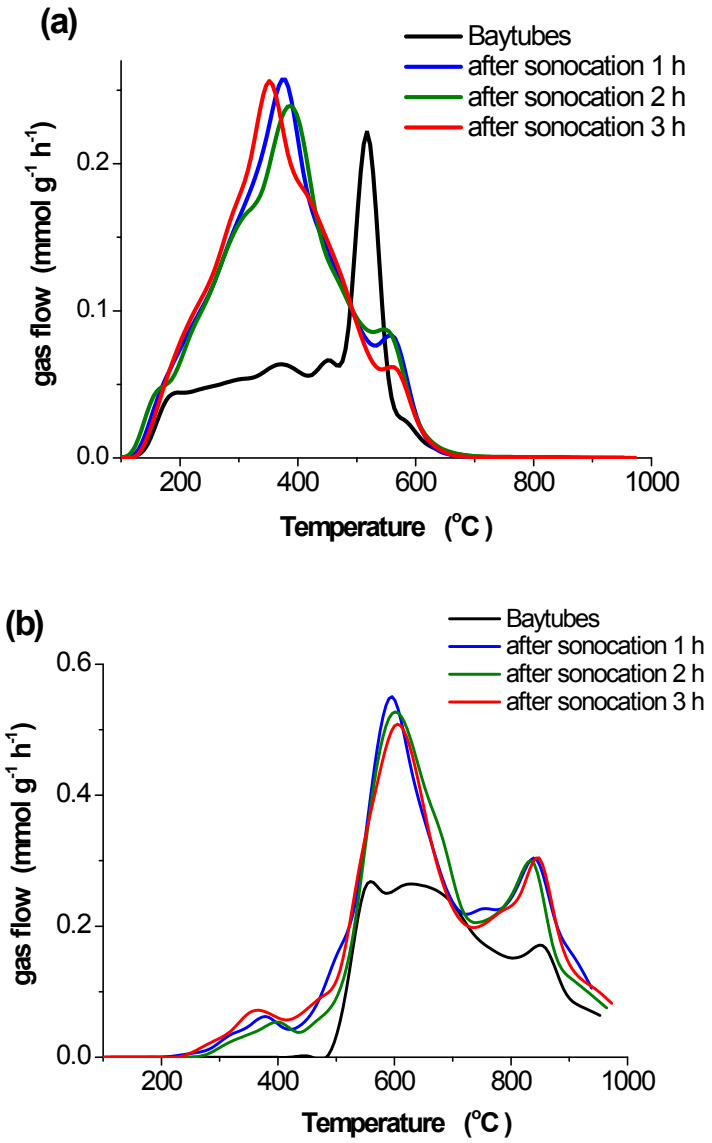

Figure 6-22. TPD profile of as-received Baytubes CNT sample and Ultrasonic treated samples in water; CO_2 signal (a) and CO signal (b).

In the first 10 min of ultrasonic irradiation the filtered solution show the highest absorption that continues to gradually decrease over time. Over the course of 3 h of irradiation the absorption occasionally increases again and continues to gradually decrease again. The decrease of the UV-Vis absorption

after ultrasonic irradiation suggests the decomposition of the dissolved compounds. The occasional increase of the absorption during the course of the ultrasonic treatment can be understood as the release of new organic compounds stripped off from the carbonaceous material into the solution. The TPD profiles demonstrate insignificant changes with sonocation time, suggesting that oxidation via OH radicals as a result of water sonolysis is not the dominant pathway (Tab. 6-1 and Fig. 6-22). The results suggest that the oxidation of CNTs is a rapid process and only took place at the beginning of the irradiation.

TEM investigation of the filtered aliquots after 3 h of irradiation revealed the presence of minute amount of carbon particles (Fig 6-26). Some of the carbon particles exhibit amorphous structure (Fig 6-26a & b) whereas some other exhibit graphitic fringes with twisted character (Fig 6-26c & d). The graphitic carbon particles support the argument that the ultrasonic irradiation stripped the CNTs. Indeed the particles looked like a cleaved, unwrapped CNT filaments. The amorphous particle may have originated from agglomeration of highly oxidized CNTs and/or pyrolytic carbon fragments. The presence of the carbon particles may have contributed the absorption in the UV-Vis region to fluctuate due to Mie scattering. However, these solid particles are so minute that it took great effort to find them in the TEM grid.

UV-Vis spectra in Fig. 6-25c show the dissolution of more organic compounds after NaOH and soxhlet washing treatments from the filtrate of CNT suspension irradiated for 150 min. The spectra strongly suggest the importance of the NaOH treatment to further dissolve organic compounds and/or carbon fragments from the sample.

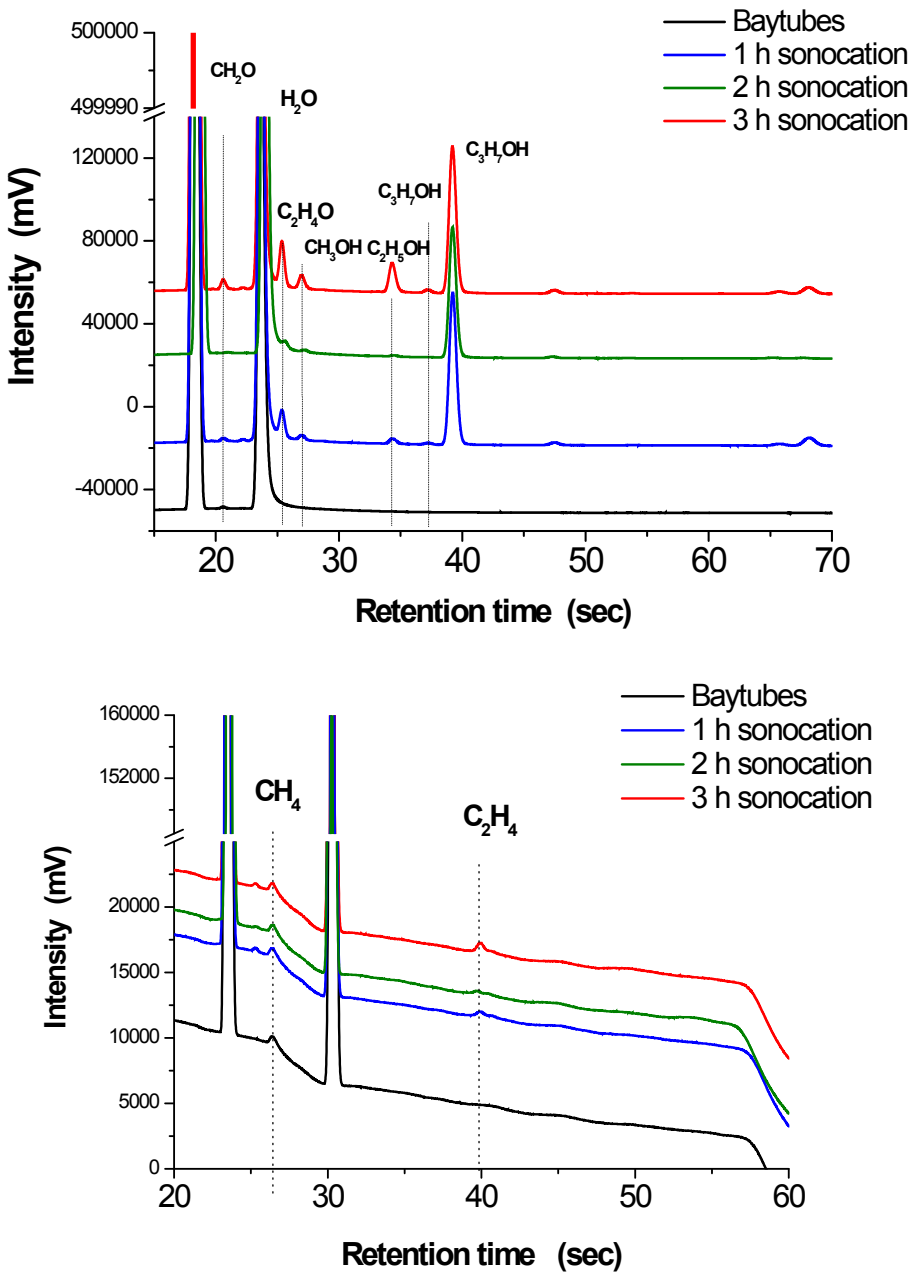

Figure 6-23. Chromatogram of gasses released at 600°C during TPD of Baytubes and ultrasonic irradiated samples in water.

FTIR investigation of the solution after water-soxhlet extraction exhibits the typical bands of C–H and C=O stretching vibrations (Fig. 6-27). The presence of aromatic groups is not clearly supported by the FTIR spectra obtained. Previous studies on the degradation of polyaromatic hydrocarbons (PAHs) with ultrasonic irradiation in aqueous solution proposed that the pyrolysis of PAHs occurs inside the microbubbles, which is the dominant pathways to evolving

gaseous products such as CO, CO_2, CH_4, and C_2H_2.[51] The observation suggests that the pyrolysis of dissolved pyrolytic carbon fragments is responsible for the cleaning effect during ultrasonic irradiation. The effect of sonolytic reactions from ethanol in the suspension during irradiation however cannot be excluded. Previous works have reported sonolysis reactions of alkanes, alcohols, ketones, and ether under irradiation condition similar to that applied in current work.[52,53,54,55]

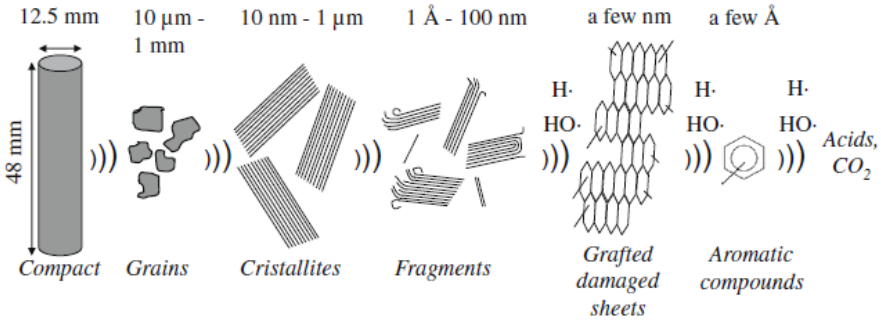

Figure 6-24. Scheme of graphite degradation by ultrasonic irradiation in water.[48]

The efficiency and nature of such ultrasonic-mediated molecular surface modification can be enhanced and possibly controlled by the type of solvent used for suspension of the CNTs. Protic and aprotic Organic solvents were chosen to for this purpose. Pristine Baytubes sample were suspended in ethanol and THF solvents and sonicated for 2 h under ice bath temperature. The vapour pressure of the ethanol (at 20°C 5.33 kPa) and THF (at 20°C 16 kPa) is lower than that of water (at 20°C 2.33 kPa). The organic solvent was expected to better dissolve the pyrolytic carbon and/or the fragments of pyrolytic carbon during ultrasonic irradiation without or with less oxidation to the CNTs. Higher vapour pressure of the solvents will moderate the acoustic cavitations. By increasing the solvent volatility the intensity of cavitational collapse, the maximum temperature and pressure reached will decrease.[46,54] The experiments using ethanol or THF

resulted in a different and moderately intensified pattern of CO_2 and CO from the TPD experiments as comparison to using water as solvent (Tab. 6-1 and Fig. 6-28). Both organic solvents functionalize to give almost similar total CO_2+CO amount with different profiles. After the ultrasonic irradiation in ethanol, the sharp peak at 500-550^{o}C attributed to anhydrides functionalities are still observed and intensified. In general sonication in ethanol gave rise to sharper peak shape of CO signal in the TPD profile. Similar to sonication in water for sonication in ethanol and THF released less CO_2 as compared to HNO_3 treatment.

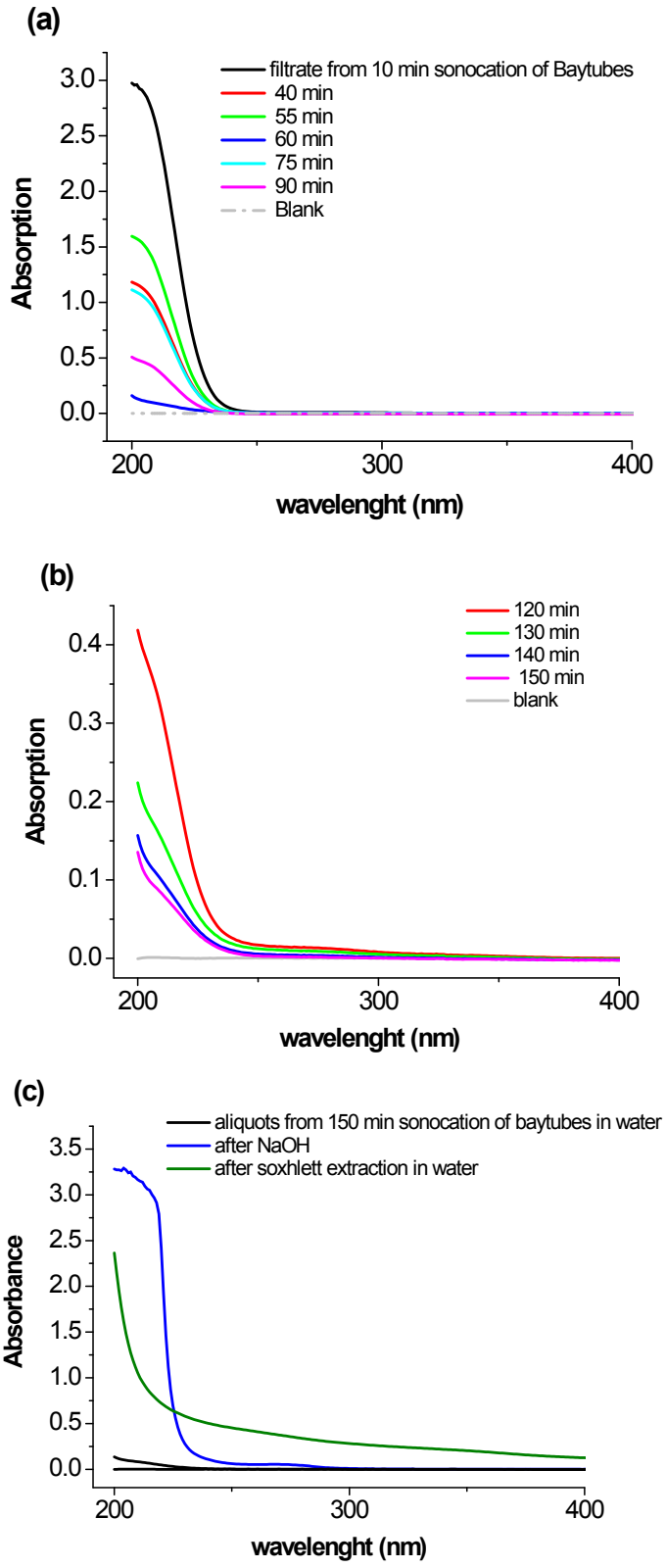

Figure 6-25. UV-Vis absorption spectrum of aliquots from the sonication of Baytubes CNT in water.

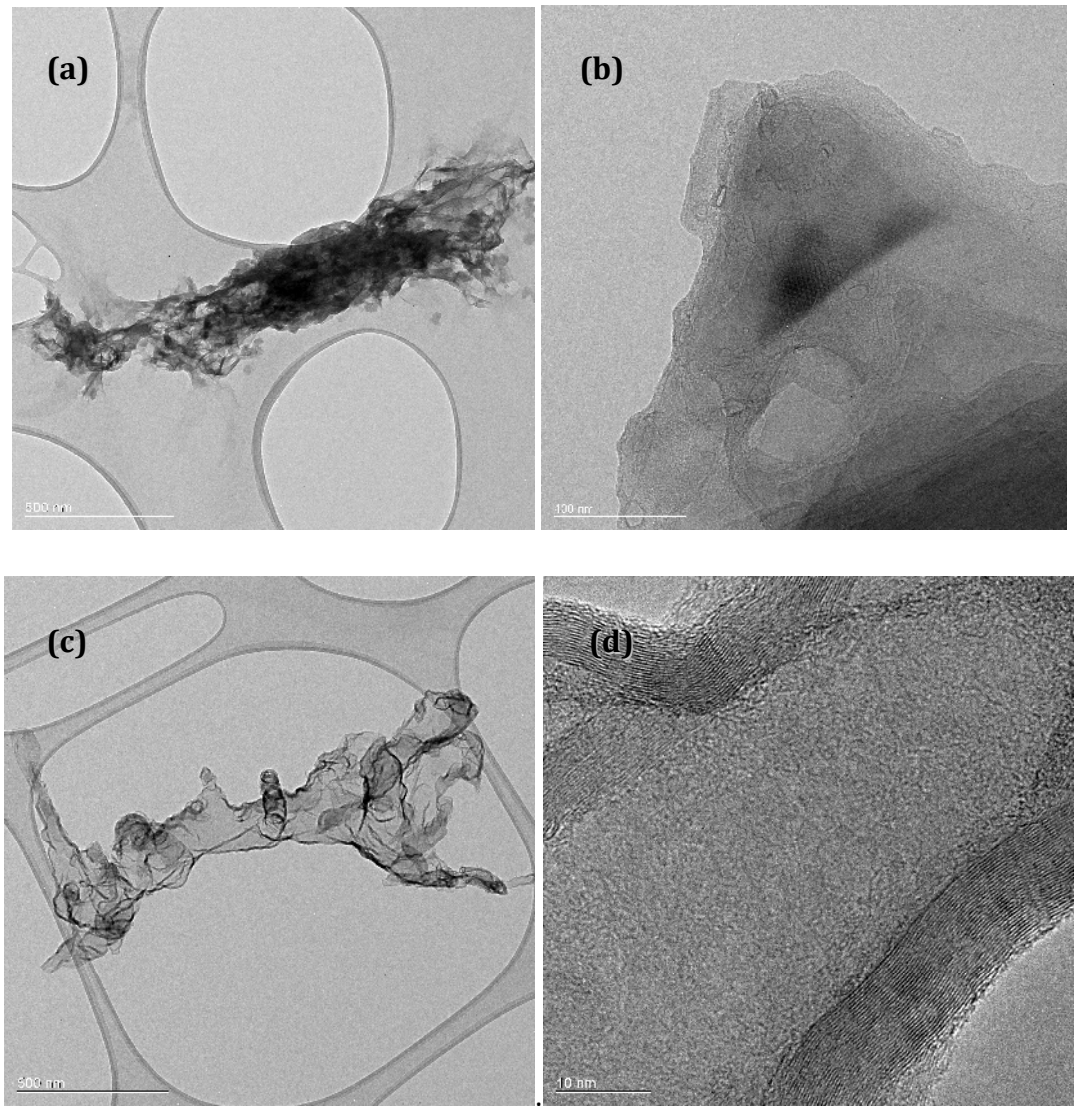

Figure 6-26. Solid disordered carbon particles suspended in aqueous solution after 3 h of sonication of Baytubes sample (a-d).

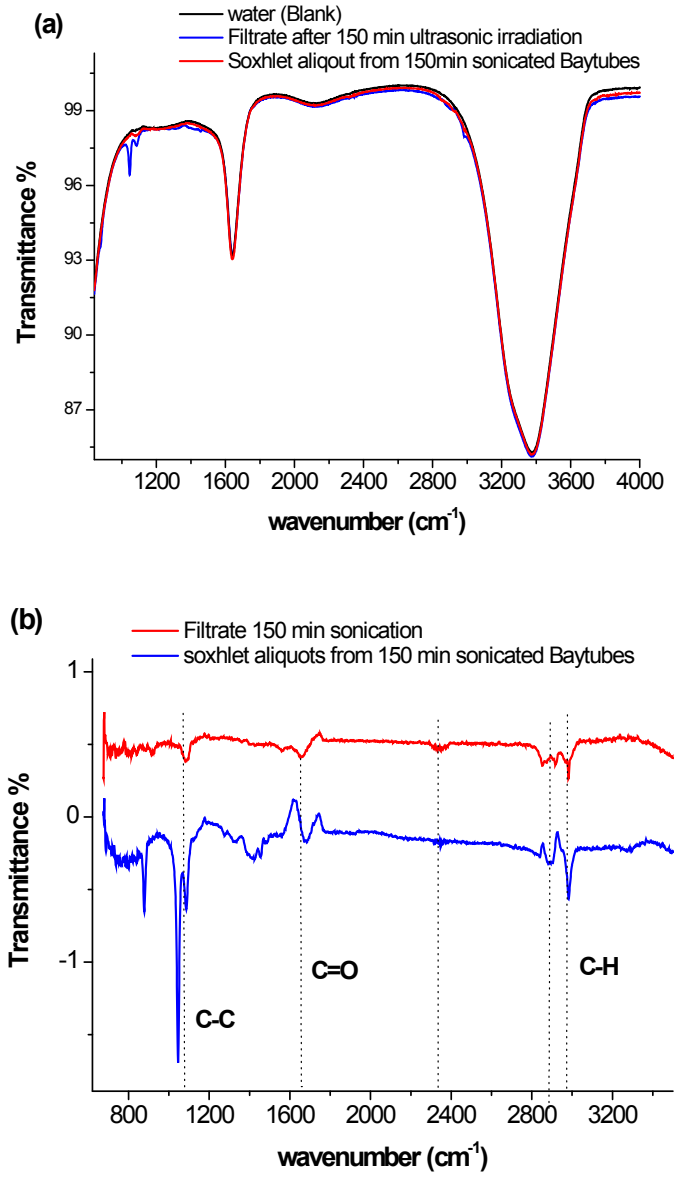

Figure 6-27. FTIR spectra of aqueous filtrate from the ultrasonic irradiation experiments (a), and the difference spectra with water as blank (b).

Similar to sonocation in water, Baytubes sample sonicated in ethanol and THF released hydrocarbons with drastically intensified pattern during TPD experiments (Fig 6-28 and Fig 6-29). Against that, pristine Baytubes samples show no indication hydrocarbons released during the course of TPD experiments. Such observations highlight the complex nature of the chemical effect on the CNT samples exerted by the ultrasonic irradiation. This again supports the argument that oxidation is not the dominant pathway for the purification process.

The functionalization of the sample with oxygen-containing surface groups and other hydrocarbons after irradiation in ethanol and THF demonstrate that the condition applied still provides enough energy to perform sonolytic reactions. The intensified hydrocarbon signal during TPD experiments for Baytubes sample after THF and ethanol sonication strongly support the argument for sonolytic reaction of the solvent that functionalize the CNT surface. It is however surprising that the amount of oxygen functionalities (calculated from CO and CO_2 TPD, Tab. 6-1) created after irradiation in ethanol and THF are higher than irradiation in water. In addition the amount of oxygen functional groups is constant up to 3 h of sonication in water. The excess water should continuously provide OH radicals potential to oxidize the carbonaceous materials.

As the water used water as-is from Micropore instrument tap and as-received solvents were also used directly, we suspect that the concentration of dissolved O_2 in the solvent may have contributed in the oxidation of the carbonaceous material.[52] A series of sonication experiments with aeration and deaeration of the solvents should allow to better understand the oxidative ability of the system.

The general trend for all three solvents is that the metal impurities were decreased after the ultrasonic irradiation (Tab. 6-1).

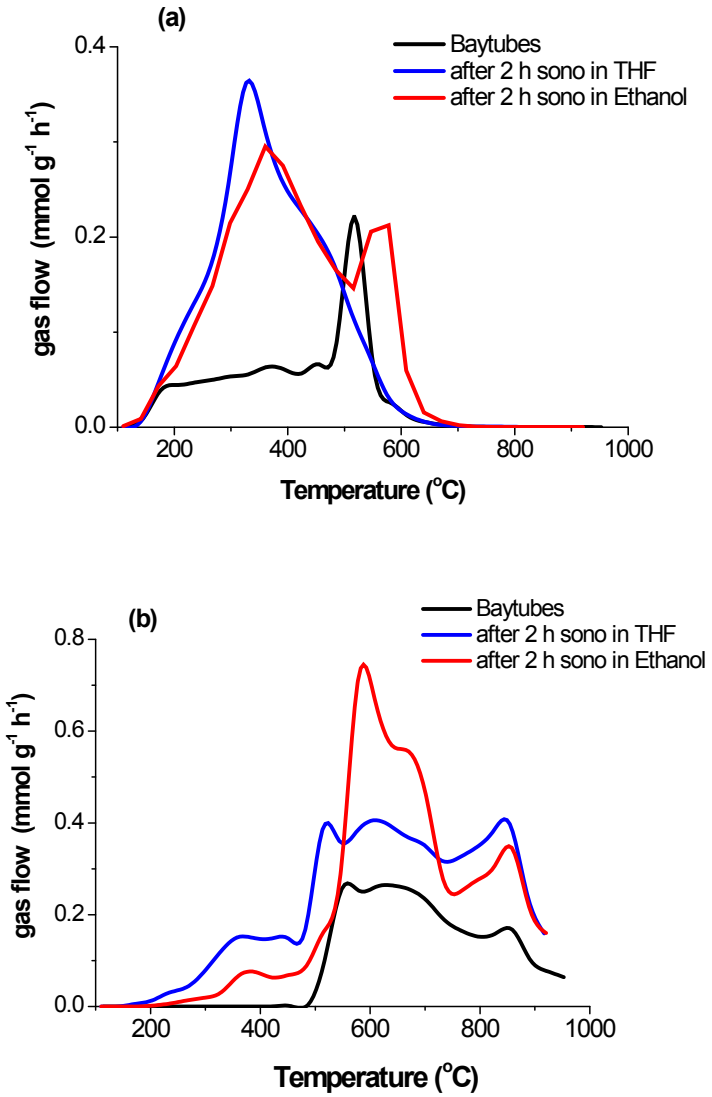

Figure 6-28. TPD profile of as-received Baytubes CNT sample and Ultrasonic treated samples in THF and ethanol; CO_2 signal (a) and CO signal (b).

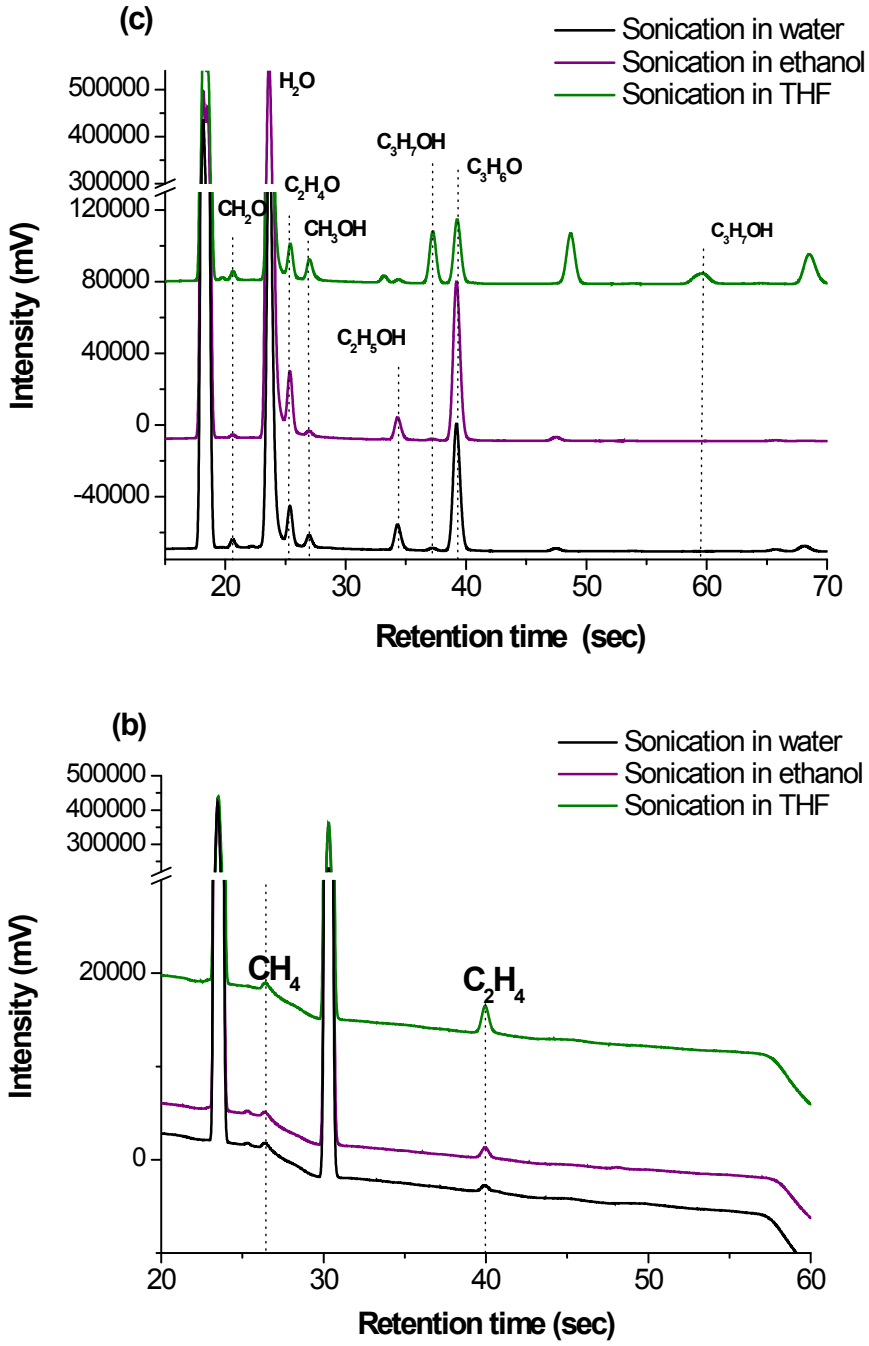

Figure 6-29. Chromatogram of gasses released at 600°C during TPD of Baytubes after 2 h ultrasonic irradiation samples in water, Ethanol and THF.

In summary the ultrasonic irradiation in water results in the gradual increase of the graphitic character of the CNT sample as demonstrated by decreasing I_D/I_G ratio with sonication time (Tab. 6-1). This is in agreement with the increase in oxidation stability of the sample and cleaner CNT surface demonstrated in thermal analysis data (Tab. 6-1) and HRTEM images (Figs. 6-21), respectively. Up to 3 h of irradiation there were no significant surface damages to the CNTs. There are however appreciable hydrocarbon and oxygen containing functionalities on the CNTs.

6.2.4.2. Ultrasonication of HNO_3-treated Baytubes

The sonocation treatment was also performed on the HNO_3 treated Baytubes sample as a test experiment to check the consistency of ultrasonic irradiation method to remove pyrolytic carbon and/or oxidation debris. The pristine Baytubes was first treated with 3M HNO_3 at 25^{o}C for 24 h followed by consecutive 1M NaOH and Soxhlet washing treatments with water and acetone as mentioned in the earlier section. The results are consistent with the ultrasonic experiments of as received Baytubes CNT in the previous section of this chapter. The TG experiments exhibit an increase in oxidation stability after the irradiation (Fig. 6-30). The ash content continues to diminish after 3 h of sonocation in agreement with the irradiation experiment with pristine Baytubes (Fig 6-20a). The profile of the TG and hence DTG shifted to higher temperature after ultrasonic irradiation. The TG slope (and thus the peak shape of DTG) is also significantly modified. The TG profiles demonstrate that the ultrasonic treatment decreases the number of active sites and increase the activation energy due to removal of metal impurities, oxidation debris and/or pyrolytic carbons.

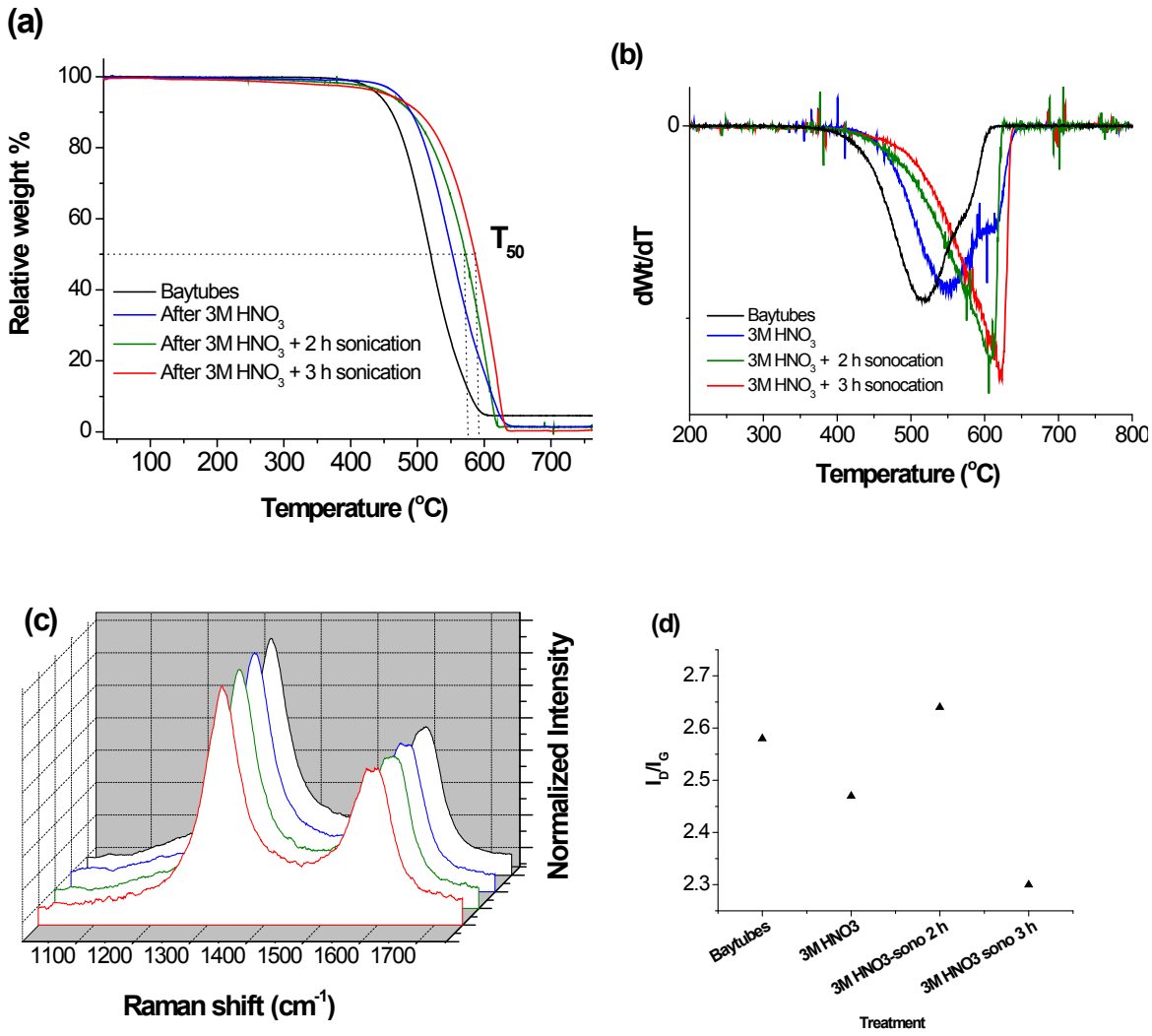

Figure 6-30. Oxidation profile (a, b) and Raman analysis (c, d) of Baytubes CNT before and after 3M HNO_3 treated CNT after ultrasonic irradiation in water.

Raman spectra of the samples reveal a decrease of I_D/I_G pointing towards decreasing defects character after 3 h of irradiation (Fig. 6-30). TEM investigation in Figure 6-31 reveals structural defects especially on the surface after 2 h of sonication. The TEM images however offer a conclusive cannot prove whether the surface damages and oxidation debris increases or decreases after 2 h of sonication in comparison to HNO_3 treated CNT. However after 3 h of ultrasonic irradiation the overview from TEM images presents cleaner CNT surface with occasional occurrence of remaining pyrolytic carbon and/or oxidation debris (Fig

6-31c & d). The observation suggests the ability of ultrasonic irradiation to remove oxidation debris and remaining pyrolytic carbon.

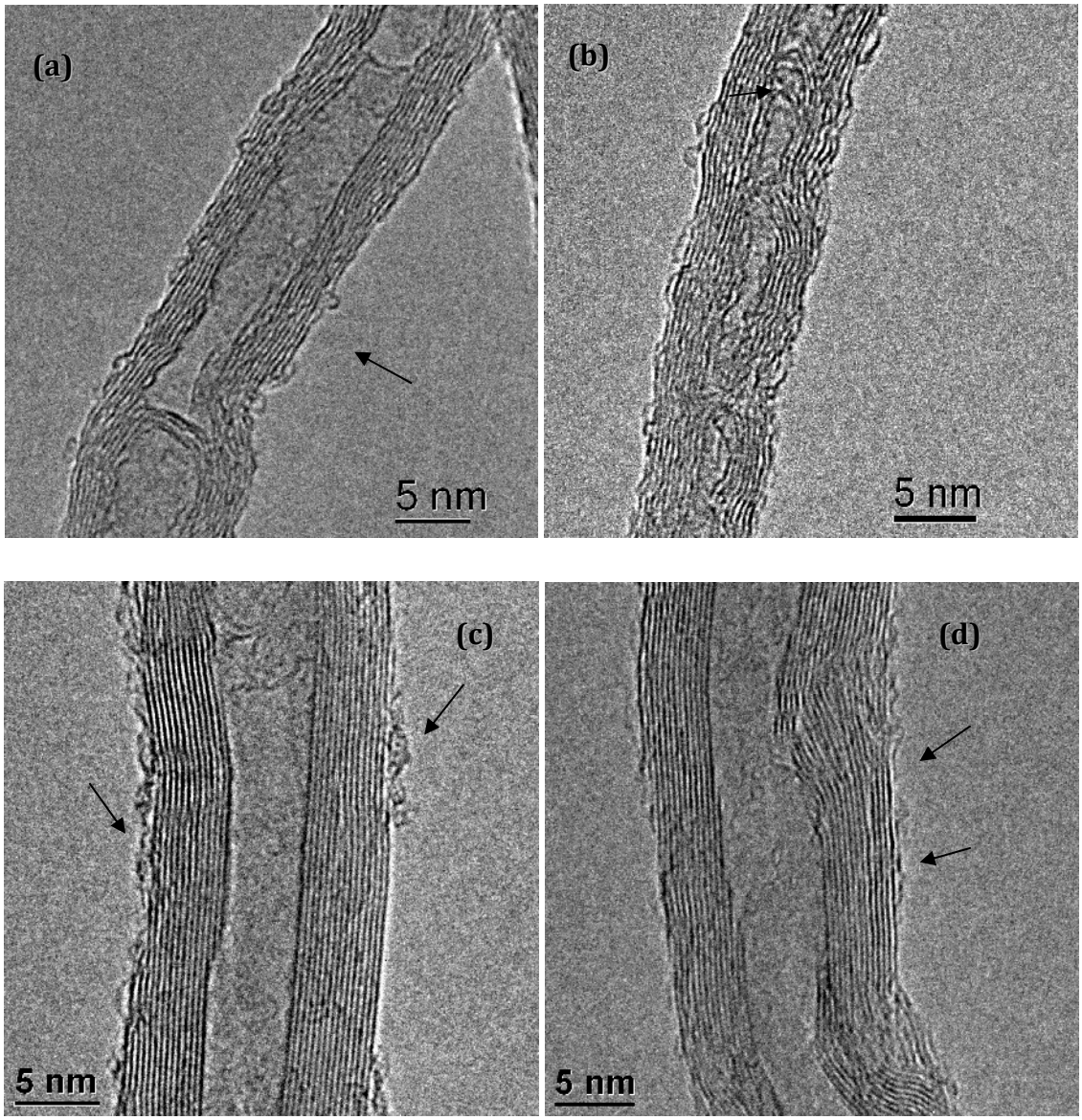

Figure 6-31. TEM images of 3M HNO_3 treated Baytubes CNT samples after 2 h (a, b) and 3 h sonication (c, d) sonication in water.

The TPD profiles of the sonicated HNO_3-treated Baytubes exhibit a decrease in the CO and CO_2 amount released (Fig. 6-32). The TPD patterns were also changed after the ultrasonic treatment. This can be attributed to the dissolution and

decomposition of the functionalized oxidation debris and/or remaining pyrolytic carbon during the ultrasonic irradiation in water. The total amount of CO_2 and CO released during TPD measurement show 20% decreased after 2 h of ultrasonic irradiation. After 3 h of irradiation the treatment resulted in a slight increase of the CO_2 amount during the TPD experiment (Fig. 6-32a). The CO signal however shows only minimum changes between 2 and 3 h of ultrasonic irradiation (Fig. 6-32b). The observation points out that the ultrasonic treatment removes the functionalized oxidation debris and/or fragments of pyrolytic carbons and also functionalizes the carbonaceous material. One can observe that the profiles of CO_2 and CO released from the TPD have been changed after the treatment. Unlike the sonication of pristine Baytubes that released more CO, the sonication of HNO_3-treated Baytubes demonstrate the favoured formation of the thermally-less stable carboxylic functional groups. The oxidation after 3 h irradiation however is in contradiction with the ultrasonic irradiation experiment of pristine Baytubes (Tab 6-1 and Fig 6-22) that demonstrated no change in their CO and CO_2 TPD profile. This observation does not support the argument that the oxidation due to sonication is limited to amount of dissolved O_2 in the solvent as the condition are similar in all set of experiments. Further investigation is required to clarify the oxidative effect of the ultrasonic irradiation.

Similar to the experiment with pristine Baytubes, ultrasonic irradiation functionalize the sample with hydrocarbon groups that releases ranges of oxidized and non-oxidized hydrocarbons during heating in inert. Fig 6-33 show the GC chromatogram of gasses released from HNO_3-treated and sonicated samples during TPD at 600^{o}C. The pristine and HNO_3-treated Baytubes sample show only very minimum sign of these hydrocarbons. The signals of these hydrocarbons are amplified after ultrasonic irradiation and the peak intensified with irradiation time. The functionalization or surface restructuring producing hydrocarbon-releasing groups can be attributed to the pyrolytic destruction of the CNT and/or reaction with organic solvent (in this case ethanol).

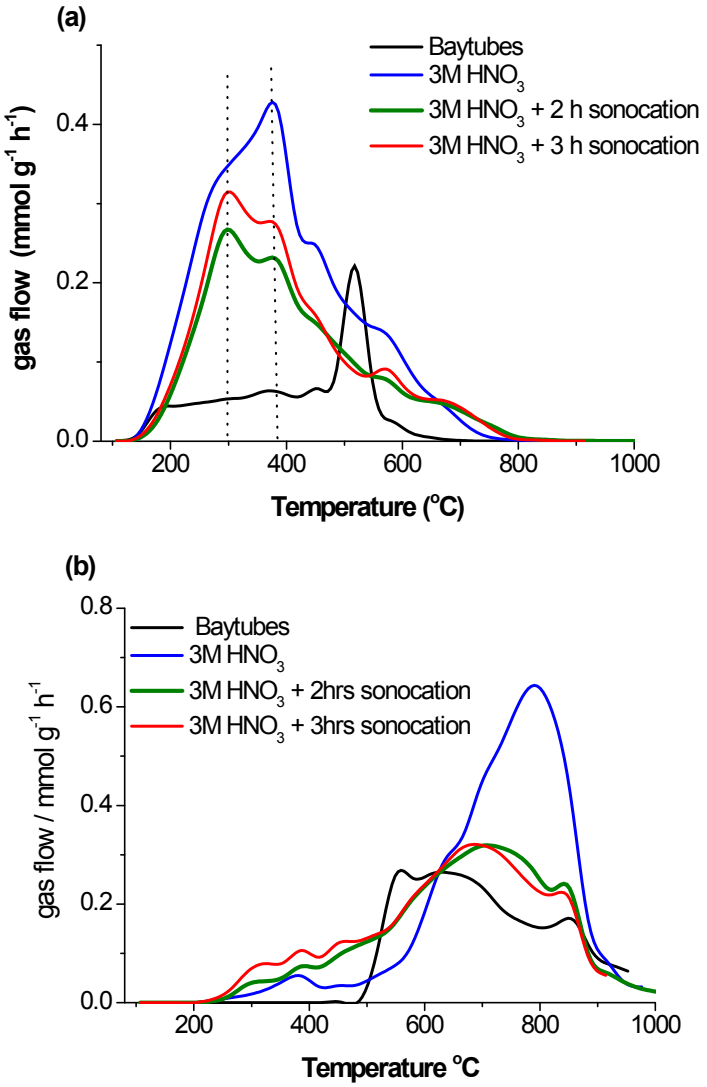

Figure 6-32. CO_2 (a) and CO (b) TPD profile of 3M HNO_3 treated Baytubes CNT sample before and after ultrasonic irradiation in water.

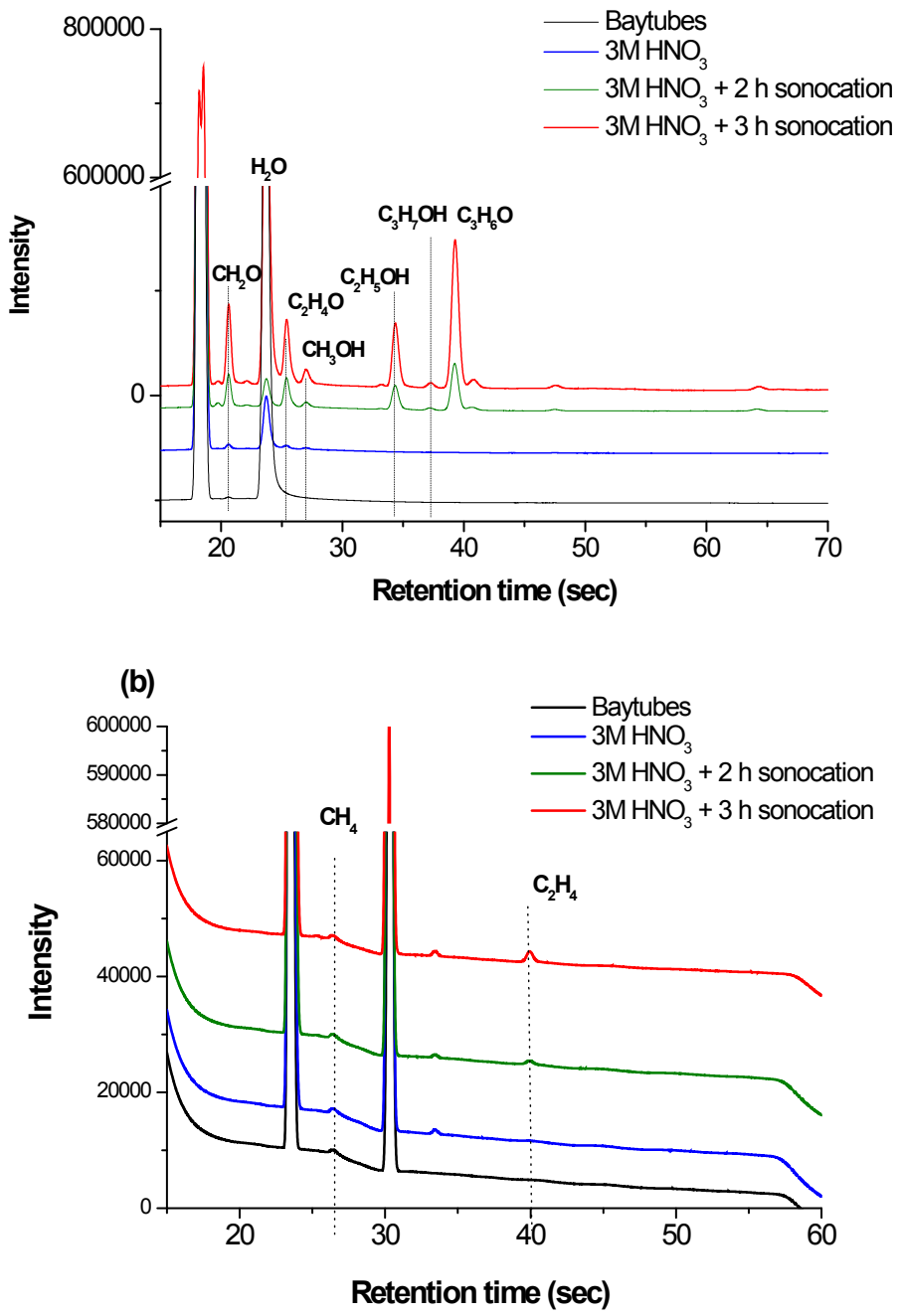

Figure 6-33. Chromatogram of gasses released at 600°C during TPD of Baytubes after ultrasonic irradiation samples in water.

The oxidation of the Baytubes sample after ultrasonic irradiation is also reflected in the diameter distribution measurements (Fig 6-34) from TEM images that show a decrease in the average diameter presumably due to wall thinning.

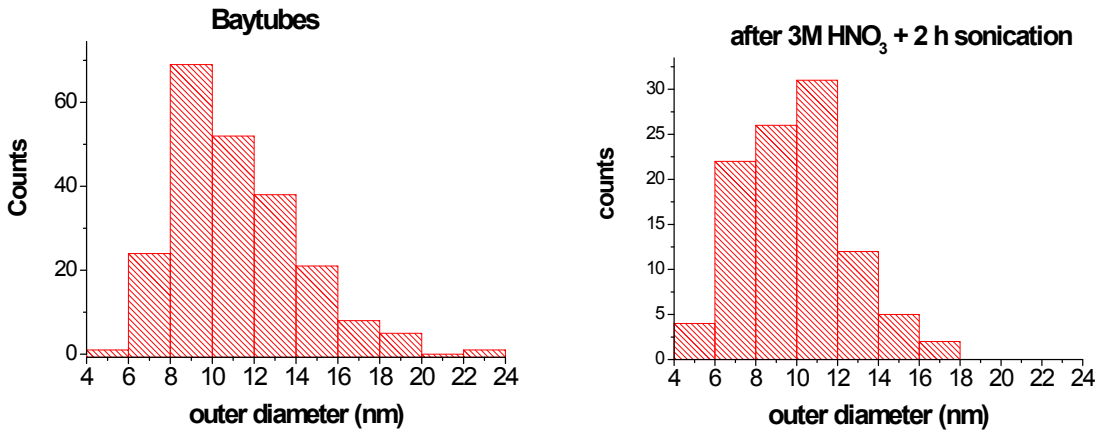

Figure 6-34. Diameter size distribution of as-received Baytubes CNT and 3M HNO_3 treated sample after 3 h of sonication.

Carbon particles were precipitated from the soxhlett aliquots precipitated after 2 weeks. The black solid exhibit amorphous structure with no graphene character detected (Fig 6-35c & d). The black solid also contains cellulose fiber from the soxhlett extraction timbel and traces of titanium possibly from the Titanium tip in the sonication instrument.

Overall similar trends between sonication of pristine and HNO_3-treated Baytubes was observed suggesting that ultrasonic irradiation removes the remaining pyrolytic carbon and the oxidation debris from the CNT surface.

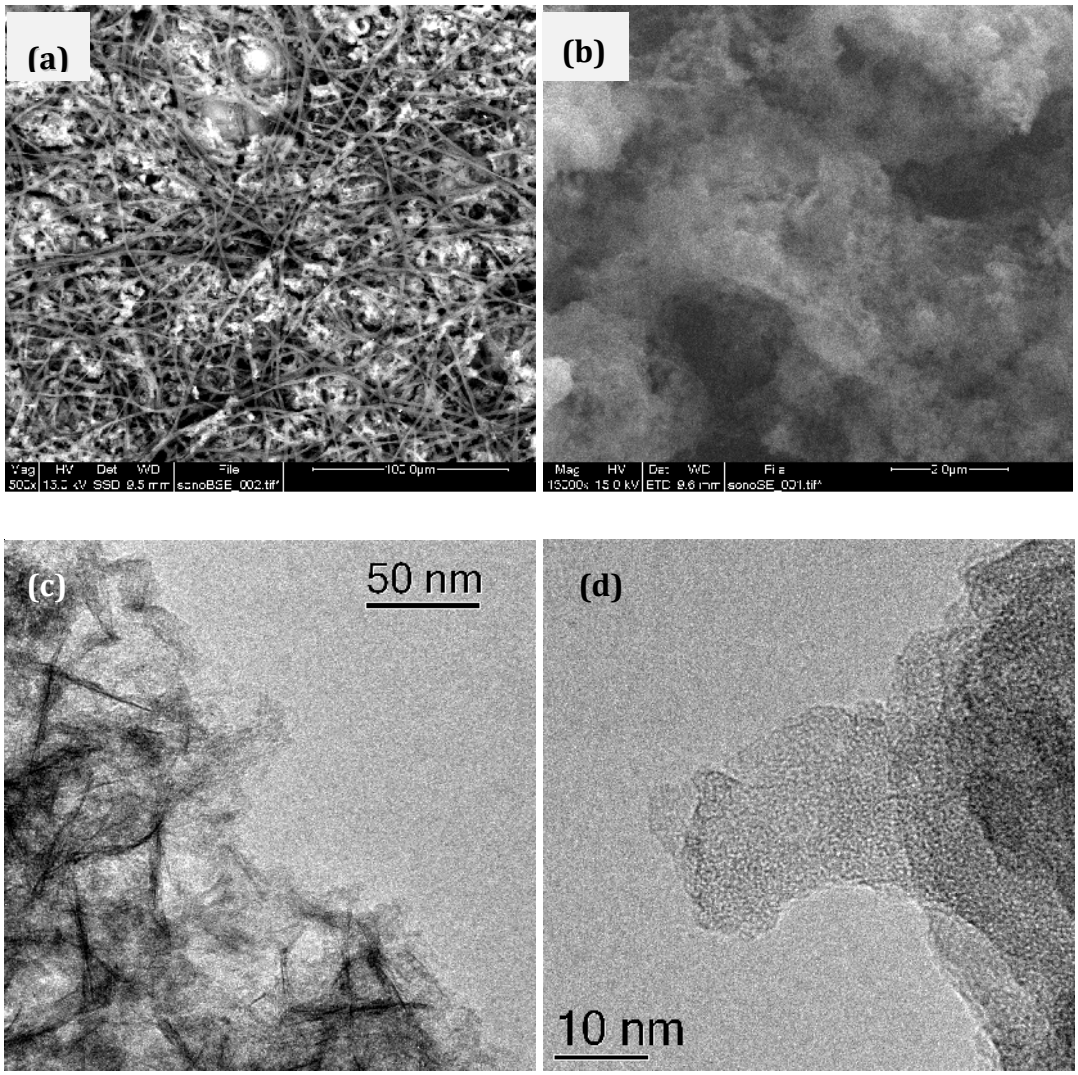

Figure 6-35. Solid disordered carbon particles suspended in aqueous solution after 3 h of sonication of HNO_3-oxidized Baytubes sample (a-d).

6.2.4.3. Consecutive treatment of air oxidation-HNO_3-sonication

Similar sonocation experiments were also performed on air-oxidized Baytubes. Pristine Baytubes was first oxidized in air for 12 h and continue treated with 3M HNO_3 to remove the metal impurities. The acid treatment was performed for 24 h and 25^{o}C under constant stirring. The physiochemical characterization of the air-oxidized sample is elaborated in section 6.2 in this chapter.

It is readily apparent from TEM investigation that after 3M HNO_3 the CNT surfaces are damaged and coated with oxidation debris, giving rough surfaces (Fig. 6-36a & b).

Graphene fragments and highly defective surfaces and edges are easily seen from TEM images (Fig. 6-36c & d). In agreement with the experiment with pristine Baytubes, these damages confirm the harsh effect exerted by the mild HNO_3 treatment to the CNT surface. The observation is in sharp contrast to Baytubes sample after air-oxidation before 3M HNO_3 (Fig. 6-5). TEM images further indicate removal of some oxidation debris from the CNT surface after the 3 h ultrasonic treatment (Fig. 6-36e &f).

It is suggested in the previous section in this chapter that the air-oxidation treatment removes pyrolytic carbon and highly defective carbon that resulted in the improvement of the sample's oxidative stability. However after the HNO_3 treatment the oxidative stability of the sample decreased significantly as shown in Fig 6-37a & b. After the ultrasonic irradiation the CNT sample partly recovers the stability. The T_{50} value increase from 515.5 to 545.5^{o}C for HNO_3-treated and sonicated samples respectively. The ash content decreases after HNO_3 treatment and ultrasonic irradiation reaching a final content of 1wt%. The change of the TG slope (and thus the DTG peak shape) suggests that the sample has higher activation energy after ultrasonic irradiation. And the profile shift can be attributed to the removal of highly defective fragments of the oxidation debris. Thus similar to irradiation of pristine and HNO_3-treated Baytubes samples mentioned earlier, the ultrasonic irradiation resulted in the improvement of sample's oxidation stability via the removal of catalyst impurities and oxidation debris.

In agreement with TEM and TG investigations, Raman spectra of the samples after 3M HNO_3 treatment exhibit an increase in the intensity of the defects band indicating the presence of more defects to the CNT sample (Fig. 6-37c). The width of the defect band at 1330 cm^{-1} demonstrates broadening after the HNO_3 treatment pointing to an increase of disorder in the sample. After the ultrasonic treatment the Raman spectrum exhibit a decrease in the defects band and thus a decrease in the I_D/I_G value suggesting the partial removal of the oxidation debris (Fig 6-37d).

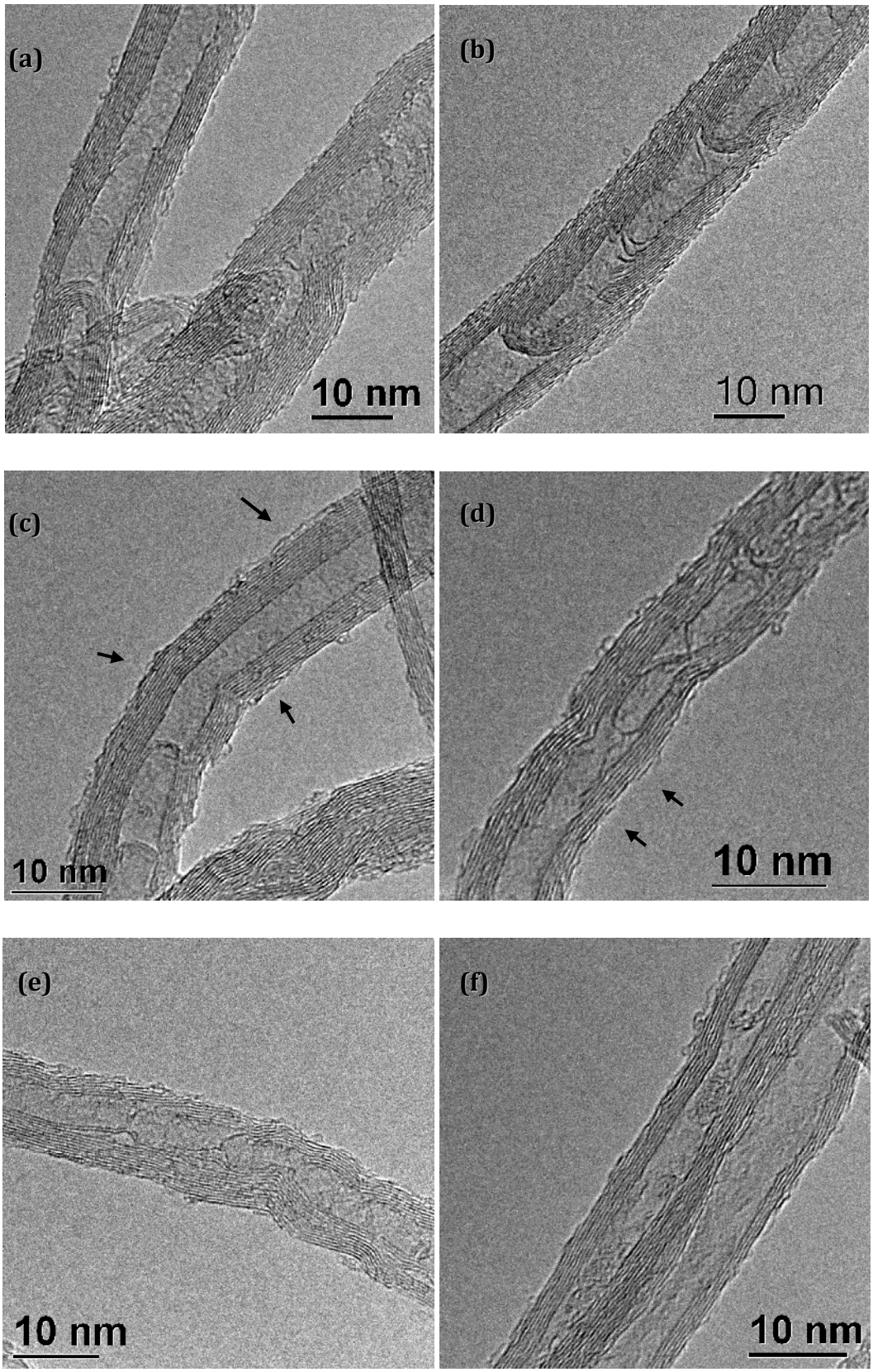

Figure 6-36. TEM images of air-oxidized Baytubes after 3M HNO_3 treatment (a-d) and after the consecutive 3 h sonication in water (e, f).

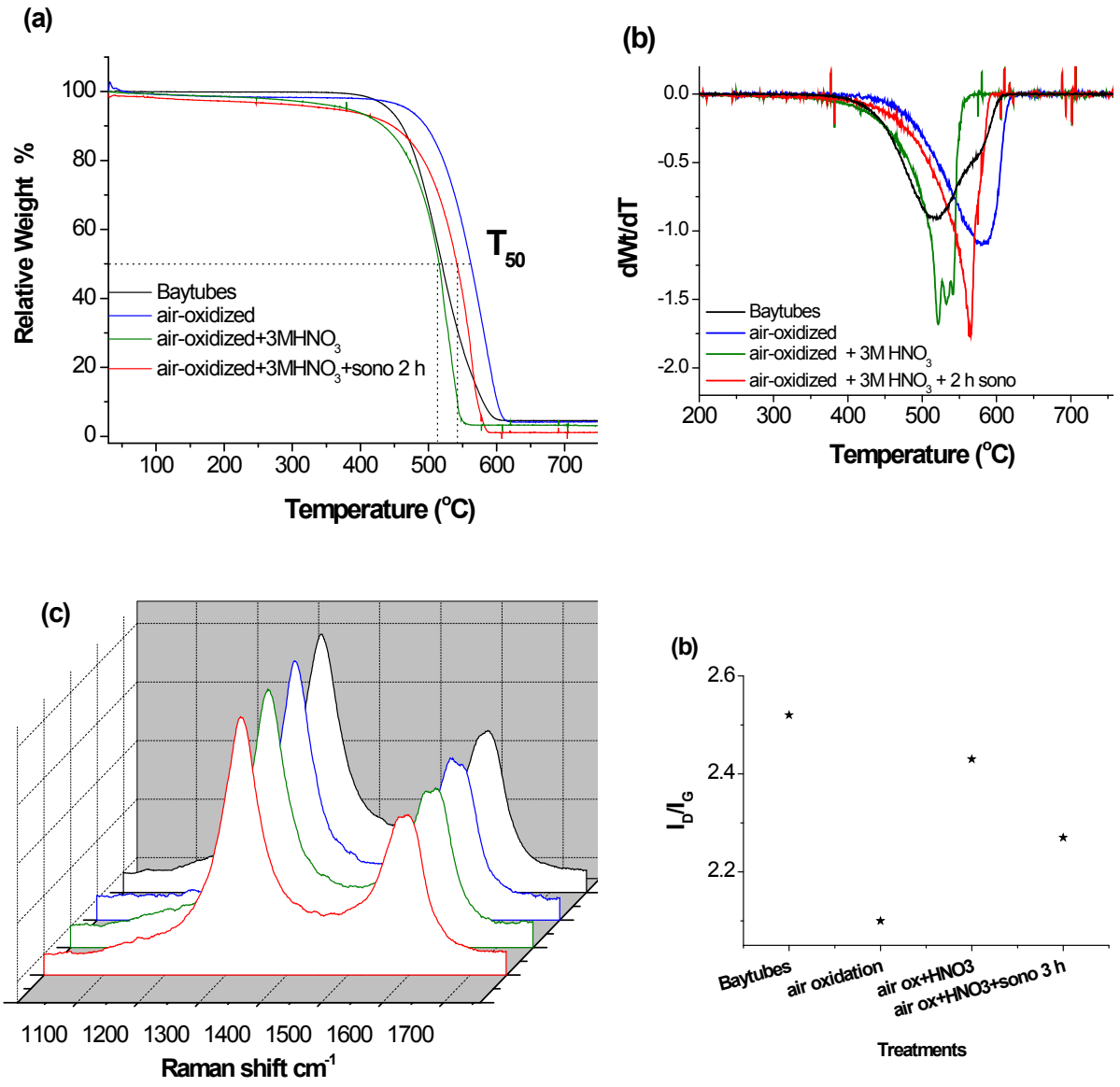

Figure 6-37. Oxidation profile (a, b) and Raman analysis (c, d) of Baytubes CNT after consecutive air-oxidation, 3M HNO_3 and ultrasonic irradiation in water.

UV-Vis spectra of aqueous filtrate from each treatment (Fig. 6-38) revealed absorption in the 200-400 nm range suggesting organic compounds being dissolved into the aqueous solutions during HNO_3 treatment, NaOH washing, sonocation and Soxhlett extraction. This evidence supports the argument that oxidation debris was produced and removed during the mild HNO_3 treatment and further removed after NaOH and sonocation treatment. Again these evidences are consistent with the

experiment presented earlier in this chapter involving mild HNO_3 washing and sonocation treatment of as-received Baytubes.

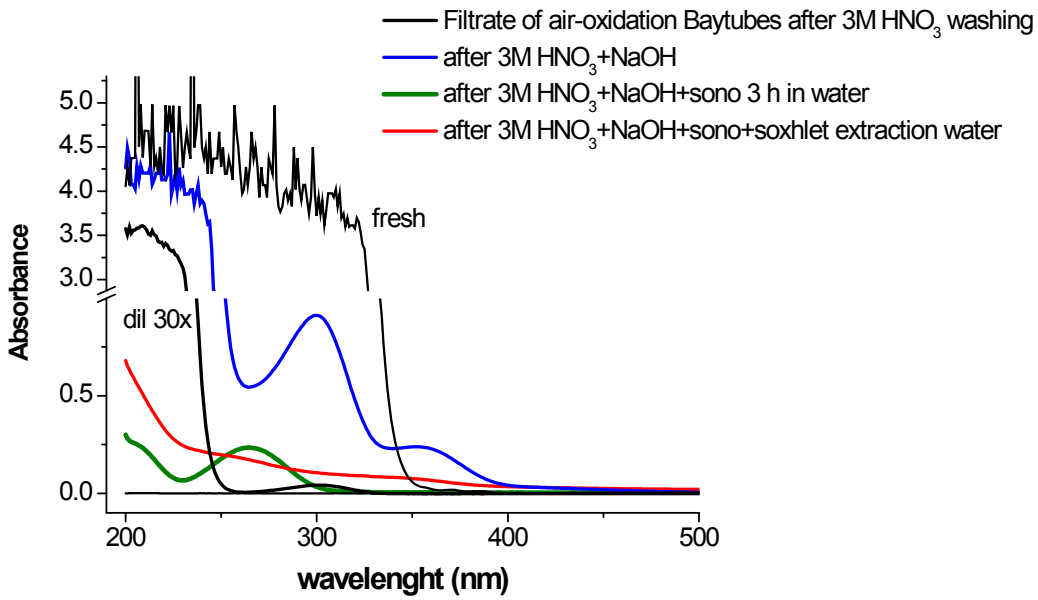

Figure 6-38. UV-Vis absorption spectrum of filtrates from the 3M HNO_3 treatment of air-oxidized Baytubes and the consecutive NaOH washing, sonocation and soxhlet extraction.

Treatment with HNO_3 have been shown throughout this chapter to have severe consequences to the surface microstructure of Baytubes CNTs even at mild condition; 3M HNO_3 25^{o}C. The damage creates more defects especially on the surface and presumably releasing organic fragments into the solution detected by UV-Vis spectra. It has also been shown that NaOH treatment is crucial to further clean the CNT surface from "sticky" organic fragments after the oxidative treatment. Ultrasonic irradiations have been shown to be effective in removing pyrolytic carbon and oxidation debris from the surface of the CNTs. The efficiency of the ultrasonic treatment has been validated by performing experiments on pristine Baytubes and oxidized Baytubes and all demonstrated consistent results. Such simple method is attractive as it only resulted in minor damage to the CNT surface.

References

(1) Jorio, A.; Dresselhaus, G.; Dresselhaus, M. S. *Carbon nanotubes*; Springer, 2008.
(2) O'Connell, M. J. *Carbon nanotubes*; CRC Press, 2006.
(3) Tessonnier, J.; Rosenthal, D.; Hansen, T. W.; Hess, C.; Schuster, M. E.; Blume, R.; Girgsdies, F.; Pfänder, N.; Timpe, O.; Su, D. S.; Schlögl, R. Analysis of the structure and chemical properties of some commercial carbon nanostructures. *Carbon* **2009**, *47*, 1779-1798.
(4) Frank, B.; Rinaldi, A.; Blume, R.; Schlögl, R.; Su, D. S. Oxidation Stability of Multiwalled Carbon Nanotubes for Catalytic Applications. *Chemistry of Materials* **2010**, *22*, 4462-4470.
(5) Howard, J. B.; McKinnon, J. T.; Makarovsky, Y.; Lafleur, A. L.; Johnson, M. E. Fullerenes C60 and C70 in flames. *Nature* **1991**, *352*, 139-141.
(6) Shui, X.; Frysz, C. A.; Chung, D. D. L. Solvent cleansing of the surface of carbon filaments and its benefit to the electrochemical behavior. *Carbon* **1995**, *33*, 1681-1698.
(7) Ruoff, R. S.; Tse, D. S.; Malhotra, R.; Lorents, D. C. Solubility of fullerene (C60) in a variety of solvents. *The Journal of Physical Chemistry* **1993**, *97*, 3379-3383.
(8) Laukhina, E. E.; Bubnov, V. P. Extraction of C60 from fullerene-containing carbon soots. *Russian Chemical Bulletin* **1995**, *44*, 1177-1179.
(9) Sadezky, A.; Muckenhuber, H.; Grothe, H.; Niessner, R.; Pöschl, U. Raman microspectroscopy of soot and related carbonaceous materials: Spectral analysis and structural information. *Carbon* **2005**, *43*, 1731-1742.
(5) Shimada, T.; Yanase, H.; Morishita, K.; Hayashi, J.; Chiba, T. Points of onset of gasification in a multi-walled carbon nanotube having an imperfect structure. *Carbon* **2004**, *42*, 1635-1639.
(11) Ajayan, P. M.; Ebbesen, T. W.; Ichihashi, T.; Iijima, S.; Tanigaki, K.; Hiura, H. Opening carbon nanotubes with oxygen and implications for filling. *Nature* **1993**, *362*, 522-525.
(12) Yao, N.; Lordi, V.; Ma, S.; Dujardin, E.; Krishnan, A.; Treacy, M.; Ebbesen, T. Structure and oxidation patterns of carbon nanotubes. *J. Mater. Res.* **1998**, *13*, 2432-2437.
(13) Borowiak-Palen, E.; Pichler, T.; Liu, X.; Knupfer, M.; Graff, A.; Jost, O.; Pompe, W.; Kalenczuk, R. J.; Fink, J. Reduced diameter distribution of single-wall carbon nanotubes by selective oxidation. *Chemical Physics Letters* **2002**, *363*, 567-572.
(14) Tsang, S. C.; Harris, P. J. F.; Green, M. L. H. Thinning and opening of carbon nanotubes by oxidation using carbon dioxide. *Nature* **1993**, *362*, 520-522.
(15) Tran, M. Q.; Tridech, C.; Alfrey, A.; Bismarck, A.; Shaffer, M. S. Thermal oxidative cutting of multi-walled carbon nanotubes. *Carbon* **2007**, *45*, 2341-2350.
(16) Hirsch, A. Functionalization of Single-Walled Carbon Nanotubes. *Angewandte Chemie International Edition* **2002**, *41*, 1853-1859.
(17) Srivastava, D.; Brenner, D. W.; Schall, J. D.; Ausman, K. D.; Yu, M.; Ruoff, R. S. Predictions of Enhanced Chemical Reactivity at Regions of Local Conformational Strain on Carbon Nanotubes: Kinky Chemistry. *The Journal of Physical Chemistry B* **1999**, *103*, 4330-4337.
(18) Ismail, A. F.; Goh, P. S.; Tee, J. C.; Sanip, S. M.; Aziz, M. A REVIEW OF PURIFICATION TECHNIQUES FOR CARBON NANOTUBES. *NANO* **2008**, *03*, 127.
(19) Hu, H.; Zhao, B.; Itkis, M. E.; Haddon, R. C. Nitric Acid Purification of Single-Walled Carbon Nanotubes. *The Journal of Physical Chemistry B* **2003**, *107*, 13838-13842.
(20) Wang, Y.; Gao, L.; Sun, J.; Liu, Y.; Zheng, S.; Kajiura, H.; Li, Y.; Noda, K. An integrated route for purification, cutting and dispersion of single-walled carbon nanotubes. *Chemical Physics Letters* **2006**, *432*, 205-208.
(21) Tessonnier, J.; Ersen, O.; Weinberg, G.; Pham-Huu, C.; Su, D. S.; Schlögl, R. Selective Deposition of Metal Nanoparticles Inside or Outside Multiwalled Carbon Nanotubes. *ACS Nano* **2009**, *3*, 2081-2089.
(22) Tessonnier, J.; Rosenthal, D.; Girgsdies, F.; Amadou, J.; Begin, D.; Pham-Huu, C.; Su, D. S.; Schlogl, R. Influence of the graphitisation of hollow carbon nanofibers on their functionalisation and subsequent filling with metal nanoparticles. *Chem. Commun.* **2009**, 7158-7160.
(23) Serp, P.; Castillejos, E. Catalysis in Carbon Nanotubes. *ChemCatChem* **2010**, *2*, 41-47.
(24) Shao, L.; Tobias, G.; Salzmann, C. G.; Ballesteros, B.; Hong, S. Y.; Crossley, A.; Davis, B.

G.; Green, M. L. H. Removal of amorphous carbon for the efficient sidewall functionalisation of single-walled carbon nanotubes. *Chem. Commun.* **2007**, 5090-5092.
(25) Mohanapriya, S.; Lakshminarayanan, V. Simultaneous purification and spectrophotometric determination of nickel present in as-prepared single-walled carbon nanotubes (SWCNT). *Talanta* **2007**, *71*, 493-497.
(26) Figueiredo, J. L.; Pereira, M. F. R.; Freitas, M. M. A.; Órfão, J. J. M. Modification of the surface chemistry of activated carbons. *Carbon* **1999**, *37*, 1379-1389.
(27) Gorgulho, H. F.; Mesquita, J. P.; Gonçalves, F.; Pereira, M. F. R.; Figueiredo, J. L. Characterization of the surface chemistry of carbon materials by potentiometric titrations and temperature-programmed desorption. *Carbon* **2008**, *46*, 1544-1555.
(28) Burg, P.; Cagniant, D. In *Chemistry and Physics of Carbon*; Radovic, L., Ed.; CRC Press; Vol. 30, p. 129.
(29) Frank, B.; Rinaldi, A.; Blume, R.; Schlögl, R.; Su, D. S. Oxidation Stability of Multiwalled Carbon Nanotubes for Catalytic Applications. *Chemistry of Materials 0*.
(30) Pumera, M. Imaging of Oxygen-Containing Groups on Walls of Carbon Nanotubes. *Chemistry - An Asian Journal* **2009**, *4*, 250-253.
(31) Tran, M. Q.; Tridech, C.; Alfrey, A.; Bismarck, A.; Shaffer, M. S. Thermal oxidative cutting of multi-walled carbon nanotubes. *Carbon* **2007**, *45*, 2341-2350.
(32) Li, Q.; Zhang, X.; Wu, G.; Xu, S.; Wu, C. Sonochemical preparation of carbon nanosheet from carbon black. *Ultrasonics Sonochemistry* **2007**, *14*, 225-228.
(33) Li, X.; Wang, X.; Zhang, L.; Lee, S.; Dai, H. Chemically Derived, Ultrasmooth Graphene Nanoribbon Semiconductors. *Science* **2008**, *319*, 1229-1232.
(34) Katoh, R.; Yanase, E.; Yokoi, H.; Usuba, S.; Kakudate, Y.; Fujiwara, S. Possible new route for the production of C6 by ultrasound. *Ultrasonics Sonochemistry* **1998**, *5*, 37-38.
(35) Katoh, R.; Tasaka, Y.; Sekreta, E.; Yumura, M.; Ikazaki, F.; Kakudate, Y.; Fujiwara, S. Sonochemical production of a carbon nanotube. *Ultrasonics Sonochemistry* **1999**, *6*, 185-187.
(36) Cataldo, F. Ultrasound-induced cracking and pyrolysis of some aromatic and naphthenic hydrocarbons. *Ultrasonics Sonochemistry* **2000**, *7*, 35-43.
(37) Katoh, R.; Yokoi, H.; Usuba, S.; Kakudate, Y.; Fujiwara, S. Sonochemical polymerization of benzene derivatives: the site of the reaction. *Ultrasonics Sonochemistry* **1998**, *5*, 69-72.
(38) Diedrich, G.; Kruus, P.; Rachlis, L. Cavitation-induced Reactions in Pure Substituted Benzenes. *Canadian Journal of Chemistry 50*, 1743-1750.
(39) Hilding, J.; Grulke, E. A.; Zhang, Z. G.; Lockwood, F. Dispersion of Carbon Nanotubes in Liquids. *Journal of Dispersion Science and Technology* **2003**, *24*, 1.
(40) Xing, Y.; Li, L.; Chusuei, C. C.; Hull, R. V. Sonochemical Oxidation of Multiwalled Carbon Nanotubes. *Langmuir* **2005**, *21*, 4185-4190.
(41) Avilés, F.; Cauich-Rodríguez, J.; Moo-Tah, L.; May-Pat, A.; Vargas-Coronado, R. Evaluation of mild acid oxidation treatments for MWCNT functionalization. *Carbon* **2009**, *47*, 2970-2975.
(42) Park, C.; Ounaies, Z.; Watson, K. A.; Crooks, R. E.; Smith, J.; Lowther, S. E.; Connell, J. W.; Siochi, E. J.; Harrison, J. S.; Clair, T. L. S. Dispersion of single wall carbon nanotubes by in situ polymerization under sonication. *Chemical Physics Letters* **2002**, *364*, 303-308.
(43) Koshio, A.; Yudasaka, M.; Zhang, M.; Iijima, S. A Simple Way to Chemically React Single-Wall Carbon Nanotubes with Organic Materials Using Ultrasonication. *Nano Letters* **2001**, *1*, 361-363.
(44) Lu, K. L.; Lago, R. M.; Chen, Y. K.; Green, M. L. H.; Harris, P. J. F.; Tsang, S. C. Mechanical damage of carbon nanotubes by ultrasound. *Carbon* **1996**, *34*, 814-816.
(45) Huang, W.; Lin, Y.; Taylor, S.; Gaillard, J.; Rao, A. M.; Sun, Y. Sonication-Assisted Functionalization and Solubilization of Carbon Nanotubes. *Nano Letters* **2002**, *2*, 231-234.
(46) Mason, T. J.; Lorimer, J. P. *Applied sonochemistry*; Wiley-VCH, 2002.
(47) Adewuyi, Y. G. Sonochemistry: Environmental Science and Engineering Applications. *Industrial & Engineering Chemistry Research* **2001**, *40*, 4681-4715.
(48) Guittonneau, F.; Abdelouas, A.; Grambow, B.; Huclier, S. The effect of high power ultrasound on an aqueous suspension of graphite. *Ultrasonics Sonochemistry* **2010**, *17*, 391-

398.
(49) TaylorJr., E.; Cook, B. B.; Tarr, M. A. Dissolved organic matter inhibition of sonochemical degradation of aqueous polycyclic aromatic hydrocarbons. *Ultrasonics Sonochemistry* **1999**, *6*, 175-183.
(50) Wheat, P. E.; Tumeo, M. A. Ultrasound induced aqueous polycyclic aromatic hydrocarbon reactivity. *Ultrasonics Sonochemistry* **1997**, *4*, 55-59.
(51) David, B. Sonochemical degradation of PAH in aqueous solution. Part I: Monocomponent PAH solution. *Ultrasonics Sonochemistry* **2009**, *16*, 260-265.
(52) Forney, M. W.; Poler, J. C. Sonochemical Formation of Methyl Hydroperoxide in Polar Aprotic Solvents and Its Effect on Single-Walled Carbon Nanotube Dispersion Stability. *Journal of the American Chemical Society* **2010**, *132*, 791-797.
(53) Suslick, K. S.; Flint, E. B. Sonoluminescence from non-aqueous liquids. *Nature* **1987**, *330*, 553-555.
(54) Suslick, K.; Gawienowski, J.; Schubert, P.; Wang, H. Sonochemistry in non-aqueous liquids. *Ultrasonics* **1984**, *22*, 33-36.
(55) Krishna, C. M.; Kondo, T.; Riesz, P. Sonochemistry of alcohol-water mixtures. Spin-trapping evidence for thermal decomposition and isotope-exchange reactions. *The Journal of Physical Chemistry* **1989**, *93*, 5166-5172.

Chapter 7:

The effect of the removal of pyrolytic carbon from commercial CNTs in catalysis

Oxidative purification with mild diluted HNO_3 followed by NaOH washing lowers the amount of pyrolytic carbon attached to multiwalled CNTs. The graphitic structure improves by further annealing in Ar at elevated temperatures, that is, 900, 1300, and 1700^{o}C. The influence of purification treatment on the catalytic activity of the CNTs was investigated for the oxidative dehydrogenation of ethylbenzene and propane as the probe reaction. All samples tend to approach an appropriately ordered structure and Raman analysis of the used samples displays a I_D/I_G ratio of 1.37 – 2.48. Oxygen functionalities are partly removed by the annealing treatment and can be rebuilt to some extent by the oxygen molecules in the ODH reactant flow. The presence of pyrolytic carbon is detrimental to the catalytic activity as it allows for unwanted functional groups occurring in parallel with the formation of selective group.

7.1. Purification and annealing of CNT sample

In comparison with the graphitic structure, disordered carbon exposes more prismatic face per unit volume and allows for additional reactivity at intraplanar defects. The pyrolytic impurities tend to enhance functionalization and thereby can induce the combustion of the graphitic CNTs by creating hotspots during their exothermic oxidations.[5]

It is necessary to distinguish in essence the roles of graphitic and disordered carbon atoms in functionalization and in application in ODH reactions. In the present investigation, a condition of mild oxidative and consecutive annealing treatment was

carried out to remove the pyrolytic carbon, to alter the surface functionalities and to restore the graphitic ordering of CNTs. The structural consequences of various steps were investigated by TEM, Raman spectroscopy, thermogravimetric analysis, and temperature-programmed desorption. Furthermore, after each treatment the CNTs were investigated for their activity in the ODH reactions of ethylbenzene and propane.

Sample denotations are assembled in Tab. 7-1 together with physico-chemical characterization data.

Table 7-1. Sample denotations and physico-chemical characterization data

Sample	Description	T_{max} (TGA) [^{o}C]	S_{BET} [$m^2 g^{-1}$]	I_D/I_G before reaction	I_D/I_G after ODH of EB
pCNT	Pristine CNT NC3100	664	320	2.2	–
oCNT	HNO_3 & NaOH treated	652	301	2.17	1.8
oCNT-900	oCNT heat treated in Ar at 900 °C	689	339	2	2.48
oCNT-1300	oCNT heat treated in Ar at 1300 °C	739	271	1.9	2
oCNT-1700	oCNT heat treated in Ar at 1700 °C	777	304	1.13	1.37

Fig. 7-1a shows the high-resolution transmission electron microscopy (HRTEM) image of the as received CNTs NC3100 sample. Detail description of this sample is mentioned in Chapter 5. The CNTs are bundled together with a certain degree of entanglement. The surfaces of CNTs are covered by pyrolytic carbon layer of varying thickness. Numerous structural and topological defects are observed in the pristine CNT sample. Against that the TEM investigation of treated samples (Fig. 7-1b-d)

shows that the graphitic walls become more ordered and the coverage by pyrolytic carbons is reduced.

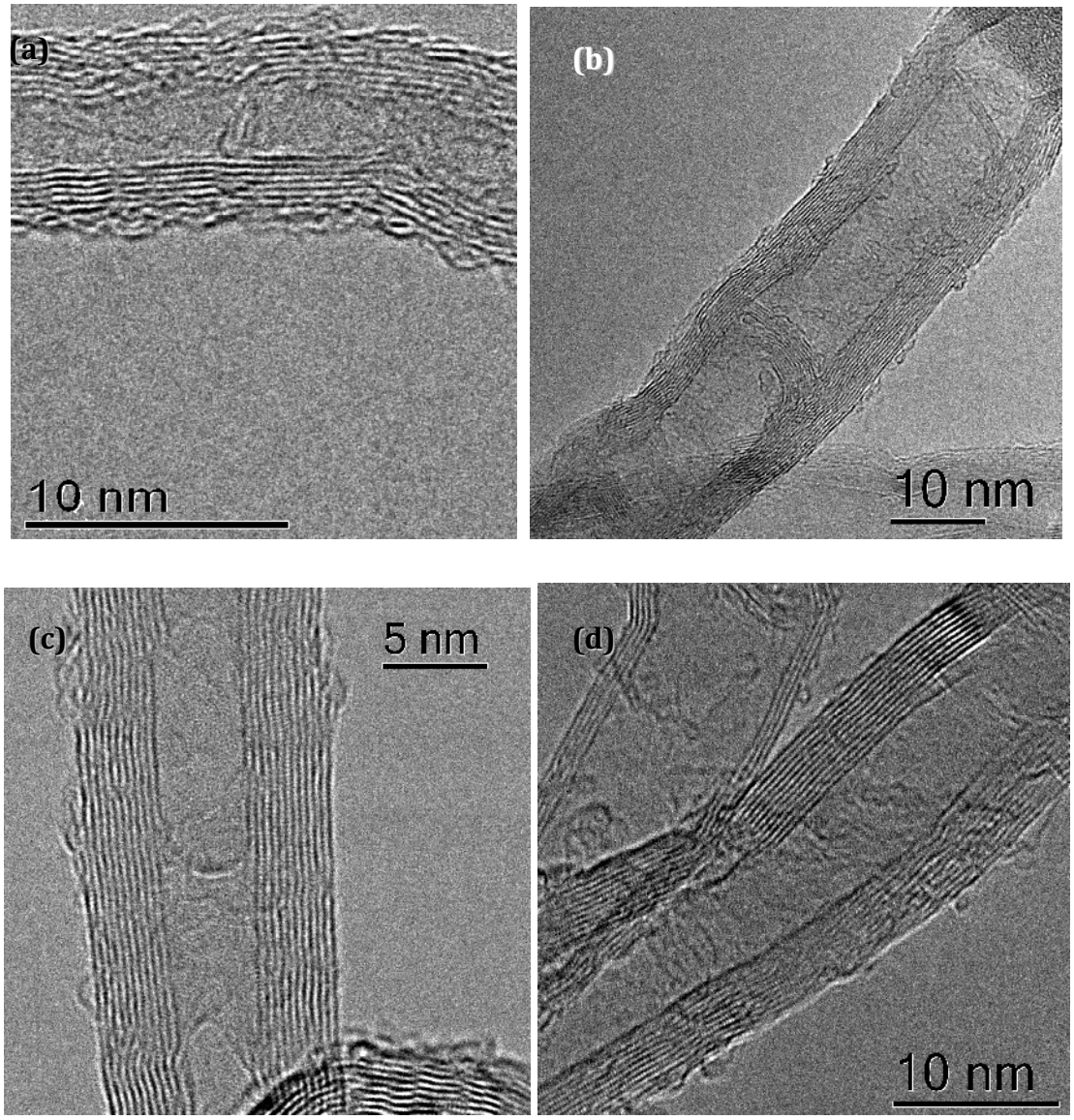

Figure 7-1. TEM representation of the pristine CNTs (a) and after chemical and thermal treatments at 900°C (b) and at 1700 °C (c-d).

Raman spectroscopy is a common method to characterize the order of carbon materials.[6-9] Raman bands of the samples and the quantitative results are summarized in Fig. 7-2 and Tab. 7-1. The D band centered at ~1320 cm^{-1} is usually attributed to defects and pyrolytic carbon impurities in the CNT sample. The G band at ~1600 cm^{-1} results from the graphitic structure of the sample.[10-12] The D` band at ~1620 cm^{-1} appears as a shoulder of the G band and is assigned to lattice vibration

similar to that of the G band but involving several graphene layers or small graphite domains on bulk graphite crystals, commonly found in defective graphite and intercalated graphite.[6,12] The D` band is more distinguishable after heat treatment especially at 1700 ^{o}C, due to peak sharpening. The first order Raman spectra of pristine and treated CNTs samples were fitted using four Lorentzian peaks at 1180 cm^{-1}, 1360 cm^{-1}, 1580 cm^{-1}, and 1620 cm^{-1} and a Gaussian peak at 1500 cm^{-1} (assigned for D3, D, G, D`, and D2 bands, respectively) following the procedure by Sadezky et al.[6] Fitting parameters are assembled in Appendix 7-1. For all samples, D3 shows no contribution to the spectra except for pCNT. The contribution of D and G bands from the fittings show peak sharpening with the oxidative treatment and the heating treatment, as observed from the full-width at half maximum (FWHM). After the oxidative purification and heat treatment at 900 ^{o}C the FWHM of the D band shows a more drastic decrease compared to the G and D` bands.

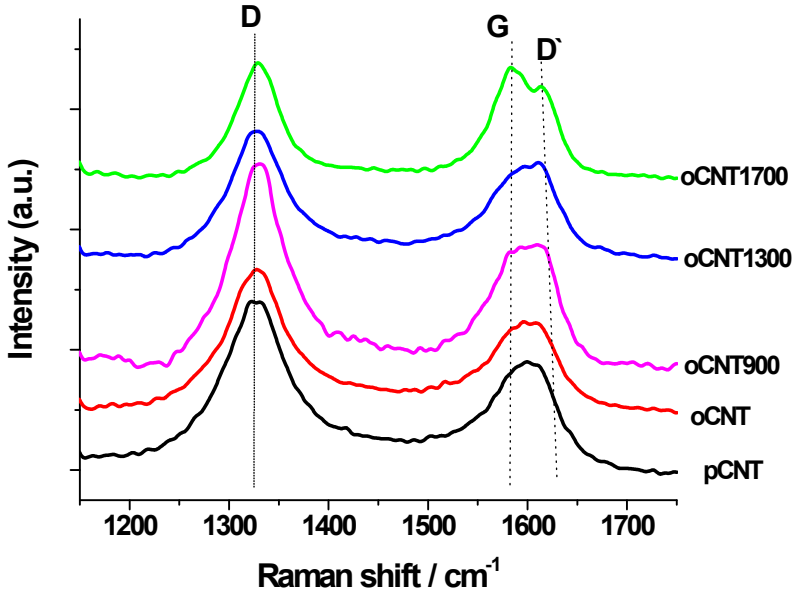

Figure 7-2. Raman spectra of as received and treated NC3100 CNTs.

The TEM and Raman spectroscopy measurements are complementary to indicate that the chemical oxidative treatment partially removes the pyrolytic carbon from the CNTs. The intensity ratio I_D/I_G continuously decreases after the thermal treatment at 1300^{o}C and 1700^{o}C indicating the rearrangements of the carbon atoms to reduce structural defects and thus to improve the graphitization of the CNTs. The

heat treatment at 900^{o}C, however, did not significantly change the I_D/I_G ratio as compared to the oCNT sample albeit a sharp loss of surface functionalities was observed by temperature-programmed desorption (TPD). The functionalization of the sample is obvious with intense desorption peaks of CO_2, and CO signals from the oCNT sample depicted in Figs. 3-39. The amount of CO_2 released between 77–400^{o}C probably originates from the decomposition of oxygenated groups such as carboxylic acid and carboxylic anhydride after the HNO_3-NaOH treatment, which sharply decreases with increasing annealing temperature indicating its positive effect on surface defunctionalization. The signals of CO_2 and CO featuring various summits between 400–930^{o}C can be attributed to the successive desorption of more stable functionalities.[13,14] The highly functionalized sample (oCNT) released the CO_2 together with CO in the range of 530–380^{o}C indicating the decomposition of carboxylic anhydrides to produce CO and CO_2 in equimolar amounts.[15] The CO_2 release above 530^{o}C is usually assigned to lactones. For pristine and annealed samples CO starts to evolve around 530–730^{o}C, due to the presence of phenol, ether, and quinone groups. The thermal stress especially at higher temperatures may induce the structural rearrangements of the carbon-carbon network (in graphitic and pyrolytic carbons network) and the re-oxidation of the reactive carbon atoms by the desorbed CO_2. Such processes could then complicate the assignments and interpretation of the TPD data.

The sample annealed at 900 ^{o}C shows a distinct sharp CO desorption peak at 630 ^{o}C. In addition, for all annealed samples the release of CO_2 and CO is detected below the respective annealing temperature with an almost similar shape. This may be referred to the reaction of active defects with water vapor, O_2, CO, and/or CO_2 from the atmosphere at room temperature exposure after the annealing procedure.[16] This observation is in agreement with the Raman spectra that show only a slight change in I_D/I_G. The CO signal is difficult to identify below 827^{o}C for samples heat treated at higher temperatures (oCNT-1300 and oCNT-1700). This observation can be related to the improved graphitic ordering of these samples derived from the Raman spectra. The experiments from Raman and TPD show that the heat treatment at 1300 ^{o}C and 1700^{o}C provides enough energy to heal the defects in the CNT sample after oxidative

purification. The highly defective and functionalized surface of pCNT and oCNT allows for the weak adsorption of an appreciable amount of water during the exposure to ambient. Water desorption during TPD above 180°C conceals its formation by structural rearrangements, i.e., condensation reactions.[17] Here, the broad rising of the signals can be inferred to the wide distribution of functionalities with different desorption energy.[18,19]

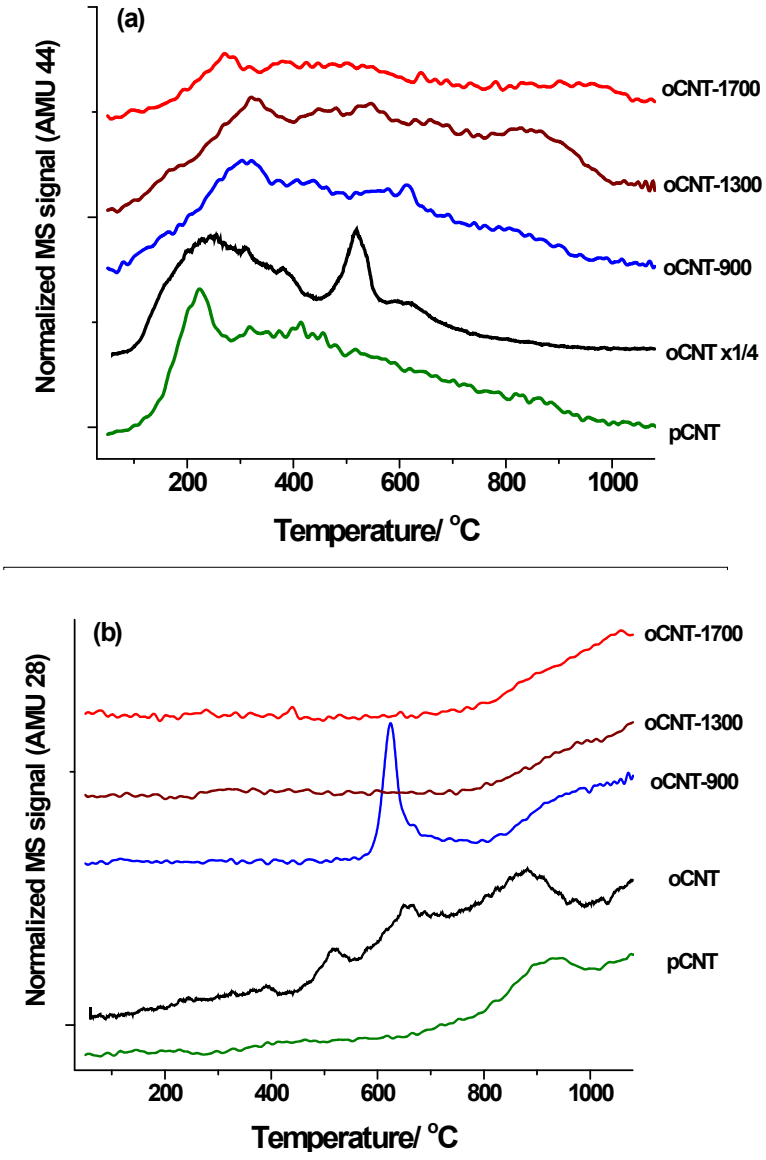

Figure 7-3. CO_2 (a) and CO (b) evolution from TPD experiments of the CNT samples.

In conclusion the TPD clearly shows different surface functional groups present on the CNT samples after different treatments. The desorption profiles are especially distinctive for the oCNT and the oCNT-900 sample.

TEM, TPD, and Raman spectroscopy investigations indicate that the chemical oxidative treatment reduces the amount of pyrolytic carbon and creates surface functional groups mostly on the defect sites on the CNT graphitic surface, however, some are still on the remaining pyrolytic carbon. The treatment under the applied conditions results in a minimum damage to the microstructure of the CNTs.

The oxidation behaviour of the CNT samples was investigated by thermogravimetric analysis (TGA). With the increase in annealing temperature, the samples (oCNT-900, oCNT-1300, oCNT-1700) become more stable against combustion, as evidenced by the upward shift of its onset temperature to 550–650^{o}C, respectively (Fig. 7-4 & 3-5a). The weight loss profile for pristine and annealed CNTs samples (Fig. 7-4) is in agreement with the consumption profiles of O_2 and there is no released gas prior to the oxidation onset temperature (Fig. 7-5a). This observation is in accordance with the decreased I_D/I_G value due to the improved graphitization of the CNTs. [20-24] The onset temperature for the oCNT sample is lower than for the pristine CNT sample although the I_D/I_G value and the TEM investigations show the partial removal of the pyrolytic carbon. This may be due to the creation of surface defects after the mild oxidative treatment and some traces of remaining Na catalyzing the transformation. TEM studies and the ash content analysis of treated samples showed less impurity than the pristine sample (Fig. 7-4), however, alkali metals are effective catalysts for carbon combustion[25,26] and Na traces may keep adsorbed at the O-functionalized CNT surface even after thorough washing. The thermogravimetric experiment with oCNT shows two weight losses. The first weight loss at 150–473^{o}C shows a gradual decrease being attributed to the removal of adsorbed water from the more hydrophilic oCNTs, decomposition of labile surface functionalities (releasing CO_2) and combustion of reactive carbonaceous material (Fig. 7-5). The enhanced amount of functional groups in oCNT showing intense overlapping peaks of labile components decomposition agrees with the data obtained from TPD experiments (Fig. 7-3). The weight loss is also related to the

oxidation debris of the remaining pyrolytic carbon, which is expected to combust at lower temperature than the CNTs and contains more hydrogen.[5,10-12,27] This assumption is confirmed by two O_2 consumption peaks in the MS signal. The second weight loss starts at 450°C and is attributed to the combustion of the CNTs. The creation of hotspots from the combustion of reactive carbonaceous species (thus inducing the combustion of the graphitic CNT) is possible and cannot be excluded from the current TG experiments.[5] One possible explanation is that the functionalization enhanced the reactivity of pyrolytic carbon debris towards oxidation with O_2 at lower temperature. Another explanation for the different oxidation reactivity between pCNT and oCNT is that, as the functional groups present in oCNT decompose during the early stage of oxidation, this creates defect sites for oxygen to react and enhance the combustion process. In addition the Raman fitting for pCNT and oCNT shows a narrowing of the D peak for oCNT which indicates an improvement of the structural order of the sample and/or a decrease in the structural heterogeneity of the carbon sample (a decrease in the pyrolytic carbon content) (Tab 7-1).

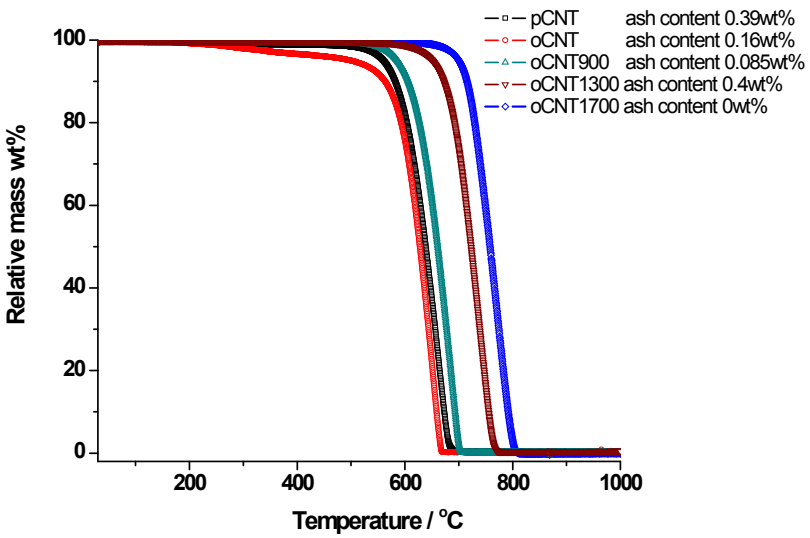

Figure 7-4. Thermogravimetric analysis, weight profile of CNT samples in 5% O_2/Ar

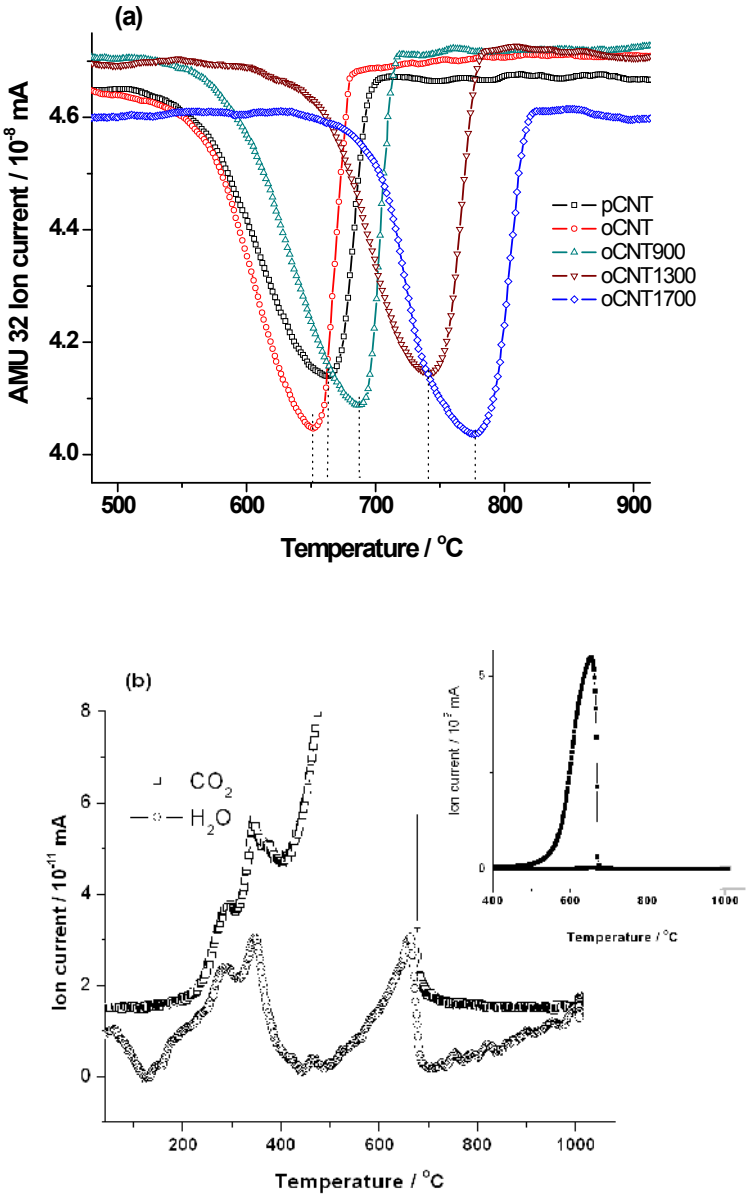

Figure 7-5. Oxidation profiles of the CNT samples under 5% O_2 /Ar at 5 °C min-1 (a), and CO_2, H_2O evolution from the oxidation experiment of oCNT (b), inset: full scale of the CO_2 and H_2O evolution.

Despite similar I_D/I_G values oCNT and oCNT-900 have clearly different oxidation stabilities as depicted in the TG curves. TPD experiments showed that after the heat treatment at 900°C most of the functional groups possibly present in both the oxidation debris and/or the CNTs were removed. The rearrangement of carbon-carbon networks in the sample in the expense of the surface functionalities decomposition is therefore possible from both the oxidation debris and/or the

CNTs.[28] The improvement of the structural ordering after the thermal treatment is well identified in the Raman spectra especially with the narrowing of the D and G peaks (Appendix 7-1). The contribution of the D2 peak was also minimized after the annealing at 900°C. For samples annealed at higher temperatures the oxidation stability further improves as seen in the TG experiment due to the enhanced order of the structures. As expected, the D and G peaks in Raman spectra are narrowing gradually with the thermal treatment.

In order to investigate the effect of the chemical oxidative treatment and the heat treatment on the samples texture, N_2 adsorption isotherms of the pristine and treated CNT samples were performed (Tab. 7-1 and Fig. 7-6). There were no significant differences in the specific surface areas of the CNT samples after the treatments, which is in agreement with the SEM investigation showing the bundled and entangled morphology of the CNTs. In conclusion the chemical oxidative treatments used in the current work caused minimum damage to the CNTs and are selective to the removal of pyrolytic carbon.

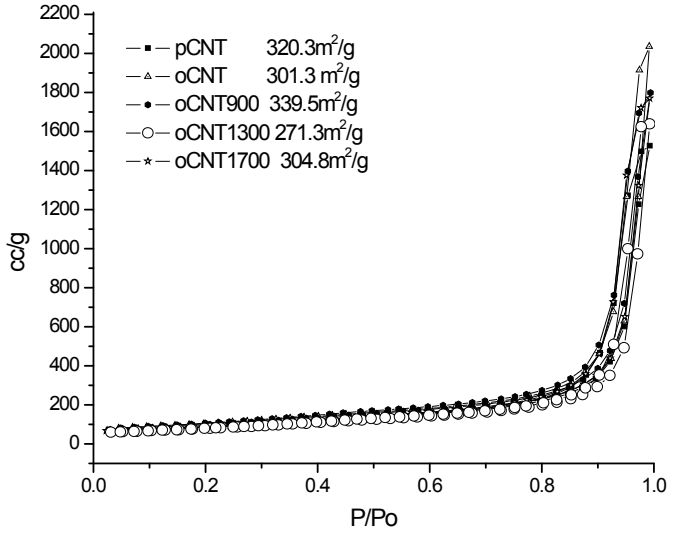

Figure 7-6. N_2 adsorption isotherms of as received and treated NC3100 CNT samples.

7.2. CNTs as catalyst for ODH reactions and the effect of purification and annealing treatment

The surface modification of the CNT samples by the above reported purification treatment has been further investigated by application of the modified CNTs as catalysts in ODH reactions, which were here applied as probe methods for structure-activity correlations. The activity and selectivity pattern of the ODH is well-known to be highly sensitive to changes in the active domain, especially for challenging substrates such as propane. The use of carbon catalysts in the ODH of ethylbenzene is an established field of research, thus we tested the samples also for this substrate.

Fig. 7-7a displays the initial evolution of the catalytic activity in the ODH of propane with time on stream. Each CNT sample displays a good stability after several hours under reaction conditions. Catalytic performances after 24 h time on stream are listed in Tab. 7-2. The ODH reaction rates are given as the amount of substrate converted per time and catalyst weight. The higher rates for EB as compared to propane ODH nicely reflect the different C-H bond strengths in these molecules (C_3H_8: 410.5 kJ mol^{-1}; EB: 357.3 kJ mol^{-1}). The higher activity of the oCNT sample as compared to pristine and heat-treated CNT samples is evident for both hydrocarbon substrates. The activity of the pristine and heat-treated samples in general gradually increases during the induction period, as shown for ODH of propane in Fig. 7-7a. This indicates the formation of active sites, i.e., oxygen functionalities, under reaction conditions. The oCNT sample in ODH of ethylbenzene is an exception: here, the activity decreases with time. This behaviour is attributed to the decomposition of surface functionalities present in oCNT sample under the reaction condition, nicely reflected in the negative change of the I_D/I_G band ratio before and after catalysis as compared to the temperature treated samples (Tab. 7-1). This might be related to the lower oxygen concentration and lower O/C ratio as compared to propane ODH experiments. Another possibility is the different requirement for spatial rearrangement of oxygenic active sites for the ODH turnover due to the quite discrepant sizes of propane and ethylbenzene molecules. The resulting loss of oxidation potential will result in a lower quasi-equilibrium surface concentration of oxygen functional groups as initially given by HNO_3 treatment. As a result, the

surface defects act as nuclei for the formation of soot, which causes the catalyst deactivation.

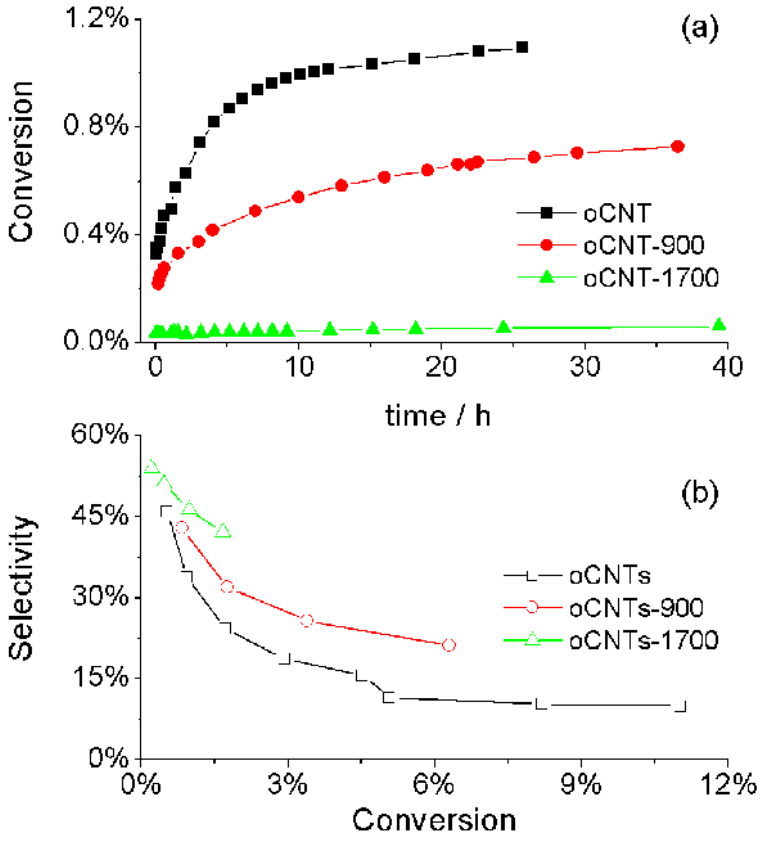

Figure 7-7. Initial activation period of selected CNTs samples during ODH of propane (a); propene selectivity as a function of propane conversion (b); 400 °C, $C_3H_8/O_2/He$ = 5:5:90.

The highest degree of surface functionalization on the oCNT sample is confirmed by TPD data showing the intense decomposition of carboxyl and anhydride groups giving rise to CO_2 and CO releases (Fig. 7-3). The CO_2 and CO signals during the TPD experiments are suppressed for pristine and heat-treated samples. In addition, the carbon surface modification during ODH reaction is clearly manifested in a change of the I_D/I_G value (Tab. 7-1). For the oCNT sample, subjection to oxidative gas phase at 400°C results in a lowering of the I_D/I_G value, attributed to further removal of pyrolytic carbon. However, as different initial behaviour in ethylbenzene and propane ODH shows, this is not directly correlated with surface functionalization. It appears that the relatively low temperature used for the reaction 400 °C provides

enough energy for the carbon-carbon rearrangements. In addition the heat treatment at 900°C did not give any significant carbon bonds rearrangements to be detected by Raman spectroscopy (Tab. 7-1). Similar observation by Delgado et al reported the decreased I_D/I_G value of graphite felt supported carbon nanofibers catalyst after ODH reaction.[29]

It is evident that the overall ODH activities of the CNTs samples are inversely proportional to their treatment temperatures (Fig. 7-7a, Tab. 7-2). This behaviour correlates with the defect density present in the CNTs samples[20-23] reflected in the intensities of D- and G-peak (Fig. 7-8) and is in accordance with the oxidation stability data from TG experiments (Fig. 7-4 & 7-5). The latter is inversely proportional to the amount of defects and/or structure graphitization of the CNT samples. The oxidation of heat-treated oCNT samples during the induction period in the ODH reaction leads to an increase of the I_D/I_G value (Tab. 7-1). Coke deposition from unselective (non-oxidative) side reactions during ODH on these samples is not straightforward and not obvious from TEM analysis (Fig. 7-9). This is all the more unlikely due to incomplete oxygen conversion during all experimental runs. The effect of surface functional groups created by the chemical oxidative treatments is obvious when comparing the activity of oCNT and oCNT-900. Despite similar I_D/I_G value, oCNT-900 with minimum surface functionalities showed half the activity of oCNT. A slow increase of activity evidences the re-formation of these functionalities (Fig. 7-7a), anyway, for oCNT-900, the given ODH reaction conditions are not able to induce the recreation of a similar amount (probably also type) of functional groups favourable for the ODH reaction within several days time-on-stream.

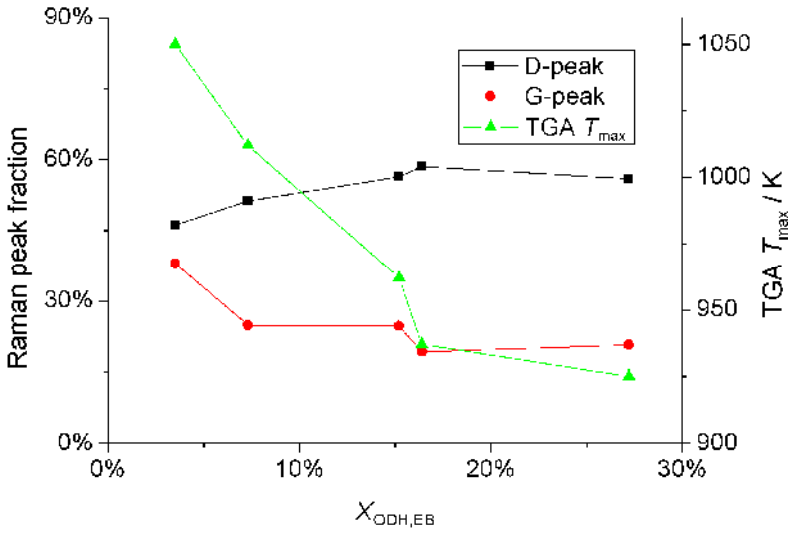

Figure 7-8. Correlation of the activity in ODH of ethylbenzene with the D- and G-peak height (Appendix 7-1) and with the maxima of oxygen consumption during TPO experiments (Tab. 7-1).

Besides overall activity, the oxidative and heat treatments also affect the formation of the desired ODH reaction products, styrene and propene. For ODH of propane, after variation of GHSV at 400°C and comparison at iso-conversion (Fig. 7-7b), a clear tendency of increasing selectivity with increasing annealing temperature can be observed. This trend also holds for the ODH of EB experiments. However, as the EB conversion is up to 27% for this substrate, the styrene selectivity is not solely affected by the catalyst microstructure but also by kinetic limitation due to consecutive styrene combustion. It appears that the higher the degree of graphitization of the CNTs, reflected in a lower I_D/I_G value, the higher is the ODH selectivity. The reason for this structure-activity relationship remains unclear. Delgado et al. observed a similar trend for the ODH activity of CNT samples with 50–100 nm in external diameter annealed at different temperature.[30] It seems that the amount of functional groups and a change in the nature of active sites on the CNT surface is responsible for enhanced formation of styrene and propene. For the ODH of ethylbenzene, the selectivity as a function of the conversion over the tested samples without variation of GHSV reveals a straight line with the pCNTs being the only exception (Fig. 7-10). This is clear evidence that the catalytically active carbon domains change during the oxidative purification. However, the consecutive annealing treatment induces further substantial change in the carbon microstructure

and the total number of active sites affecting the selectivity of ODH catalytic turnover (Fig. 7-7b). It is an interesting analogy that also for the ODH of propane over VO_x/Al_2O_3 a higher surface concentration of vanadia active sites results in a lower propene selectivity at iso-conversion[31], however, a mass transfer barrier lowering the propene yield can be excluded due to the low overall activity of the carbon catalysts.[32] On the other hand, Zhang et al. reported that during ODH reaction of *n*-butane, the desorption of labile functional groups creates new defects that under O_2 exposure will generate new electrophilic oxygen sites lowering the selectivity to butene.[3] Thus it is reasonable to assume that under similar analogy the pyrolytic carbon will facilitate the creation of labile functional groups due to its combustion reactivity in comparison to graphitic carbon. It is therefore suspected that the difference in styrene selectivity between pCNT and oCNT-900 may be attributed to the removal of pyrolytic carbon, as both samples were shown from TPD experiments to have similar evolution from surface functionalities decomposition (Fig. 7-3). The similar activity (EB conversion) of both samples supports the arguments that they have similar amount of oxidative sites.

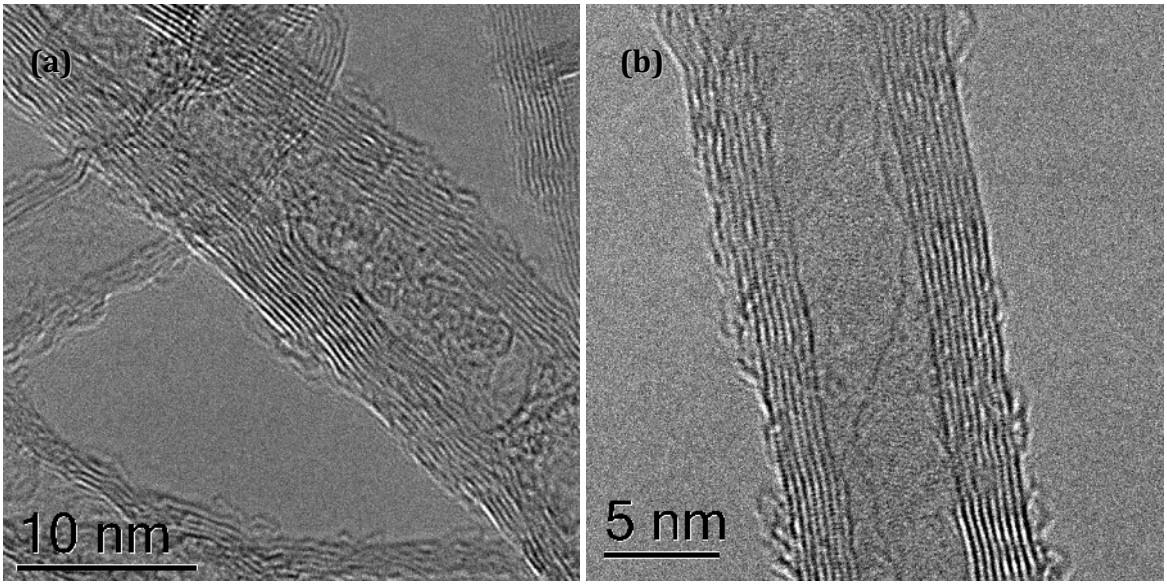

Figure 7-9. TEM image of oCNT-1700 after ODH of ethylbenzene.

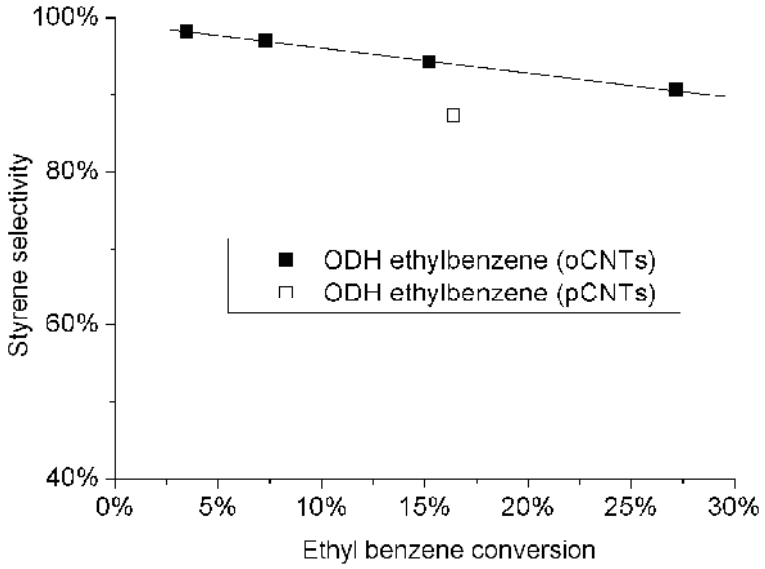

Figure 7-10. Selectivity in the ODH of ethylbenzene over the as received and HNO_3-oxidized CNTs

Table 7-2. Catalytic performance of pristine and treated CNTs in oxidative dehydrogenation of ethylbenzene and propane at 400°C.

Sample	ODH of propane	ODH of EB		
	Rate [mmol g^{-1} h^{-1}]	Rate [mmol g^{-1} h^{-1}]	Conversion [%]	Selectivity [%]
pCNT	-	2.54	16.4	87.3
oCNT	1.36	4.21	27.2	90.6
oCNT-900	0.85	2.36	15.2	94.2
oCNT-1300	-	1.13	7.3	97.0
oCNT-1700	0.068	0.55	3.5	98.2

7.3. Conclusion

The above results show that pyrolytic carbon is partially removed after the mild oxidative HNO_3 and NaOH washing. The chemical treatment introduced a significant amount of surface functionalities in a broad range of thermal stability onto the CNTs and possibly also on the remaining amorphous debris. The annealing process under inert atmosphere further removes the surface functionalities, heals the graphitic structure and improves the oxidation stability of the CNTs with increasing annealing temperature. CNT samples after each treatment showed different activity for ODH reactions but provided similar trends for both EB and propane. With increasing annealing temperature the activity of the CNTs towards ODH dropped as a consequence of structural rearrangements of the carbon networks resulting in the removal of functionalities and defects in the CNT sample (Fig. 7-8). The selectivity towards styrene and propene for the ODH of EB and propane respectively showed a positive trend towards the more graphitic character of the sample. The origin of such pronounced structure-activity relationship may be found in the different structure and surface concentration of oxygen functionalities present either on pyrolytic carbon deposits (oCNTs) or on the edges of surface defects in the outer graphene layer(s) of the annealed CNT samples.

References

(1) Zhang, J.; Su, D.; Zhang, A.; Wang, D.; Schlögl, R.; Hébert, C. Nanocarbon as Robust Catalyst: Mechanistic Insight into Carbon-Mediated Catalysis13. *Angewandte Chemie* **2007**, *119*, 7460-7464.

(2) Liu, X.; Su, D. S.; Schlögl, R. Oxidative dehydrogenation of 1-butene to butadiene over carbon nanotube catalysts. *Carbon* **2008**, *46*, 547-549.

(3) Zhang, J.; Liu, X.; Blume, R.; Zhang, A.; Schlogl, R.; Su, D. S. Surface-Modified Carbon Nanotubes Catalyze Oxidative Dehydrogenation of n-Butane. *Science* **2008**, *322*, 73-77.

(4) Frank, B.; Zhang, J.; Blume, R.; Schlögl, R.; Su, D. Heteroatoms Increase the Selectivity in Oxidative Dehydrogenation Reactions on Nanocarbons13. *Angewandte Chemie International Edition* **2009**, *48*, 6913-6917.

(5) Shimada, T.; Yanase, H.; Morishita, K.; Hayashi, J.; Chiba, T. Points of onset of gasification in a multi-walled carbon nanotube having an imperfect structure. *Carbon* **2004**, *42*, 1635-1639.

(6) Sadezky, A.; Muckenhuber, H.; Grothe, H.; Niessner, R.; Pöschl, U. Raman microspectroscopy of soot and related carbonaceous materials: Spectral analysis and structural information. *Carbon* **2005**, *43*, 1731-1742.

(7) Tuinstra, F. Raman Spectrum of Graphite. *J. Chem. Phys.* **1970**, *53*, 1126.

(8) Sato, K.; Saito, R.; Oyama, Y.; Jiang, J.; Cançado, L.; Pimenta, M.; Jorio, A.; Samsonidze, G.; Dresselhaus, G.; Dresselhaus, M. D-band Raman intensity of graphitic materials as a function of laser energy and crystallite size. *Chemical Physics Letters* **2006**, *427*, 117-121.

(9) Nakamura, K.; Fujitsuka, M.; Kitajima, M. Disorder-induced line broadening in first-order Raman scattering from graphite. *Phys. Rev. B* **1990**, *41*, 12260.

(10) Osswald, S.; Flahaut, E.; Ye, H.; Gogotsi, Y. Elimination of D-band in Raman spectra of double-wall carbon nanotubes by oxidation. *Chemical Physics Letters* **2005**, *402*, 422-427.

(11) Osswald, S.; Flahaut, E.; Gogotsi, Y. In Situ Raman Spectroscopy Study of Oxidation of Double- and Single-Wall Carbon Nanotubes. *Chemistry of Materials* **2006**, *18*, 1525-1533.

(12) Osswald, S.; Havel, M.; Gogotsi, Y. Monitoring oxidation of multiwalled carbon nanotubes by Raman spectroscopy. *Journal of Raman Spectroscopy* **2007**, *38*, 728-736.

(13) Figueiredo, J. L.; Pereira, M. F. R.; Freitas, M. M. A.; Órfão, J. J. M. Modification of the surface chemistry of activated carbons. *Carbon* **1999**, *37*, 1379-1389.

(14) Szymanski, G. S.; Karpinski, Z.; Biniak, S.; Swiatkowski, A. The effect of the gradual thermal decomposition of surface oxygen species on the chemical and catalytic properties of oxidized activated carbon. *Carbon* **2002**, *40*, 2627-2639.

(15) Calo, J. M.; Cazorla-Amorós, D.; Linares-Solano, A.; Román-Martínez, M. C.; De Lecea, C. S. The effects of hydrogen on thermal desorption of oxygen surface complexes. *Carbon* **1997**, *35*, 543-554.

(16) Zhuang, Q.; Kyotani, T.; Tomita, A. The change of TPD pattern of O2-gasified carbon upon air exposure. *Carbon* **1994**, *32*, 539-540.

(17) Aksoylu, A. E.; Madalena, M.; Freitas, A.; Pereira, M. F. R.; Figueiredo, J. L. The effects of different activated carbon supports and support modifications on the properties of Pt/AC catalysts. *Carbon* **2001**, *39*, 175-185.

(18) Schlögl, R. In *Handbook of Heterogeneous Catalysis*; Ertl, G.; Knözinger, H.; Schüth, F.; Weitkamp, J., Eds.; Wiley-VCH, 2008; pp. 357-427.

(19) Ma, M.; Brown, T.; Haynes, B. Evaluation of thermal desorption spectra for heterogeneous surfaces: application to carbon surface oxides. *Surface Science* **1993**, *297*, 312-326.

(20) Kim, Y. A.; Hayashi, T.; Osawa, K.; Dresselhaus, M. S.; Endo, M. Annealing effect on disordered multi-wall carbon nanotubes. *Chemical Physics Letters* **2003**, *380*, 319-324.

(21) Kim, Y.; Muramatsu, H.; Hayashi, T.; Endo, M.; Terrones, M.; Dresselhaus, M. Thermal stability and structural changes of double-walled carbon nanotubes by heat treatment. *Chemical Physics Letters* **2004**, *398*, 87-92.

(22) Behler, K.; Osswald, S.; Ye, H.; Dimovski, S.; Gogotsi, Y. Effect of Thermal Treatment on the Structure of Multi-walled Carbon Nanotubes. *Journal of Nanoparticle Research* **2006**, *8*, 615-625.
(23) Endo, M.; Kim, Y.; Hayashi, T.; Yanagisawa, T.; Muramatsu, H.; Ezaka, M.; Terrones, H.; Terrones, M.; Dresselhaus, M. Microstructural changes induced in "stacked cup" carbon nanofibers by heat treatment. *Carbon* **2003**, *41*, 1941-1947.
(24) Tessonnier, J.; Rosenthal, D.; Hansen, T. W.; Hess, C.; Schuster, M. E.; Blume, R.; Girgsdies, F.; Pfänder, N.; Timpe, O.; Su, D. S.; Schlögl, R. Analysis of the structure and chemical properties of some commercial carbon nanostructures. *Carbon* **2009**, *47*, 1779-1798.
(25) Wen, W. Mechanisms of Alkali Metal Catalysis in the Gasification of Coal, Char, or Graphite. *Catalysis Reviews: Science and Engineering* **1980**, *22*, 1.
(26) McKee, D. Mechanisms of the alkali metal catalysed gasification of carbon. *Fuel* **1983**, *62*, 170-175.
(27) Ramesh, P.; Okazaki, T.; Sugai, T.; Kimura, J.; Kishi, N.; Sato, K.; Ozeki, Y.; Shinohara, H. Purification and characterization of double-wall carbon nanotubes synthesized by catalytic chemical vapor deposition on mesoporous silica. *Chemical Physics Letters* **2006**, *418*, 408-412.
(28) Conway, N.; Ilie, A.; Robertson, J.; Milne, W.; Tagliaferro, A. Reduction in defect density by annealing in hydrogenated tetrahedral amorphous carbon. *Applied Physics Letters* **1998**, *73*, 2456-2458.
(29) Delgado, J.; Su, D.; Rebmann, G.; Keller, N.; Gajovic, A.; Schlögl, R. Immobilized carbon nanofibers as industrial catalyst for ODH reactions. *Journal of Catalysis* **2006**, *244*, 126-129.
(30) Delgado, J.; Chen, X.; Tessonnier, J.; Schuster, M.; Del Rio, E.; Schlögl, R.; Su, D. Influence of the microstructure of carbon nanotubes on the oxidative dehydrogenation of ethylbenzene to styrene. *Catalysis Today* **2010**, *150*, 49-54.
(31) Schwarz, O.; Frank, B.; Hess, C.; Schomäcker, R. Characterisation and catalytic testing of VOx/Al2O3 catalysts for microstructured reactors. *Catalysis Communications* **2008**, *9*, 229-233.
(32) Frank, B.; Dinse, A.; Ovsitser, O.; Kondratenko, E.; Schomäcker, R. Mass and heat transfer effects on the oxidative dehydrogenation of propane (ODP) over a low loaded VOx/Al2O3 catalyst. *Applied Catalysis A: General* **2007**, *323*, 66-76.

Chapter 8

Conclusion and outlook

One of the aims in nanocarbon research is to produce material with uniform and controlled microstructure. It is important in the final application to have defined “active” sites for interacting with other matrices. Direct synthesis of uniform, pyrolytic carbon-free, minimum catalyst impurities is desired for mass production. Another approach is post-treatment to remove the nanocarbon samples from unwanted pyrolytic carbons and inorganic elements.

This thesis is composed of two works with the objective for controlled modification of CNTs from direct synthesis and post treatment. The first aspect of the work deals with the study of catalytic synthesis of CNT/CNFs on carbon-supported Ni catalyst and the second is the purification of commercial CNT samples.

The first part of this thesis (Chapter 4 & 5) presents sets of experiments to investigate metal-carbon support interaction with the final goal for controlled modification of the carbon surface via carbon interconnect (carbon-carbon composite). Ni nanoparticles supported on various carbon supports were used in this investigation. In chapter 4 it is obvious that there exist support effect when growing CNF/CNF with Ni catalyst. Ni/Graphite exhibit significantly higher activity to grow graphitic nanocarbons as compared to Ni/Activated Carbon and Ni/herringbone CNF. In Chapter 5 Vapor grown carbon nanofiber (VGCNF) annealed at 900^{o}C and 3000^{o}C were used as “model” carbon support for defective and graphitic carbon respectively. The experiments resulted in several profound observations. First is the influence of graphitic character of the support in governing the activity of the metal catalyst. The choice of CNT synthesis as the probe reaction is beneficial from the standpoint that one can directly visualizes the effect exerted by the support to the metal catalyst. The second important observation is that the effect exerted by the support persisted even though the catalyst have

lost contact with the support as the CNTs grow away from the support with a tip-based mechanism. Investigations of the Ni/VGCNF catalysts with HR-TEM, in situ XRD and in situ XPS strongly suggest that carbon atoms from support dissolved into the bulk and surface/subsurface of the Ni catalyst. The bulk carbon dissolution is observed for Ni/defective carbon while the subsurface and surface dissolution is for Ni/graphitic carbon. The characterizations of the catalyst demonstrate that Ni catalyst suffers structural and electronic modification with the dissolution of carbon atoms. The effect of the dissolved carbon is clearly thermodynamic with respect to the CNT growth. The HRTEM and in situ XRD characterizations of the catalyst demonstrate that reduced Ni catalyst suffers structural modification such lattice expansion, lattice defects, dislocations, strains with the dissolution of carbon atoms from the defective support. The Ni2p XPS spectrum shows higher contribution of the carbidic Ni binding energy in the defective carbon support as compared to Ni/graphitic carbon.

Several facts have been proven from the work in this thesis regarding carbon materials as catalyst support. One is the role of reactive carbon support to provide carbon atoms into the surface and/or the bulk of metal catalyst. Second carbon dissolution from the support is temperature dependent character and third the dissolved carbon is responsible in modifying the activity of a catalyst. The perspective is now clear on the importance of carbon support treatment prior to catalyst deposition and activation of supported catalyst. The use of reactive carbon as catalyst supports such as defective CNTs, porous carbons, carbon blacks, highly oxidized CNTs, and finally amorphous carbon should be taken into great care to avoid over contamination of the catalyst leading to full deactivation. A wrong way of functionalizing the carbon support may eventually lead to the favored formation of this dissolved carbon phase. The appropriate calcination and reduction temperature/conditions are among several important parameters that can have great influence in carbon contamination and the final catalytic activity.

Incomplete combustion of metal-organic precursor and solvent pyrolysis via ultrasonic irradiation has also been reported to introduce some interstitial carbon into metal catalyst.[1]

Several further future experiments are proposed in this chapter to further shed light into the CNT mechanism and the role of metal-carbon interaction in general. The proposed experiments are:

1. As there is a registry between the Ni surface orientations with graphene, thus a perfect Ni surface will provide a template for perfect graphene, whereas a distorted or defective Ni surface will result in precipitation of defective graphene. Proposed experiments to prove this are by investigating Ni/SiO_2 or Ni/Al_2O_3 or even Ni/graphitic carbon and reduce the catalyst in two different ways that it produces Ni metal with different crystallinity (e.g. by different rate and time). By performing the CNT growth from these two states of Ni metal crystalinity (perfect Ni and defect-rich Ni or incomplete Ni reduction) the resulting CNT microstructure open more facts onto whether dissolved carbon gives only a chemical barrier to carbon diffusion or only structural barrier.

2. As clearly seen throughout TEM images, between herringbone, platelet and tubular CNT carbon diffuses at different rates on different metal facets. This equilibrium is somewhat only determined in the beginning of the growth. Further pulsing experiments with other systems and/or other metal should provide a universal understanding of CNT growth mechanism.

3. In situ heating TEM experiments can be very useful to check if the Ni catalyst is hardened/less mobile after carbon dissolution. As frequently used in material science dissolved carbon is used as a hardening agent for Ni. Active catalyst in CNTs and graphitization is known to have one similarity; they all have liquid-like mobility although the bulk of material is observed to be crystalline solid.[2] Helveg et al observed that the continuous formation of step edges is partly responsible for the precipitation f graphitic carbon. [3] If the mobility of Ni metal is disrupted and accompanied with the loss graphitic CNT microstructure, then one can make a strong argument about the role of dissolved carbon.

4. Synthesizing CNT with Ni-Cu or Ni-Al intermetallic compound allowing the other element Cu, Al to act as a chemical barrier for carbon to dissolve into the intermetallic

compound during ethylene exposure. Similar approach has been proven to work by using Pd-Ga intermetallic compound for selective acetylene hydrogenation to ethylene with longer lifetime.[4,5]

5. Core-shell nanoparticles is also an interesting candidate to be used as catalyst with the shell being Ni (or Co, Fe) and the core being another element with minimum or no carbon solubility. The concept is to provide a chemical and geometrical barrier for the carbon to diffuse through.

6. A set of experiments to perform re-grow of CNT from an already growing CNT (after cooling down) from a given catalyst system will also contribute to the understanding of metal-carbon support interaction. It will of interest to know if the catalyst still retain the microstructure of the CNT or developed new structural modification (after probably a regeneration treatment: calcination/oxidation and reduction).

7. Performing CNT growth with CCVD of ethylene under UV exposure. The function of the UV radiation (~160nm for ethylene) is to excite the ethylene molecules (or longer wavelengths for more conjugated carbon precursor, or carbon molecules intermediates in the CVD chamber). The excited ethylene molecules can introduce different kind of reactivity that plausibly will change the way CNT grow by the interaction of the excited organic molecules (ethylene and/or more developed hydrocarbons or short carbonaceous material) with the catalyst and/or with the edges/defects of the growing CNTs. From this point of view this approach is novel. Chemical modification of the CNT surface with carbonaceous material is possible.

Test experiments by pre-dosing the Ni/graphitic carbon with ethylene prior to the growth step further support the argument that dissolved carbon is responsible for the change of the CNT microstructure (Chapter 5 p130-5). The experiments suggest that there is a relationship between the amount of carbon dissolved at a specific temperature with the final microstructure of CNTs. The disorientation of graphene layers in the CNTs relative to the

filament axis is obvious after the pre-dosing with ethylene (Fig 5-14). This observation tempted the speculation that the dissolved carbon change the way the carbon atoms diffuses in and/or on the Ni catalyst during CNT growth.

It is still not clear however whether the carbons dissolved prior to the CNT growth were ejected as solid carbons and regenerated by the incoming ethylene or they remain dissolved in the catalyst all the time.

In second part of this thesis, three post-treatment methods have been used and investigated to remove pyrolytic carbon from the surface of commercial CNTs (Chapter 6). The post-treatment methods are gaseous oxidation, mild HNO_3 washing and ultrasonic irradiation. The first two represent the most common method used in the literatures, whereas the ultrasonic irradiation is relatively new. It is observed that the ultrasonic irradiation is the best method that would compromise between removal of pyrolitic carbon, with minimum loss of material and minimum damage to the CNT surface itself. Surprisingly the ultrasonication method is also able to remove the metal content from the commercial sample. The mechanism on how that particular effect works is yet to be identified. Another interesting finding from the ultrasonication method is the controlled functionalization of the CNT surface with hydrocarbon molecules as a result of sonolytic reaction with the organic solvents used in the suspension. These hydrocarbon functionalities can be easily decomposed above $600^{o}C$ under inert atmosphere. The functionalization from ultrasonic irradiation resulted in a different distribution of surface functional groups as compared to HNO_3 treatment. Selectivity towards quinone and hydroquinone is more pronounced than HNO_3 treatment (Fig 6-22).

On the other hand these functionalities offer an interesting way to modify the surface of CNTs to interact with other substrates. There may well be opportunity to functionalize the carbon surface with Nitrogen containing hydrocarbons from ultrasonic irradiation with N-containing organic solvents. The structural integrity and the constant amount of CO and CO_2-releasing groups suggest that the sonication method functionalize the CNT surface with better dispersion than e.g. HNO_3 treatment. Simple dispersion experiment (carried out during the TEM

sample preparation of CNTs) show that THF-sonicated CNTs has much faster affinity to dispersed in polar organic solvents.

The ultrasonication irradiation method also proves to be an effective treatment to remove oxidation debris from highly oxidized CNT samples. The flexibility of this method to remove loose structural carbon impurities (pyrolytic carbon and oxidation debris) from the graphitic CNT surface renders this method for application such as catalysis. However further experiments and characterization of functional groups is of importance to exploit this simple way to functionalize the CNT surface.

The effect of the disordered carbon impurities is also addressed in this thesis with the reactivity of the CNT samples (as-received and treated) for the oxidative dehydrogenation of (ODH) styrene and propane (Chapter 7). The presence of metal and disordered carbon impurities is demonstrated to be detrimental for the integrity of the CNT catalyst and selectivity of the reactions.

Future experiments with Br_2 treatment to destroy the C=C groups especially within the pyrolytic carbon impurities can potentially be a good method to purify the CNT sample. This method allows the functionalization and shortening of the pyrolytic carbon allowing for easy detachment from the bulk of the CNT. Another interesting and novel method to functionalize and remove pyrolytic carbon is by the exploitation of photochemistry. Soot is suggested to have fullerene-like structure. Reaction with singlet oxygen and/or other reactive oxygen species after photo irradiation of the CNT sample can potentially have the effect to oxidize the fullerene-like disordered carbon impurities to be selectively oxidized. The presence of reactive oxygen species were previously reported to be enhanced by fullerene.[6,7] This approach relies for the fullerene-like carbons to act as the catalyst for their own destruction. These methods may finally offer more selective functionalization/oxidation of the disordered carbon impurities in CNT.

As a final word, carbons have found paramount importance in the various applications including catalysis in the last century. The lack of understanding of this material and especially its interaction with metal catalyst hindered their further exploitation. With this thesis I hope to contribute to the general understanding into the metal-carbon support interaction, the

mechanism of how CNT growth and eventually for the chemical and physical modification of the CNTs.

Reference

(1) Mason, T. J.; Lorimer, J. P. *Applied sonochemistry*; Wiley-VCH, 2002.
(2) Anton, R. On the reaction kinetics of Ni with amorphous carbon. *Carbon* **2008**, *46*, 656-662.
(3) Helveg, S.; Lopez-Cartes, C.; Sehested, J.; Hansen, P. L.; Clausen, B. S.; Rostrup-Nielsen, J. R.; Abild-Pedersen, F.; Norskov, J. K. Atomic-scale imaging of carbon nanofibre growth. *Nature* **2004**, *427*, 426-429.
(4) Armbrüster, M.; Kovnir, K.; Behrens, M.; Teschner, D.; Grin, Y.; Schlögl, R. Pd−Ga Intermetallic Compounds as Highly Selective Semihydrogenation Catalysts. *Journal of the American Chemical Society* **2010**, *132*, 14745-14747.
(5) Kovnir, K.; Armbrüster, M.; Teschner, D.; Venkov, T.; Jentoft, F.; Knop-Gericke, A.; Grin, Y.; Schlögl, R. A new approach to well-defined, stable and site-isolated catalysts. *Sci. Technol. Adv. Mater.* **2007**, *8*, 420-427.
(6) Juha, L.; Hamplov?, V.; Kodymov?, J.; ?palek, O. Reactivity of fullerenes with chemically generated singlet oxygen. *J. Chem. Soc., Chem. Commun.* **1994**, 2437.
(7) Carofiglio, T.; Donnola, P.; Maggini, M.; Rossetto, M.; Rossi, E. Fullerene-Promoted Singlet-Oxygen Photochemical Oxygenations in Glass-Polymer Microstructured Reactors. *Adv. Synth. Catal.* **2008**, *350*, 2815-2822.

Appendix

Appendix 3-1. Temperature profile measure *inside* the quartz reactor.

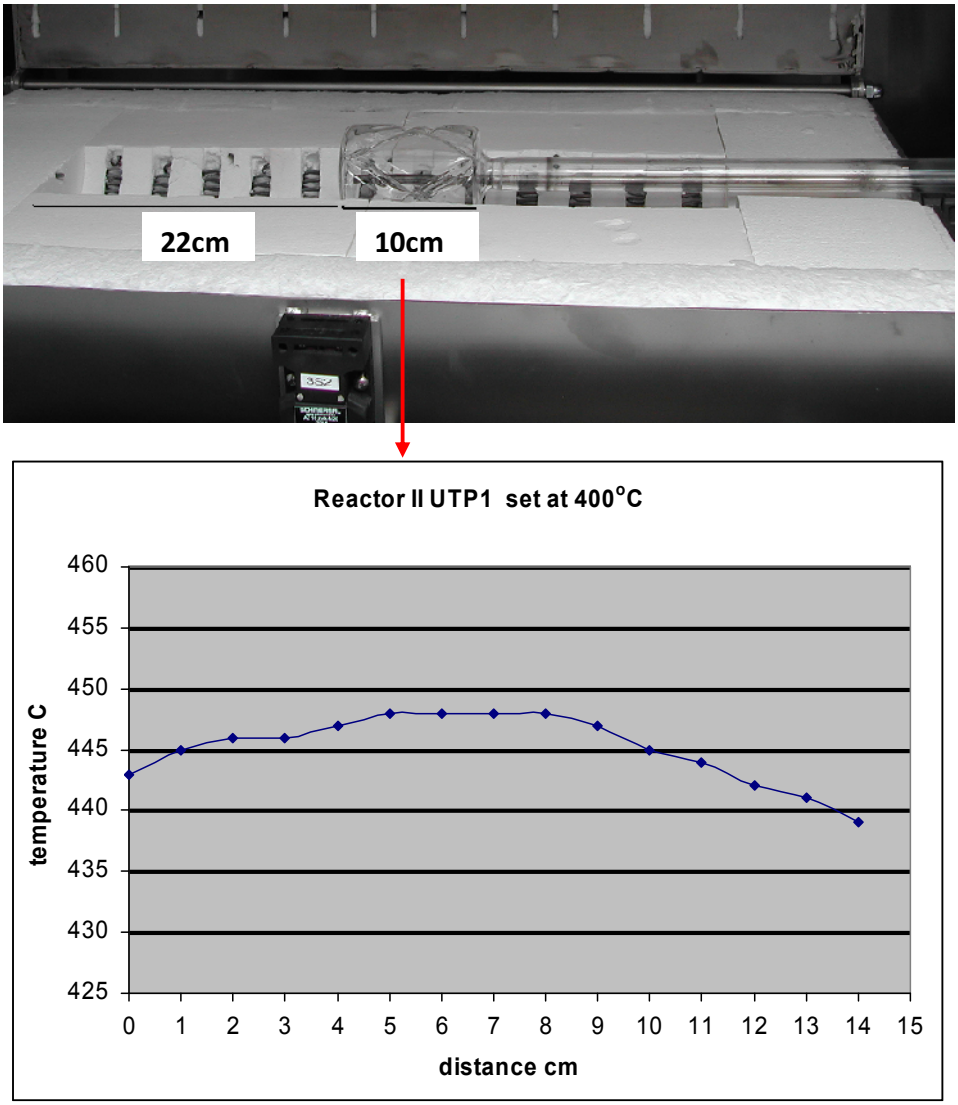

Appendix 3-2. Simulated Temperature programmed oxidation profile of Carbon samples demonstrating variation of degree of thermal runaway, amount of amorphous carbon, Energy of activation, and amount of defects (k) presented as TG plot.

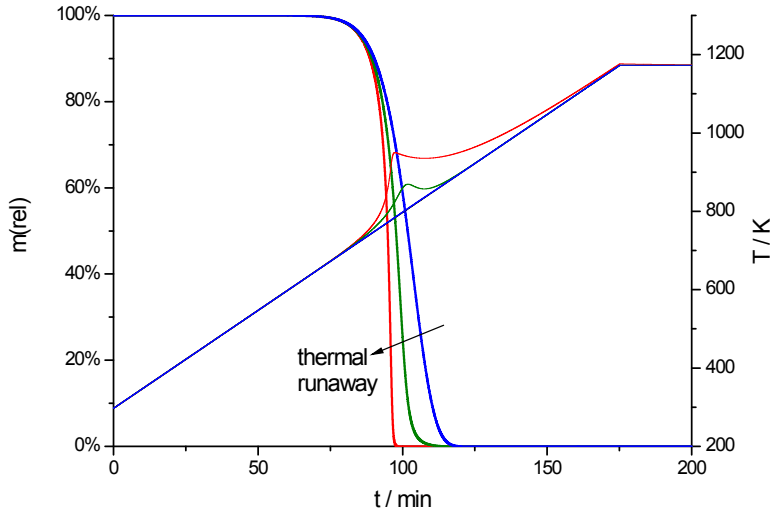

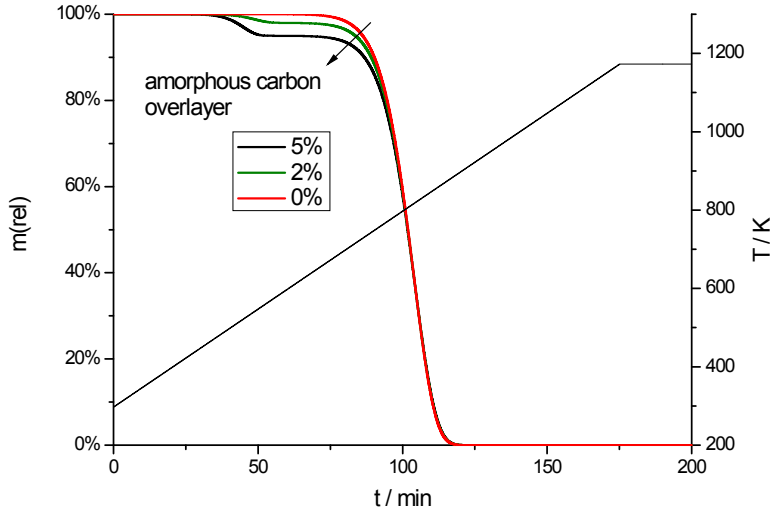

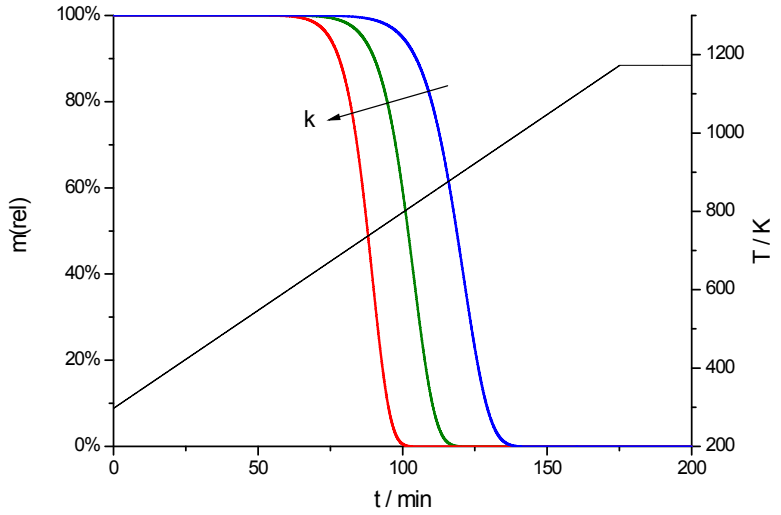
100%
80%
60%
40%
20%
0%
m(rel)
0
50
100
150
200
t / min
1200
1000
800
600
400
200
T / K
k

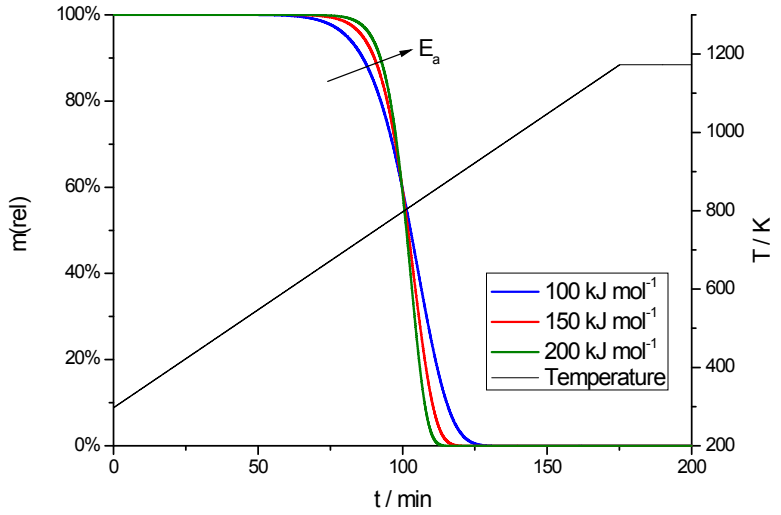
100%
80%
60%
40%
20%
0%
m(rel)
0
50
100
150
200
t / min
1200
1000
800
600
400
200
T / K
E_a
100 kJ mol-1
150 kJ mol-1
200 kJ mol-1
Temperature

Appendix 6-1. Fitting parameter of Raman spectra for Baytubes, HNO_3 treated and ultrasonic irradiation samples.

Sample	Description	Position [cm^{-1}]	Height (a.u.)	FWHM [cm^{-1}]
Baytubes	D3	1180.7	1.41	93.9
	D	1326.2	58.5	79.9
	G	1586.1	19.3	58
	D`	1614.4	9.5	36.7
	D2	1493.7	10.6	172.3
HNO_3	D3	-	-	-
	D	1326.7	55.9	66.9
	G	1584	20.7	57.3
	D`	1614	12	37.4
	D2	1469.4	10.7	207.2
HNO_3-sono 2 h	D3	-	-	-
	D	1328.8	56.3	61.2
	G	1583.9	24.7	55.3
	D`	1616.3	11.3	30.7
	D2	1430.7	5.7	190
HNO_3-sono 3 h	D3	-	-	-
	D	1327.9	51.2	58.7
	G	1581.9	24.9	56.8
	D`	1614.2	16.1	36.2
	D2	1449.2	7.1	199.6
Baytubes-sono 1 h	D3	-	-	-
	D	1329.3	46.1	45.3

	G	1583.5	37.9	42.6
	D`	1617.5	14.5	26.8
	D2	-	-	-
Baytubes-sono 2 h	D3	-	-	-
	D	1329.3	46.1	45.3
	G	1583.5	37.9	42.6
	D`	1617.5	14.5	26.8
	D2	-	-	-
Baytubes-sono 3 h	D3	-	-	-
	D	1329.3	46.1	45.3
	G	1583.5	37.9	42.6
	D`	1617.5	14.5	26.8
	D2	-	-	-

Appendix 7-1. Sample denotations and comparison of the fit parameters from the peaks fitted in the Raman spectra of NC3100 CNT samples.

Sample	Description	Position [cm^{-1}]	Height (a.u.)	FWHM [cm^{-1}]
NC3100	D3	1180.7	1.41	93.9
	D	1326.2	58.5	79.9
	G	1586.1	19.3	58
	D`	1614.4	9.5	36.7
	D2	1493.7	10.6	172.3
oCNT	D3	-	-	-
	D	1326.7	55.9	66.9
	G	1584	20.7	57.3

	D`	1614	12	37.4
	D2	1469.4	10.7	207.2
oCNT900	D3	-	-	-
	D	1328.8	56.3	61.2
	G	1583.9	24.7	55.3
	D`	1616.3	11.3	30.7
	D2	1430.7	5.7	190
oCNT1300	D3	-	-	-
	D	1327.9	51.2	58.7
	G	1581.9	24.9	56.8
	D`	1614.2	16.1	36.2
	D2	1449.2	7.1	199.6
oCNT1700	D3	-	-	-
	D	1329.3	46.1	45.3
	G	1583.5	37.9	42.6
	D`	1617.5	14.5	26.8
	D2	-	-	-